University of Illinois at Urbana-Champaign

ACRC

Air Conditioning and Refrigeration Center A National Science Foundation/University Cooperative Research Center

Use of Nano-Indentation and Nano-Scratch Techniques to Investigate Near Surface Material Properties Associated With Scuffing of Engineering Surfaces

S. R. Pergande, A. A. Polycarpou, and T. F. Conry

ACRC TR-193 December 2001

For additional information:

Air Conditioning and Refrigeration Center
University of Illinois
Mechanical & Industrial Engineering Dept.
1206 West Green Street
Urbana, IL 61801

(217) 333-3115

Prepared as part of ACRC Project #127
Fundamental Investigation on the Tribological
Failure Mechanisms of Compressor Surfaces -Scuffing
A. A. Polycarpou and T. F. Conry, Principal Investigators

The Air Conditioning and Refrigeration Center was founded in 1988 with a grant from the estate of Richard W. Kritzer, the founder of Peerless of America Inc. A State of Illinois Technology Challenge Grant helped build the laboratory facilities. The ACRC receives continuing support from the Richard W. Kritzer Endowment and the National Science Foundation. The following organizations have also become sponsors of the Center.

Alcan Aluminum Corporation
Amana Refrigeration, Inc.
Arçelik A. S.
Brazeway, Inc.
Carrier Corporation
Copeland Corporation
Dacor
Daikin Industries, Ltd.
Delphi Harrison Thermal Systems
General Motors Corporation
Hill PHOENIX
Honeywell, Inc.
Hydro Aluminum Adrian, Inc.
Ingersoll-Rand Company
Invensys Climate Controls
Kelon Electrical Holdings Co., Ltd.
Lennox International, Inc.
LG Electronics, Inc.
Modine Manufacturing Co.
Parker Hannifin Corporation
Peerless of America, Inc.
Samsung Electronics Co., Ltd.
Tecumseh Products Company
The Trane Company
Valeo, Inc.
Visteon Automotive Systems
Wolverine Tube, Inc.
York International, Inc.

For additional information:

Air Conditioning & Refrigeration Center
Mechanical & Industrial Engineering Dept.
University of Illinois
1206 West Green Street
Urbana, IL 61801

217 333 3115

Abstract

Scuffing is a very complex process, without a clear understanding of the fundamental causes behind its occurrence. It is clear that there are many factors that affect this process, but it is only through obtaining an in-depth understanding of the actual conditions (i.e. chemical, topographical, mechanical, and microstructural analyses), that a fundamental cause can be determined. Most prior research has focused on examination of subsurface changes at the micron level. Recent findings suggest that the most significant changes occur in the top 50 – 100 nm of the surface, not at the micron level as previously suggested. The goal of this project is to substantiate this claim that the most significant changes occur in the top 50 – 100 nm, and to quantify the changes in material properties at this level. Microstructural analysis and nano-mechanical methods of determining thin film material properties are used to accomplish these goals.

The nano-mechanical methods that will be used in this work are nano-indentation and nano-scratch techniques. These methods are routinely used in such applications as semi-conductors and magnetic storage hard disk drives. Applying these methods to engineering surfaces is anticipated to be somewhat difficult (and thus, the lack of published works in this area), due to significant roughness, non-homogeneous surfaces and inconsistent layers of unknown and non-uniform thicknesses. Through careful examination and analysis of individual data, it is shown that these methods can in fact be applied to engineering surfaces.

Table of Contents

Page

Abstract iii

List of Figures vii

List of Tables xi

Chapter 1: Introduction 1

1.1 Background 1

1.2 Project Objectives 5

1.3 Tribological Testing and Sample Preparation 6

1.3.1 Materials 6

1.3.2 Tribological Scuffing Experiments 7

Chapter 2: Micro-structural Analysis 8

2.1 Introduction 8

2.2 Sample Preparation: Polishing/Etching 8

2.2.1 Cross Section Sample Preparation 9

2.3 Results 10

2.3.1 Surface / Bulk Microstructure 10

2.3.2 Cross-Sectional Microstructure 11

2.4 Conclusions 14

Chapter 3: Macro-/Micro-Hardness Tests 16

3.1 Introduction 16

3.2 Macro-/Meso-methods: Brinell, Rockwell B, Rockwell C 16

3.2.1 Rockwell B Hardness Test 16

3.3 Micro Hardness Methods: Vickers, Knoop 19

3.3.1 Vickers Hardness Test 19

3.4 Scale Conversions 27

3.5 Conclusions 28

Chapter 4: Nano-Indentation Technique 30

4.1 Introduction 30

4.2 Instrumentation 30

4.3 Nano-Indenter Tips and Tip Area Calibrations 31

4.4 Calculation of Material Properties (E_r and H) 36

4.5 Loading functions 37

4.6 Procedure 41

4.6.1 Sensor Drift 41

4.6.2 Sample/Tip Cleaning 41
4.6.3 Air Indent 41
4.6.4 Fused Quartz Check 42
4.6.5 Measurement Area - Peak vs. Valley 42
4.7 Nano-Indentation Experiments on Fused Quartz 44
4.8 Nano-Indentation Experiments on Silicon 48
4.9 Engineering Sample Obstacles: Al390-T6 50
4.9.1 Surface Roughness / Peak vs. Valley Measurement 50
4.9.2 Choice of Loading Function 51
4.9.3 Exclusion of Data - Silicon Particles 52
4.9.4 Statistical Analysis of Data 56
4.10 Engineering Sample Preparation for Nano-Indentation Testing 57
4.10.1 Test Area 57
4.10.2 Sample Mounting 58
4.11 Al390-T6 Results 59
4.11.1 Virgin Results 59
4.11.2 Al390-T6: ¼ Scuffed Results 63
4.11.3 Al390-T6: ½ Scuffed Results 67
4.11.4 Al390-T6: ¾ Scuffed Results 70
4.11.5 Al390-T6: Scuffed Results 73
4.12 Al390-T6 Sample Trends 78
4.13 Conclusions 80
Chapter 5: Nano-Scratch Technique 85
5.1 Introduction 85
5.2 The Instrument Used for Nano-Scratch Experiments 86
5.3 Calculation of Material Hardness 86
5.4 Nano-Scratch Tips 87
5.5 Procedure 88
5.5.1 Transducer Constants 88
5.5.2 Test Procedure 92
5.6 Constant Force Scratches 94
5.6.1 Fused Quartz Results 96
5.6.2 Silicon (111) Results 106
5.6.3 Al390-T6 Results 111
5.7 Ramp Load Scratch Profile 120
5.7.1 Fused Quartz Results 122
5.7.2 Silicon Results 124
5.7.3 Al390-T6 Results 127

5.8 Conclusions 135
Chapter 6: Conclusions and Recommendations 141
6.1 Introduction 141
6.2 Conclusions from this Study 141
6.3 Recommendations 143
References 144

List of Figures

Page

Figure 1: Dry contact surface cross-section SEM image [Sheiretov, 1997] 3
Figure 2: Starved lubrication surface cross-section SEM image [Yoon, 1999] 4
Figure 3: Critical condition for scuffing at a given speed [Yoon, 1999] 4
Figure 4: Al390-T6 disk sample with wear track, and 52100 steel pin 6
Figure 5: Typical scuffing experiment data obtained from HPT; [Patel, 2000, Figure 2.17] 7
Figure 6: Cross section sample attachment 9
Figure 7: Al390-T6 'bulk' surface microstructure; SEM image 11
Figure 8: Virgin sample SEM surface cross-section profile; low magnification 12
Figure 9: Virgin sample, SEM surface cross-section profile – 5 µm 12
Figure 10: Scuffed sample, SEM surface cross-section profile – 3 µm 13
Figure 11: Scuffed sample, SEM cross-section profile – 1 µm 14
Figure 12: Scuffed sample SEM cross-section profile – 500 nm 14
Figure 13: Box and whisker plot of Rockwell B hardness data 18
Figure 14: Rockwell B residual indent on Al390-T6 19
Figure 15: Virgin surface, Vickers Hardness 22
Figure 16: 1/4 Scuffed surface, Vickers Hardness 22
Figure 17: 1/2 Scuffed surface, Vickers Hardness 23
Figure 18: 3/4 Scuffed surface, Vickers Hardness 23
Figure 19: Scuffed surface, Vickers Hardness 24
Figure 20: Residual Vickers indent impressions on virgin surface 24
Figure 21: Residual Vickers indent impressions on scuffed surface 25
Figure 22: Cross-section image of 300 pond-load Vickers indent; SEM image 26
Figure 23: Cross-section image of 'deformation' area from Vickers indent; SEM image 26
Figure 25: Berkovich tip image (courtesy of Hysitron, Inc.) 32
Figure 26: 90° – cube corner tip image (courtesy of Hysitron, Inc.) 32
Figure 27: SEM image of 90° - cube corner tip showing blunting at tip 33
Figure 28: Load-displacement curve and associated parameters 34
Figure 29: Cross-section profile of an ideal indent 34
Figure 30: Tip area function least squares fit; 90° - cube corner tip 36
Figure 31: Linear, ramp loading profile, without hold at peak load 37
Figure 32: Linear ramp loading profile with hold at peak load 38
Figure 33: 'Pul-load' loading profile 39
Figure 34: Loading curve of *'pul-load'* vs. ramp load, fused quartz 40
Figure 35: Fused quartz hardness resulting from *'pul-load'* vs. ramp load 40
Figure 36: Air indent with corrected electro-static force 42
Figure 37 a, b, c: Indenter dependency on peak, valley, and flat 43
Figure 38: Peak vs. valley indentation material property correlation, 90° cube corner tip 43
Figure 39: Peak vs. valley indentation material property correlation, Berkovich tip 44
Figure 40: 90° cube corner tip loading curves on Fused quartz 45
Figure 41: Berkovich tip loading curves on Fused Quartz 45

Figure 42: Fused Quartz indentation data after tip calibration; 90° cube corner tip 46
Figure 43: Fused Quartz indentation data after tip calibration; Berkovich tip 47
Figure 44: Fused Quartz indentation data for both 90° cube corner and Berkovich tips 47
Figure 45: Residual image of a 140 µN indent on Silicon; 90° cube corner image 48
Figure 46: Silicon loading curves for both 90° cube corner and Berkovich tips 49
Figure 47: H, E_r depth profile of silicon; 90° – cube corner tip 49
Figure 48: H, E_r depth profile of silicon; 90° cube corner and Berkovich tips 50
Figure 49: Trapezoidal loading functions on virgin Al390-T6 sample 51
Figure 50: Trapezoidal loading function calculated properties comparison 52
Figure 51: Silicon criteria line for 90° cube corner tip; virgin surface 54
Figure 52: Silicon criteria line for 90° cube corner tip; ¼ scuffed surface 54
Figure 53: Silicon criteria for Berkovich tip 55
Figure 54: Effects of including Silicon particle data on Al390-T6 56
Figure 55: 3/4 Scuffed sample test area 58
Figure 56: Scuffed sample test area 58
Figure 57: Samples prepared for AFM use 59
Figure 58: Virgin Sample; all single-loading curves using 90° cube corner tip 60
Figure 59: Virgin sample loading curves; Berkovich tip 61
Figure 60: Virgin sample hardness profile 61
Figure 61: Virgin sample reduced elastic modulus profile 63
Figure 62: 1/4 Scuffed sample loading curves, 90° – cube corner tip 64
Figure 63: 1/4 Scuffed sample loading curves, Berkovich tip 65
Figure 64: 1/4 Scuffed sample hardness profile 66
Figure 65: 1/4 Scuffed sample reduced elastic modulus profile 67
Figure 66: 1/2 Scuffed sample loading curves, 90° cube corner tip 68
Figure 67: 1/2 Scuffed sample loading curves, Berkovich tip 68
Figure 68: 1/2 Scuffed sample hardness profile 69
Figure 69: 1/2 Scuffed sample reduced elastic modulus profile 70
Figure 70: 3/4 Scuffed sample loading curves, 90° – cube corner tip 71
Figure 71: 3/4 Scuffed sample loading curves, Berkovich tip 72
Figure 72: 3/4 Scuffed sample hardness profile based on original test area data 73
Figure 73: 3/4 Scuffed sample reduced elastic modulus profile 73
Figure 74: Scuffed sample loading curves, 90° – cube corner tip, single indents 74
Figure 75: Scuffed sample loading curves, 90° – cube corner tip, *'pul-load'* 75
Figure 76: Scuffed sample loading curves, Berkovich tip 76
Figure 77: Scuffed sample hardness profile 77
Figure 78: Scuffed sample reduced elastic modulus profile 77
Figure 79: All samples linear fit of data, hardness profile 79
Figure 80: All samples linear fit of data, reduced elastic modulus profile 80
Figure 81: Virgin sample H and Er continuum 82
Figure 82: 1/4 Scuffed sample H and E_r continuum 82
Figure 83: 1/2 Scuffed sample H and E_r continuum 83

Figure 84: 3/4 Scuffed sample H and E_r continuum....83
Figure 85: Scuffed sample H and Er continuum....84
Figure 86: Multimode AFM and 2-D transducer....86
Figure 87: Nano-scratch tip profile....87
Figure 88: 60°, 1 µm radius conical tip; SEM image....88
Figure 89: x-axis-calibration-scratch profile....89
Figure 90: Air scratch from -25µm to +25µm, with Image Position set to 0....90
Figure 91: Resulting data from x-axis-calibration-scratch from -4 µm to +4 µm....91
Figure 92: Data after transducer constants are calibrated....91
Figure 93: Pre-scratch and scratch profile; tip loss of contact during pre-scratch scan....93
Figure 94: Pre-scratch scan and scratch profile with set point = 8 µN, scan load = 20 µN....94
Figure 95: Constant force scratch profile....95
Figure 96: Constant force scratch profile with a 20 µN pre-scan load; test profile....96
Figure 97: Constant load scratch with a 20 µN pre-scan and post-can load....96
Figure 98: 1000 µN and 400 µN constant force scratches on Fused Quartz....97
Figure 99: 1000 µN constant force scratch on Fused Quartz....97
Figure 100: Residual scratch profile; 1000 µN constant force scratch; Fused Quartz....98
Figure 101: Raw data from a 1000 µN, constant force scratch on Fused Quartz....98
Figure 102: Constant force, 1000 µN scratch on Fused Quartz with tilt correction....99
Figure 103: Friction coefficient on Fused Quartz....100
Figure 104: Several constant load scratches on fused quartz; 60°, 1 µm radius conical tip....101
Figure 105: Several constant load scratches on fused quartz; 60°, 1 µm radius conical tip....102
Figure 106: Steady state normal displacement; Fused Quartz; 60°, 1 µm radius conical tip....103
Figure 107: Friction coefficient; Fused Quartz; 60°, 1 µm radius conical tip....103
Figure 108: Average friction coefficient; Fused Quartz, 60°, 1 µm radius conical tip....104
Figure 109: Scratch hardness profile, Fused Quartz....104
Figure 110: Nano-scratch tip; SEM image; this is not an image of the tip used in tests....105
Figure 111: Calculated effective tip radius at the 60°, 1 µm radius conical tip....105
Figure 112: Tilt corrected data from a 300 µN constant force scratch on Silicon....106
Figure 113: Friction data from a 300 µN constant force scratch on Silicon....106
Figure 114: 300 µN constant force scratch on Silicon, residual image....107
Figure 115: Scratch cross-section profile of a 300 µN constant force scratch on Silicon....107
Figure 116: Constant force scratches on Silicon; 60°, 1 µm radius conical tip....109
Figure 117: Steady state normal displacement as a function of constant normal load....109
Figure 118: Friction coefficient of several constant force scratches on silicon....110
Figure 119: Steady-state friction coefficient for several constant force scratches on silicon....111
Figure 120: Pre-scan of virgin aluminum surface; 8 µm x 8 µm....112
Figure 121: Virgin surface, post-scratch image of 200 µN scratch; 8 µm x 8 µm....112
Figure 122: Virgin surface, post-scratch image of 200 µN scratch; zoomed in....113
Figure 123: Section analysis of 200 µN scratch on virgin aluminum....113
Figure 124: 8 µm scratch on Virgin surface; 200 µN constant load....114
Figure 125: 8 µm scratch on Virgin surface; 800 µN constant load....115

Figure 127: Friction coefficient, 8 mm scratch, constant load; Virgin surface 116
Figure 128: 8 µm scratch on Scuffed surface; 200 µN constant load 117
Figure 129: 8 µm scratch on Scuffed surface; 800 µN constant load 118
Figure 130: Normal penetration of 8 mm scratches on scuffed surface 119
Figure 131: Average nano-scratch penetration depths 119
Figure 132: Friction coefficient, 8 µm scratch, 200 µN constant load, Scuffed surface 120
Figure 133: Ramp load scratch profile 121
Figure 134: Ramp -load scratch profile, with pre -scan of surface 122
Figure 135: Normal load (ramp profile) of several 8 µm length scratches on fused quartz 123
Figure 136: Normal displacement of several 8 µm length scratches on fused quartz 123
Figure 137: Coefficient of friction of several 8 µm length scratches on fused quartz 124
Figure 138: Normal load (ramp profile) of several 8 µm scratches on Silicon 125
Figure 139: Normal displacement of several 8 µm scratches on Silicon 126
Figure 140: Coefficient of friction of several 8 µm scratches on Silicon 127
Figure 141: Normal load profile of an 8 µm scratch on the virgin surface 128
Figure 142: Normal displacement of an 8 mm scratch on the virgin surface 129
Figure 143: Normal displacement difference of an 8 mm scratch on the virgin surface 129
Figure 144: Normal displacement of an 8 µm scratch on the virgin surface 130
Figure 145: Coefficient of friction of an 8 µm scratch on the virgin surface 131
Figure 146: Ramp load normal displacement profile, virgin surface 131
Figure 147: Ramp load friction profile, virgin surface 132
Figure 148: Ramp load scratch profile on scuffed surface 133
Figure 149: Ramp load roughness corrected scratch profile on scuffed surface, zoomed in 133
Figure 150: Ramp load friction coefficient profile on scuffed surface 134
Figure 151: Ramp load, normal displacement profile, scuffed surface 134
Figure 152: Ramp load, friction coefficient profile, scuffed surface 135
Figure 153: Nano-scratch average penetration depth, 200 µN normal load 137
Figure 154: Nano-scratch average penetration depth, 800 µN normal load 138
Figure 155: Nano-indentation hardness profile, Al390-T6 virgin surface 139
Figure 156: Nano-indentation hardness profile, Al390-T6 scuffed surface 139

List of Tables

Page

Table 1: Al390-T6 specified alloy composition 7
Table 2: Rockwell B Hardness Data 17
Table 3: Approximate hardness conversion for non-austenitic steels from reference [E-140-88] 28

Chapter 1: Introduction

1.1 Background

In the engineering world, contacting surfaces are everywhere around us. From gears to pistons, splines to bearings, compressors to magnetic storage drives, cyclical contacts under high speed, load, and pressure, often lead to gradual, and sometimes abrupt, isolated wear (damage) of these contacting surfaces. In the context of contacting surfaces in air conditioning compressors, the sudden, catastrophic damage of these surfaces is known as scuffing, and is the focus of this project.

Scuffing is a common term used in the engineering world, although its definition is not well accepted. It has been described as failure of lubricant films, desorption of active chemical species, destruction of oxides, large plastic deformation of the surface, unstable growth of contact junctions, accumulation of wear debris, and bulk subsurface failure [Sheiretov, 1997]. Possibly the most accepted definition is that set forth by the Organization for Economic Cooperation and Development (OECD), which states that "scuffing is localized damage caused by the occurrence of solid-phase welding between sliding surfaces without local surface melting" [Wear Control Handbook]. The definition used in this study is both operational and post-mortem. During a wear test, scuffing is a sudden event consisting of adhesive material transfer between the two surfaces in contact. This results in an increased frictional force, a drop in contact resistance and possibly a catastrophic seizure of motion. Other effects include increased noise, vibration and increased operating temperatures. All of these effects are undesirable in an engineering application. Examination of the surfaces from a post wear test shows a gradual wear process (without significant wear or material transfer), formation of wear tracks , and then a sudden change in appearance of a small portion of the contact region (i.e. scuffed region). The scuffed surface appears as if the surface has been welded (adhered due to very high adhesion) at certain points, resulting in a significantly different area from the surrounding regions, noted by changes in surface texture, color and finish.

It is generally accepted that scuffing is affected by pressure, velocity, temperature, lubrication, surface topography, materials and metallurgical aspects, and surface coatings of surfaces in contact. Insights leading to an understanding and minimization of the scuffing mechanism have long been sought. Throughout history, many first efforts have focused on methods of avoiding, and/or minimizing, the occurrence of scuffing. One solution is to improve the selection of the material pair combinations to that which shows the greatest resistance to scuffing. It has also been shown (with limited success), that the application of certain surface coatings seems to increase the usable life of certain components by limiting scuffing on the surfaces [Bradley, 1967]. In 1937, Blok postulated the first ideas towards the underlying causes of scuffing. He suggested that scuffing occurs when a critical surface temperature is reached, thus lowering the shear strength of the material interface [Blok, 1937].

Other approaches have focused on understanding the changes in the layers of fluid film that separate the contacting surfaces. Using Elasto-Hydrodynamic Lubrication theory (EHL), Dyson was able to hypothesize that scuffing occurs when the thickness of the fluid film between the surfaces is reduced to a level less than the average asperity heights of the surfaces [Dyson, 1976]. Park and Ludema extended this work to include the material properties of the contacting surfaces through a plasticity index parameter [Greenwood and Williamson, 1966], which is a measure of the degree of elastic/plastic asperity deformation due to contact. Through their findings, they

were unable to correlate a relationship between the plasticity index and the occurrence of scuffing [Park and Ludema, 1994]. Continuing the examination of scuffing under a different approach, Somi Reddy has concluded that scuffing results from bulk subsurface failure. He states that the subsurface material has a lower shear strength that that at the surface, and thus reduced resistance to shear [Somi Reddy *et al*, 1995]. Others have studied the formation of oxides on the surface (due to pressure, temperature, velocity) under a wide range of conditions, and linked the presence of these protective layers to scuffing resistance [Cavatorta, 2000].

Recently, more fundamental studies have been conducted to examine the surface/subsurface changes that occur during the wear/scuffing process. Several studies have been conducted on those contacting surfaces associated with air conditioning swash plate compressors, as used in the automotive industry. Due to the configuration of these compressors [see Sheiretov, 1997], high load, cyclical contact is observed on several surfaces resulting from plate on shoe contacts. This analysis began with the examination of the 'simple' dry contact case [Sheiretov, 1997], and proceeded to the more realistic, starved lubrication case [Yoon, 1999, Cavatorta, 2000, Patel, 2001]. Though this application is specific, the knowledge of the underlying mechanism can be applied towards much more general cases, in which scuffing is observed.

The first study in this series began with the analysis of scuffing mechanism observed under dry contact conditions (i.e. no lubricant) [Sheiretov, 1997]. The analysis began with the most extreme case in order to obtain a fundamental understanding of the surface/subsurface changes that occur during the wear/scuffing process. The material combinations studied were those of 1018 steel disks, and Al390-T6 pins. R134a was used as the refrigerant to model typical conditions observed in compressor applications. The creation of the individual scuffing samples is the same for all tests, and is discussed at a later point. Using chemical and microstructural analysis methods, it was found that a transformed layer on the scuffed sample, resulting from the formation of oxides at high temperatures, exists at depths up to 3 – 30 μm below the surface. Sheiretov hypothesized that the formation of these layers actually protects surfaces from scuffing (due to a hardness several times higher than that of the bulk material, [Bhushan, 1999]), and it is when these layers are removed that scuffing occurs. Further analysis shows that plastically deformed layers, resulting from extreme temperatures and stresses, can be observed at depths up to 100 – 150 μms. It is in this plastically deformed region that voids and cracks form below the surface (see Figure 1).

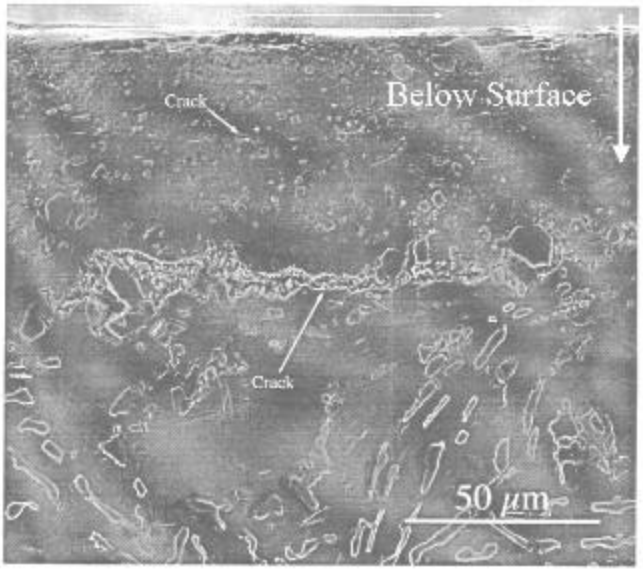

Figure 1: Dry contact surface cross-section SEM image [Sheiretov, 1997]

As the wear process proceeds, subsurface cracks propagate, leading to the removal of sections of the surface material (i.e. protective films). This, in turn exposes bare metal (which is highly reactive with oxygen from the opposing surface) that immediately forms cold welds to the opposing surface. Sheiretov concludes that, "scuffing under dry sliding conditions is due to a sub-surface failure." This hypothesis has significant merit for dry contact in that it has incorporated many ideas of prior studies, such as the effects of shear strength of the material, temperature effects, subsurface failure and subsequent removal of the protective oxide coating. But, as mentioned, this analysis is based on an extreme case resulting from dry contact, and is not representative of actual applications.

Yoon [Yoon, 1999] extended this analysis to the more realistic, starved lubrication case. In this analysis, the material combination was composed of Al390-T6 disks, in contact with 52100 steel shoes. A PAG (Polyalkylene glycol) lubricant (some tests were performed with POE lubricant), mixed with R134a refrigerant, was applied as a mist to the contact surface at a lubricant supply rate of 40 mg/min. This relatively low lubricant supply rate leads to a starved lubrication condition, which simulates observed operating conditions. Note that if full lubrication conditions are used, scuffing is not observed. Thus, the focus is on the starved lubrication case. Yoon first considered the effects of material pair and lubricant selection on the minimization of scuffing. He also found that increased scuffing resistance is found for smoother surfaces. Through examination of subsurface microstructure, no deep subsurface damage (i.e. cracks / voids) could be observed, contrary to dry contact analysis. This lack of subsurface damage was attributed to the effects of reduced friction, local stresses, and temperatures observed with the starved lubrication case compared to the dry contact case. Further analysis shows that the thickness of the transformed layer (due to oxidation at high temperatures/pressures) is smaller, on the order of 5 – 10 μm thick, as well as the thickness of the plastically deformed region, which is on the order of 50 – 60 μm thick (Figure 2). Yoon hypothesized that thin films (transformed layers) protect the surface from large scale adhesion. At certain conditions, these films are removed (because of high local temperatures/pressures, see Figure 3), leading to

adhesion of the bulk material. Yoon also suggested that the plastic deformation below the surface (present up to 60 nm deep) destabilizes the protective oxide layer, thus leading to its removal. Once the bare aluminum material is exposed, it is highly reactive, and bonds to either the oxygen or iron oxide on the steel pin. Thus, microscopic adhesion leads to large-scale macroscopic adhesion.

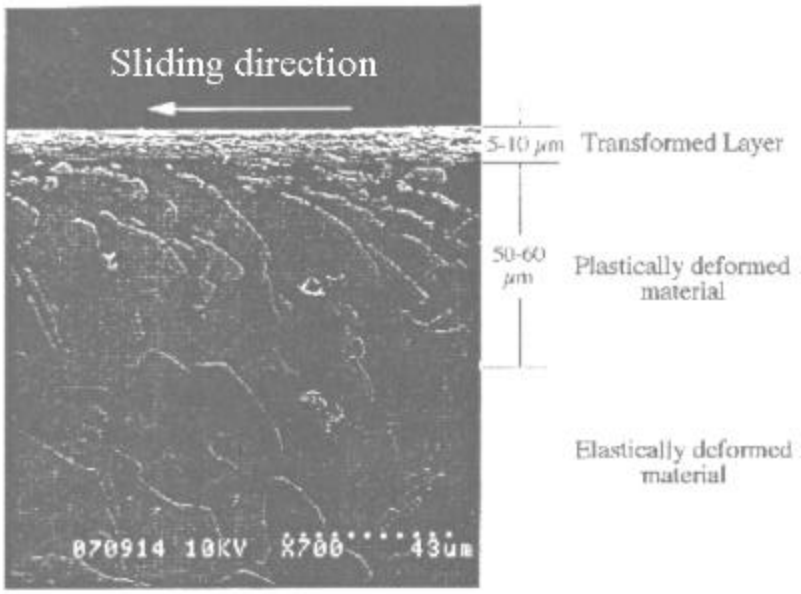

Figure 2: Starved lubrication surface cross-section SEM image [Yoon, 1999]

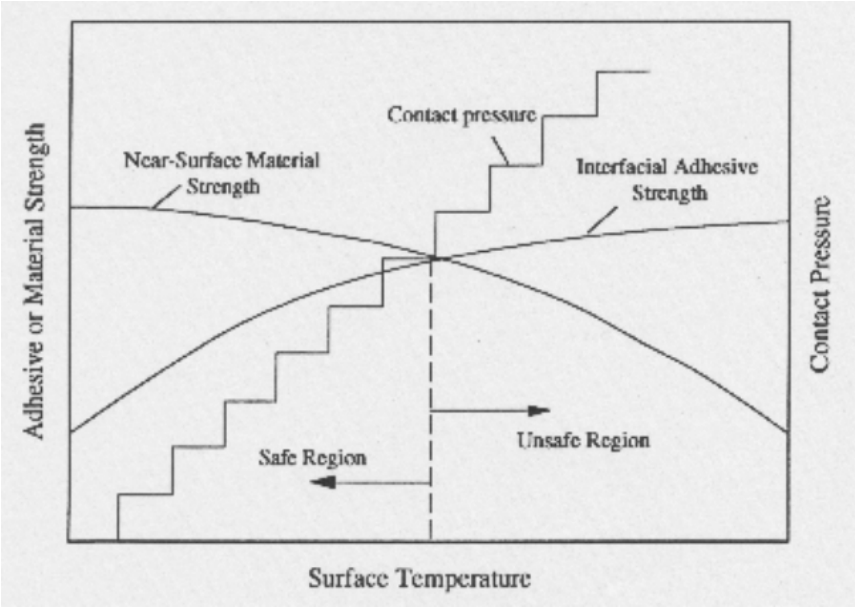

Figure 3: Critical condition for scuffing at a given speed [Yoon, 1999]

The results from the studies by Sheiretov and Yoon have many similarities. Both attribute the occurrence of scuffing to the removal of the protective o xide film known as the transformed layer. Sheiretov finds that this layer is on 3 – 30 μm thick under dry contact conditions, while Yoon finds that this layer is 5 – 10 μm thick for

contact under starved lubrication conditions. They both hypothesize that subsurface deformation/cracks at depths of 10 – 150 μm, ultimately lead to the removal of this layer, thereby exposing bare metal, which is highly reactive and forms adhesive bonds with the opposing surface, i.e. scuffing.

Most previous studies, as mentioned earlier, have focused on reducing the occurrence of scuffing. Patel [Patel, 2001] further analyzed the scuffing mechanism, but used a different approach. His study was more of a fundamental investigation to develop an understanding of the underlying causes of scuffing, in the context of surface topographical and near surface chemical changes that occur during the scuffing process. Sheiretov's, Yoon's, and Cavatorta's, studies focused on changes that occur at and below the surface, at the micron-level. Patel's work shifted from changes at the micron-level to the nano-meter level, aided with several advanced tools commonly used in the semi-conductor industry. The material pairs studied were Al390-T6 disks, in combination with 52100 steel pins. A POE lubricant, mixed with R410a refrigerant, was applied as a mist to the contact surface, at a lubricant supply rate of 40 mg/min. This replicated the starved lubrication condition analyzed by Yoon. Through statistical analysis of surface topography, several trends during the wear process were analyzed. All virgin surfaces have slightly positive surface height skewness, while this becomes negative almost immediately after the test is initiated. Thus, asperity peaks are worn off almost immediately after contact. It was also shown that the radius of the asperities increases with the wear progression, as expected. From the chemical analysis, it was found that as the wear process proceeds there is a significant depletion of the concentration of silicon near the surface. This was a significant finding because silicon is added to the alloy in order to strengthen the material, and if removed, will weaken the surface. The chemical analysis of oxygen, carbon, aluminum and silicon concentrations showed that the most significant changes occur at depths up to 50 – 100 nm below the surface. This was an extremely important finding because it contradicts many of the earlier results in which the most significant layers were present at depths of several microns.

1.2 Project Objectives

The focus of this project is to substantiate findings that the most significant changes occur in the top 50 – 100 nm below the surface, and to quantify changes in material properties at this level. Microstructural analysis will be used in an effort to examine the subsurface microstructural changes that accompany the scuffing process. This analysis will also provide a basis of microstructural understanding for subsequent analysis of hardness and indentation data. Macro, meso, micro, and nano scales of subsurface depth will be analyzed for changes in material properties at all depths, using a combination of meso, micro, and nano mechanical methods. It will be shown that there are no significant changes at macro, meso, or micro depths, thus gaining support for examination of the material properties at the nano level. By comparing hardness data from several samples at different stages of scuffing, we hope to substantiate Patel's finding that silicon is depleted at the surface, thus causing a weakening of the upper-most surface layers. Finally, a second nano-mechanical method of analyzing thin film material properties will be incorporated to confirm the weakening of surface/subsurface films. Through this analysis, the goal is to support Patel's findings and show that the most critical layers relating to material scuffing resistance have thicknesses in the 50 – 100 nm range, not in the micron range, as previously studied.

Macro (large scale dimensions > 1mm) and meso scales (i.e. dimensions of ~100 μm – mm range) have been studied historically, and provide bulk material understanding for homogeneous materials. Analysis at the micron level (~100 nm - ~100 μm) was developed to examine local hardness variations in order to evaluate surfaces in which hardness changes dramatically (Ex. examine changes in hardness in the vicinity of welds). Nano level analysis stems from advances in the semi-conductor and magnetic storage Hard Disk Drive industries, in which it is increasingly critical to examine films at the nano level because thin films have material properties dramatically different from those of 'bulk' material [Bhushan, 1999].

The nano-mechanical methods that will be used in this work are nano-indentation and nano-scratch techniques. These methods are routinely used in such applications as semi-conductors and magnetic storage hard disk drives. Applying these methods to engineering surfaces is anticipated to be somewhat difficult (and thus, the lack of published works in this area), due to significant roughness, non-homogeneous surfaces and inconsistent layers of unknown an non-uniform thicknesses. Nonetheless, the applicability of these methods on engineering surfaces will be examined, in hopes of obtaining consistent, meaningful results.

1.3 Tribological Testing and Sample Preparation

1.3.1 Materials

The engineering material studied is an Al390-T6 disk, in contact with a 52100 steel pin (see Figure 4). The Al390-T6 has a specified hardness of 72 HRB, while the steel pin has a specified hardness of 62 HRC. These materials are commonly found in automotive air conditioner swash-plate compressors. The aluminum chemical composition specifications were obtained from the supplier, Shotic America Corporation, and are listed in below. A relatively significant amount of silicon is added to strengthen the material. The microstructure will be discussed and analyzed later.

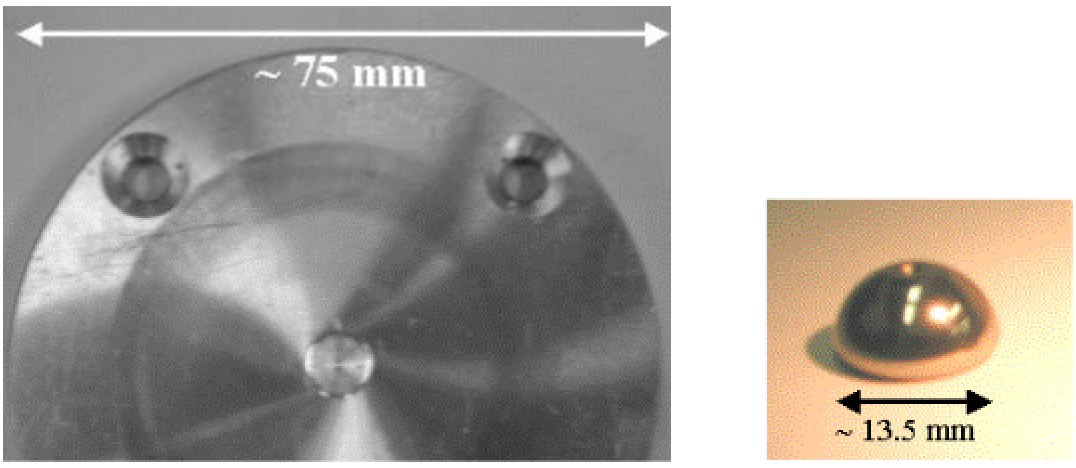

Figure 4: Al390-T6 disk sample with wear track, and 52100 steel pin

Table 1: Al390-T6 specified alloy composition

	Al	Si	Fe	Cu	Mn	Mg
Specified Weight %	Balance	16.0-18.0	<0.5	4.0-5.0	<0.1	0.45-0.65

1.3.2 Tribological Scuffing Experiments

Since this work is an extension of the analysis of the scuffing mechanism work by Jayesh Patel, the samples studied are the same Al390-T6 disks prepared from his work [Patel, 2000]. The High Pressure Tribometer is a tribological testing machine capable of generating worn or scuffed samples, under prescribed test conditions. The material combinations of interest are Al390-T6 disks, in contact with 52100 steel shoes. R410A was used as a refrigerant, in combination with a POE lubricant at a supply rate of 40 mg/min to model starved lubrication conditions. The chamber pressure was set at 50 psi, while the temperature of the disks and shoes was set at 121°C. These conditions model an aggressive application of a typical swash-plate compressor contact. Under these fixed conditions, several tests were conducted to quantify the time for the aluminum surface to reach the scuffed state. The scuffed state occurs when there is significant material transfer from one material to the other. It is quantified by both a dramatic increase in friction, and a dramatic drop in contact resistance, as shown in Figure 5 (the time to scuff is approximately 6.3 minutes).

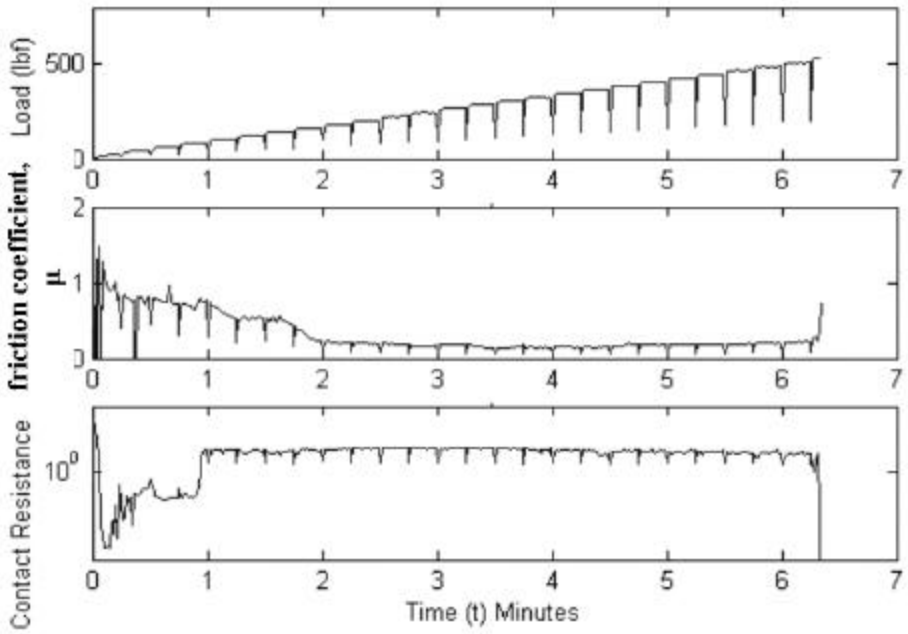

Figure 5: Typical scuffing experiment data obtained from HPT; [Patel, 2000, Figure 2.17]

It was found that, under these test conditions, the time to scuff was extremely repeatable for different samples. Five samples were prepared at various stages of scuffing, corresponding to virgin, ¼ time to scuff, ½ time to scuff, ¾ time to scuff, and scuffed samples. The wear track consists of the entire area of the disk that was in direct contact with the pin face, often noted as a polished and/or scuffed region (see Figure 4). Samples were then stored in a plastic storage case for subsequent analysis and further testing.

Chapter 2: Micro-structural Analysis

2.1 Introduction

Indentation methods quantify hardness as a resistance to plastic deformation. These measurements are performed at discrete locations on the surface of the material. Ideally, the entire surface would have a uniform structure and composition, translating to extremely repeatable, consistent results. In reality, this is often not the case. Some elements may be soluble in matrix, while others may precipitate out of solution. Additionally, grain boundaries versus actual grains also become a source of concern. A macro-test is often not concerned with these issues. The indenter, as well as the load, is large. This translates into a relatively large area affected by the presence of the indenter (as large as several mm), and an averaging of the effects of microstructure. As the indentation tips get smaller and the loads lighter, the volume of material deformed by the indenter becomes smaller and smaller. Eventually, the volume of material deformation will approach the same relative size as the microstructural dimensions of the material. At this point, the microstructure is a major issue, and should be considered when analyzing data at this level.

Nano-indentation and nano-scratch techniques use extremely small indenter tips and low loads, as discussed above. The affected area from an indent is of the same order of magnitude or smaller than some of the microstructural dimensions. Thus, in order to fully understand the results obtained, and to develop a clear explanation of trends associated there in, one must have a clear understanding of the microstructure of the material.

Additionally, surface cross-sectional profiles are used to study the deformed layers of a virgin and a scuffed surface. These profiles will be used to further understand and explain some of the trends observed from the nano-indentation and nano-scratch experiments.

2.2 Sample Preparation: Polishing/Etching

Careful sample preparation techniques are essential to obtain functional microstructural pictures. Once the sample is cut to the appropriate dimensions, a mechanical polish with successively finer grit size is used to remove most scratches. A final chemical etch is used to remove the fine scratches as well as display grain boundaries.

An 11-step procedure, based on a technical note by Buehler Inc. [Vander Voort, 1999], was used to polish the samples. Al390-T6 contains a large percent of silicon (see Section 1.3.1), which makes polishing somewhat difficult. Prior to each step, all materials (polishing paper, polishing wheels, samples, gloves) were rinsed thoroughly to avoid contaminating a finer polish with larger particles. The polishing procedure is as follows:

1.) Cut sample with diamond saw. This blade minimizes scratches due to cutting, which would have to be removed via later polishing steps otherwise. Orienting the sample such that the blade turns into the face to be analyzed will help to minimize split-out of face material and obtain better results.
2.) Polish with 320-grit paper until all original scratches are removed. A water stream is used to carry particles away from the specimen.
3.) Polish using 9? m METADI® solution on nylon cloth at 150 rpm for 5 minutes (or until all scratches from 320-grit paper are removed).

4.) Polish using 3µm METADI® solution on nylon cloth at 150 rpm for 3 minutes (or until all scratches from 9µm METADI® solution are removed).

5.) Polish using Mastermet® Colloidal Silica Polishing solution (0.06 µm) with Mark V Lab Alpha A Cloth® at 150 rpm for 2 minutes (until smooth).

6.) Gently clean sample with a cotton swab soaked in de-ionized water.

7.) Clean sample in ultra-sonic cleaner with acetone for 5 minutes.

8.) Remove acetone residue with a cotton swab soaked in ethanol.

9.) Dry using air hose.

10.) Chemically etch with a 0.5% HF solution for approximately 10 seconds. Wipe on etch using a solution-soaked cotton swab. If the etch is left on for too long of a time, it will 'burn' the sample.

11.) Clean with acetone, then ethanol, and dry appropriately.

The chemical etch helps display individual grains and grain boundaries by dissolving different grains and grain boundaries at different rates. It was found that inclusions could be observed better without a chemical etch. Thus, under some conditions, the polishing procedure was stopped at step 9.

2.2.1 Cross Section Sample Preparation

Viewing cross-sectional microstructure poses some unique challenges. A coarse polishing procedure will always place a radius on the sharp edges of the sample. These edges will not be polished during subsequent polishing steps, and thus, when viewed under the microscope, will appear extremely rough. When surface layers several microns thick are examined, this radius can be considered negligible, but when trying to view layers on the order of a few hundred nano-meters and less, the radius is very significant. In order to eliminate this problem, two samples were cut and glued together (using Crystal Ox® bonding agent) with wear surfaces facing each other (see Figure 6 below). The new, common face displays a cross-sectional view of the altered surface layers of the wear surface. By polishing this common face, a smooth profile can be obtained on the inner edges. The samples can then be separated (bonding agent dissolves in acetone, while leaving oxide films unaffected), resulting in two polished surfaces with extremely sharp edges.

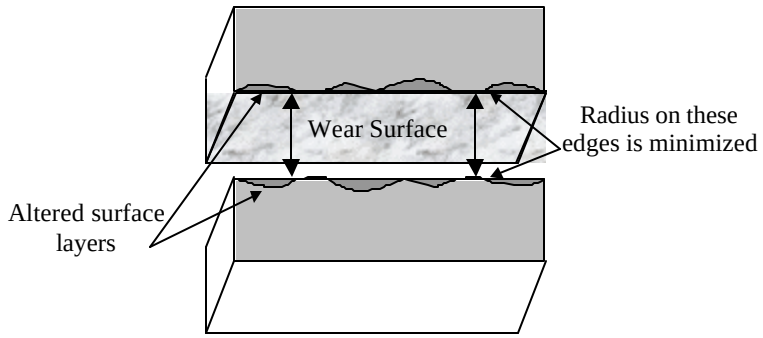

Figure 6: Cross section sample attachment

Microstructures were examined with a high power Hitachi 4700-S Scanning Electron Microscope (SEM), which is capable of 500,000X magnification [http://facilities.mrl.uiuc.edu/cmm/]. Subsequent chemical analysis was performed on a Zeiss 960 SEM equipped with an energy dispersive x-ray spectroscopy system (EDX). Using the x-rays, it is possible to obtain a full chemical analysis of the specimen based on the analysis of peak energy intensity patterns. The instrument is capable of examining areas less than 1 μm in diameter. Both instruments are located in the Center for Microanalysis of Materials, in the Materials Research Laboratory at the University of Illinois.

2.3 Results

2.3.1 Surface / Bulk Microstructure

Two different samples were prepared and used to examine the bulk microstructure of the Al390-T6 alloy. One sample was prepared as a cross-sectional specimen and imaged in the center of the sample, approximately 3 mm from the surface (i.e. bulk section). The second sample was prepared by polishing the virgin surface directly. Due to the polishing procedure, the top surface layers of the material are removed (on the order of 10's of μms), and thus the microstructure resembles that obtained from bulk cross-section. Figure 7 illustrates an SEM image obtained from the virgin sample, but it representative of all sample's un-affected or 'bulk' microstructure. The sample was etched with 0.5% HF solution for approximately 10 seconds.

Examination of the microstructure shows that there are several areas of different structure. The corresponding chemical analysis has been verified through chemical analysis of these features, using the Zeiss 960 SEM, as discussed earlier. The large, black particles (1) correspond to silicon grains. They are rather oblique in shape, and average between ten and twenty microns in width. The manufacturer of the Al390-T6 states that primary silicon average surface area is approximately 7-13% of the total surface area. This seems consistent with the observations of this image. The smaller black particles (2) are a silicon rich SiAl compound, possibly Si_3Al. They are generally rounded in shape, and average two to three microns in diameter. The somewhat darker gray regions (3) are a mix of Al, Fe, Mn, Cu, and Ni. These areas do not display any general shape trends, and vary in size from a few microns to tens of microns long. The lighter areas (4) correspond to a CuAl compound. The lighter and darker gray areas seem to be more prominent in areas lacking larger silicon particles. The majority of the surface is represented by the aluminum matrix (5), which contains a small amount of copper and silicon dissolved into solution. Rough estimates show that the matrix is comprised of approximately 94% aluminum, 3% copper, and 3% silicon. In general, the consistency is much the same throughout the sample, indicating that the silicon particles, etc. are dispersed evenly throughout the sample.

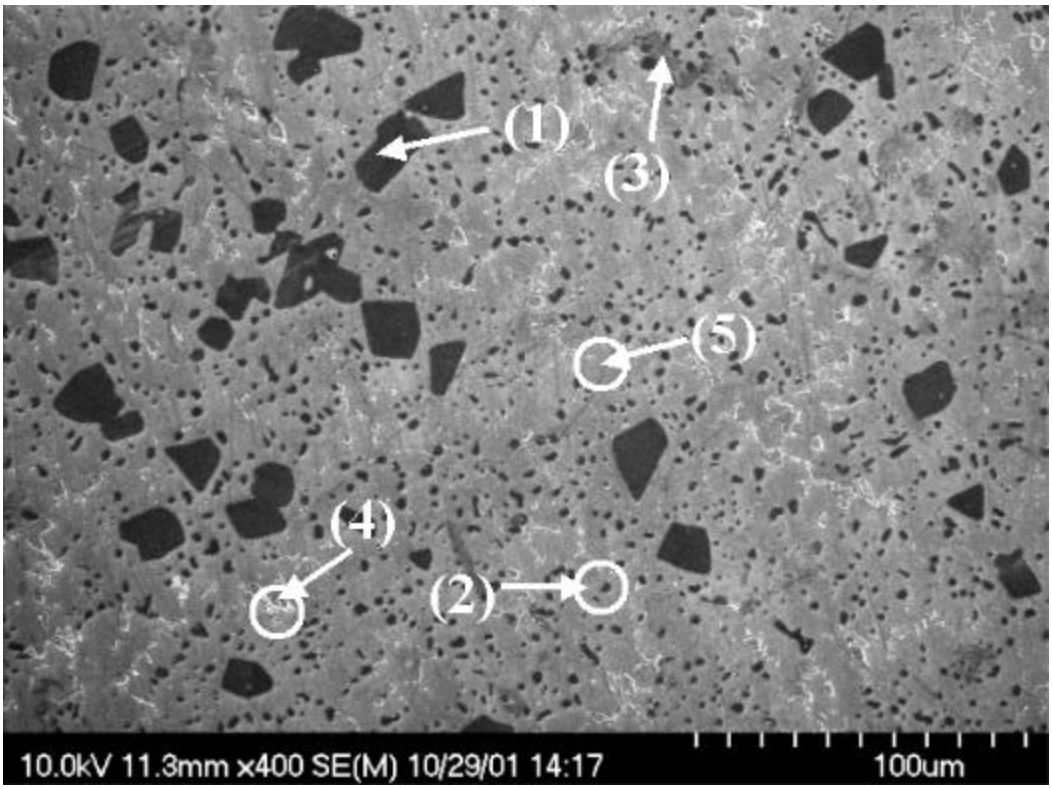

Figure 7: Al390-T6 'bulk' surface microstructure; SEM image

2.3.2 Cross-Sectional Microstructure

Using the polishing procedure described above in Section 2.2, cross-sectional samples were prepared with extremely sharp edges. One of the goals of this analysis is to view inclusions within the sample, thus no chemical etch was used (although, silicon particles and some other grains can still be seen without chemical etching). Virgin and scuffed surfaces were examined.

Figure 8 and Figure 9 below illustrate a virgin sample cross-section, showing different magnifications. Comparison of the surface layers to the 'bulk' microstructure shows that the 'bulk' microstructure (i.e. large silicon particles, smaller Si_3Al particles, CuAl compounds, etc.) is observed beyond a depth of approximately 2 µm. Figure 9 illustrates a higher magnification view of the surface microstructure. The light/dark contrast areas on the surface represent surface roughness behind the image face. A very thin layer (on the order of a few hundred nano-meters at most) is observed as a lighter area on the surface. This represents an artifact associated with the imaging and the backscatter of electrons on the surface edge. Smaller Si_3Al particles can be observed within a few microns of the surface. The darker, blotchy areas have been chemically analyzed, and do not show any significant chemical changes from the surrounding areas. Thus, it is concluded that the darker appearance is not caused by a different chemical composition in these regions. It is also possible that these areas result from either a thermal or a mechanical strain on the material, causing changes in the grain structure. During the manufacture of the sample, the material is first cast, followed by a subsequent surface machining process, to obtain the desired form and finish. The casting procedure involves a mold, which invokes a different cooling rate on the edges of the surface than in the center of the part. This would potentially cause a thermal gradient near the surface, which would alter the surface

microstructure. The machining of the surface causes large amounts of surface and subsurface mechanical strain, which also could affect the microstructural properties. This blotchy appearance could also be caused by mechanical mixing of different phases. Nonetheless, it seems that bulk material is reached after, at most, 2 μm.

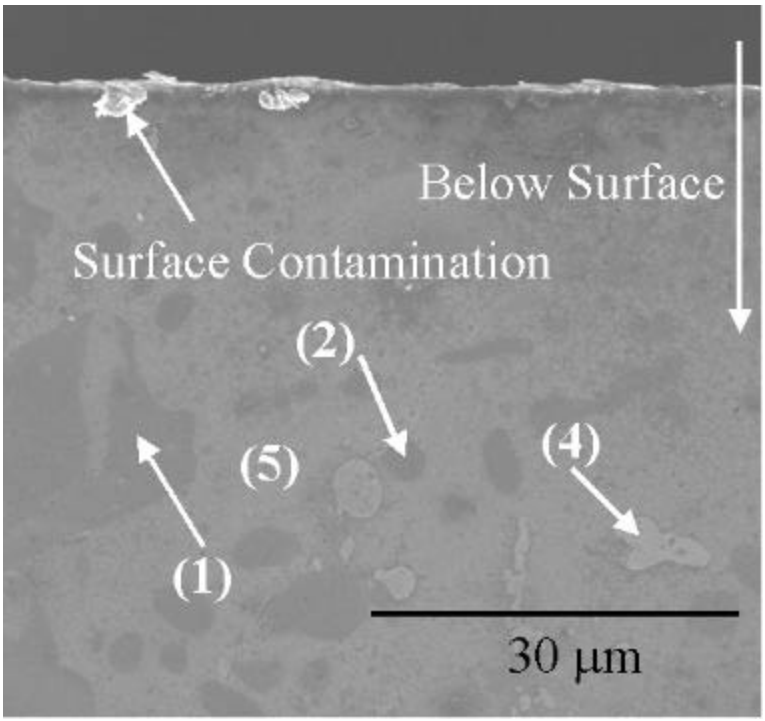

Figure 8: Virgin sample SEM surface cross-section profile; low magnification

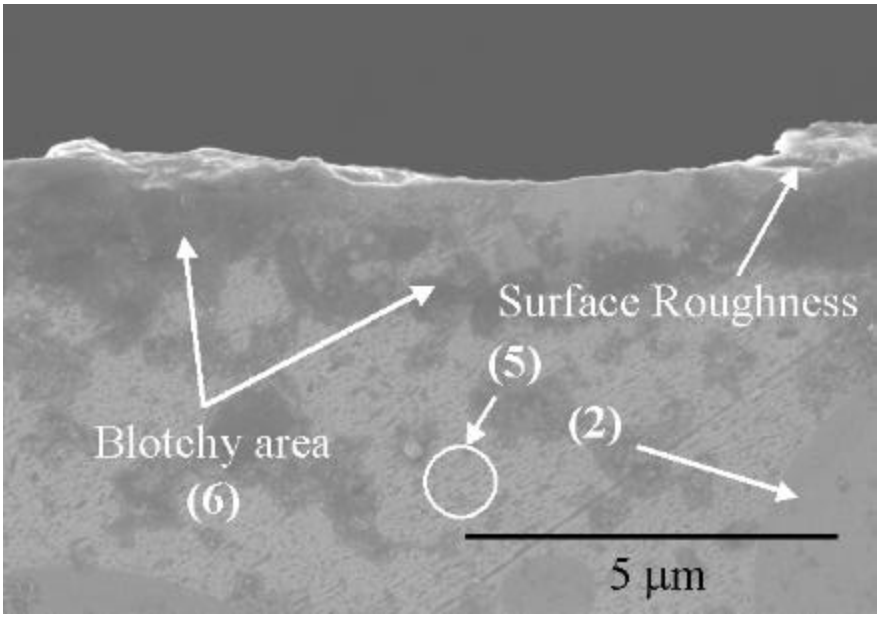

Figure 9: Virgin sample, SEM surface cross-section profile – 5 μm

Figure 10 through Figure 12 illustrate a cross-sectional image of the scuffed sample microstructure. The first figure shows that the affected surface layers are on the order of 2-3 μm thick. The very top surface layers (approximately the top 1 μm), seem to show a mechanical mixing of the different phases such that none are easily distinguishable, similar to the virgin surface. Subsurface cracks in a large silicon particle can also been seen, as well as the darker area of mechanical/thermal strain, which was also observed in the virgin sample. The image in Figure 11 indicates the presence of some cracks in the top 200-300 nm of the surface, as well as smaller, possibly broken up silicon particles due to the high strain that is placed on these surfaces. The last image (Figure 12) clearly shows that silicon is an inhibitor of deformation on the surface. The deformed layers grow right up to the large silicon particle, but are unable to proceed beyond its boundaries. Close examination shows several large cracks in the silicon, which may indicate the potential splitting of this particle into smaller particles. The deformed layers are 500 to 700 nanometers thick, and contain much smaller particles than those observed in the 'bulk' microstructure. This is attributed to the large subsurface strain initiated by the wear test, causing the breakup of larger particles into smaller ones.

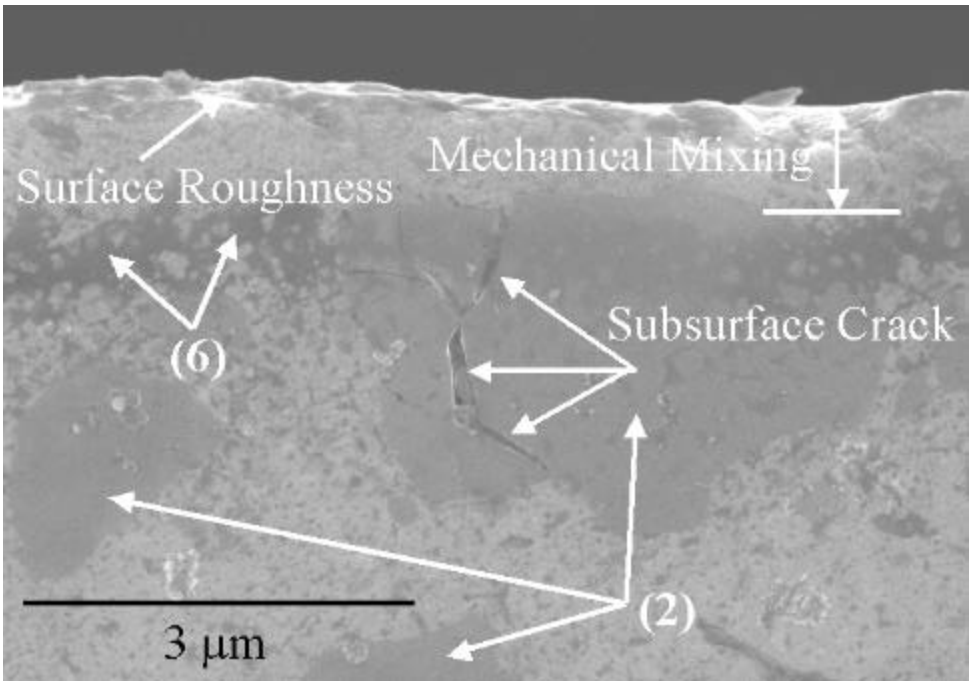

Figure 10: Scuffed sample, SEM surface cross-section profile – 3 μm

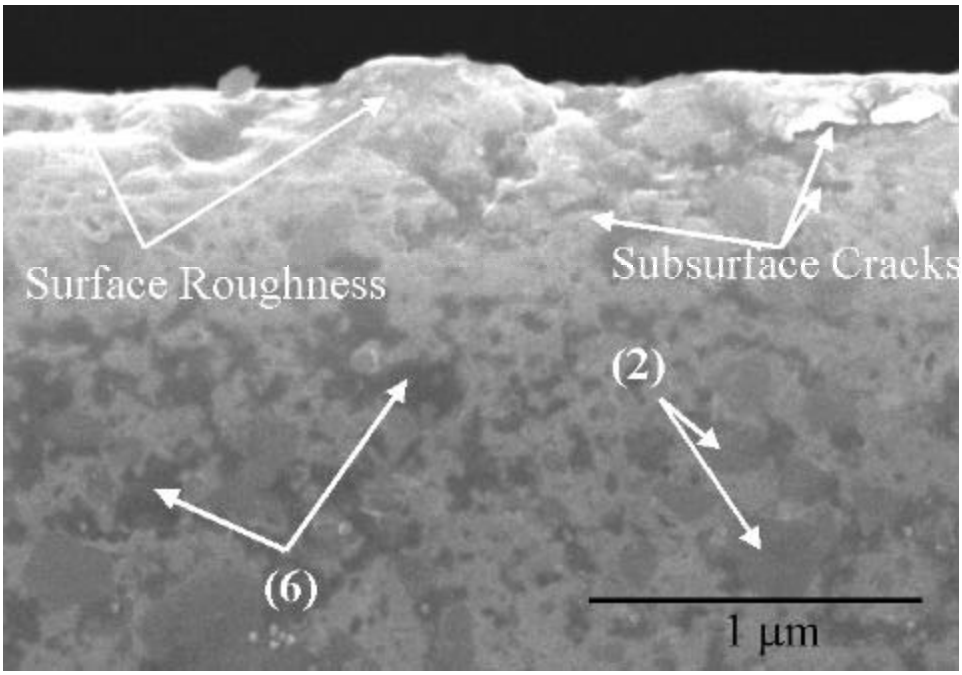

Figure 11: Scuffed sample, SEM cross-section profile – 1 μm

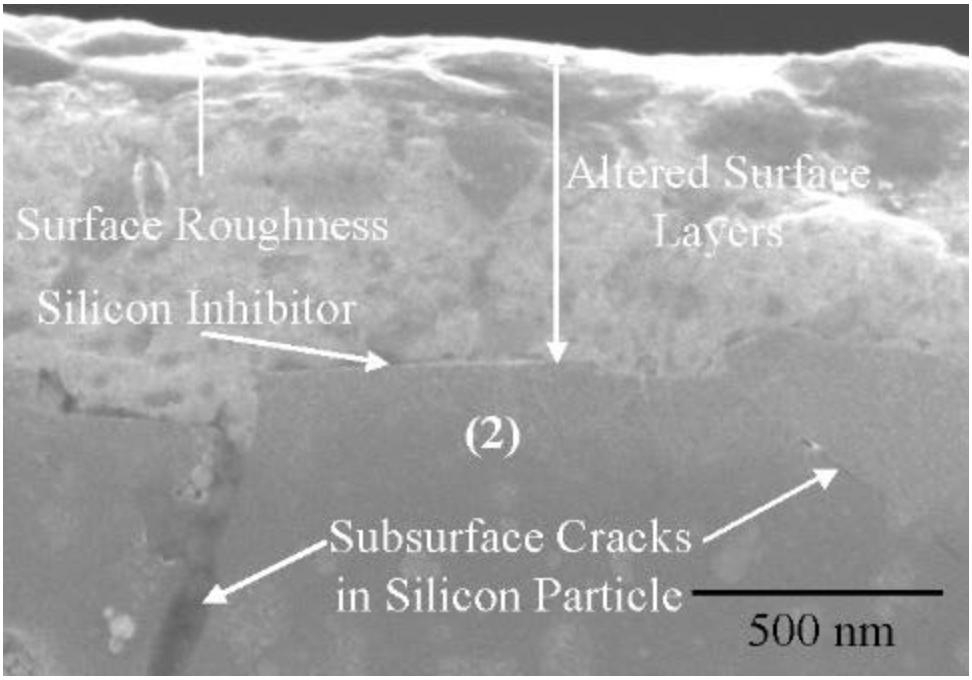

Figure 12: Scuffed sample SEM cross-section profile – 500 nm

2.4 Conclusions

Microstructural analysis serves two main purposes. First, it is needed to gain a better understanding of the microstructural properties/particle size of the uppermost layers, which will aid in the later analysis of indentation data. Secondly, cross-sectional analysis will lead to a better understanding of the thickness of the microstructurally

deformed surface layers due to the wear test. These are both pertinent in the explanation of trends associated with mechanical property data.

Samples have been prepared through a combination of mechanical and chemical methods. The bulk microstructure, and corresponding chemical analysis, shows the presence of different grains and compositions associated with the bulk material. Large silicon particles can be observed, with an average width of ten to twenty microns. They occupy approximately 10% of the material surface. Smaller Si_3Al particles exist, with an average diameter of two to three microns. There are other areas that have correspondingly different compositions. The majority of the surface area (> 50%) is covered by the aluminum matrix.

Cross-sectional profiles have been used to examine the microstructural changes that occur below the surface during the wear test. The virgin surface shows an area of mechanical/thermal strain present in the top two microns of the surface, caused by either the casting or subsequent machining procedures. Beyond this depth, 'bulk' microstructural properties are observed. Other than the mechanical strain, no differences can be observed between the surface layers and the 'bulk' material (based on the resolution of the instrument). Thus, it is concluded that the microstructurally deformed surface layers are less than a few hundred nanometers thick. The analysis of the scuffed sample also shows the presence of the mechanical strain up to three microns below the surface (as seen on the virgin surface). It has also been established that the microstructurally transformed surface layers, due to the wear experiment, are on the order of 500 to 700 nanometers thick. These results have some similarities and differences, compared to the proposed findings by Yoon [Yoon, 1999] for a starved lubrication test. He concludes that the plastically deformed layer can be 50 – 60 nm thick, while the transformed layer is on the order of 5 – 10 mm thick, and the protective oxide layer may be less than one micron thick. From these findings, it is concluded that the plastically deformed layer is 3 – 5 μm thick, which is much smaller than that proposed by Yoon. Also, it seems that the transformed layer thickness is 500 – 700 nm thick.

Chapter 3: Macro-/Micro-Hardness Tests

3.1 Introduction

Macro/micro hardness tests are utilized to establish a basis for further hardness tests, and to gain further support for the examination of hardness at the nano-scale. By quantifying the changes in hardness at the macro/micro-level, a continuum hardness profile at a wide range of depths can be obtained. This will add to the understanding of any potential changes in the material properties at these levels.

3.2 Macro-/Meso-methods: Brinell, Rockwell B, Rockwell C

There are three main non-destructive methods of determining the material hardness at the macro-/meso-scale: the Brinell Hardness Test, the Rockwell B Hardness Test, and the Rockwell C Hardness Test. All are capable of obtaining bulk material hardness values, but differ in their approach.

The Brinell Hardness Test uses a 10 mm steel ball to slowly impact the test material, using a vertical load between 500 and 3000 kgf. These large dimensions and large loads make this test truly a macro-method. The projected diameter of the residual deformation in the material is measured, which is then related to a material hardness parameter (denoted BHN) by calculating the maximum load divided by the projected area of the residual deformation [Kurath]. See ASTM standard E-10-84 for further details about this test. This test is time consuming, allows for inconsistencies due to operator error, and leaves relatively large indents making it difficult to obtain multiple readings on small samples.

The Rockwell Hardness tests are the most widely used hardness testing method in the United States. The test has many advantages including ease of use, reliability, repeatability, and the ability to obtain quick results. Another major advantage is that little surface preparation is needed to obtain accurate and repeatable results. The Rockwell B and Rockwell C hardness tests incorporate a similar test procedure, but utilize different indenter geometries and loads, although both are meso-scale. The Rockwell B Test uses a $^{1}/_{16}$? diameter steel ball under a 100 kgf major load, while the Rockwell C Test uses a pointed diamond cone under a 150 kgf major load. Based on these geometrical and load differences, the Rockwell C test is used for harder materials, while the Rockwell B test is used for softer materials. A minor load of 10 kgf is applied during the entire test. This helps to minimize the effect of any small imperfections or inconsistencies in the material surface. The machine automatically records the difference in the depth of penetration before and after the application of the major load (under the minor load), and uses this value to compute an arbitrary material hardness value (denoted HRB, HRC). The Rockwell B scale is valid up to HRB = 100, while the HRC scale is not valid below HRC = 20. These tests are fully automated, which eliminates operator inconsistencies, minimizes test variation, and greatly improves the speed of the tests. The indenter also leaves a much smaller permanent impression in the material, making it more suitable for applications in which multiple tests must be performed in a relatively small area.

3.2.1 Rockwell B Hardness Test

Due to the automation of the test, as well as the ability to obtain multiple tests data within a relatively small area, the Rockwell B test was chosen as the meso-test method. Aluminum is a relatively soft material, thus necessitating the need for the Rockwell B scale. A Wilson® Rockwell® Instron® Model 523, located in the Materials

Instructional Laboratory in Talbot Laboratory at The University of Illinois at Urbana-Champaign, was used to complete the tests. This instrument provides a digital read-out of material hardness.

3.2.1.1 Procedure

The test material is placed on the instrument stage, and the indenter tip is slowly brought into contact with the material. Once the tip is engaged, the test is fully automated. The machine first applies the minor load, then the major load, and then removes the major load. When finished, the machine displays a digital readout of the material hardness. The Rockwell B Hardness Test was performed 5 different times on each sample. It is suggested that all indents be placed at a location at least 3 diameters away from any other indents to avoid strain-hardening effects.

3.2.1.2 Results

The results of the Rockwell B Hardness Test on the Al390-T6 samples are shown in Table 2. Each sample has a relatively small standard deviation between measurements, while the average hardness reading between samples is also very consistent. An analysis of variance approach is a common statistical method of sample analysis and relative comparisons [Walpole]. Through examination of different sample variations, conclusions about the sample means, based on statistically significant criteria (i.e. α = 95% confidence level, etc.), can be developed. A one-way analysis of variance approach was also used to compare sample hardness means, and test the null hypothesis that all sample means are equal. From this analysis, the p-value is 0.0359, which is less than (1 - 95% = 0.05), thus indicating that the sample means are significantly different at the 95% confidence level. These differences are attributed to slight material differences between samples, as the average hardness between samples is relatively consistent. Further analysis is needed to conclude that all samples have the same sample mean.

Table 2: Rockwell B Hardness Data

	Virgin	**1/4 Scuffed**	**1/2 Scuffed**	**3/4 Scuffed**	**Scuffed**
Measurement #1	81.3	83.7	83.3	82.6	83.3
Measurement #2	83.4	83.8	83.4	83	82.6
Measurement #3	83.1	84.3	83.9	83.1	83.5
Measurement #4	83.2	83.6	83.5	83.2	82.9
Measurement #5	83.1	83.2	83.6	83.3	82.6
Average	**82.8**	**83.7**	**83.5**	**83.0**	**83.0**
standard deviation	0.9	0.4	0.2	0.3	0.4

Figure 13 illustrates a "box and whisker" plot of the data (see Walpole, pg. 209). The box has horizontal lines at the lower quartile (25%), median, and upper quartile (75%) values. The whiskers are the vertical lines extending from each end of the box and show extreme observations in the sample. Outliers are data with values beyond the ends of the whiskers (denoted by a '+' symbol). This display illustrates the median location, variability and degree of asymmetry of the sample. Examination of this plot shows that the quartile ranges of all samples (relative height and position of the box) are approximately the same. The virgin sample shows the presence of an outlying data point that is not representative of the sample hardness. Based on this analysis, as well as the analysis of variance approach stated earlier, at the meso-level, there are no significant differences in the hardness of the

samples, i.e. there are no hardness differences from the virgin to the scuffed samples, at the meso-scale. It follows that since there are no differences at the meso-level, there are certainly no differences at the macro-level.

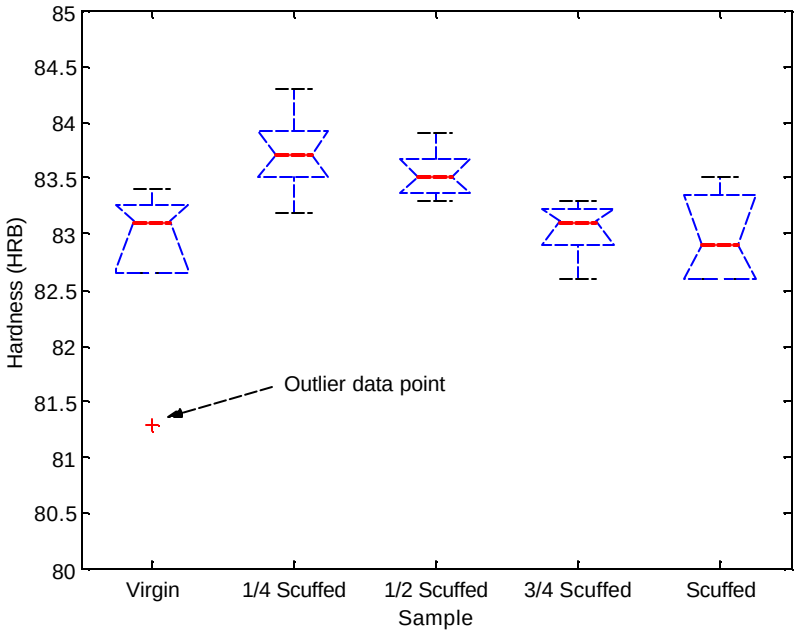

Figure 13: Box and whisker plot of Rockwell B hardness data

Shown below in Figure 14 is a residual indent from the Rockwell B Hardness Test on the Al390-T6 material. Assuming that residual indentation is relatively spherical below the surface (the indenter is spherical in shape), the residual depth can be calculated from the diameter of the residual indent, based on a few simple calculations:

$$R^2 = \left(\frac{D}{2}\right)^2 + a^2 \quad (1)$$

$$depth = R - a \quad (2)$$

R is the radius of the indenter (1/16”), D is the diameter of the residual indent, a is the distance from the center of the indenter to the surface plane, a the depth is the depth of the residual indentation. For these measurements, the diameter of the residual indent is roughly 0.7-0.8 mm long, making the residual depth approximately 130 µm. Looking back at the microstructure in Section 2.3, the average size of a large silicon particle was between 10-20 µm in diameter. Thus, the area affected by a Rockwell B indent in much larger than that of any single silicon particle. This results in an averaging effect of the microstructure, and very consistent results, as discussed above. Since there are no differences at the meso-/macro-scale, we decided to also investigate the mechanical properties at the micro-scale using a Vickers indenter, as described in the next section.

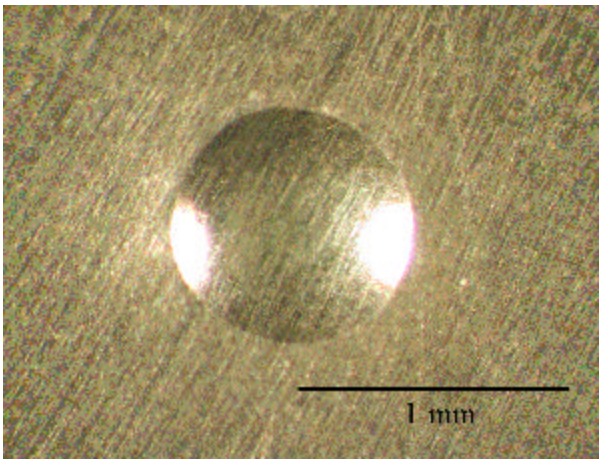

Figure 14: Rockwell B residual indent on Al390-T6

3.3 Micro Hardness Methods: Vickers, Knoop

There are two standard methods of micro-hardness testing: the Vickers and the Knoop hardness tests. They mainly differ on the geometry of the diamond indenter. The Vickers Hardness Test is more commonly used, and is therefore selected for this aspect of the project.

3.3.1 Vickers Hardness Test

The Vickers Hardness Test is a standard method that is both widely practiced and accepted. Due to the smaller size of the pyramidal shaped indenter, in combination with relatively small loads (compared to a Rockwell B test), the Vickers test can be used to evaluate changes in material hardness at smaller, micro-scales (i.e. appropriate for non-homogeneous materials).

3.3.1.1 Test Details

A Micromet® II Microhardness Tester (Digital Model) manufactured by Buehler was used for the Vickers Hardness Test. The machine is located in Professor Sehitoglu's Advanced Materials Laboratory (Room 35B MEB), at The University of Illinois at Urbana-Champaign. It is equipped with a Vickers indenter, which is a 4-sided pyramidal, diamond indenter with a 136° angle between opposing faces. During a test, a user-defined load is applied to the indenter tip, causing plastic deformation of the test material surface. The diameters of the corresponding plastic deformation of the material are measured (i.e. residual deformation), and based on the geometry of the tip, and Vickers Hardness Number (VHN) can be computed using

$$VHN = \frac{1854 \times P}{d_{avg}^2} \qquad (3)$$

P is the load applied to the indenter, while d_{avg} is the average of the two residual indent diagonals measured. Thus, the Vickers Hardness Number is a load divided by a projected area. The constant (1854) is a factor based on the geometry of the tip. The residual depth can be estimated based on the geometry of the tip, such that the residual depth is approximately 1/7 of the average diagonal length.

3.3.1.2 Procedure

The micro-hardness tester should be placed on a vibration isolation table, isolated from all vibrations that could affect the test results. For best results, the surface should be polished to a smooth finish to allow accurate measurement of diagonal lengths. The general test procedure is described below:

1.) Clean sample surface: wipe clean using an acetone-soaked cotton swab; repeat with ethanol-soaked cotton swab; dry using hot air dryer
2.) Clean indenter tip using an acetone-soaked cotton swab; dry using hot air dryer
3.) Coarsely focus on sample surface using 10X objective
4.) Fine focus on sample surface using 40X objective
5.) Select desired test load (10-500 ponds; 1 pond = 1 gram); adjust both weight and dial for correct hardness computation
6.) Set desired load time (20 seconds)
7.) Release weight and wait until LED indicates that test is completed (~ 45 seconds)
8.) Measure diagonals of residual deformation indents on test material, using instrument crosshairs
    a. Switch to 40X objective lens and zero crosshairs when positioned on top of one-another
    b. Position crosshairs on opposite corners to measure the length of the diagonal
    c. Include any plastic deformation present in the material due to the indenter contact
    d. Maintain consistency in measuring; i.e. make sure that the same edge of the measuring line is used for both ends of the diagonal, such that the width of the line is not included in the diagonal length
    e. Rotate lens and repeat for other diagonal
9.) Vickers Hardness Number (VHN) automatically calculated based on applied load and average diagonal length
10.) Repeat for 3-4 indents per load, per material
    a. See Section 4.10 for position of indents on each respective sample

3.3.1.3 Results

The results of the Vickers Hardness Test for the Al390-T6 samples are shown in Figure 15 through Figure 19 below. For each sample, loads of 25, 50, 100, 300 and 500 ponds (grams) were used, and repeated 3-4 times per sample. The indent depth is calculated as 1/7 of the average diagonal length.

Examining the data, there is generally more scatter at lower depths than at the larger depths (see Figure 19 for an example). There are several reasons that can be attributed to this effect: surface roughness, diagonal measurement precision, and surface microstructure. Foremost, these samples are engineering surfaces left unpolished, because a polishing procedure would alter the wear surface of interest. This increases the difficulty in obtaining a uniform indent, as well as defining and measuring the length of the diagonals. At higher depths (i.e. higher loads), the residual indent in the surface is larger, while it is also easier to define the edges of the indent. At small depths, the residual indent is very small, making it difficult to accurately define the edges of the diagonal as well as obtain an accurate measurement (see the discussion below of Figure 20 through Figure 23). The measurement of the diagonal becomes an issue for small indents. Each diagonal length is measured by positioning two cross hairs at opposite ends of the diagonal, and measuring the distance between them. The cross hairs have a

finite width, which may alter results if careful measurement techniques are not practiced. This error is insignificant for large indents, but becomes much more appreciable for smaller indents. Lastly, the surface microstructure plays a major role, as discussed earlier. Based on the microstructural analysis, it was found that large silicon particles average 10-20 μm across. At these depths, the diagonals measure from 10-70 μm across. Thus, at low loads (i.e. low depths), it is possible for an indent to be directly on a silicon particle, and thus mainly influenced by the properties of the silicon particle. Other indents may be placed directly in the matrix, which will increase the variability in the measurements. At higher loads, more of an averaging effect of the microstructure is observed, thus increasing the repeatability of the results.

An analysis of variance test was performed on each sample to examine differences in the measured hardness of each independent sample, as a function of the depth of the indent. A null hypothesis is a proposed relationship between variables. In this case, sample means are compared through examination of the difference between their mean values. This analysis assumes a Gaussian distribution of both data sets. A probability density function (pdf) is constructed, based on the difference between the sample means, where a difference of zero indicates that there are no significant differences between the mean values of the samples. Through the analysis of variance approach, it is possible to quantify a p-value, which corresponds to the sum of the areas under the distribution for the two tails of the distribution. If this area is less than a certain level of significance, then it can be concluded that there is a difference in sample means, at this level of significance. If the p-value is greater than the level of significance, then it cannot be concluded that there is a difference between sample means.

A null hypothesis was tested to check if all depths may have the same sample mean, and thus, the sample hardness is independent of the sample depth. From this analysis, only the scuffed and the ¼ scuffed samples have a p-value less than 0.05. This indicates that there is a significant difference between one or more of the depth hardness readings of these samples. Examination of these graphs shows that this difference occurs only at one middle depth of the sample, and all other depths show the same sample hardness. This is most likely caused by material and/or sample variability, and is not an inherent difference in the hardness of the samples. Thus, it can be concluded that, at the 95% level of significance, there is no change in the hardness of the material as a function of depth of the indent.

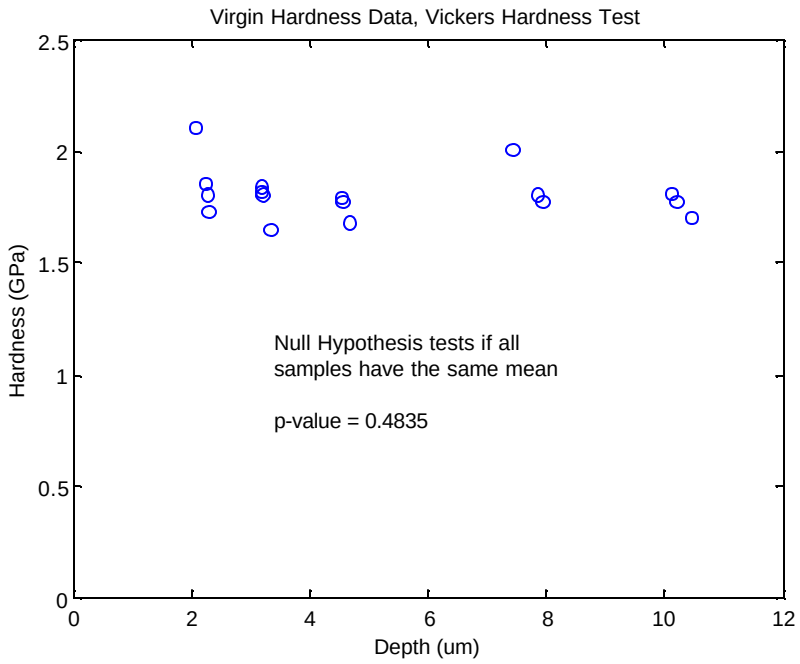

Figure 15: Virgin surface, Vickers Hardness

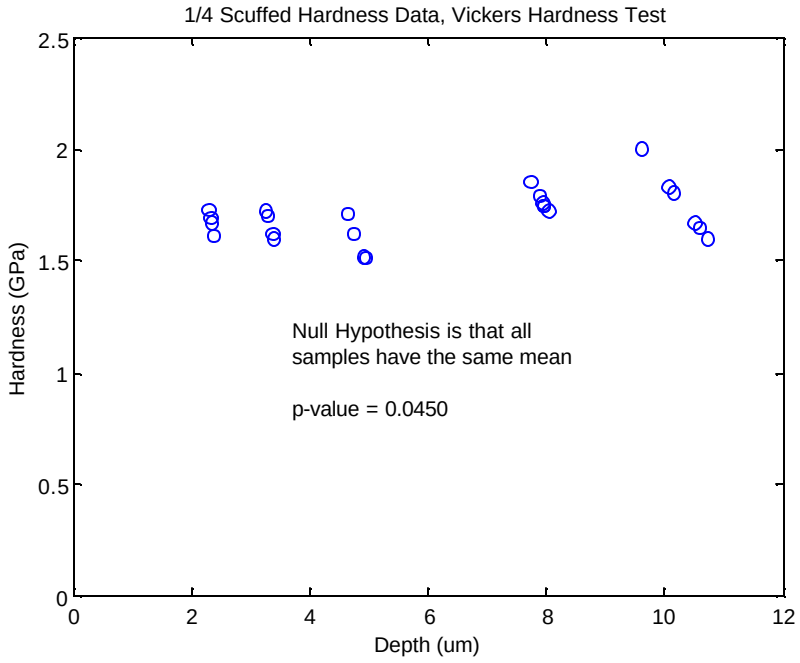

Figure 16: 1/4 Scuffed surface, Vickers Hardness

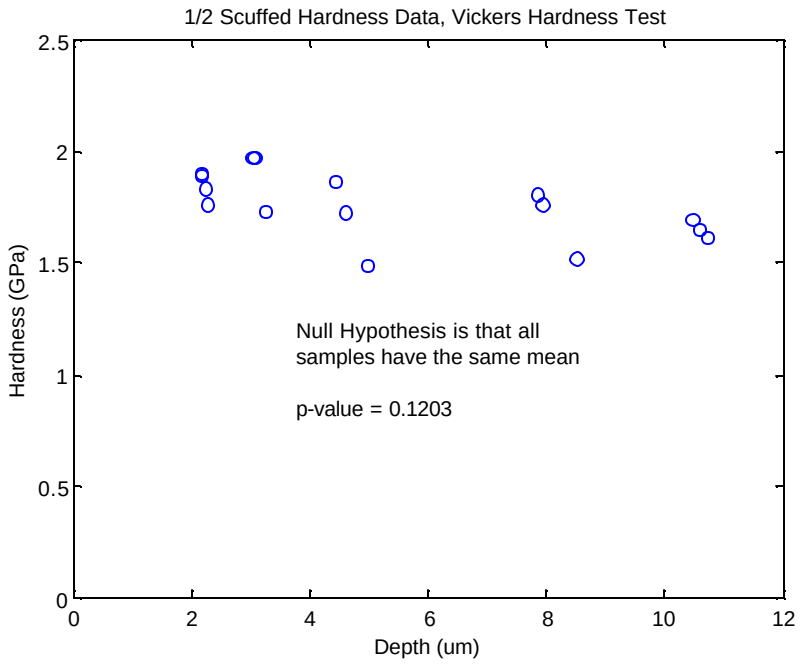

Figure 17: 1/2 Scuffed surface, Vickers Hardness

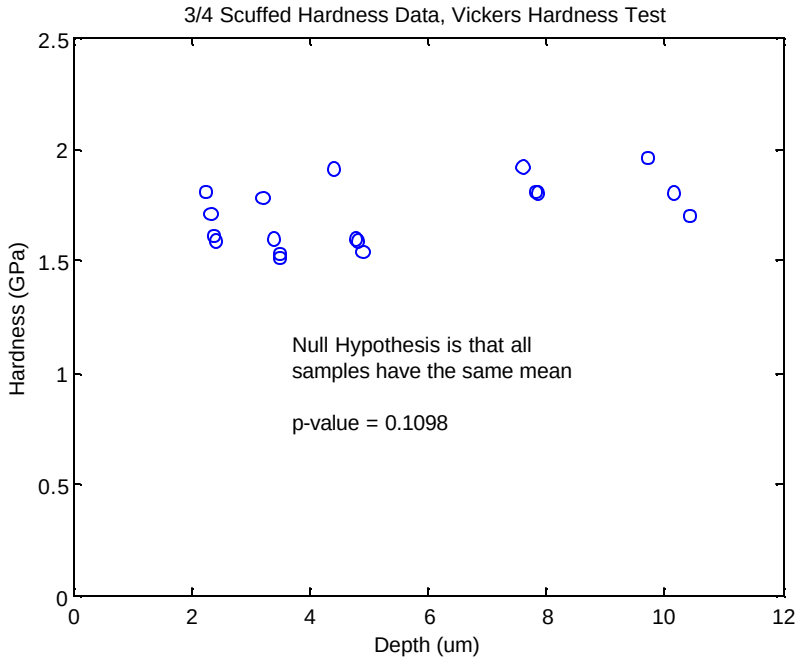

Figure 18: 3/4 Scuffed surface, Vickers Hardness

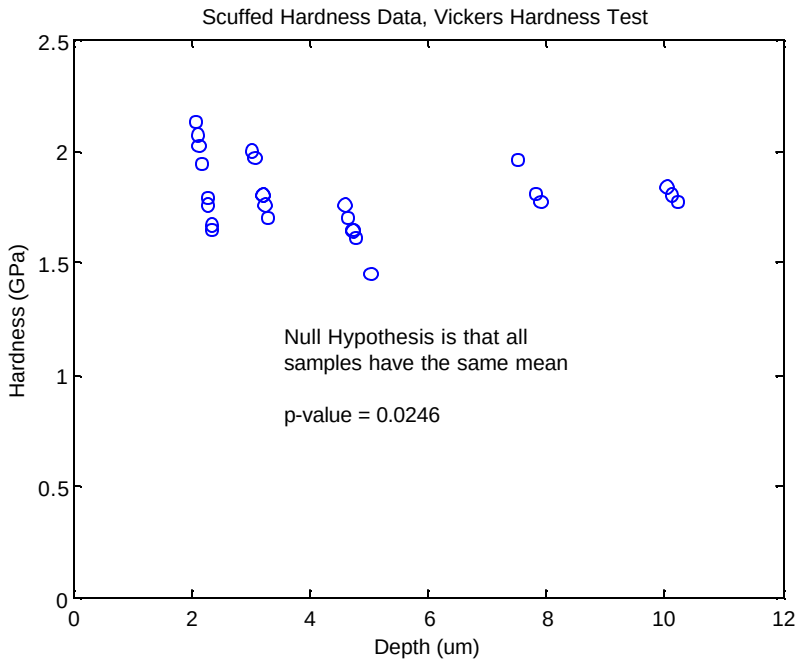

Figure 19: Scuffed surface, Vickers Hardness

Several Vickers indents are shown below (Figure 20 and Figure 21) to illustrate typical residual indents on the sample surface. The larger indents (caused by the larger respective loads of 300 and 500 ponds/grams) are clear and repeatable, while the smaller indents (caused by low loads) are more difficult to distinguish the edges. The residual indent diagonal length varies from 10 – 70 μm (25 – 500 pond loads, respectively).

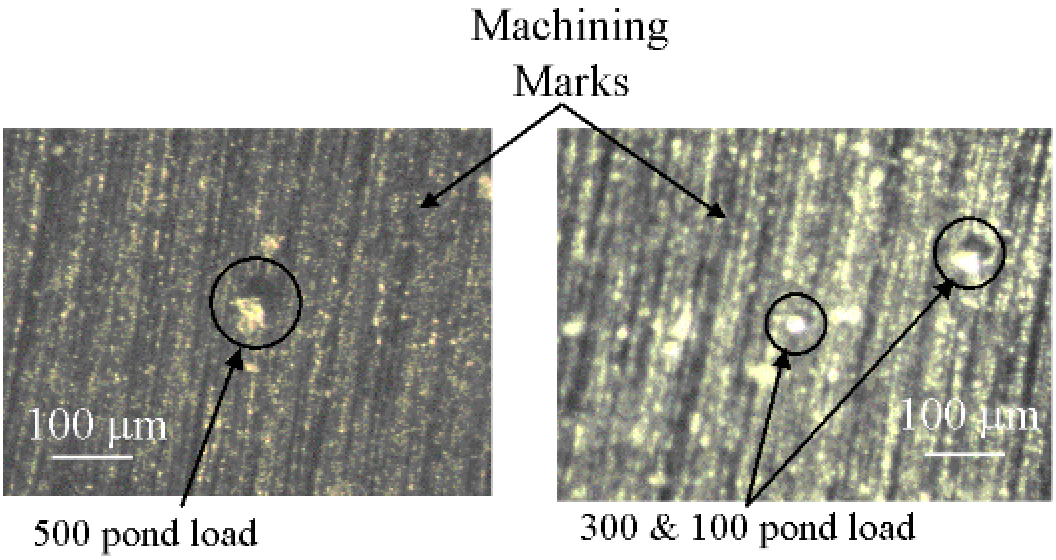

Figure 20: Residual Vickers indent impressions on virgin surface

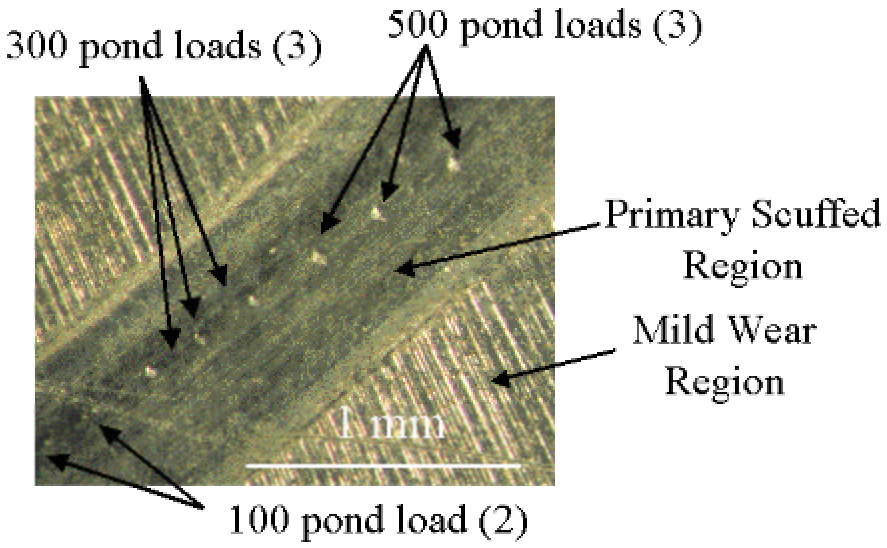

Figure 21: Residual Vickers indent impressions on scuffed surface

Examining the microstructure in Section 2.3 again, leads to some conclusions about the consistency of the results. At high loads, the residual indent measures approximately 60-70 µm in diagonal. This is much larger than the size of any large silicon particle. Thus, the indent size is influenced by an average of the microstructure, which leads to consistent results. At lower loads, the residual diagonal length is much smaller, as small as 10 µm. This is roughly the same size as, or even smaller than, a silicon particle. An indent at these loads is extremely sensitive to the microstructure and results in very localized deformation, which results in a wide scatter in the data at these low loads. Figure 22 further illustrates this point. A cross-section profile of a Vickers indent (300 pond load) is shown on a scuffed sample. From this image, it can be seen that there is deformation due to the indenter, well beyond the residual indent. Analysis shows that this deformation is present at an area approximately two to three times the length of the residual indent diagonal, at the very minimum. This draws further support that larger indents are influenced by an average of the microstructure below the surface, and thus provide more consistent results. Figure 23 is a close-up of the deformation region that appears 'crack-like' in the first image. No differences in chemical composition can be observed between the light and the dark regions. Thus, it is assumed that this area is a high concentration of mechanical strain associated with the indent. This region is similar to the dark 'blotchy' regions mentioned in the microstructure analysis (Section 2.3.2).

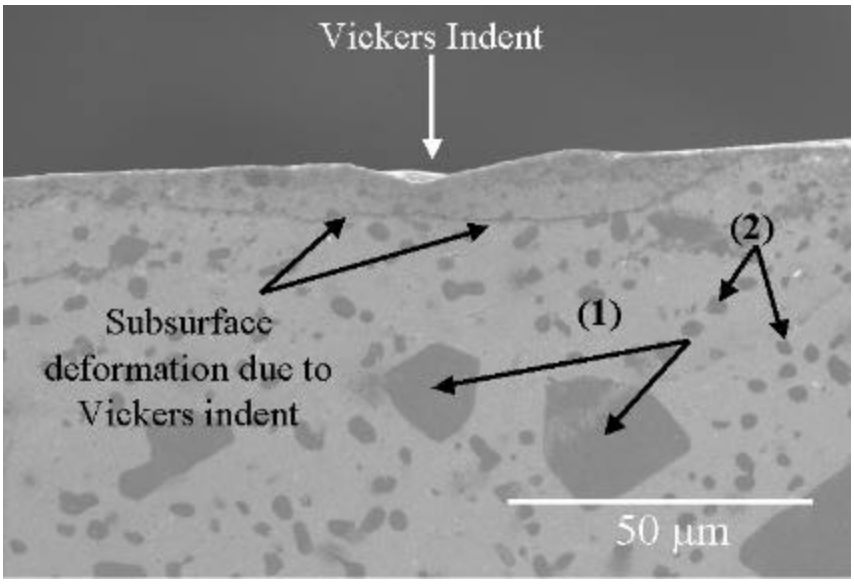

Figure 22: Cross-section image of 300 pond-load Vickers indent; SEM image

(1) – Silicon particle, see Section 2.3 (2) – Si_3Al particle, see Section 2.3

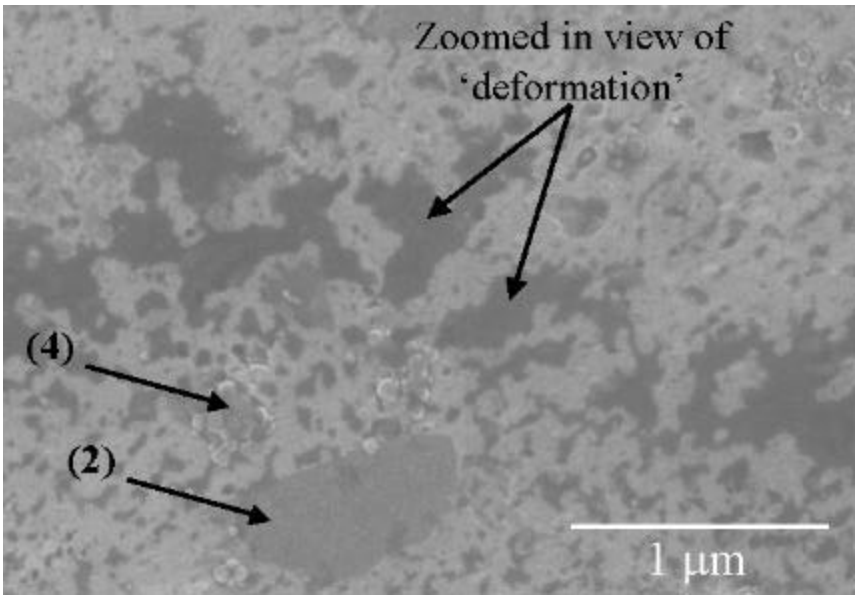

Figure 23: Cross-section image of 'deformation' area from Vickers indent; SEM image

Figure 24 below illustrates the average hardness readings at each depth, for each sample. Once again, an analysis of variance test was conducted to determine if there is significant differences between the hardness of each sample, at a respective depth. The test null hypothesis is that all samples have the same hardness at a respective depth (i.e. load). Based on an analysis of variance test (p-value of 0.05), it cannot be concluded that there are any differences between the samples at deeper penetrations (i.e. p-value is greater than 0.05). Analysis of the lower depths (loads) shows that the scuffed sample reading at 50-pond load is an outlier (as discussed prior). If this data is

ignored, there are no significant differences between the samples at the second smallest depth. The differences at the smallest depth are borderline significant, at the 95% level. Thus, it cannot be concluded that there are any significant hardness differences between the samples, at respective depths.

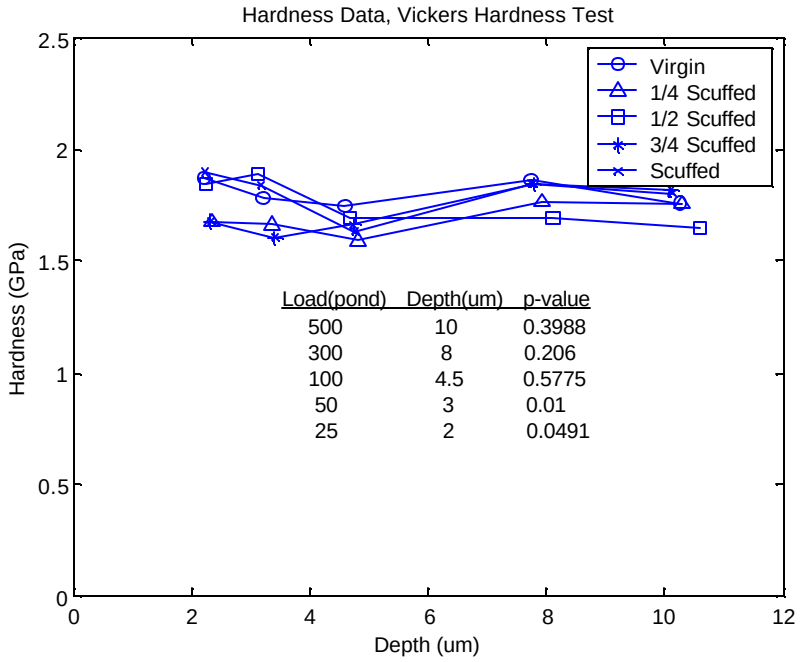

Figure 24: Average Vickers Hardness values, all samples

3.4 Scale Conversions

The ASTM Annual Book of Standards publishes tables for approximate hardness conversions between different scales. This allows the macro- and the micro- hardness readings to be compared on a similar, continuous scale. [E-140-88, ASTM Annual Book of Standards] This also allows hardness readings from the arbitrary Rockwell scale to be converted to a more meaningful hardness scale in which hardness is equal to the maximu m load divided by the projected area of the residual indent (i.e. Vickers Hardness Number). The conversion table is shown in the Table 3.

Table 3: Approximate hardness conversion for non-austenitic steels from reference [E-140-88]

Rockwell B Scale 100-kgf Load 1/16-in. Ball	Vickers Hardness Number	Brinell Hardness 3000-kgf Load 10-mm Ball	Knoop Hardness 500-g Load and Over	Rockwell A Scale 60-kgf Load Diamond Cone
100	240	240	251	61.5
99	234	234	246	60.9
98	228	228	241	60.2
97	222	222	236	59.5
96	216	216	231	58.9
95	210	210	226	58.3
94	205	205	221	57.6
93	200	200	216	57.0
92	195	195	211	56.4
91	190	190	206	55.8
90	185	185	201	55.2
89	180	180	196	54.6
88	176	176	192	54.0
87	172	172	188	53.4
86	169	169	184	52.8
85	165	165	180	52.3
84	162	162	176	51.7
83	159	159	173	51.1
82	156	156	170	50.6
81	153	153	167	50.0
80	150	150	164	49.5
79	147	147	161	48.9
78	144	144	158	48.4
77	141	141	155	47.9
76	139	139	152	47.3
75	137	137	150	46.8
74	135	135	147	46.3
73	132	132	145	45.8
72	130	130	143	45.3
71	127	127	141	44.8
70	125	125	139	44.3
69	123	123	137	43.8
68	121	121	135	43.3
67	119	119	133	42.8
66	117	117	131	42.3
65	116	116	129	41.8
64	114	114	127	41.4
63	112	112	125	40.9

3.5 Conclusions

Meso and micro hardness tests have been performed on the surface of each of the five pre-scuffed and scuffed samples. The Rockwell B Hardness test was used for examination of the surface hardness at the meso scale. The results are extremely repeatable and consistent. This consistency is, in part, due to an averaging effect that a relatively large indenter has on the smaller microstructure of the material. From the data analysis, it can be concluded that there are no differences between the samples at the meso-level. The Vickers Hardness test was used to examine the surface hardness of the samples as a function of depth at the micro-level. There is more scatter in these data compared to that of the meso test, especially at lower penetration depths. This can, in part, be attributed to an increasing microstructural dependency of the indent as the size of the indent approaches the relative size of microstructural features. By using an analysis of variance technique, it can be concluded that there are both, no

apparent differences in the surface hardness as a function of depth at the micron level, and that there are no apparent differences between samples. This is the point at which most conventional researchers stop their study. This project is different in that the focus now shifts to the examination of the surface hardness at the nano-level, in an effort to identify and quantify changes in material properties, both as a function of depth and to examine differences between samples.

Chapter 4: Nano-Indentation Technique

4.1 Introduction

The current study has progressed from the examination of surface mechanical properties at the meso-scale, to the further investigation of these properties at the micro-scale. Trends have been analyzed, but no appreciable differences between samples have been observed. Thus, in order to continue this investigation, it is necessary to examine the mechanical properties at the nano-scale.

Several methods exist for the determination of thin film material properties (at the nano-scale), but most rely on separation of the films from the substrate, and subsequent analysis of individual films (or individual film analysis before depositing the layer) [Naghavi *et al*, 2000]. These methods are impractical on engineering surfaces, as surface films are unknown and cannot be removed for analysis purposes. A technique known as nano-indentation was developed to solve these issues.

Similar to meso/micro hardness tests, nano-indentation is based on a material resistance to permanent plastic deformation. This technique presses an extremely sharp, hard tip into a surface, under a certain, prescribed load. Through examination of the tip load and displacement data, a material hardness and elastic modulus can be calculated. This technique allows one to examine thin film material properties on very complex surfaces, without having to separate and examine each layer individually. The differences between this test and the meso/micro test are that the tip geometry and loads are much smaller, and corresponding indentations/penetrations are in the nano-meter scale.

Nano-indentation is a tool commonly used in the semi-conductor and magnetic storage Hard Disk Drive (HDD) industries. Thin films exist, but are of known materials and thicknesses. Surfaces are uniform, and also extremely smooth. This technique has proven to be very effective in characterizing the changes in hardness associated with different layers on these surfaces. Engineering samples studied in this research are a very different application. Surfaces are extremely rough, sometimes with a surface roughness more than two orders of magnitude greater than those observed on semi-conductor surfaces. Semi-conductor surfaces have Ra values of tens of nano-meters; HDD surfaces have Ra values on the order of 1 nm, while these engineering surfaces have Ra values of 100 nm to 1 µm. Non-uniform surface layers exist, and usually unknown. Surfaces are also non-uniform in nature, and vary depending on the microstructural distribution. The various issues will be examined in an effort to use this method to characterize the nano-scale surface material properties of these engineering surfaces.

4.2 Instrumentation

Several companies market nano-indentation instruments. Hysitron [http://www.Hysitron.com], MTS [http://www.mts.com] and CSEM [http://www.microphotonics.com/nht.html] are some of the most well known names.

The Materials Research Laboratory at The University of Illinois at Urbana-Champaign is equipped with a Triboscope Nano-Indenter made by Hysitron, Inc. The Triboscope® is an attachment to a current Digital Instruments Multimode SPM (Scanning Probe Microscope) [http://www.di.com/Products/Multi/MMMain.html]. The SPM has the added benefits of extremely fine lateral displacement positioning and in-situ imaging of the indenting surface. The Triboscope® mainly consists of a three-plate capacitive transducer, and other associated

hardware and necessary attachments. The transducer is capable of a force resolution of less than 1 nN and a displacement resolution of 0.0002 nm [Kuhn, 1998]. With noise, the force and displacement resolutions are approximately 100 nN and 0.2 nm, respectively (Figure 36 discussed later shows a normal force resolution of 2 μN, but this can be decreased slightly by adjusting the gains appropriately). Based on these resolutions, the setup is capable of indentation loads of less than 10 μN, and displacements of less than 5 nm.

4.3 Nano-Indenter Tips and Tip Area Calibrations

Hysitron offers a wide assortment of nano-indentation tips. Tips are usually made of diamond, and consist of an angular geometry with a spherical tip at the point. Their uses vary depending on the intended material, intended depths of penetration, and presence of surface layers. Each specific application defines an ideal tip geometry for that specific purpose. Several aspects must be considered when choosing a tip. The first requirement is plastic deformation of the material. Hardness is defined as a resistance to permanent plastic deformation. Thus, if the plastic deformation of the material does not dominate over the elastic recovery of the material, then hardness will not be a constant material property. Plastic deformation can be achieved through either increasing the aspect ratio (ratio of vertical tip dimension to that of the horizontal) or decreasing the radius of curvature of the tip, thus providing more localized, plastic behavior. The tip radius must reflect the hardness of the material tested. For softer materials, the radius of curvature of the tip must be larger to avoid excessive local plastic deformation. For harder materials, it must be smaller in order to achieve adequate plastic deformation. In order to examine very shallow depths, a very small radius with a high aspect ratio tip is needed to achieve the required plastic deformation at shallow depths. To examine deeper depths, a larger radius and a lower aspect ratio is required to prevent blunting of the tip. Two tips have been chosen for this aspect of the project: 1) Berkovich tip (based on the referenced paper by Berkovich); 2) 90° – cube corner tip.

The Hysitron Berkovich tip is intended for deeper nano-indentation penetrations. The tip is a 3-sided pyramid with an included angle of 142.3o, where the angle from the normal to a face is 65.35o (see Figure 25). At the tip of the indenter is a "sphere" with a radius of curvature between 100-200 nm. In this figure, the indenter contacts the material only at the very peak of the tip. Because of its relatively large radius of curvature and relatively low aspect ratio, it is recommended that the tip be used for penetrations greater than 50nm deep.

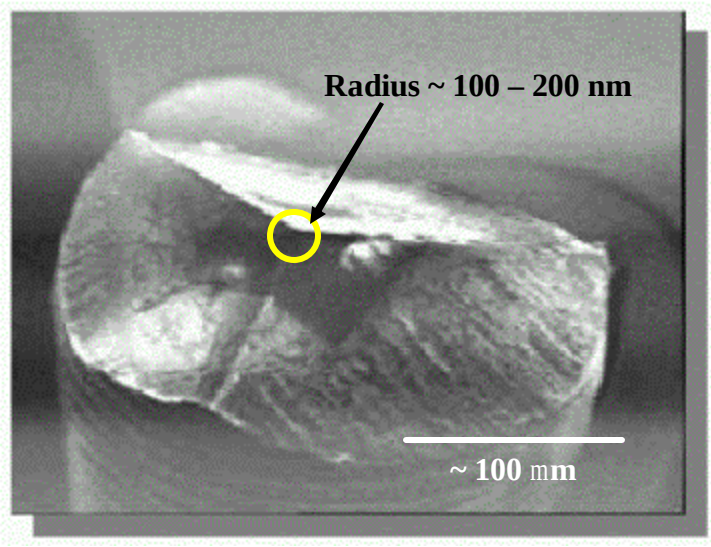

Figure 25: Berkovich tip image (courtesy of Hysitron, Inc.)

The 90° – cube corner tip is also a three-sided pyramid, but the included angle is smaller, 90° (see Figure 26). The radius of curvature of the tip is on the order of 50 nm. The area of the indenter in contact with the material during a test is very small, and located only at the very tip of the geometry. Thus, because of the higher aspect ratio and the decreased radius of curvature of the tip, this tip is more appropriate for shallower penetrations and the determination of properties of thin films less than 50 nm deep. In order to prevent blunting of the tip, it is not recommended to consistently use the tip at depths much greater than 50 nm. Other tips with a higher aspect ratio and a finer tip radius of curvature are available, but their use is recommended only for very specialized applications.

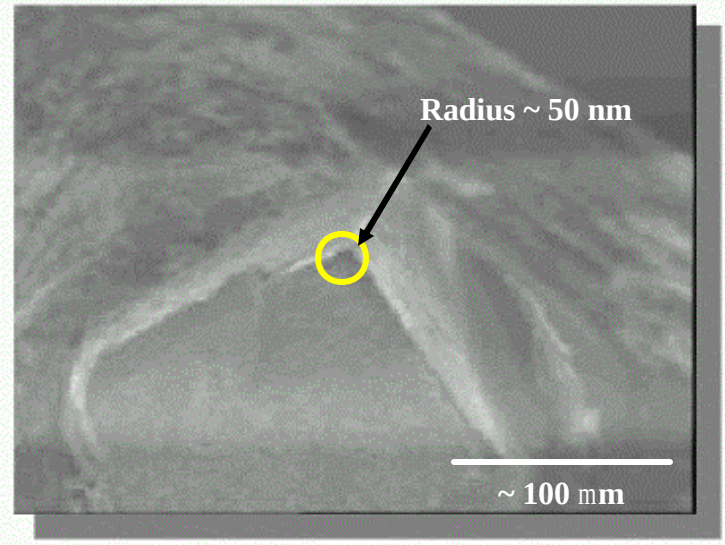

Figure 26: 90° – cube corner tip image (courtesy of Hysitron, Inc.)

The projected area of the tip, in contact with the material during an indent, is used directly in the calculation of material properties, E_r (defined in Section 4.4) and H. Individual tip geometry may vary depending on

machining inconsistencies as well as wear associated with the tip, i.e. radius of curvature at the tip. Shown below (Figure 27) is an SEM image of a 90° – cube corner tip after it has been extensively used at high loads. Significant blunting can be observed at the peak of the tip, on the order of 500 nm in width. During an indent, the projected area of the tip is usually less than one hundred nanometers. Thus, nano-indentations performed with this tip will take place entirely within the blunted region of the tip. The large particles on the edges of the tip represent contamination from the test materials. The streaks represent a smearing of the contamination due to a cleaning procedure. Thus, both blunting of the tip and machining differences will have a significant effect on the area of the tip in contact with the indenting surface. Therefore, individual calibration of the tip area is essential for accurate and repeatable results. The calibration procedure is done once with all new tips, and then checked each time that the tip is used (see Section 4.6.4). If the tip shape has been significantly altered, the calibration procedure is repeated. Note that this is not the tip that was used for nano-indentation tests, but it does illustrate the effects of using the tip at loads higher than its recommended use.

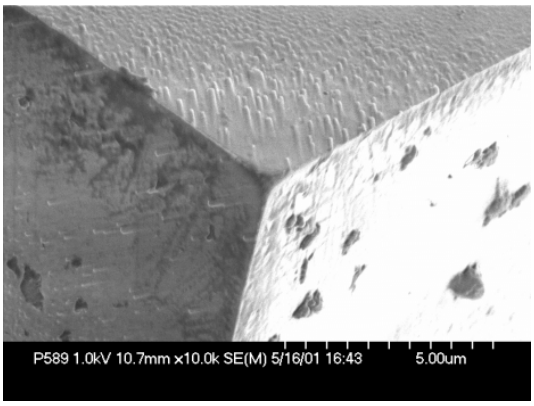

Figure 27: SEM image of 90° - cube corner tip showing blunting at tip

Since the diamond indenter is ideally a rigid body, the contact area profile can be accurately determined as a function of the depth of the indent. Other researchers have examined the case of a non-rigid indenter and found that such cases can also be treated [Lo *et al*, 1999]. The rigid body indenter method, developed by Oliver and Pharr [Oliver, 1988], uses data from the load/unload curves as well as established material properties of a known material to obtain a tip contact area profile as a function of the contact depth. Assuming that there is no pile-up during indenting (i.e. pile-up of material around the edges of the indent due to conservation-of-volume principles), this area function will be accurate for all materials. Thus, the area is a function of the contact depth of the indenter (explained later in this section), $A = f(h_c)$.

The first step is to define the relevant geometrical parameters. Figure 28 illustrates an actual load displacement curve of a typical indent as well as some key parameters. Pmax is defined as the maximum load, while hmax is the indentation depth at the maximum load. The contact stiffness, $S = \frac{\partial P}{\partial h}$ evaluated at P = Pmax is defined as the slope of the unloading curve at the maximum load. Doerner and Nix suggest that this region can be obtained from a linear fit of the top one-third of the unloading curve.

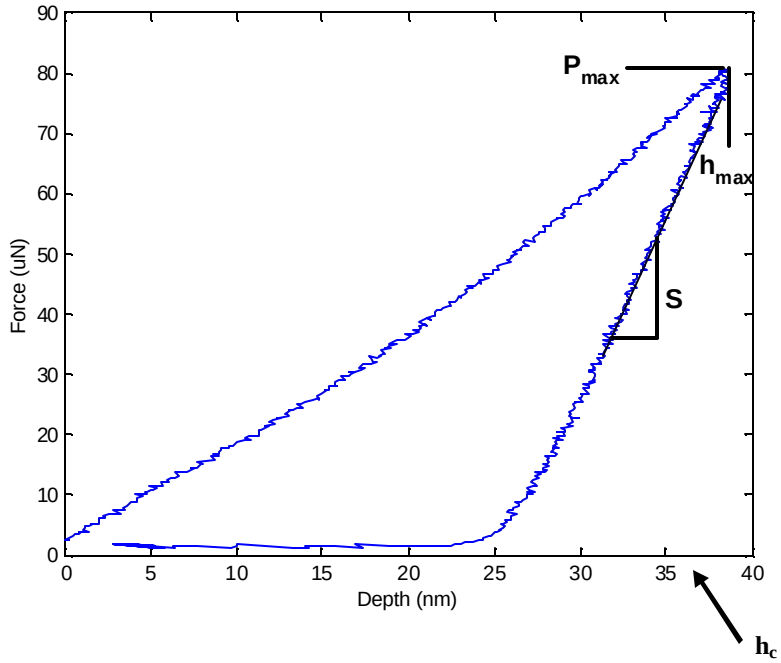

Figure 28: Load-displacement curve and associated parameters

Figure 29 shows a cross-section profile of an ideal indent, also showing several key parameters. Once again, hmax is the depth of the indent at the maximum load. The deflection of the surface at the perimeter of the indenter is defined as hs while the contact depth, hc, is defined as the difference, $h_c = h_{\max} - h_s$. (In Figure 29, capital H corresponds to lower case h)

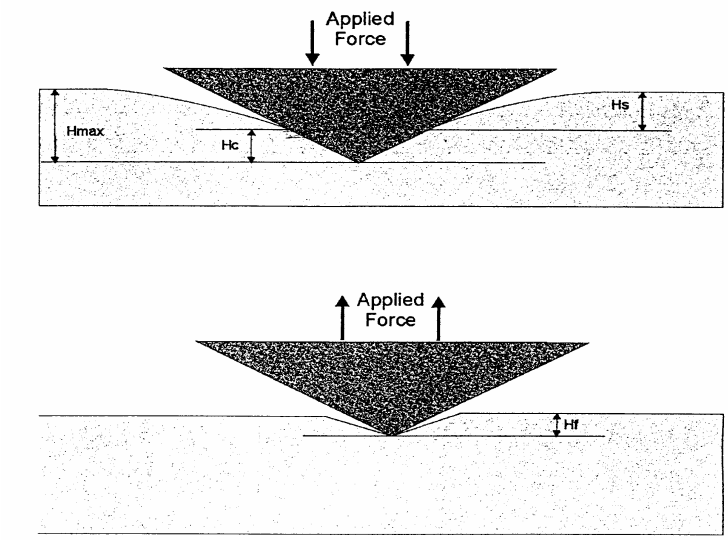

Figure 29: Cross-section profile of an ideal indent

The calibration procedure, developed by Oliver and Pharr [Oliver, 1988], states that the contact area for each respective contact depth can be calculated from:

$$A = g \cdot \frac{4 \cdot S^2}{p \cdot E_r^{\,2}} \tag{4}$$

This assumes that E_r is known and independent of penetration depth. The γ-factor arises from the radial displacements inside the indentation [Hay, 1999], and is a factor of both poison's ratio of the material and the indenter semi-angle. The γ-factor shows the greatest effects for sharper tips such as the 90° – cube corner tip. In this calibration procedure, γ is assigned a value of one, thus ignoring the area function dependence on it. Fused quartz is usually chosen as the calibration material. It has no known surface layers, and a known value for the reduced elastic modulus (see Equation 4 below) of $E_r = 69.6\,\text{GPa}$, and a hardness of approximately $H \approx 9.6\,\text{GPa}$.

By plotting the calculated contact area as a function of contact depth for a variety of depths within the desired tip indent depth range, the tip area function can be defined. The ideal tip area function is defined as $A = C_0 \cdot h_c^2$, ($A = f(h_c)$),where C_0 is fixed constant depending on the geometry of the tip, i.e. for a Berkovich tip, C_0 = 24.5, and for a 90° cube corner tip C_0 = 2.598. In order to compensate for the finite tip radius, as well as machining differences, additional terms are added, such that

$$A = C_0 \cdot h_c^2 + C_1 \cdot h_c + C_2 \cdot h_c^{\frac{1}{2}} + C_3 \cdot h_c^{\frac{1}{4}} + C_4 \cdot h_c^{\frac{1}{8}} + C_5 \cdot h_c^{\frac{1}{16}} \tag{5}$$

The first constant, C_0, is once again fixed depending on the geometry of the tip, while the other constants are curve fitted in a least squares method (based on Er = 69.6 GPa, see Figure 30). Thus, the tip contact area can be calculated based on the known contact depth, h_c, within the calibration range. This fitting function is not exact, but is a reasonable approximation. The Berkovich tip is calibrated well beyond the spherical point of the tip. Thus, the area function is dominated by the Berkovich geometry, and the tip area function is a good approximation. For the 90° – cube corner tip, the tip radius is significant within the lower depths of the calibration range. Thus, the tip area function is not necessarily a good approximation in this range. Based on comparing the curve fitted area function to an area function obtained from a spherical fit of the tip (assumes tip is spherical at tip, with a radius of 50 nm), the tip area function may under predict the tip area for depths between 5 and 16 nm, and have an associated error of up to 5%. This is a relatively small error, and is the best that can be achieved with a single area function.

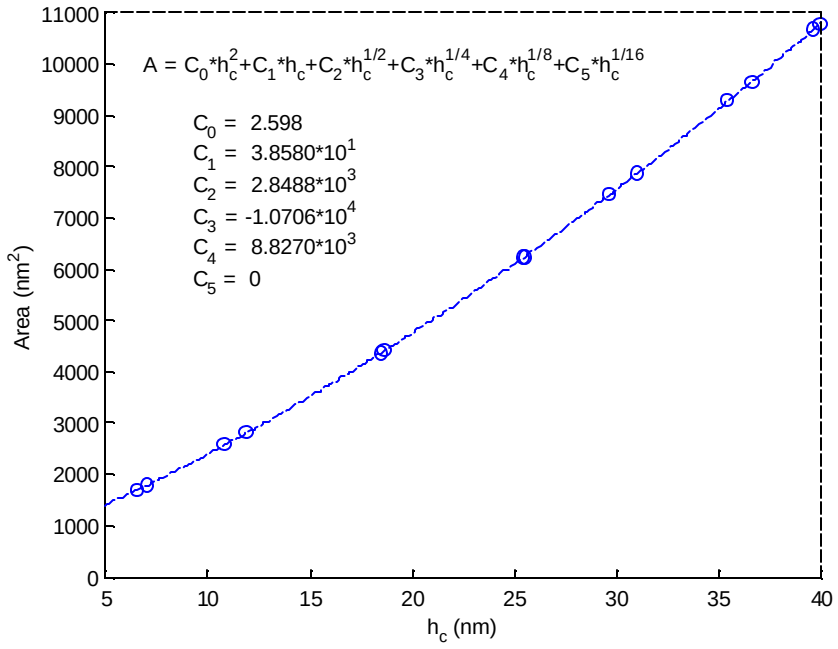

Figure 30: Tip area function least squares fit; 90° - cube corner tip

The tip area function constants for these specific cube corner and Berkovich tips are given as:

CubeCornerTip	*BerkovichTip*
$C_0 = 2.598$	$C_0 = 24.5$
$C_1 = 3.8580 \cdot 10^1$	$C_1 = 1.0097 \cdot 10^4$
$C_2 = 2.8488 \cdot 10^3$	$C_2 = -5.2274 \cdot 10^5$
$C_3 = -1.0706 \cdot 10^4$	$C_3 = 2.9513 \cdot 10^6$
$C_4 = 8.8270 \cdot 10^3$	$C_4 = -2.8290 \cdot 10^6$
$C_5 = 0$	$C_5 = 0$

The cube corner tip is calibrated for a contact depth range of 6.5 nm to 40 nm, while the Berkovich tip is calibrated for a range of 47 to 250 nm. The maximum calibration range for the Berkovich tip is limited by the maximum load of the instrument.

4.4 Calculation of Material Properties (E_r and H)

Oliver and Pharr [Oliver, 1988] analyzed the load-displacement data and developed equations for calculating two important material properties, hardness (H) and reduced elastic modulus (E_r), using:

$$E_r = 2 \cdot S \cdot \sqrt{\frac{p}{A}} \qquad (6)$$

$$H = \frac{P_{max}}{A} \tag{7}$$

where the tip contact area, A, is a function of the contact depth derived from the tip area calibration Equation (5), S and P_{max} are constants defined prior, while E_r is the reduced elastic modulus given by:

$$\frac{1}{E_r} = \frac{(1-n^2)}{E} + \frac{(1-n_i^2)}{E_i} \tag{8}$$

E and ν are the elastic modulus and Poisson's ratio of the specimen, while E_i and ν_i are material constants for the indenter tip. This equation assumes that the deflection of the tip is zero, which is a reasonable assumption since the diamond tip is extremely rigid, with E_i = 1,140 GPa and ν_i = 0.07, respectively.

4.5 Loading functions

A major decision in the nano-indentation procedure is the choice of the loading function. Based on prior work [Kuhn, 1998], a loading/unloading profile linear with time (called ramp loading) is chosen (see Figure 31). This profile starts and finishes at a tip load of 0 μN (neglecting the set point – load applied to the tip during tip engagement such that the tip maintains contact with the surface). The peak load is reached at the mid-time of the profile duration, with a linear relationship between these points. Thus, the times to load and unload the tip are the same. To maintain consistency, it is important to maintain a constant loading/unloading rate, independent of the peak load. Thus, the segment times must be adjusted accordingly. Also note that if the loading profile is too long in its duration, significant electrical drift may be a major problem (instrumentation problem).

Figure 31: Linear, ramp loading profile, without hold at peak load

Certain samples (i.e. polymers, etc.) exhibit creep, such that under constant load, an increased normal displacement will be observed. This will affect the slope of the unloading curve and the maximum penetration,

resulting in incorrect calculations of H and E_r. In order to compensate for this effect, a 'hold' at peak load segment is added to the load profile, yielding a trapezoidal loading function (Figure 32). The duration of this hold segment is determined experimentally such that a maximum penetration depth is reached prior to unloading. Thus, the unloading curve and the maximum depth will be accurate, resulting in more accurate material property calculations. The use of this function is examined in Section 4.9.2.

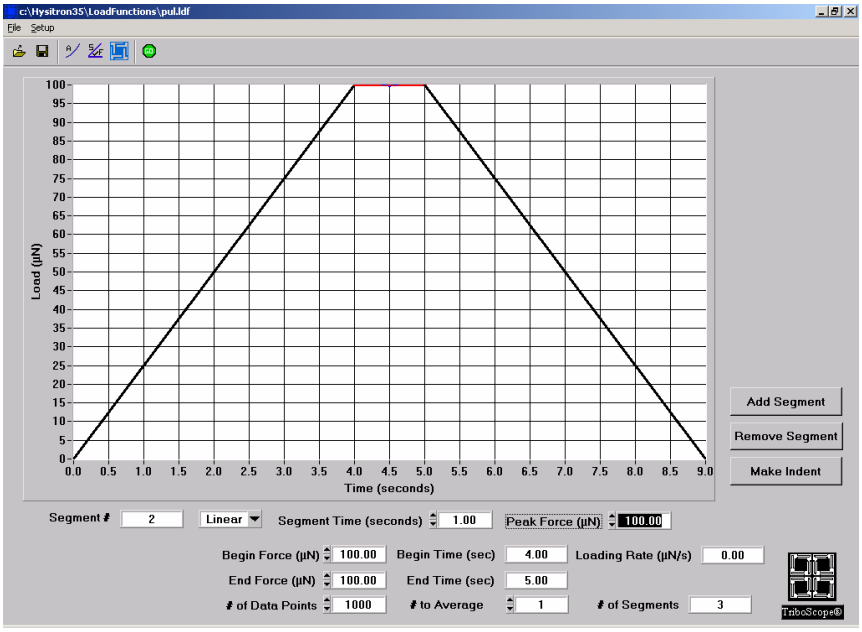

Figure 32: Linear ramp loading profile with hold at peak load

Once the nano-indentation procedure and calculation of reduced elastic modulus and hardness has been verified, the goal shifts to obtaining a larger number of reproducible data points in a short amount of time. Thus, the Hysitron-defined '*pul-load*' loading profile was examined. The loading profile as a function of time can be seen in Figure 33 below. Note that it consists of a saw-tooth loading profile that loads the tip up to a certain force, releases part of the load (roughly 1/3), and then loads to a slightly higher load. This loading procedure is repeated ten times until the final load is reached. This loading profile is similar to the single indent loading profile in that it is linear with respect to time for each single loading and unloading profile. Releasing approximately one-third of the load each during each unload cycle before the load is subsequently increased provides a linear region of the unloading curve and releases a significant portion of the elastic strain in the material such that computation of the hardness and reduced elastic modulus can be accurately completed. One important procedural note is that the number of data points obtained from the indent must be increased to approximately 8000 points (1000 for single indents), such that there are enough data to provide an accurate curve fitting of all unloading functions. The major advantage of using such a profile is the ability to obtain a large amount of data points in a small amount of time. Roughly speaking, ten times more data points can be obtained in the same amount of time that it takes to perform a single indent on the material. Another advantage is that using successively deeper indents in exactly the same area on the sample will allow the user to obtain a hardness/reduced modulus of elasticity profile as a function of depth for precisely that location. This will aid in the analysis by minimizing variability in the data, as well as provide valuable insight into

the changing material properties as a function of depth. This loading profile should yield results very similar to those obtained with multiple ramp load indents. Strain hardening is not an issue because each successive load segment has a greater load than the previous load curve, thus indenting material that has not been indented before.

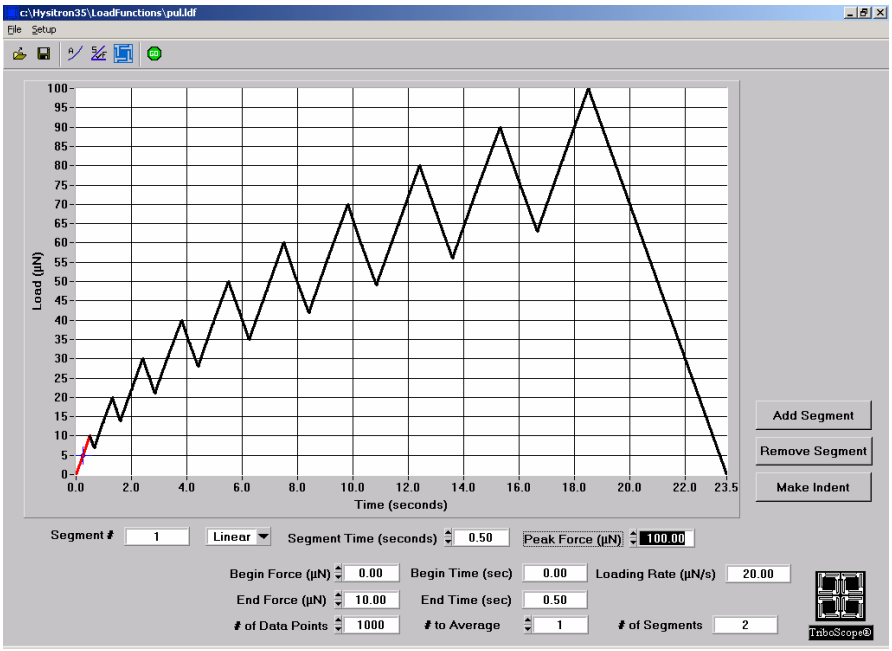

Figure 33: 'Pul-load' loading profile

In order to verify that the '*pul-load*' loading profile provides consistent and accurate results, several indents were performed on fused quartz, and their results were compared to those of the single indents under the same loads. The resultant loading profiles are shown in Figure 35 below. Note that the '*pul-load*' loading function basically overlays those of the single indents at different loads and that the unloading curves are of consistent shape and slope. Thus, the calculated material properties of the two loading functions should be consistent, which can be seen in Figure 35 below. Note that the tip calibration procedure is to a minimum depth of 10 nm, and that the area function is not accurate below this depth, thus yielding inaccurate hardness values at low depths.

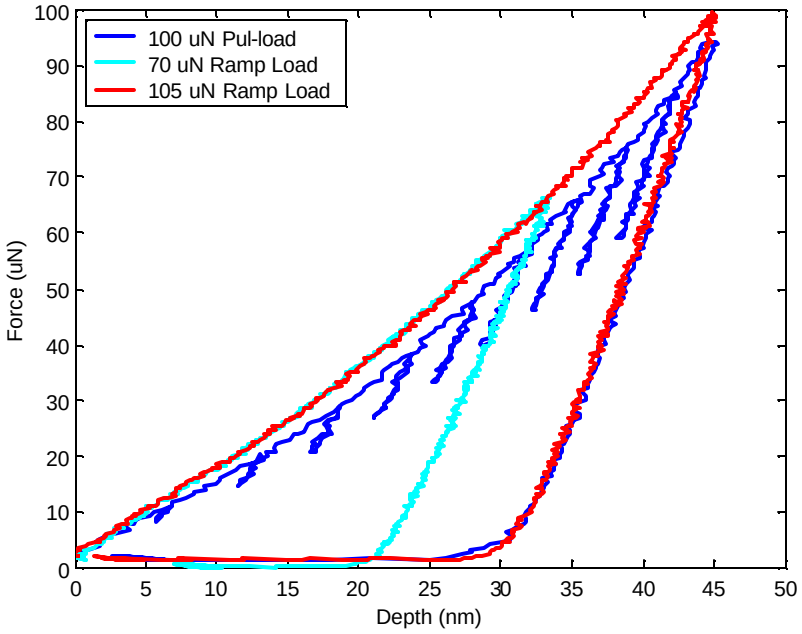

Figure 34: Loading curve of *'pul-load'* vs. ramp load, fused quartz

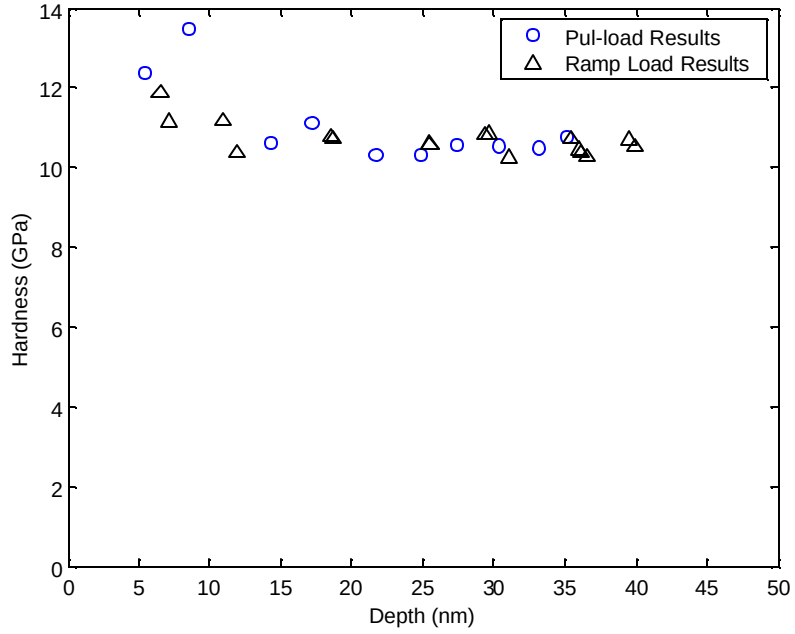

Figure 35: Fused quartz hardness resulting from *'pul-load'* vs. ramp load

Based on the previous analysis, it is concluded that it is appropriate to use the *'pul-load'* loading function for the nano-indentation procedure. Its use will improve data consistency, maximize efficiency of data acquisition, as well as aid in the data analysis.

4.6 Procedure

The nano-indentation procedure and experimental set-up must be consistent and precise such that qualitative analysis can be completed with the utmost accuracy.

4.6.1 Sensor Drift

The drift of the piezo-electric sensor can be a major issue during instrument operation. Based on personal experience, there are two control boxes, which, if the electronics are not warmed up, will cause significant drift. The NanoScope control box must be turned on at least two-hours before running any meaningful experiments. The Triboscope control box must be turned on at least one-half hour before testing. By allowing the electronics of these instruments to reach steady state, the drift of the sensor can be minimized. Also, when a piezo-offset is changed, it takes the sensor a few minutes to reach a steady condition. This effect is magnified for larger offsets. If an indent is performed before this steady state condition is reached, significant thermal drift will result. The drift correction should always be turned on when running tests such that any drift that is present will be compensated for in the data measurements. A maximum drift rate (0.0100 nm/sec) is set such that the instrument will not take data until the drift rate is less than the prescribed value. A *'pul-load'* is approximately 23 seconds in duration, and therefore the drift is less than 0.23 nm.

4.6.2 Sample/Tip Cleaning

Before performing nano-indentation experiments on each sample, the sample must be cleaned to remove any contamination that may have occurred as a result of storage or handling. First, the sample surface was lightly brushed with a cotton swab soaked in acetone. A second cotton swab soaked in ethanol was used to remove acetone remnants, and dry nitrogen was used to dry the surface. The probe tip may also pick up contaminants from storage, but may also pick up material particles from the material being tested. These contaminants will change the tip area such that the fitted tip area function is no longer accurate. Thus, it is important to clean the tip before testing, when changing samples, and periodically during testing if many indents are to be performed. It was found that a cotton swab soaked in ethanol did not remove all of the particles, while a cotton swab soaked in acetone did a much better job. Thus, cleaning the tip consisted of lightly brushing a fluffed, acetone soaked cotton swab towards the tip, while trying to put minimal lateral force on the tip.

4.6.3 Air Indent

Once the nano-indenter is set-up and the proper tip is cleaned and installed, it is necessary to obtain the correct Electro-static force constant. This constant defines the attractive force between the plates at various spacing, and is similar to an adhesive force between the plates. By accounting for this force, a correct force measurement can be obtained at all indenter depths. Finding the Electro-static force constant is accomplished through an indent in the air, i.e. an air indent. The tip is positioned sufficiently far from the sample, and a loading function is executed. A good choice is a 50 μN maximum load, with loading and unloading segments of equal 2-second durations. Since the tip is not in contact with the surface, no load will be measured, and the loading function will time out at approximately 270 nm in depth.

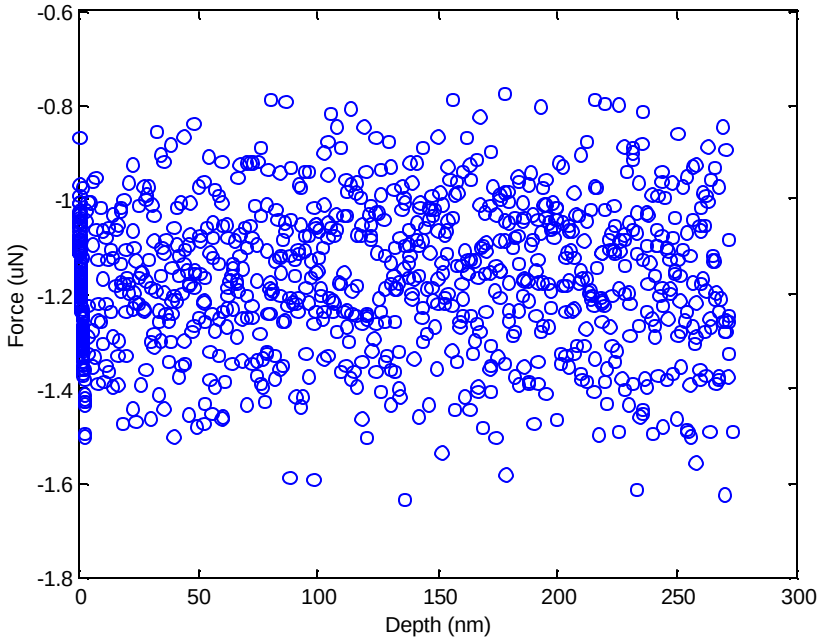

Figure 36: Air indent with corrected electro-static force

Displayed on the force versus depth graph will be a series of points, mostly reflecting noise in the measurement. By adjusting the electro-static force, this graph can be leveled such that the force is constant, ranging between ± 2 μN for all depths (see Figure 36 for an example).

4.6.4 Fused Quartz Check

Before running any tests on experimental samples, the set-up is always verified through several indents on a known fused quartz sample ("calibration standard"). By comparing the maximum loads and corresponding depths as well as E_r and H to the calibration data on fused quartz, it can be verified that the tip, as well as the set-up, is in good working condition. Using the 90° cube corner tip, two indents, one at 100 μN and the other at 35 μN are performed. These loads were chosen based on the desired indentation depths and give an accurate understanding of the relative condition of the tip (i.e. blunting of the tip, etc.) at all desired depths. Based on the calibration data, these indents should penetrate to approximately 43 nm and 19 nm respectively, with E_r ~ 69.6 GPa and H ~ 10.4 GPa. The procedure for the Berkovich tip is similar, with loads of 800 μN and 6000 μN. The respective maximum penetration depths are 69 nm and 211 nm, with E_r ~ 69.6 GPa and H ~ 9.5-10.0 GPa.

4.6.5 Measurement Area - Peak vs. Valley

The indenter measures a resistance to deformation, and is sensitive to the location of the indent. Shown below in Figure 37 a, b, c is an indenter in contact with three different surfaces: a peak, a flat, and a valley. As the indenter pushes into the material, the surrounding material resists further deformation. In the case of a indenting on a peak, (a), the resistance to further deformation will be less than on the flat surface in (b), and much less than the valley surface in (c), resulting in very different loading curves.

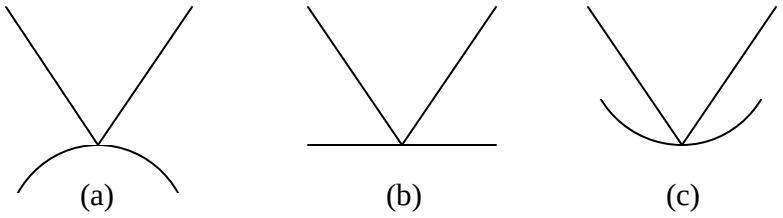

Figure 37 a, b, c: Indenter dependency on peak, valley, and flat

Ideally, indents should be placed on an area that is flat, level, free of contaminants and of consistent microstructure. This is not a problem when dealing with extremely smooth samples such as fused quartz or silicon. Engineering samples pose a very different problem. Surfaces are usually rough, making it nearly impossible to find a flat area, large enough to place an indent. Since these particular samples were generated from a wear experiment, it is assumed that the peaks come into contact with one-another, and thus reflect the true condition of the sample. Therefore, it was decided that the indents should ideally be placed on top of a large peak, or secondly on a large flat area. The valleys are not representative of the surface of the sample, and thus should not be indented. Shown below (Figure 38) are several indents on the ½ scuffed sample, using the 90° – cube corner tip. Several indents are performed on independent peaks and valleys, and the results compared. It is concluded that the asperity slopes are very small compared to the size of the indents, resulting in insignificant differences in the material properties obtained from an indent on a peak compared to those obtained from an indent on a valley.

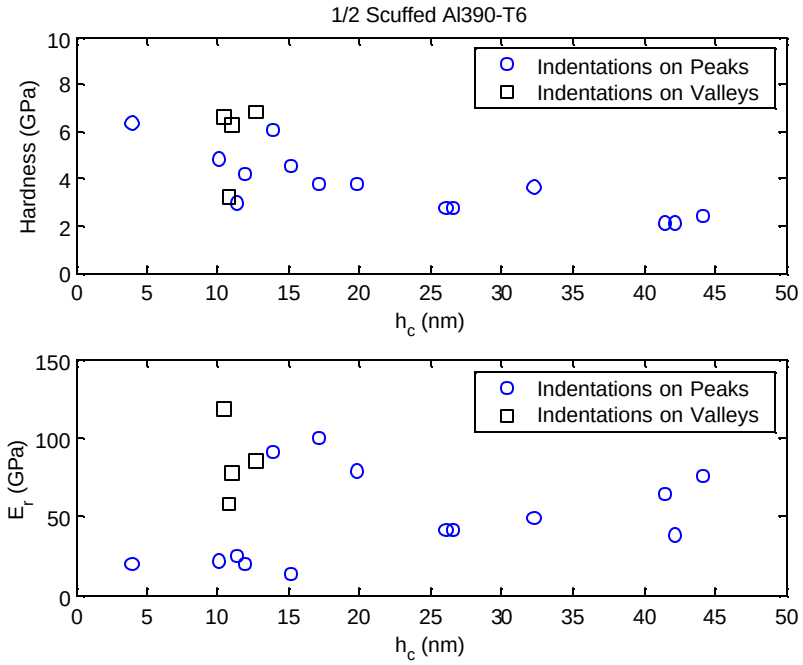

Figure 38: Peak vs. valley indentation material property correlation, 90° cube corner tip

A similar peak-valley analysis test was performed with the Berkovich tip (virgin sample). The results (Figure 39) show a higher hardness observed from indentations on valleys, compared to those indentations on peaks.

The projected area of the Berkovich tip is much greater than that of the 90° – cube corner tip, both, because the aspect ratio is much smaller and because the indents are much deeper. These differences have been considered, and since this is a wear test, it is concluded that it is important to make measurements on the asperity peaks as these areas will be indicative of the actual wear surface.

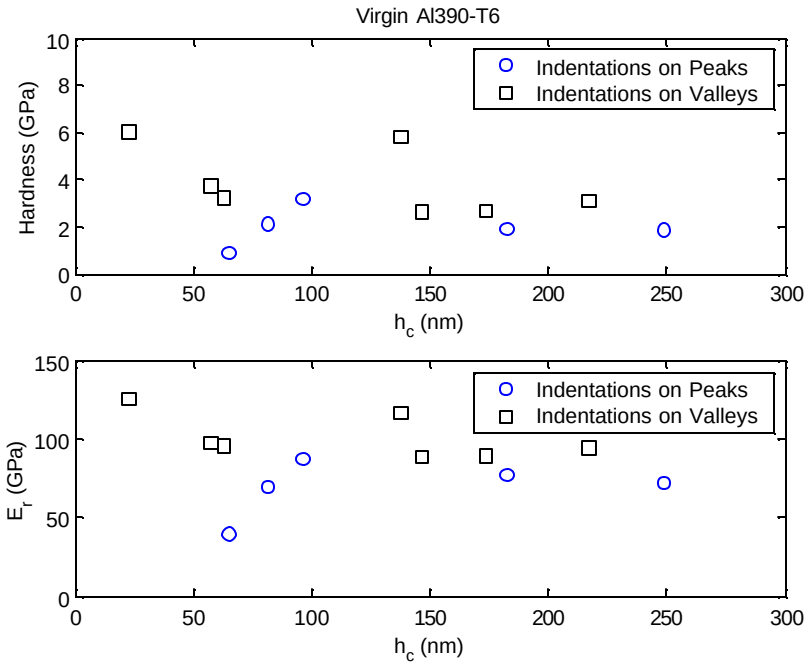

Figure 39: Peak vs. valley indentation material property correlation, Berkovich tip

Once these procedural steps are performed, the equipment is clean and verified in good working order. The test sample can be installed, the desired loading function loaded, and the tests completed.

4.7 Nano-Indentation Experiments on Fused Quartz

Fused quartz is a homogeneous material with no known surface layers. Its material properties are consistent throughout its depth. Accepted values of the reduced modulus of elasticity, E_r, and hardness, H, are E_r = 69.9GPa and H ˜ 9.6GPa respectively. It is also a fairly smooth sample with R_a < 5 nm. In order to gain confidence on the nano-indentation instrument and procedure, as well as the calculation of material properties, several single nano-indentations were performed on fused quartz at various depths. The loading profile shown in Figure 31 was used. Shown in Figure 40 and Figure 41 are a few typical loading curves for the 90° – cubic corner tip and Berkovich tip, respectively. Note that the curves overlap one-another, independent of the user-defined loading force and corresponding depth of indent. Also note that the unloading curves are of the same shape and loading slope for each test.

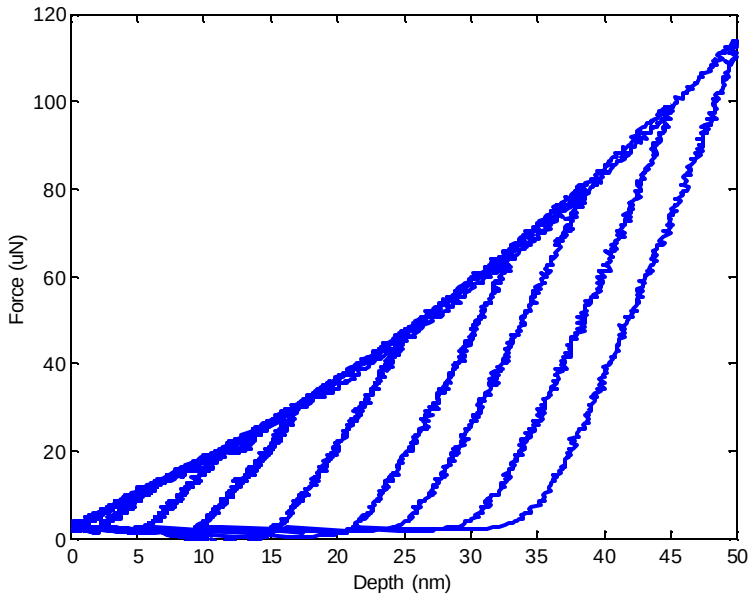

Figure 40: 90° cube corner tip loading curves on Fused quartz

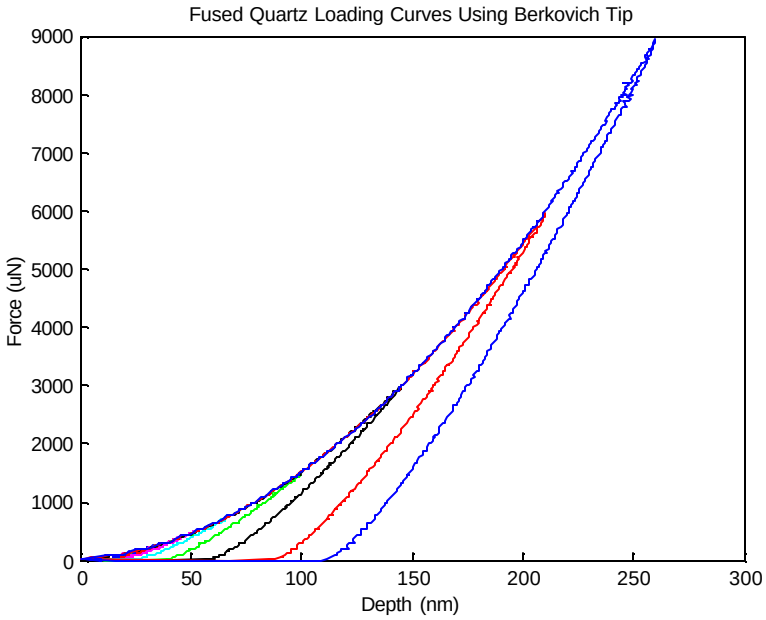

Figure 41: Berkovich tip loading curves on Fused Quartz

Since fused quartz is a consistent material with no known surface layers, the reduced elastic modulus and hardness should be the same for all curves, independent of depth of penetration. This can be seen in Figure 42 through Figure 44 below. The hardness and the reduced elastic modulus are both plotted as a function of the contact depth. Figure 42 displays the results from indents using the 90° cube corner tip, while Figure 43 displays the results from indents using the Berkovich tip. Examining the data from the 90° cube corner tip, the reduced elastic modulus

is constant, and equal to approximately 69.6 GPa as expected (tip was calibrated on Fused Quartz to obtain this relationship). Looking at the hardness, it is relatively constant at approximately 10.4 GPa, which is a little higher than the established H = 9.6 GPa for Fused Quartz. This is in part due to inaccuracies of the area function at low depths (see Section 4.3). Also note that the hardness increases slightly for extremely shallow depths of approximately h_c = 6 nm. This corresponds to the lower limit of the calibration of the tip area function. Trying to fit an area function below this value will result in non-constant hardness values for other depths. The radius of the tip forces the tip area function through a non-ideally shaped curve, which will cause the fit to be less accurate at other depths. This is also in part due to the γ-term mentioned in Equation (4), where for smaller tip angles (i.e. 90° – cube corner), this term is larger than one, thus increasing the projected tip area function and decreasing the measured hardness value.

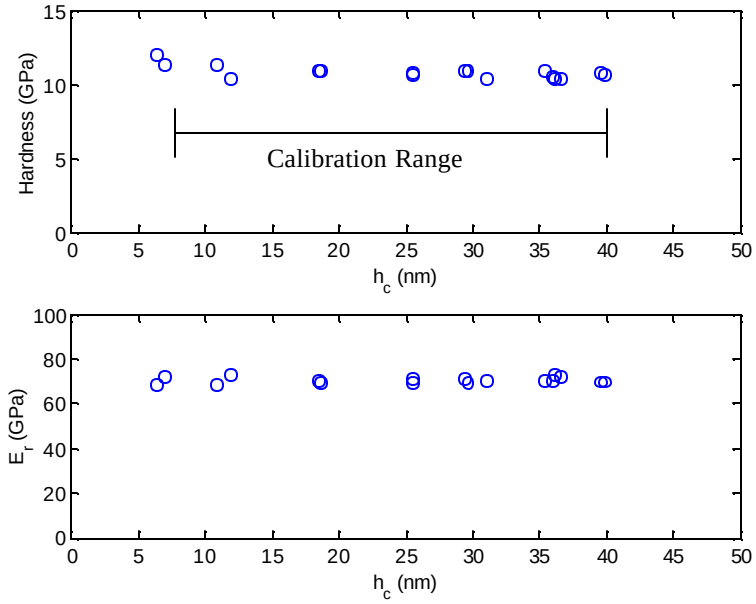

Figure 42: Fused Quartz indentation data after tip calibration; 90° cube corner tip

Examining the data from the Berkovich tip leads to similar conclusions. The reduced elastic modulus is extremely consistent as is the hardness, for all depths. In this case, both the reduced elastic modulus and the hardness curves yield results that are consistent with the ideal Fused Quartz sample. A slight non-linearity is present in the hardness curve around h_c = 32 nm, which represents the lower limit of the tip area calibration.

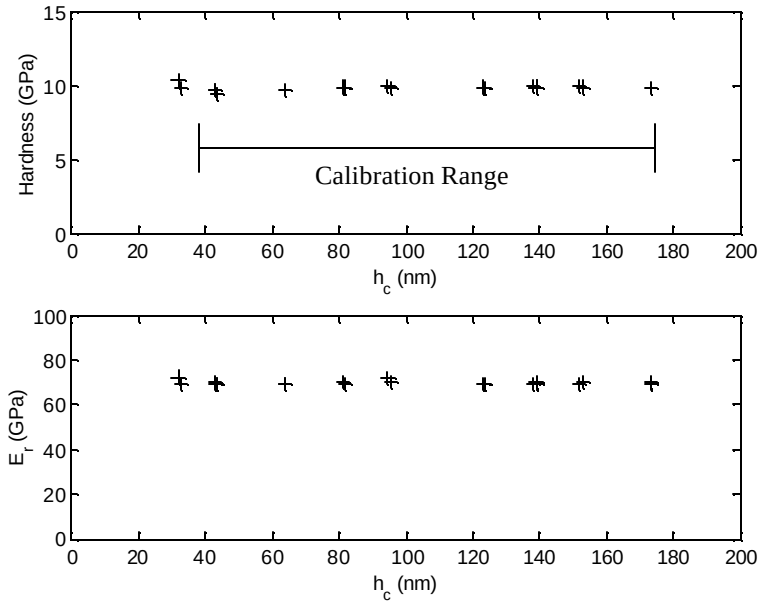

Figure 43: Fused Quartz indentation data after tip calibration; Berkovich tip

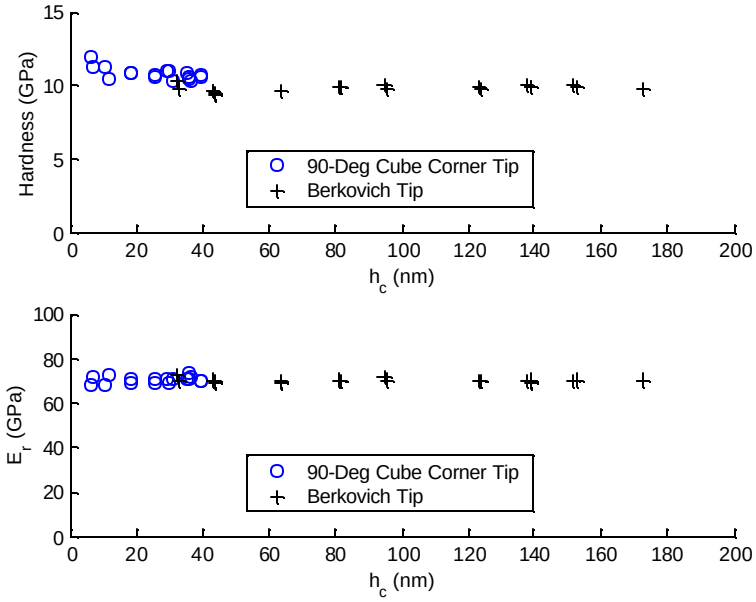

Figure 44: Fused Quartz indentation data for both 90° cube corner and Berkovich tips

Figure 44 displays the combined results of both tips. The reduced elastic modulus curve is constant and continuous for both tips. There is a slight discontinuity in the hardness plot due to differences in the measured hardness as discussed earlier (inaccuracies of area function and tip differences). This discontinuity is small (~6%), and relatively insignificant when looking at the data as a whole.

4.8 Nano-Indentation Experiments on Silicon

A subsequent test to demonstrate the accuracy of the nano-indentation instrument is a series of nano-indentations performed on a silicon sample, i.e. a silicon wafer. Silicon is a material with a very thin (~5nm) oxide layer on the surface, whereas the rest of the material is a homogeneous material. The accepted 'bulk' material properties of silicon are H ˜ 12.0 GPa and Er ˜ 150 GPa. The silicon sample is also very smooth when compared to the fused quartz sample, with an R_a value of approximately 1 nm. Figure 45 shows a residual indent from a 140 µN peak load indent on the silicon sample, using a 90° cube corner tip. Note the relatively smooth surface appearance, compared to the fused quartz.

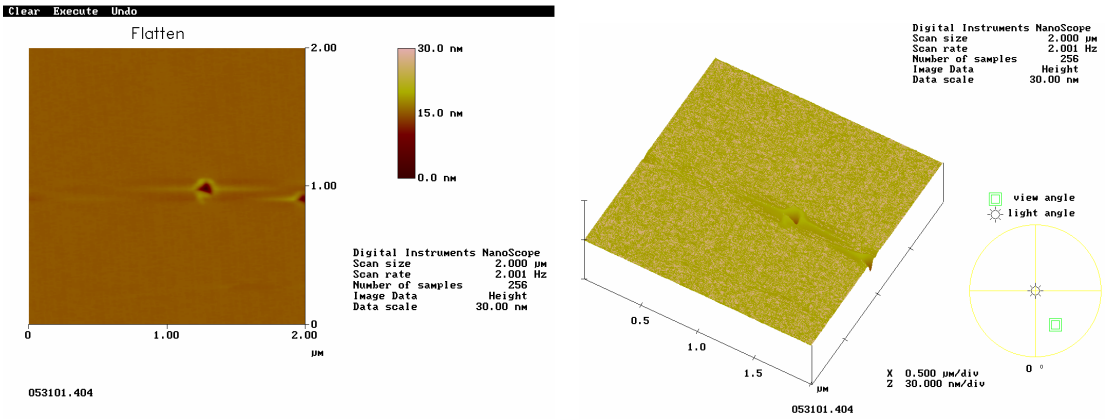

Figure 45: Residual image of a 140 µN indent on Silicon; 90° cube corner image

A sample of the appropriate dimensions was cut from the wafer using a diamond saw and mounted to an AFM disk appropriately. A series of nano-indentations were performed at various depths, using both the 90° – cube corner tip and the Berkovich tip. Figure 46 illustrates a few representative loading curves, while Figure 47 and Figure 48 show the hardness and reduced elastic modulus as a function of the contact depth. Looking at the loading curves, the results are very consistent. Examining the 90° – cube corner loading curve (a), it is obvious that there is change in slope of the loading curve at approximately 5nm. This change in slope corresponds to the presence of an oxide layer at approximately this depth, and is supported by published papers [Lo *et al*, 1999]. The change in slope is indicative of the tip punching through the harder oxide layer, into the softer substrate material. A higher slope indicates greater resistance to deformation, and thus a greater hardness value. Looking at the hardness and modulus plots for the 90° cube corner tip (Figure 47), the experimental values correlate very well with the expected theoretical values. Below 20 nm, E_r and H are approximately constant. Above 20 nm, the oxide layer significantly affects the data, increasing the hardness and reduced elastic modulus correspondingly. Bhattacharya and Nix have found (through FEM) that in order to obtain properties of a layer, without the influence of a substrate, the maximum depth of an indent must not exceed 10-20% of the overall layer thickness [Bhattacharya and Nix, 1988]. Since the oxide layer in this case is approximately 5 nm thick, indents with a maximum depth of 0.5-1.0 nm would be needed

to fully characterize the layer, independent of the substrate. These needs are not within the capabilities of the current instrument.

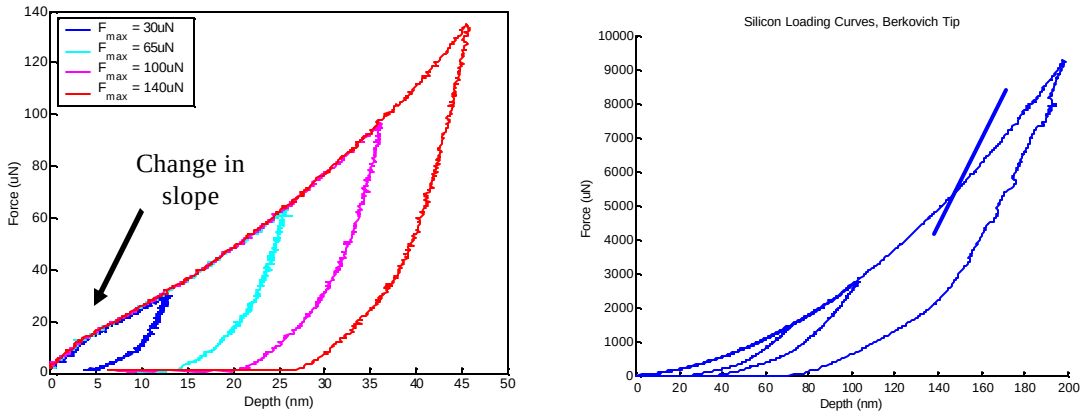

Figure 46: Silicon loading curves for both 90° cube corner and Berkovich tips

Figure 48 illustrates the combined profile resulting from both the 90° – cube corner and the Berkovich tips. There is continuity between the two tips in both the reduced elastic modulus and the hardness profile.

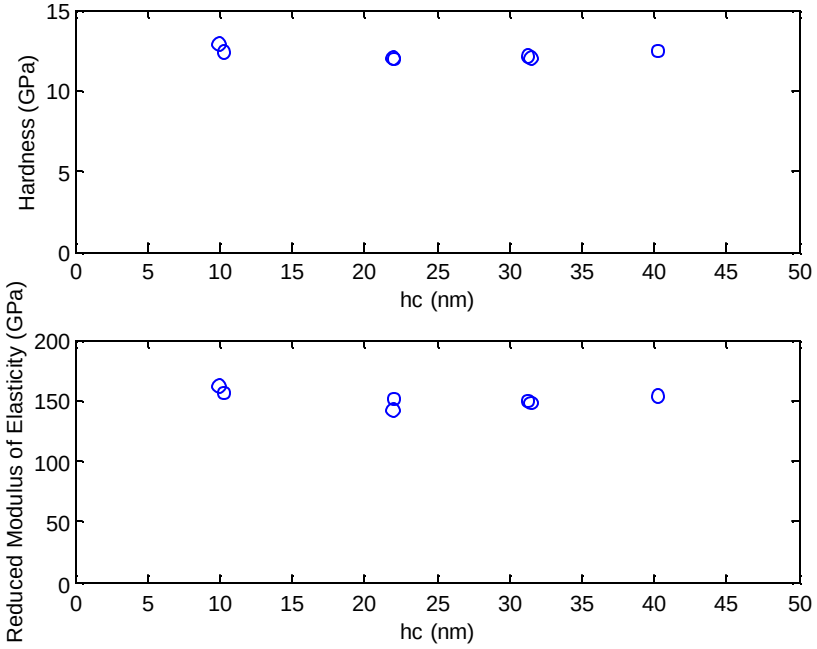

Figure 47: H, E_r depth profile of silicon; 90° – cube corner tip

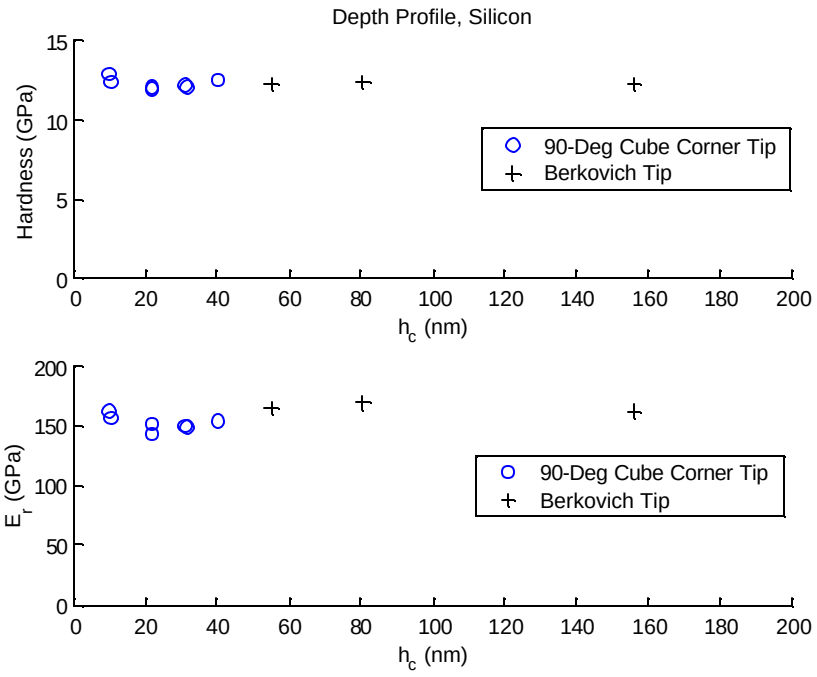

Figure 48: H, E_r depth profile of silicon; 90° cube corner and Berkovich tips

This analysis has further illustrated the repeatability and accuracy of using nano-indentation to obtain material properties. Based on the analysis of fused quartz and silicon samples presented thus far, the experimental equipment and accuracy of the tip calibration routine has been verified. Continuity of hardness and reduced elastic modulus calculations between different tip geometries has been shown for a range of contact depths of 6 nm to 180 nm. Surface layers can be identified and analyzed appropriately. The next step is to illustrate the applicability of this method on rougher engineering surfaces.

4.9 Engineering Sample Obstacles: Al390-T6

Engineering samples pose several problems relating to the use of nano-indentation to obtain thin film mechanical properties. Surfaces are extremely rough, which is quite contrary to the extremely smooth surfaces that this method was developed to analyze. The surface, as well as the layer thickness, is usually unknown and non-uniform in nature. Also, the microstructure, non-homogeneous, as discussed earlier, is a major concern. These obstacles will be individually analyzed in hopes of obtaining consistent, repeatable data on such surfaces.

4.9.1 Surface Roughness / Peak vs. Valley Measurement

Engineering samples are extremely rough, when compared to typical nano-indentation samples. As discussed in Section 4.6.5, nano-indentation measurements on peaks or valleys may affect the load versus displacement response of the indent curve, and thus its material properties. These samples, in particular, are from a wear experiment. Asperity peaks contact one another at extremely high temperatures and pressures, eventually leading to failure. Assuming that the top surface layers are mainly altered by the contact (i.e. thermal effects due to heat diffusion are less significant), the properties of the asperity peaks will be altered by the experiment, while the properties of the valleys may not change. For this reason, it is necessary to make nano-indentation measurements on

the asperity peaks. Measurements were made on the largest asperities possible, in the flattest, most level area, in order to minimize the error. This is possible because the asperities are typically spherical in shape with large (5 – 10 μm) radii. Since the indents are in the nanometer range, this is acceptable.

4.9.2 Choice of Loading Function

The choice of a loading function is based on the response of the material. Thus, it must be determined if Al390-T6 exhibits significant creep, which could alter the results based on the calculation of the slope, S (see Section 4.5). Several tests were run with such a trapezoidal loading function (Figure 32) on the virgin aluminum-silicon sample. The peak load segment was held long enough to ensure that a steady state maximum depth was reached before the unloading segment was initiated (approximately 5-7 seconds). The resultant loading curves are depicted in Figure 49, and the calculated material properties (based on these curves) are shown below in Figure 50. Also shown are results from the use of a ramp loading profile (Figure 31), on the same virgin sample surface. These results show that any amount of creep present has a minimal effect on the calculated material properties of the surface. Thus, a linear loading profile (Figure 31) is appropriate for this engineering surface. A *'pul-load'* loading profile (Figure 33) was also used for some samples in order to improve the speed of the data acquisition at various depths.

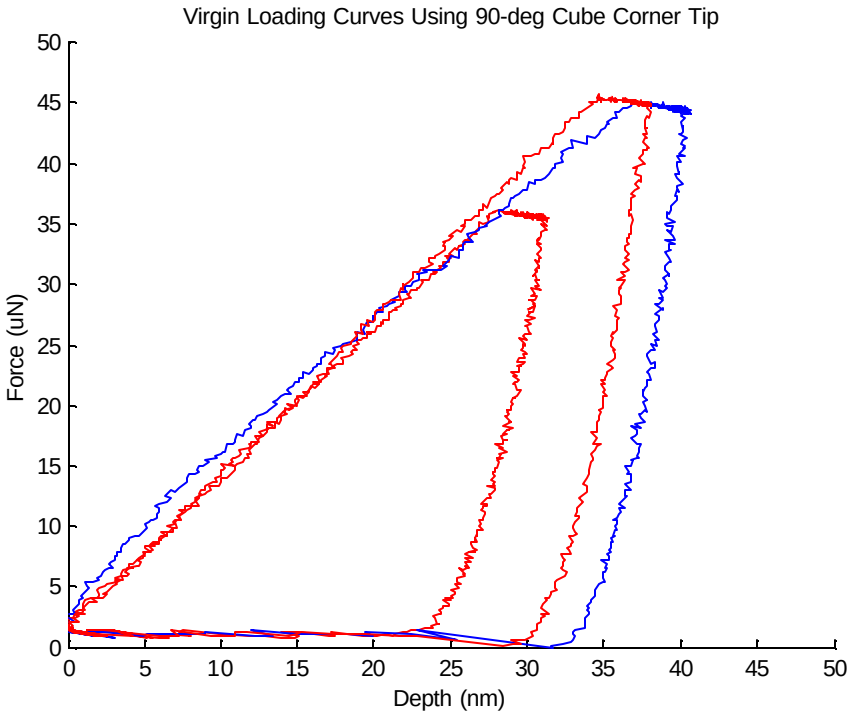

Figure 49: Trapezoidal loading functions on virgin Al390-T6 sample

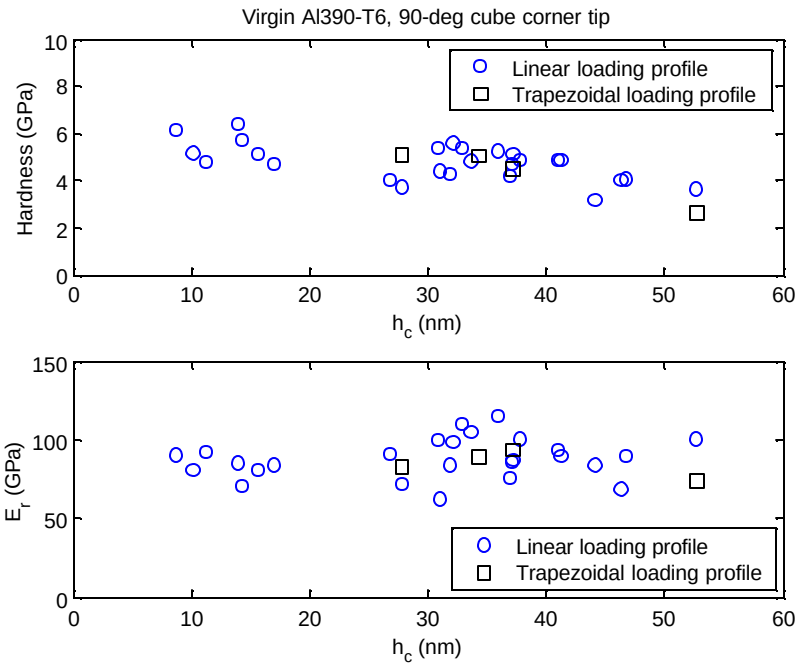

Figure 50: Trapezoidal loading function calculated properties comparison

4.9.3 Exclusion of Data - Silicon Particles

The ultimate goal of the nano-indentation study is to characterize changes in the material properties of the uppermost layers that eventually lead to scuffing (i.e. failure). Referring to the Al390-T6 surface microstructure discussed in Section 2.3.1, the surface is non-homogeneous and contains many different areas consisting of very different chemical compositions. These areas will, by nature, have different mechanical properties. The size of a nano-indentation is roughly on the same order of magnitude as many of the microstructural features. Thus, the mechanical properties will be dependent on the microstructure of the surface in the vicinity of the indent. Referring to the microstructure in Section 2.3.1, large silicon particles have an average diameter of 10-20 µm. Since the contact area of a nano-indentation indent is less than a few hundred nano-meters, it is very feasible that, for some points, a silicon particle will be indented. Since the silicon particle is extremely large, when compared to the diameter of the indent, these data should reflect the data obtained from an indent on a silicon sample (assuming negligible influence of aluminum matrix due to relatively large size of silicon particle) as discussed in Section 4.8.

Based on the work of Archard [Williams, 1998], etc., and subsequently Archard's Wear Equation, the wear rate is inversely proportional to the material hardness. Thus, softer surfaces have a higher wear rate than harder materials. Silicon is a harder material than the aluminum, and has the ability to block dislocation motion. Thus, in this case, the silicon is added to the aluminum matrix for strength, and to increase the hardness of the overall material. Thus, any indents on a silicon particle will show a significantly higher hardness than indents on other areas of the surface. But, the ultimate goal is to quantify changes in the material properties that eventually lead to scuffing. Assuming that eventual failure will occur in the softer areas of the surface (based on Archard's Wear Equation), it is necessary to exclude data obtained from indents on a silicon particle to accurately quantify the surface properties that eventually lead to failure. Including data obtained from indents on a silicon particle will

show a surface hardness higher than is actually present on the area of the surface that eventually fails. Also note that the surface area occupied by silicon particles is roughly 10% (Figure 7). Since indents are performed on only six to seven grossly separated locations (greater than 1 mm) per sample, there will be a large variation in the number of indents on silicon particles between samples. Thus, inclusion of silicon data will significantly skew the results between samples, and nullify any potential comparisons. Two solutions exist: either exclude all silicon data, or normalize each sample to adequately compensate for variations in the amount of indents on a silicon particle. A normalization procedure will be both extremely difficult and possibly inaccurate due to variations in silicon concentrations between the samples. Based on the earlier discussion, the inclusion of these data points will also skew the data and mask any potential changes and/or trends in the samples that may lead to eventual failure. Thus, the most effective solution is to exclude silicon data from the individual surface analysis.

The next step is to determine a method to differentiate between a loading curve resulting from an indent on a silicon particle, from that resulting from an indent on another area of the surface. Silicon is a significantly harder material than aluminum, and has very different mechanical properties. Thus, loading curves resulting from an indent on a silicon particle should be dramatically different fromthose obtained from indents elsewhere. First, examine the 90° – cube corner loading curves. Loading curves on both the virgin and the ¼ scuffed surface were analyzed (Figure 51 and Figure 52). The loading curves on the virgin surface (Figure 51) do not show any distinct groupings of the data, nor do they any resemblance to the loading curve of silicon. Thus, no indents were performed on a silicon particle for this sample. Quite to the contrary, examination of the loading curves from the ¼ scuffed surface yields two distinct groups of data. One group similarly corresponds to those curves obtained on the virgin surface, and are labeled as data representative of the surface of interest. The loading curves of the second group are very similar to those obtained from an indent on a pure silicon sample in Section 4.8, which is also shown on the graph. Thus, these curves are labeled as those obtained from indents on a silicon particle. In order to distinguish between these two sets of curves, an upper bound on the representative surface loading curves was established, based on the data observed on these two samples. This line, shown on both graphs, serves as a differentiation boundary between loading curves performed on a silicon particle and those obtained on the representative surface. Subsequent loading curves will be compared to this line in an effort to differentiate between indents performed on a silicon particle, or those performed on the representative surface. Any curves with a significantly greater loading curve slope (based on operator judgment) will be excluded from the analysis. This line has been used on all samples, showing very repeatable results.

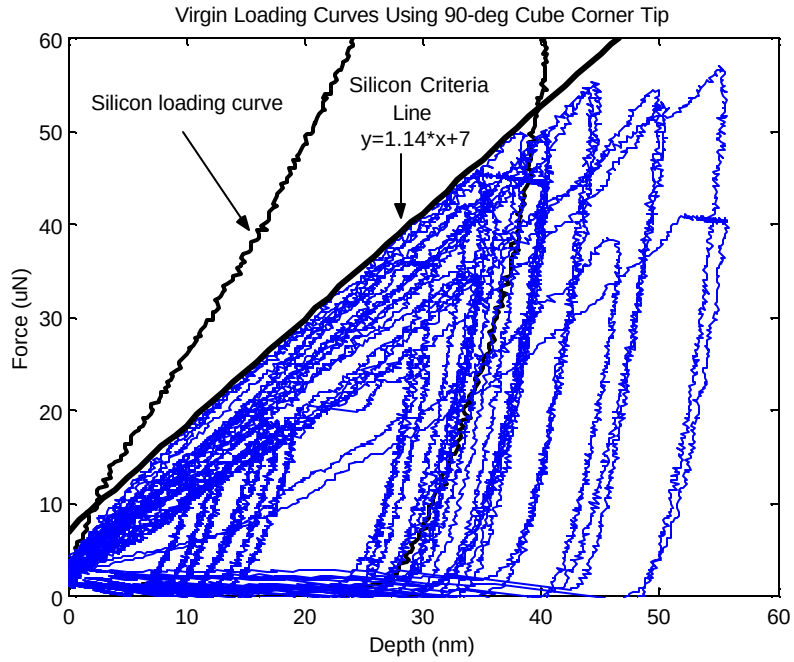

Figure 51: Silicon criteria line for 90° cube corner tip; virgin surface

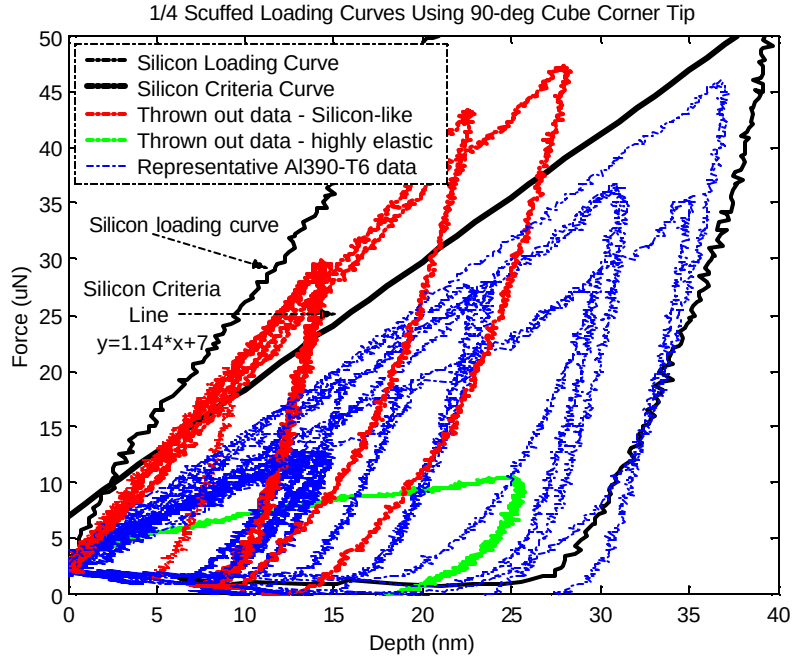

Figure 52: Silicon criteria line for 90° cube corner tip; ¼ scuffed surface

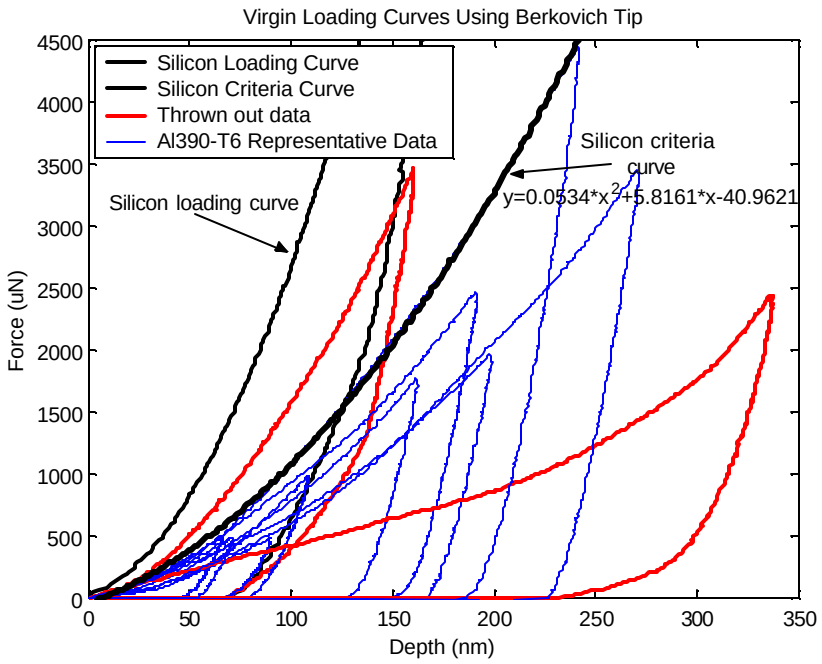

Figure 53: Silicon criteria for Berkovich tip

A similar criterion was developed for the Berkovich tip loading curves. A second order polynomial was fitted to a single loading curve that represents an upper bound of a grouping of data (based on the virgin surface). This curve then represents a differentiation boundary between those indents on a silicon particle and those on an area more representative of the surface. Once again, operator judgment is used to distinguish significantly different curves from the rest of the grouping. This boundary curve has been used on all samples, yielding very repeatable results.

To illustrate further the effects of including data obtained from indents on a silicon particle in the analysis of hardness trends, consider Figure 54 below. The calculated hardness values are based on the ¼ scuffed sample loading curves shown in Figure 52. Hardness values obtained from both groups (i.e. indents on silicon particles and indents on the representative surface) are shown. Note that the calculated hardness values for those curves corresponding to indents on a silicon particle are much greater than those obtained from indents on the representative surface. A least squares linear fit is shown for two sets of data: one corresponding to a fitting of all the data (including both silicon and representative surface data), and a second corresponding to a fit of only the representative surface data (excluding silicon data). Note the dramatic differences in the sample trendlines due to the skewing effect of the silicon particles. This further emphasizes the need to exclude the silicon data in order to obtain an accurate surface profile.

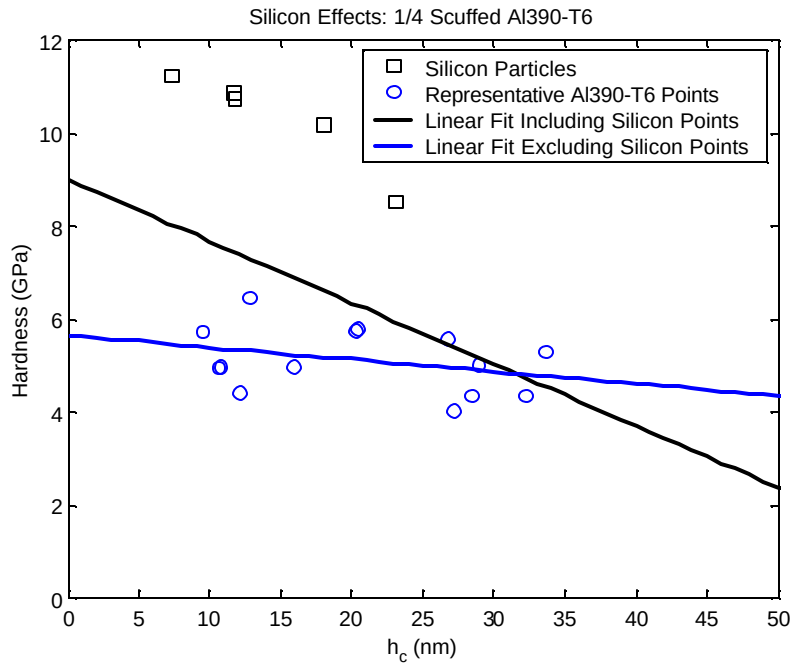

Figure 54: Effects of including Silicon particle data on Al390-T6

As discussed earlier, this study focuses on engineering samples,. Thus, there is a fair amount of scatter in the data pertaining to sample roughness, non-uniform layers, and micro-structural inconsistencies. Many of these inconsistencies are representative of actual differences in the surface of the material, and not necessarily experimental errors. It is therefore extremely vital to closely examine all loading curves, and minimal data, if any, should be ignored (except silicon data discussed earlier). As for the analysis of individual samples, all loading curves will be shown, and any discarded data will be first examined in great detail.

4.9.4 Statistical Analysis of Data

Due to microstructural differences and many inconsistencies associated with an engineering sample, it is imperative to take a large number of data points at a variety of different locations throughout the samples. This will help to obtain results that are more consistent and representative of the true sample surface. A good approach is to engage the tip, make three to four indents at various loads within the desired depth limits (within the 10 µm range of the piezo-sensor), and then disengage the tip and move to a new region at least 1 mm from the previous area. The procedure, repeated in five to six different locations, should provide accurate and representative results of the sample surface.

Due to a finite sample size, it is necessary to use statistics to gain insight into the true trends associated with experimental data. Researchers [Lu *et al*, 2001] have used error bars to quantify the spread in the data observed for a constant peak load. Although accurate, this does not explicitly give insight into the true surface properties. Another method is to use confidence and prediction intervals to quantify the entire data set as a whole. When comparing samples, one is generally interested in the true sample mean and the values of the most extreme points. By understanding these trends, unbiased analysis of the samples can be used for sample comparisons. As defined in

Walpole [Walpole, 1998], a confidence interval defines a band, which has a certain probability of containing the true sample mean. This band takes into account the size of the sample and the standard deviation of the data about its sample mean, and computes a (1-α)% confidence interval for the true mean, for all x (see Equations 7 and 8). There is then a (1-α)% chance that the true sample mean lies within this band.

$$\hat{y}_0 - t_{a/2} s \sqrt{\frac{1}{n} + \frac{(x_0 - \bar{x})^2}{S_{xx}}} < m_{Y|x_0} < \hat{y}_0 + t_{a/2} s \sqrt{\frac{1}{n} + \frac{(x_0 - \bar{x})^2}{S_{xx}}} \quad (9)$$

$$S_{xx} = \sum_{i=1}^{n} (x_i - \bar{x})^2 \quad (10)$$

The $\hat{y}_0$ term is developed from a linear least squares fit of the experimental data, and is the estimate of y at some desired x, namely x_0. The s-term is the standard deviation of all experimental y-values from their estimate and n is the sample size, x_0 is a desired x-value, while $\bar{x}$ is the mean x-value. The $t_{?/2}$ term is the value of the t-distribution for v = n-2 degrees of freedom at a level of significance of α/2. The true sample mean at each respective x_0 is given as $\mu_{Y|x0}$.

Also defined in Wiley [ref] is a prediction interval, which defines a band that has a certain probability of containing a single new event (i.e. the next data point has a (1-α)% chance of falling within this interval). Similar to the confidence interval, the prediction interval takes into account the size of the data set and the standard deviation of this data about its sample mean, and computes a (1-α)% prediction interval on the value of the next event (see Equation 9).

$$\hat{y}_0 - t_{a/2} s \sqrt{1 + \frac{1}{n} + \frac{(x_0 - \bar{x})^2}{S_{xx}}} < m_{Y|x_0} < \hat{y}_0 + t_{a/2} s \sqrt{1 + \frac{1}{n} + \frac{(x_0 - \bar{x})^2}{S_{xx}}} \quad (11)$$

In the analysis that follows, both a confidence interval and a prediction interval will be used to determine true trends from the samples. Both are calculated based on a level of significance of 95%, which is common in the statistics field.

When comparing samples, general trends are desired. A linear fit of the data is the easiest, both to compute and to analyze. Although this is not the most accurate form of curve fitting, it allows analysis of trends between the samples. A linear curve fit to two different regions is used. Based on prior chemical analysis performed on these samples [Patel, 2001], it was found that the top 50-60 nm produced the most dramatic changes in chemical composition. Thus, a linear fit to the data of the top 60nm, as well as a linear fit to the rest of the data between 60 nm and 250 nm is used.

4.10 Engineering Sample Preparation for Nano-Indentation Testing

4.10.1 Test Area

Each of the five scuffing samples has different regions present within the wear track. On a macro-scale, different regions can be noted by changes in color and/or surface finish (see Figure 55). When performing nano-

indentation, it is critical to note which area was tested, as chemical composition and thus material properties may vary between regions within the same sample. As noted [Patel, 2001], a primary wear track can be observed for all samples, and seems to occur on the inner half of the wear track. It appears as a highly polished region of approximately 1-2 mm wide. This is the area of the sample that eventually scuffs, and is thus most representative of the scuffing state of the sample. Therefore, it is imperative that this region is examined in the subsequent analysis. For very small regions, a rectangular box was placed around the desired test area using a permanent marker (see Figure 56).

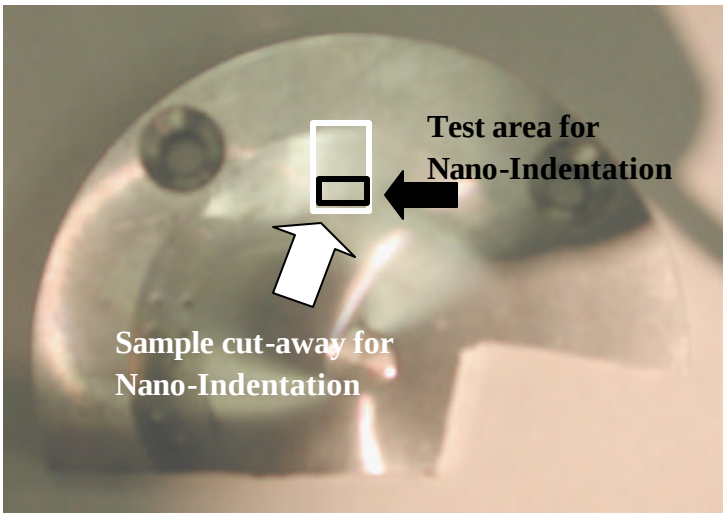

Figure 55: 3/4 Scuffed sample test area

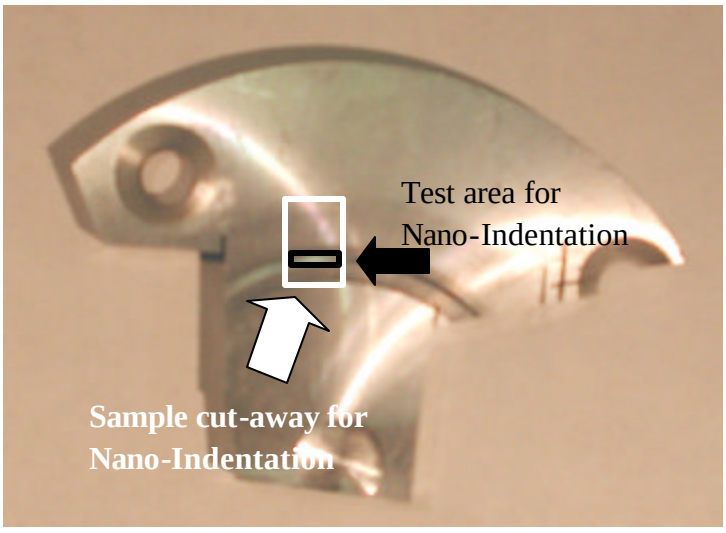

Figure 56: Scuffed sample test area

4.10.2 Sample Mounting

In order for the samples to be compatible in the AFM (Atomic Force Microscope) for either nano-indentation or nano-scratch testing, these samples must be cut down to the appropriate dimensions. The final disk sample must be inscribed within, and mounted to a 15mm steel disk, with a sample height not greater than 2.5mm.

The steel disk is held magnetically to the sample stage, and acts as a sample holder for the nano-indentation samples. The samples were thinned down to 2.2mm, and a rectangular section within the wear track (with approximate dimensions of 8 mm by 12 mm, see Figure 55 and Figure 56) was cut from each sample, using a band saw. See Figure 57. Careful cutting procedures must be practiced in preparing these samples. The wear surface must not be touched, in order to prevent the destruction of wear surface. Also, it is important that the wear surface remain parallel to the mounting face, after the thinning procedure. Thus, nano-indentations will be performed perpendicularly to the wear surface, and minimizing errors associated with indents on a tilted surface.

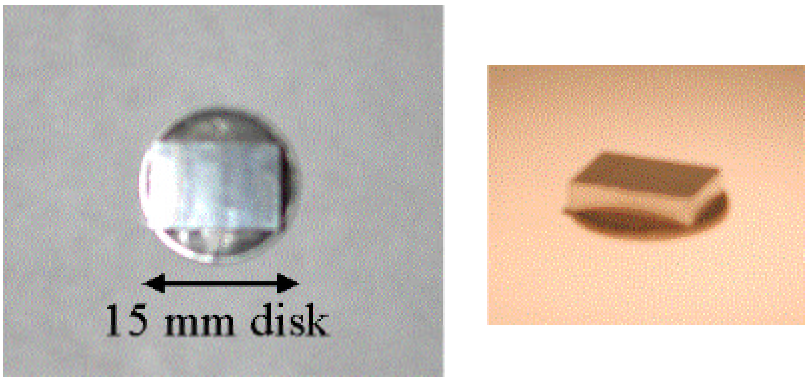

Figure 57: Samples prepared for AFM use

Each sample, along with a steel AFM disk (used for sample mounting as discussed earlier), was then soaked in acetone and placed in an ultrasonic cleaner for 10 minutes. This ensured that the sample was clean of any dust, oils, or other impurities. Acetone, if left on the sample, may break down the adhesive used to attach the sample to the disk. Thus, each sample and corresponding disk was then wiped clean with a cotton swab soaked in ethanol and dried with a hot air dryer. Once the sample and the disk were clean and dry, a very small amount of super glue (Ross Super Glue Gel® was used for these tests) was applied to the disk. The sample was placed on top of the disk, and a small amount of pressure was applied to the sample until the sample and disk were attached. Although it sounds relatively simple, the type and amount of adhesive used is critical. Ultimately, when nano-indentation tests are performed on a sample, the adhesive used to attach it to the steel disk will affect the force and measured indentation depth on the sample. Using a small amount of a rigid adhesive will minimize this interaction, while the use of a rubbery adhesive or too thick of a layer will decrease the force while increasing the measured penetration depth. Super glue was chosen such that it dries rigid and strong, thus meaning that a very small amount can be applied to maintain contact between the sample and disk (recommended by Materials Research Laboratory (MRL) staff at University of Illinois). Each prepared sample was then allowed to air-dry for at least two days in order to fully cure the glue. Samples were then stored in individual plastic cases with a small amount of lint-free tissue paper to minimize movement and vibrations.

4.11 Al390-T6 Results

4.11.1 Virgin Results

All loading curves for the virgin sample, using both the 90° – cube corner and the Berkovich tips are shown in Figure 58 and Figure 59 respectively. They were obtained using a combination of ramp, trapezoidal and 'pul-

load' loading curves as described in Section 4.5, with varying peak loads. Also shown is the silicon loading curve for each respective tip and a silicon criterion line, as discussed in Section 4.9.3.

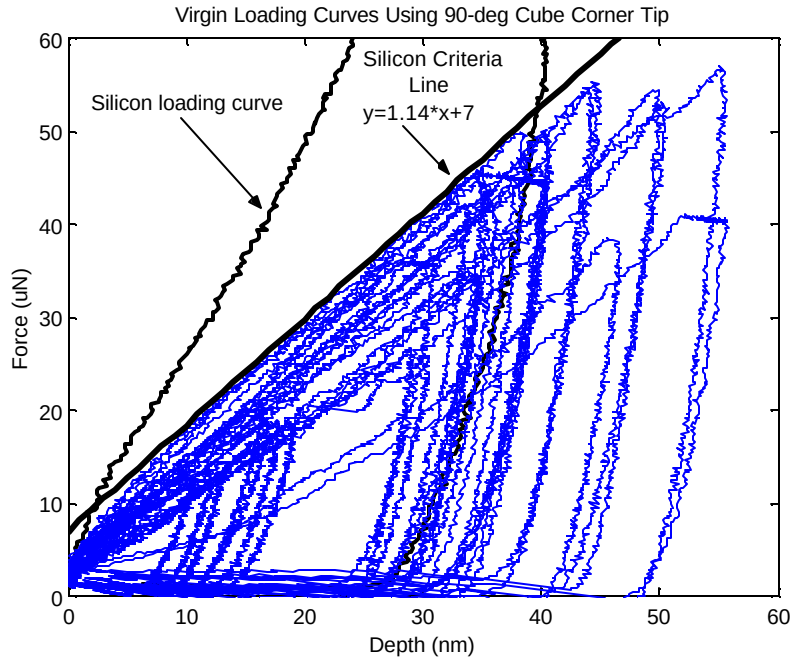

Figure 58: Virgin Sample; all single-loading curves using 90° cube corner tip

There is a fair amount of scatter in the data, compared to the tests on fused quartz and silicon. As stated earlier, this is an engineering sample, which introduces many more inconsistencies (roughness, non-uniform layers, microstructural differences), especially at shallow depths (see Section 4.9). In Figure 59, a single silicon-like curve was excluded from the analysis, as well as an extremely elastic curve that does not fit with the rest of the data and might represent an indent on a dust particle. In Figure 58 (90° – cube corner tip loading curves), note that there is a change in the slope of the loading curves at approximately three to five nanometers depth, indicating that the top three to five nanometers are harder than the material below the surface. The thickness of this layer is consistent with the published thickness of the natural oxide layer on the surface of pure aluminum [Dowling, 1999], thus showing good experimental agreement with published values.

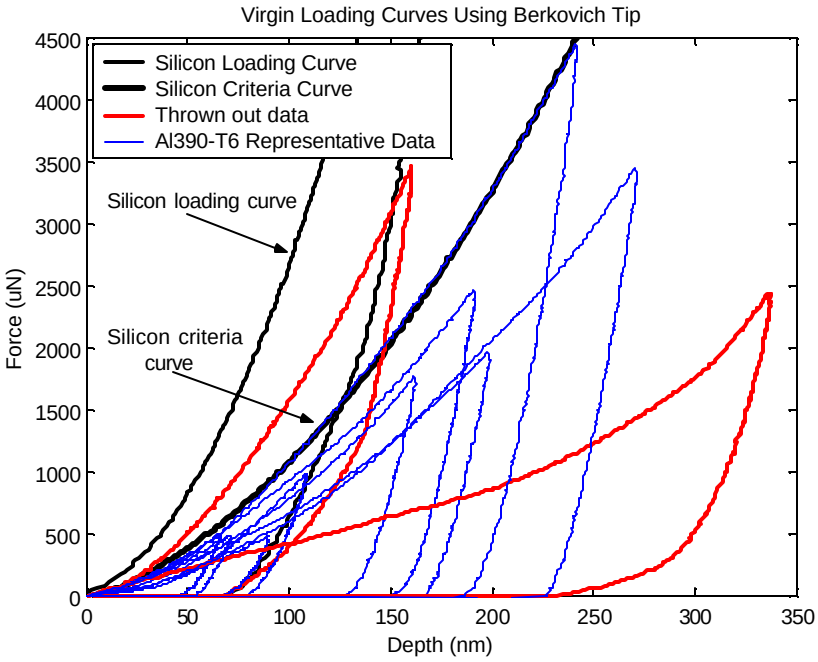

Figure 59: Virgin sample loading curves; Berkovich tip

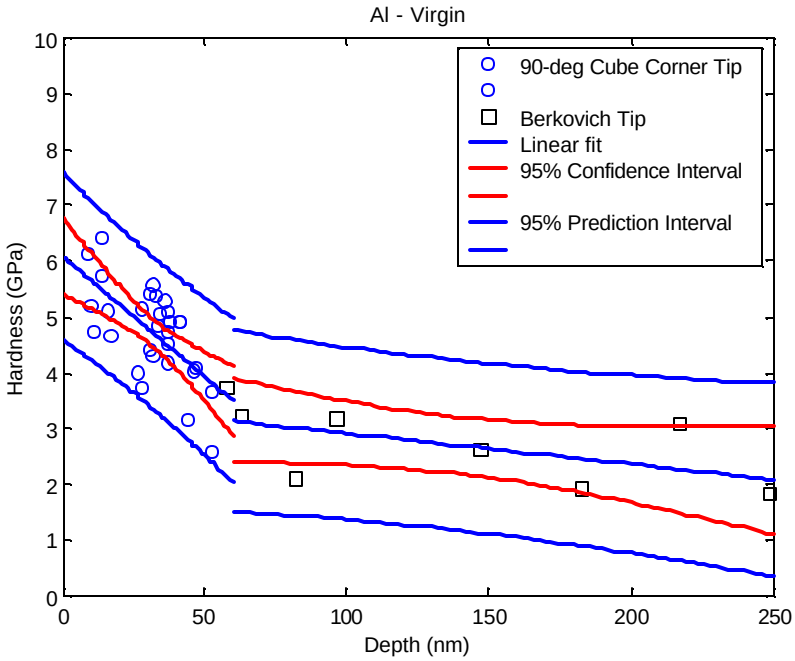

Figure 60: Virgin sample hardness profile

The virgin loading curves have been analyzed, and material properties have been calculated based on the calculations described in Section 4.4. Figure 60 and Figure 61 show the hardness and reduced elastic modulus profile as a function of the contact depth for both tips. Different markers are used to illustrate calculated material

properties based on different tip geometries. Also shown is the linear least squares fit and the 95% confidence interval and prediction intervals for each region, as discussed in Section 4.9.4.

Examination of the virgin surface hardness data in Figure 60 shows several trends. Foremost, indents performed close to the surface (i.e. shallow depths) have a hardness greater than those indents performed at a deeper depths. Re-examining the data obtained from indents on both fused quartz and silicon materials (Sections 4.7 and 4.8) it was shown that, for a uniform/semi-uniform material, the calculated material hardness is relatively independent of either indenter depth or tip geometry. Thus, the increased hardness trends observed on the surface are real trends of this material. Closer examination of the data shows that there are approximately two regions with distinct trends: one from the surface to 60 nm deep, and the other from 60 nm to 250 nm deep. It is important to note that these regions also roughly correspond to the calibration ranges for each respective tip, but based on the analysis in Sections 4.7 and 4.8, it was shown that the indenter geometry has a negligible effect on the calculated material properties. Linear trend lines were fit to the data of these regions, respectively, independent of the tip geometry. There is a fairly rapid and steadily decreasing hardness trend for the first region, defined from the surface to 60 nm deep. The average hardness decreases from 6 GPa on the surface to approximately 3.5 GPa at a depth of 60 nm. In the second region, the hardness decreases much less rapidly and is almost constant, and independent of the depth of the indenter. The hardness decreases from about 3.2 GPa at a depth of 60 nm to approximately 2.1 GPa at a depth of 250 nm. The bulk material hardness as measured by either the Vickers or the Rockwell B test is approximately 1.6 – 1.8 GPa (see Section 3.2.1.2 and 3.3.1.3). Thus, it can be concluded that the most significant changes occur in the first 60 nm. The discontinuity between the two trend lines results from the curve fitting of a discrete number of data points, as well as defining an exact depth to define the edges of the region. These data further support the results from the chemical analysis [J. Patel], stating that the most significant changes in chemical composition occur in the uppermost 50-60 nm of the surface.

The 95% confidence and predication intervals are also shown for both regions. As described in Section 4.9.4, the confidence interval is an estimation of the sample mean, while the prediction interval is an estimation of a single, new event. By definition, there is more uncertainty in the prediction interval than that of the confidence interval depicting a mean parameter based on the acquired data. Thus, the prediction interval is wider than that of the confidence interval. The confidence interval has a bowed appearance because it is calculated based on the mean of the x-values (depth) of the sample. Points farther from the mean value have less surrounding points, and thus exhibit more uncertainty in the estimation of the mean, resulting in a wider confidence interval. The prediction interval is also bow shaped, but to a much less extent than that of the confidence interval. All data fall within the 95% prediction interval, and therefore no additional data points are disregarded. Examining the low depth region, the data are fairly tightly packed, and the prediction interval indicates that the minimum expected hardness will vary from approximately 4.5 GPa on the surface to approximately 2.0 GPa at an indenter depth of 60 nm. These minimum values are important to note when comparing differences between respective samples in subsequent analysis as it is softer areas that commonly fail first (see Section 4.9.3). The average width of the prediction interval is approximately 3.0 GPa. Examining the second region (60 nm to 250 nm) yields similar results in scatter associated with the data. Both, the confidence and the prediction intervals are wider because there are less data

points, and therefore more uncertainty in the data. Based on the microstructural analysis in Section 2.3.2, features on the surface are on the order of tens of microns to several hundred microns in size. Thus, extremely small indents are representative of very localized behavior, while deeper indents average the microstructure and are much more representative is the actual surface. Examination of the predication interval associated with the second region is not appropriate as there is an extremely limited amount of data in this region.

Figure 61 illustrates the reduced elastic modulus of the virgin surface, as a function of the depth of the indent. The linear fit of the data was obtained for the two depth regions discussed earlier, the first corresponding to the surface to 60 nm deep, and the second corresponding to 60 nm to 250 nm deep. 95% confidence and prediction intervals are also shown. Examining these data, the modulus is relatively constant between 80 and 90 GPa, and there is no clear relationship between the elastic modulus and depth of the indent. The material elastic modulus can be calculated from the reduced elastic modulus based on Equation (7), and knowing the poisson's ratio and the elastic modulus of the diamond indenter, as given in Section 4.4. These ranges are roughly the same (80 – 90 GPa) for the material elastic modulus. The theoretical single crystal aluminum elastic modulus is 70 GPa [Dowling], such that this seems like a reasonable value. Thus, it is concluded that the elastic modulus is independent of the depth from the surface. There is relatively low scatter in the data, with a prediction interval average range of approximately 50 to 60 GPa.

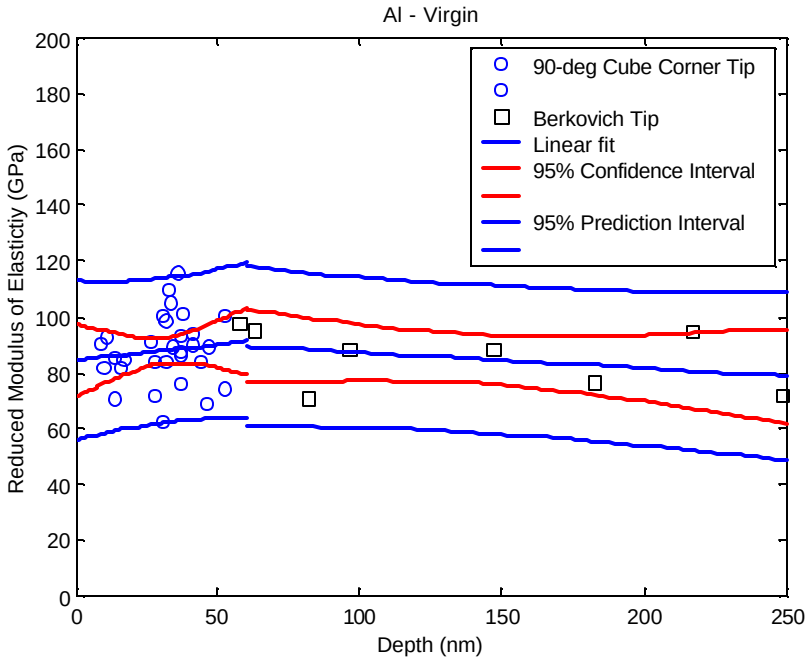

Figure 61: Virgin sample reduced elastic modulus profile

4.11.2 Al390-T6: ¼ Scuffed Results

All nano-indentation loading curves for the ¼ scuffed sample, using both the 90° – cube corner and the Berkovich tip, are shown below in Figure 62 and Figure 63, respectively. These curves were obtained using a linear loading profile, as discussed in Section 4.5. Also shown is the silicon loading curve and the silicon criterion line for each respective tip.

Examination of the loading curves obtained from the 90° cube corner tip, Figure 62, shows the scatter associated with an engineering sample. Also note that there are several curves that greatly differ from the majority of the curves. Comparison of these curves to the loading curve on pure silicon and to the silicon criterion line, leads to the conclusion that these curves were obtained from an indent on a silicon particle. Based on the discussion in Section 4.9.3, these curves are excluded from subsequent analysis. Also excluded is a very soft, highly elastic curve that possibly reflects an indent on a dust particle. Most curves also include a change in slope of the loading curve at approximately 3-4 nm. The slope of this initial region is higher than that for the majority of the curve, thus indicating the presence of a harder surface layer. As discussed earlier, the thickness of this layer is consistent with that of the oxide layer observed on pure aluminum samples.

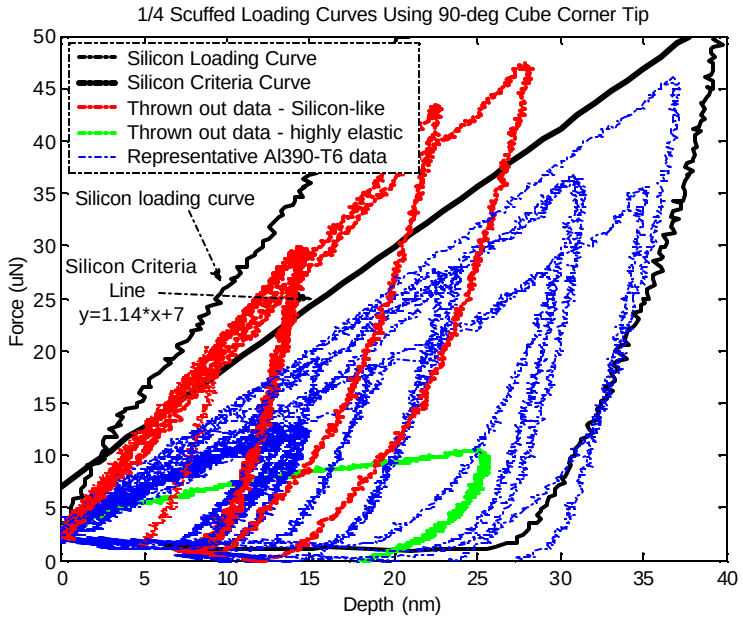

Figure 62: 1/4 Scuffed sample loading curves, 90° – cube corner tip

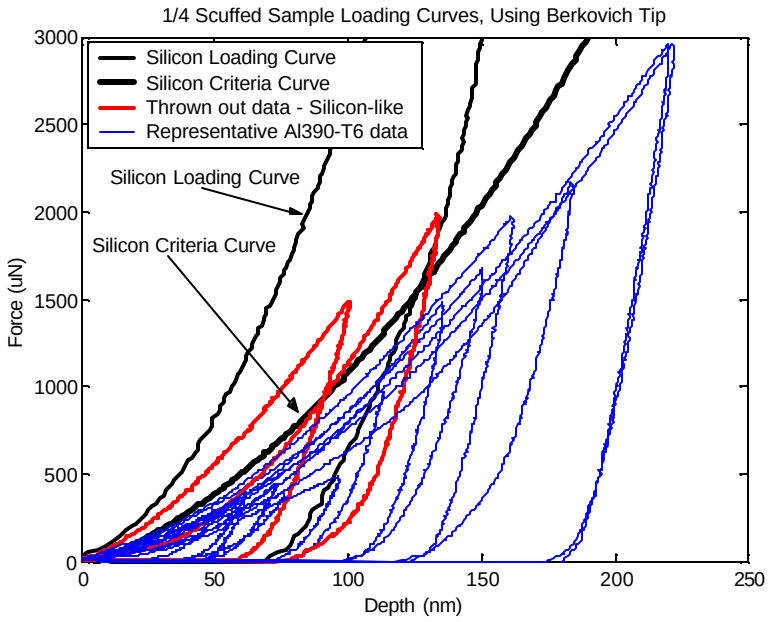

Figure 63: 1/4 Scuffed sample loading curves, Berkovich tip

The loading curves on the ¼ scuffed sample, using the Berkovich tip, are shown in Figure 63. The curves are fairly consistent, but there are two curves that significantly differ from the rest. When comparing these curves to the loading curve obtained from the silicon sample and to the silicon criterion curve, it is concluded that these curves represent indents on silicon particles. Thus, these curves are excluded from the subsequent data analysis.

The loading curves presented in Figure 62 and Figure 63 are analyzed, and the resulting material properties (H and Er) are shown in Figure 64 and Figure 65 below. The properties corresponding to different tip geometries are shown with different data markers, to further aid in the analysis. A linear fit of the data was obtained for two different regions, as discussed prior: the first region consists of all data up to 60 nm deep, while the second consists of data between the depths of 60 nm and 250 nm. 95% confidence and prediction intervals are also shown.

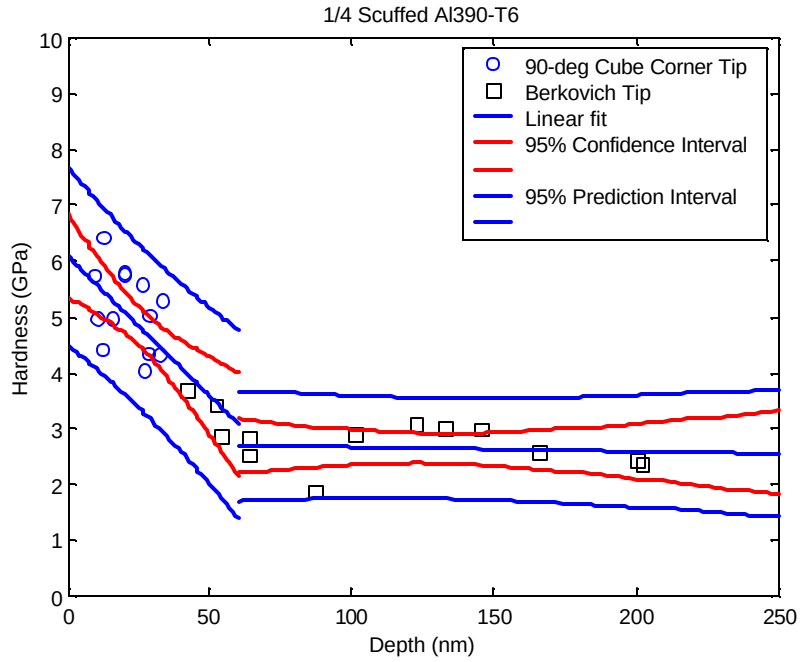

Figure 64: 1/4 Scuffed sample hardness profile

Examination of Figure 64 shows trends very similar to those observed on the virgin sample. The top 60 nm shows significantly higher hardness than the rest of the data. At the surface, the hardness is approximately 6 GPa, dropping off to approximately 3 GPa at a depth of 60 nm. The prediction interval shows that the minimum hardness decreases from 4.5 GPa at the surface to 1.5 GPa at a depth of 60 nm. These lower bounds on the hardness are slightly less than those observed on the virgin sample. Beyond 60 nm, the hardness is relatively constant at 2.5-2.7 GPa. Below 60 nm, there are no real differences between the ¼ scuffed and the virgin samples. For both regions, the scatter is approximately the same as observed on the virgin sample.

The reduced elastic modulus profile of the ¼ scuffed sample is shown in Figure 65 below. There is a fair amount of scatter in both regions, and no real trends can be observed from the sample.

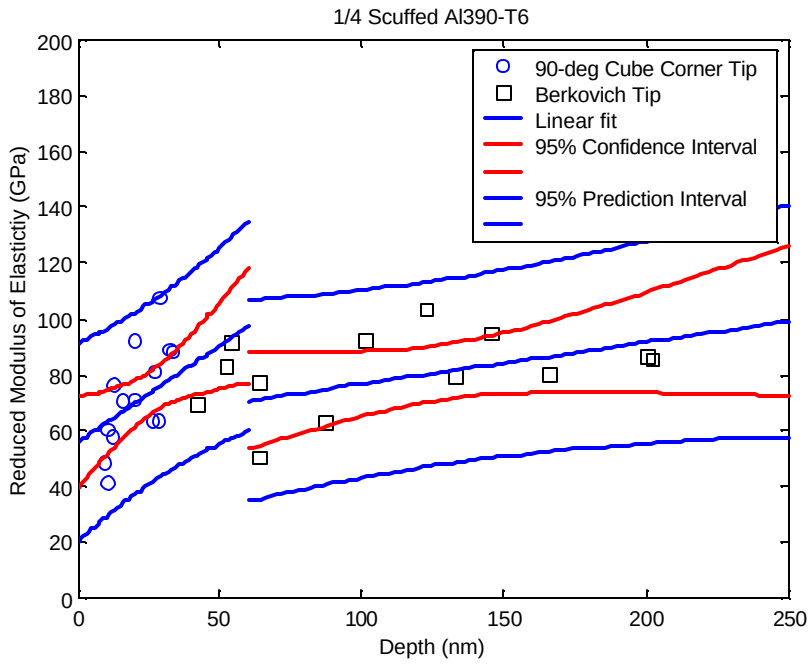

Figure 65: 1/4 Scuffed sample reduced elastic modulus profile

4.11.3 Al390-T6: ½ Scuffed Results

The loading curves obtained from the ½ scuffed sample using the 90° – cube corner and Berkovich tip are shown below in Figure 66 and Figure 67, respectively. They were obtained through the use of a linear loading profile as shown in Figure 31. The corresponding silicon loading curve and silicon criteria line for each tip is also shown. The 90° – cube corner data illustrates a change in slope of the loading curves at approximately 3-4 nm in depth, corresponding to the presence of the native oxide layer. Two curves obtained with the 90° – cube corner tip are excluded from the data analysis as these curves exhibit extremely elastic characteristics not shown by any other curves. No loading curves violated the silicon criteria line. Examining the Berkovich loading curves, one curve displays an extremely large loading slope, thus violating the silicon criteria line. This indent was placed on a silicon particle, and thus excluded from further data analysis.

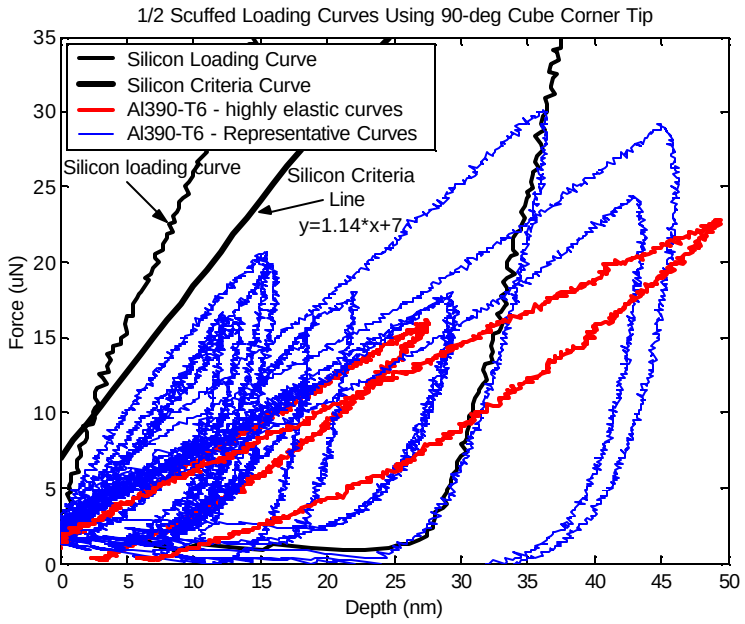

Figure 66: 1/2 Scuffed sample loading curves, 90° cube corner tip

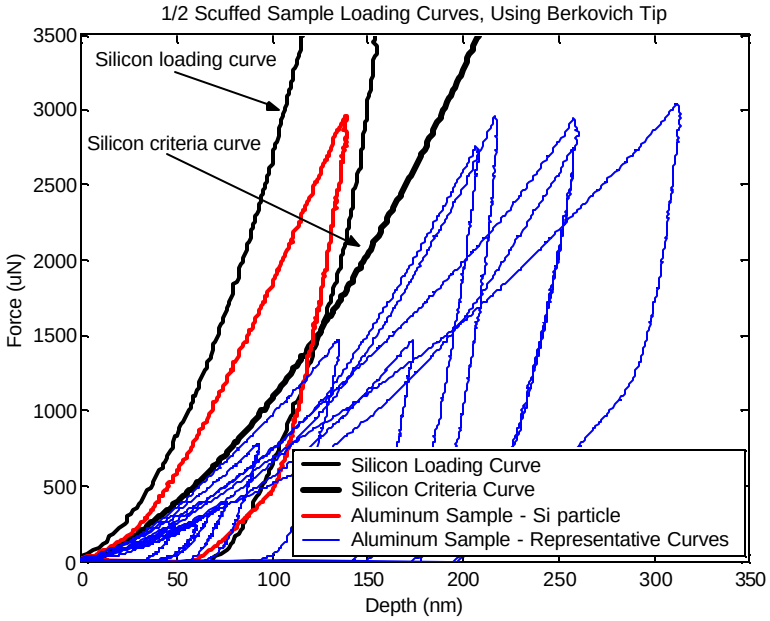

Figure 67: 1/2 Scuffed sample loading curves, Berkovich tip

The ½ scuffed loading curves have been analyzed, and material properties calculated (see Figure 68 and Figure 69). Linear trendlines of two regions, one from the surface up to 60 nm depth, and another from 60 nm to 250 nm depth have been inserted. Corresponding 95% confidence and prediction intervals are also included.

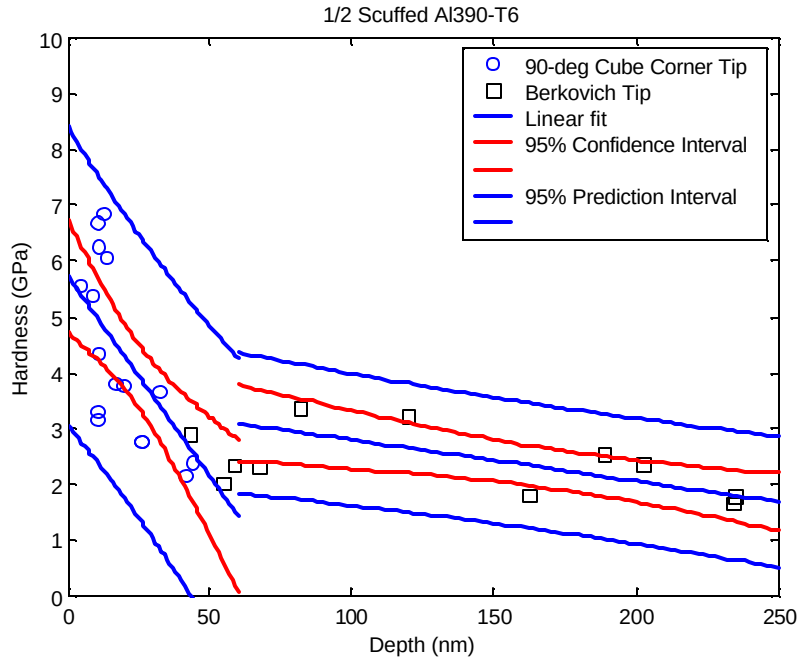

Figure 68: 1/2 Scuffed sample hardness profile

The hardness plot in Figure 68 once again shows that the top 60 nm is significantly harder than the rest of the data. At the surface, the hardness is approximately 5.7 GPa, while at a depth of 60 nm, it falls to approximately 1.5 GPa. There is also more scatter in this data, as represented by a larger width of the prediction intervals. The minimum predicted hardness at the surface is 3 GPa, while there is no minimum bound at a depth of 60 nm. These values are much smaller than those observed on either the virgin or ¼ scuffed surfaces, thus indicating a gradual weakening of these surface layers. Also note that a hardness of 3 GPa is reached at approximately 30 nm depth, which is much earlier than that observed on either the virgin or the ¼ scuffed surfaces. This seems to indicated that the uppermost surface layers are being gradually removed, or thinned down, as the wear process proceeds. Examination of the data in the region from 60 – 250 nm in depth shows results very consistent with those observed on the virgin and ¼ scuffed surfaces. The decreasing hardness trend is much less significant than that observed on the surface.

Figure 69 illustrates the reduced elastic modulus profile of the ½ scuffed sample. There is significant scatter in the data, especially at lower depths. Examination of the entire range of data seems to show a relatively constant elastic modulus, independent of the depth of the measurement. No significant differences from the virgin or ¼ scuffed samples can be concluded.

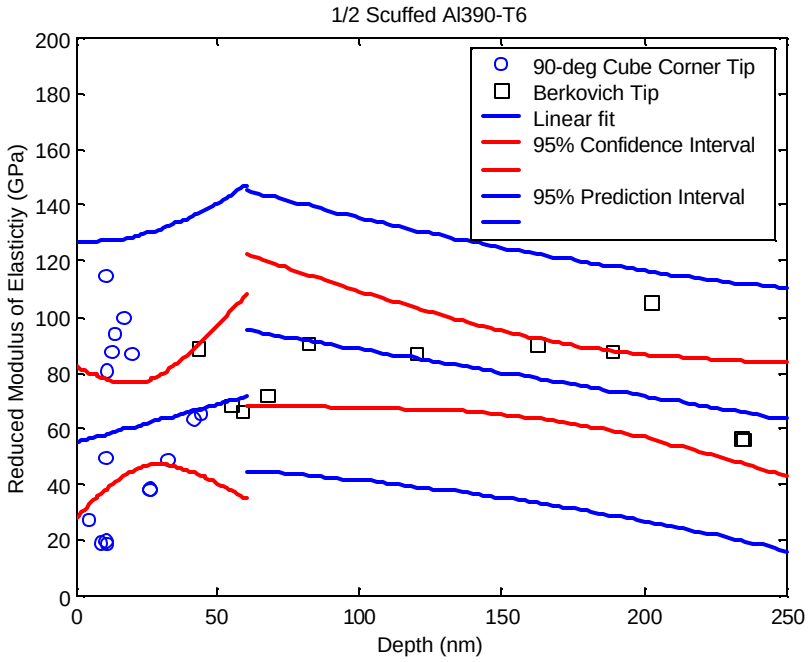

Figure 69: 1/2 Scuffed sample reduced elastic modulus profile

4.11.4 Al390-T6: ¾ Scuffed Results

Loading curves on the ¾ scuffed sample are shown below. These results were obtained with the linear load profile shown in Figure 31. The results shown in Figure 70 and Figure 71 correspond to those loading curves obtained with the 90° – cube corner and Berkovich tip, respectively. Also shown is the corresponding silicon loading curve and silicon criterion line for each tip.

First examine the data obtained using the 90° – cube corner tip (Figure 70). Two curves have loading slopes significantly greater than that of the silicon criterion line. Thus, these respective indents were placed on a silicon particle and the resulting data is excluded from subsequent data analysis. Further examination of the ¾ scuffed sample curves illustrates the presence of the 3-4 nm oxide layer, denoted by a change in slope of the loading curve at this point. This is consistent with results seen on other samples.

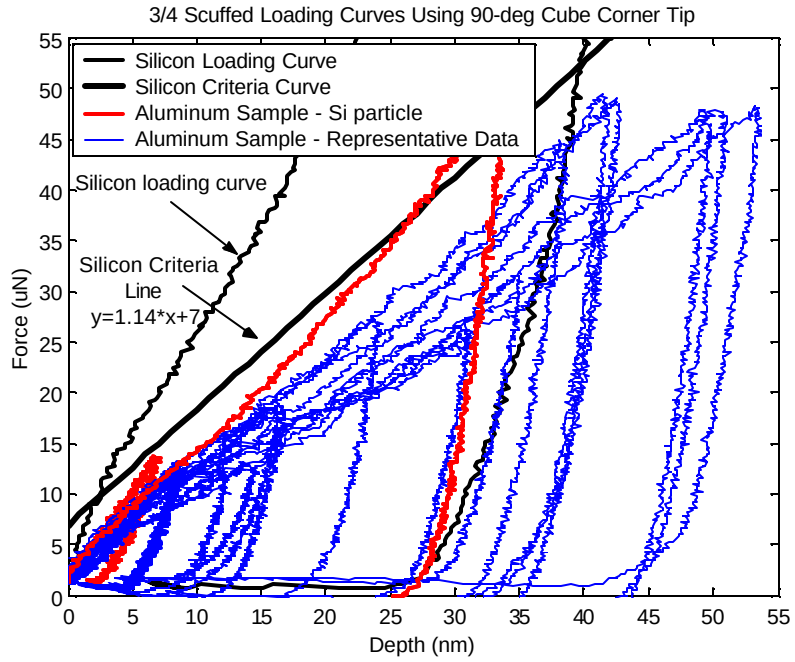

Figure 70: 3/4 Scuffed sample loading curves, 90° – cube corner tip

Figure 71 illustrates the sample loading curves obtained on the ¾ scuffed surface, using the Berkovich tip. One curve exhibits a very high loading curve slope, greater than that of the silicon criteria. It is concluded that this indent was placed on a silicon particle, and thus the resulting data is excluded from subsequent data analysis. Several curves have behavior very similar to that of the silicon criteria line, but do not significantly differ, and therefore are not excluded from the subsequent analysis.

The loading curves shown in Figure 70 and Figure 71 have been analyzed. The corresponding material properties are shown below in Figure 72 and Figure 73. In both graphs, a linear fit of the data has been performed to the two regions discussed prior. The first region corresponds to the material surface to a depth of 60 nm, while the second region consists of depths of 60 nm to 250 nm. The 95% confidence and prediction intervals are also shown.

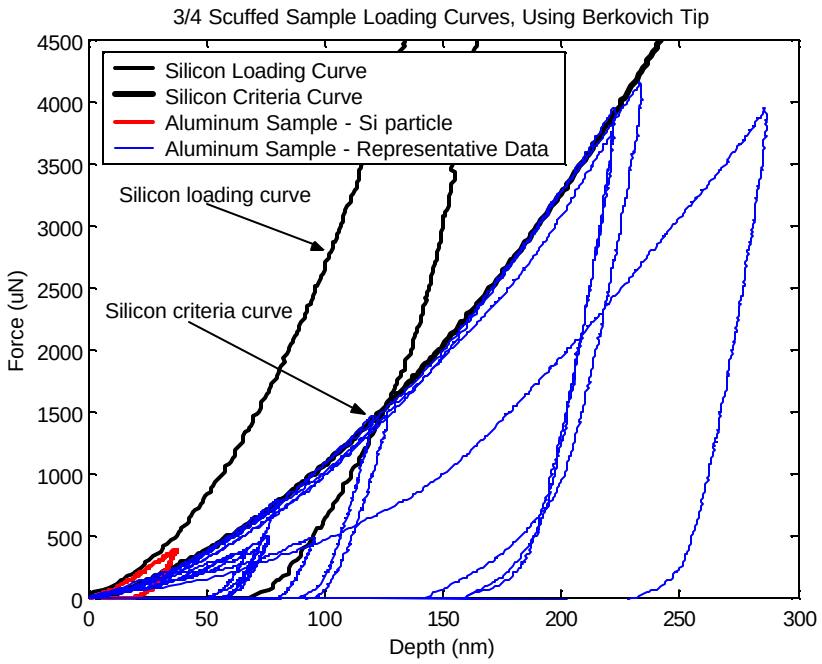

Figure 71: 3/4 Scuffed samp le loading curves, Berkovich tip

The ¾ scuffed sample hardness profile is illustrated in Figure 72. The material surface shows a significantly higher hardness than that obtained by deeper measurements, which is consistent with prior sample analysis. In particular, the top 60 nm shows a higher hardness, which is also rapidly decreasing. The surface hardness is approximately 5.7 GPa, while the hardness at a depth of 60 nm drops to approximately 3.2 GPa. The surface hardness seems to be slightly less than prior samples. The scatter associated with this sample at the low depth range is fairly small (compared to other samples), while the minimum predicted hardness ranges from 4.2 GPa at the surface to 2.8 GPa at a depth of 60 nm. Beyond 60 nm, the material hardness is nearly constant at a value of 3 GPa.

The elastic modulus plot of the ¾ scuffed surface is shown below in Figure 73. The data shows a constant elastic modulus, independent of the depth of the indent, which is consistent with the results from the virgin sample. The average reduced elastic modulus ranges from 90 – 100 GPa. The scatter in the data is also fairly small, with prediction interval widths of 50 – 70 GPa.

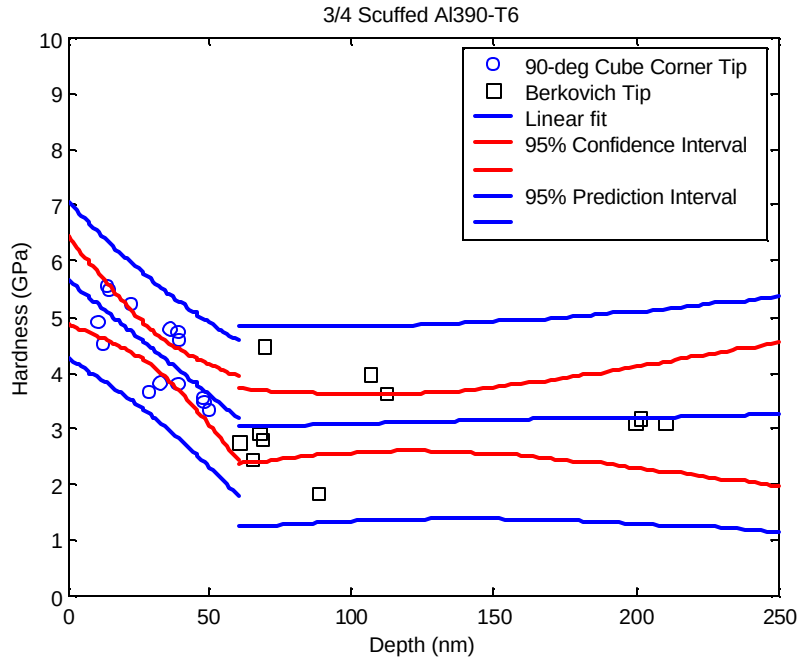

Figure 72: 3/4 Scuffed sample hardness profile based on original test area data

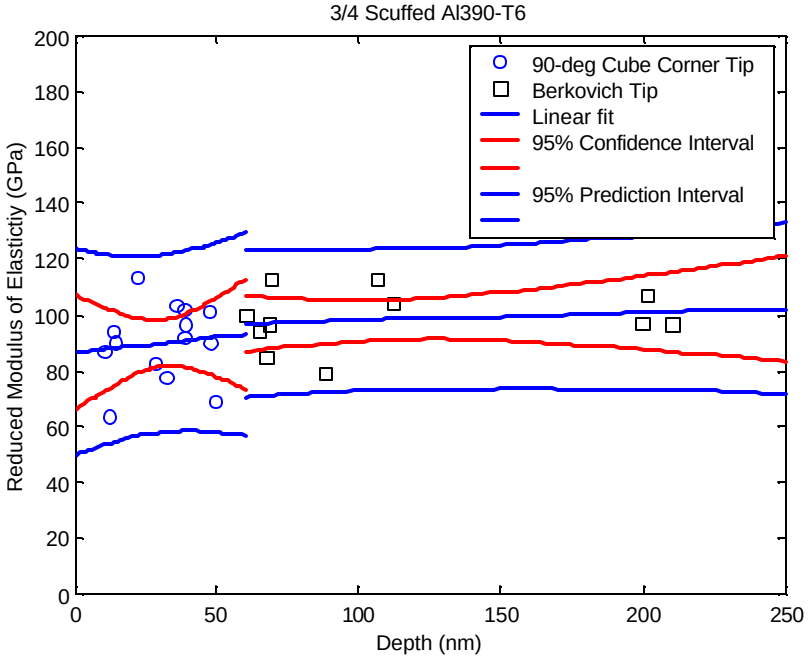

Figure 73: 3/4 Scuffed sample reduced elastic modulus profile

4.11.5 Al390-T6: Scuffed Results

Loading curves on the scuffed sample were obtained using both a linear and a "pul-load" loading profile. The results from the use of the 90° – cube corner and the Berkovich tips are shown in Figure 74 through Figure 76 below. Also included are the respective silicon loading curves and the silicon criterion curves for both tips.

Figure 74 shows the loading curves obtained with a linear loading profile using the 90° – cube corner tip. There is more variation associated with these loading curves (i.e. the scuffed sample), compared to that observed with previous samples. Some of the curves show a change in slope of the loading curve at approximately two to three nanometers depth (representative of the natural oxide layer on aluminum), while others do not. This is due to a very complex and non-uniform material composition on the surface of the scuffed sample. Two curves show loading slopes significantly higher than the rest of the curves, and violate the silicon line criteria. These curves result from an indent on a silicon particles, and are thus excluded from subsequent analysis.

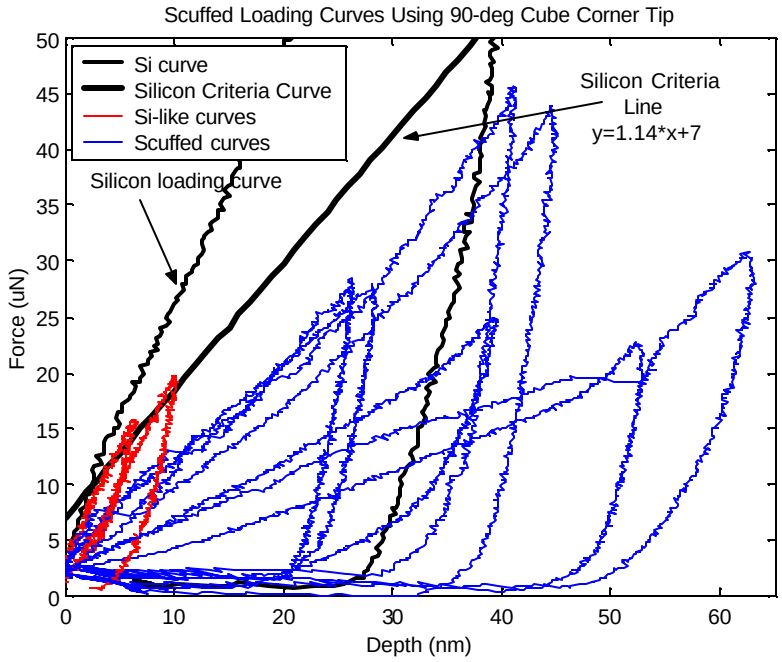

Figure 74: Scuffed sample loading curves, 90° – cube corner tip, single indents

Figure 75 illustrates the loading curves obtained the scuffed sample with a *'pul-load'* loading profile and the 90° – cube corner tip. The *'pul-load'* was incorporated to obtain more data from the sample, in a short amount of time. These curves also show a large amount of scatter, more than was observed on previous samples. This is due to the very complex nature the scuffed surface. The loading curves do not clearly exhibit a change in slope at low depth, thus, it is possible that the natural oxide layer on the aluminum has been removed. One curve has a significantly higher loading slope than any of the other curves in addition to violating the silicon criteria curve. This curve resulted from an indent on a silicon particle and is thus excluded from subsequent analysis.

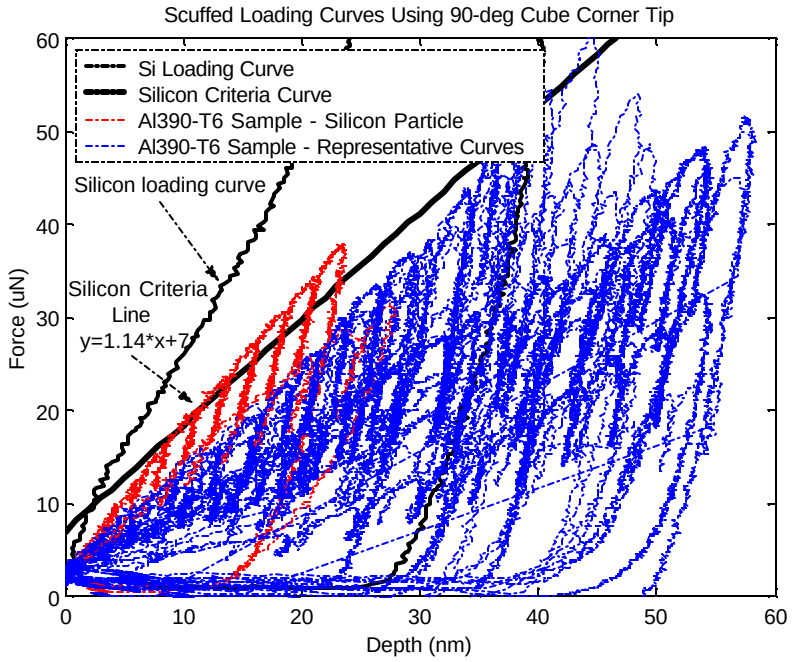

Figure 75: Scuffed sample loading curves, 90° – cube corner tip, *'pul-load'*

The loading curves on the scuffed sample obtained with the Berkovich tip are shown below in Figure 76. Similar to the trends observed from the use of the 90° – cube corner tip, there is a greater amount of scatter associated with this sample than that observed on previously analyzed samples. One curve has a loading slope slightly higher than that of the silicon criterion curve, but this is not a significant difference. Thus, this curve is analyzed along with the rest of the data.

Based on the analysis of the scuffed sample loading curves presented earlier, the resulting hardness and reduced elastic modulus profiles are shown below in Figure 77 and Figure 78. Data obtained with the 90° cube corner tip and the Berkovich tips are shown with different markers. Linear trendlines have been fit to the data corresponding to the two regions discussed earlier: surface to 60 nm depth, and 60 nm to 250 nm depth. Also shown are the 95% confidence and prediction intervals.

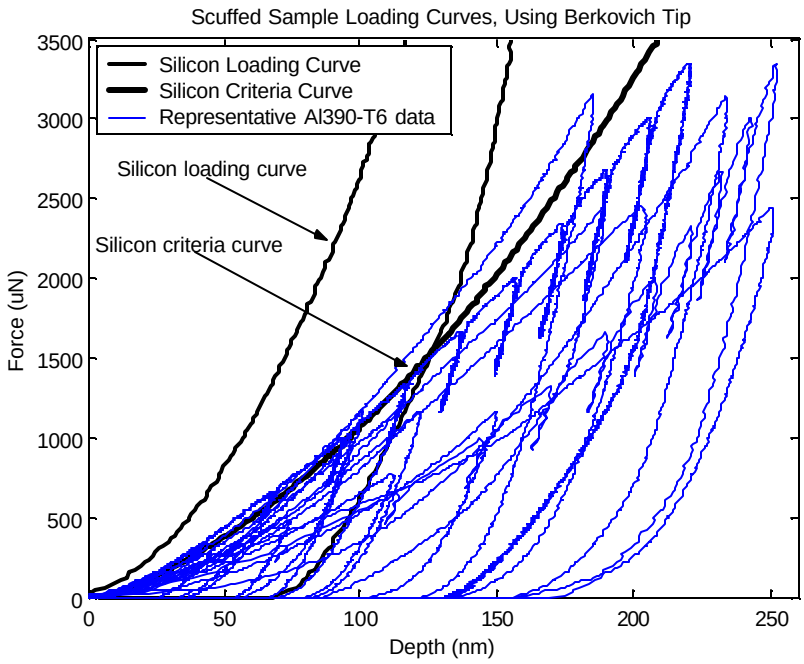

Figure 76: Scuffed sample loading curves, Berkovich tip

The hardness profile shown in Figure 77 shows some interesting trends. Foremost, the surface seems to show higher hardness than the subsurface data (deeper than 60 nm), but not as significant as on the other samples. There is a large amount of scatter in the data, especially at low depths. An important observation is that a common lower bound of all data seems to exist at approximately 1.5 GPa. This value corresponds to that obtained from the macro and micro hardness tests discussed in Section 3. Higher hardness readings similar to other samples are also observed on the surface. This seems to indicate that the scuffed surface is extremely non-uniform. In some areas, the entire protective surface layer is removed, resulting in a measured surface hardness consistent with the bulk material. In other areas, the surface layers remain relatively unaffected. One explanation is that the asperity peaks have not contacted in these areas, thus the surface has not been significantly altered by the wear experiment. The lower bound shown by the prediction interval is much lower than observed on any of the prior samples. It shows a minimum hardness of approximately 1.7 GPa on the surface, while no lower bound exists at a depth of 60 nm. Examining the data in the region from 60 to 250 nanometer depths shows a decreasing hardness trend, although not as significant as the uppermost layers. There is a fair amount of scatter, especially at lower depths associated with the region. Thus, the most significant hardness changes occur in the uppermost 60 nm.

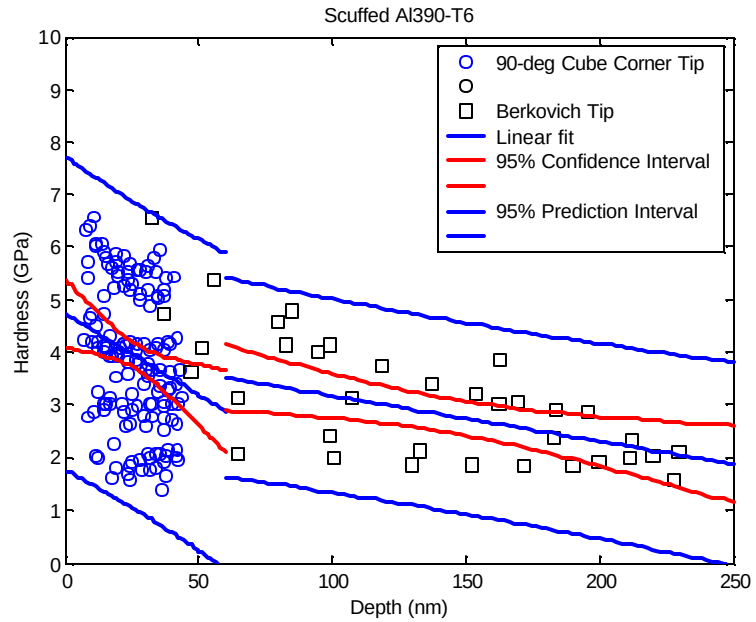

Figure 77: Scuffed sample hardness profile

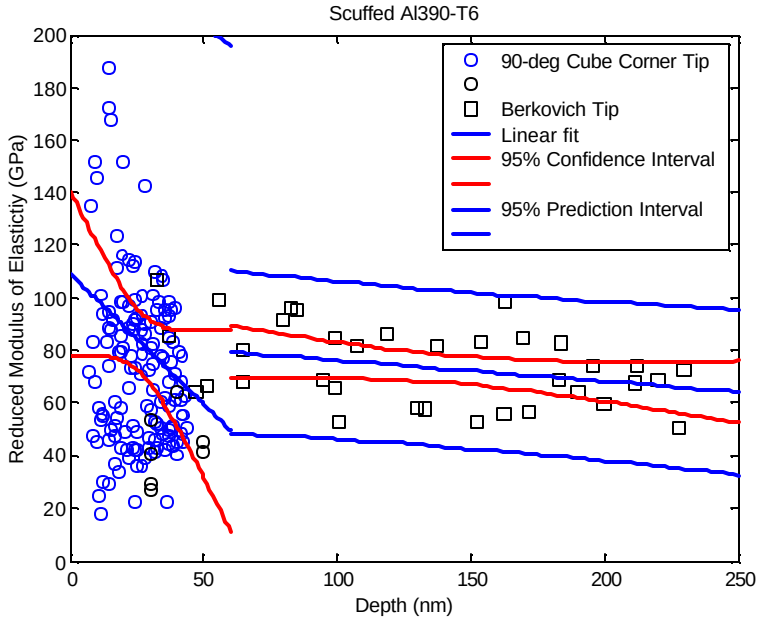

Figure 78: Scuffed sample reduced elastic modulus profile

The reduced elastic modulus data from the scuffed sample is shown in Figure 78 below. There is an extremely large amount of scatter associated with the data at low depth. The 95% prediction intervals do not appear on the plot because their width is larger than scales displayed on the graph. The large amount of scatter shown on the surface is consistent with that observed in the hardness plot, and can be attributed to a very complex structure on

the surface. As greater depths are achieved, the scatter is significantly reduced and the confidence interval predicts a mean reduced elastic modulus value between 65 and 85 GPa.

4.12 Al390-T6 Sample Trends

Prior discussions have dealt with the examination of individual sample data. The focus now shifts to the examination of relative comparisons and/or trends between the samples. Through this analysis, insight will be gained into the surface changes that occur during the wear and scuffing process.

In Section 4.11, a linear least squares curve fit was fit to the data of all samples, for two different depth regions. The first region corresponds to depths from the surface up to 60 nm below the surface, while the second region corresponds to 60 nm to 250 nm below the surface. The linear trendlines for all five sample's hardness and reduced elastic modulus values are shown in Figure 79 and Figure 80 below.

First examine the hardness as a function of depth shown in Figure 79. All samples show that the surface hardness on the top 60 nm is significantly higher than that observed below the surface. All samples also show decreasing hardness trend in this top 60 nm, to values more consistent with those obtained from 'bulk' material measurements. The virgin surface has the highest hardness in this region. The ¼ scuffed, ¾ scuffed and scuffed samples show a gradual weakening trend of this uppermost layer, indicated by correspondingly lower hardness values. The ½ scuffed curve is very different, and thus, further analysis of the underlying data is needed. Referring to Figure 68 (½ scuffed hardness data) and Figure 66 (1/2 scuffed loading curves), it seems that the surface hardness change is negligible beyond approximately 25 nm below the surface. But, from Figure 66 it appears that more tests are needed between the depths of 20 – 45 nm. This would give a more accurate representation of the data. Thus, a linear trendline fit to the entire region of data from the surface to a depth of 60 nm is grossly inadequate, resulting in a misrepresentation of the actual data. Thus, this data can be ignored, and a gradual weakening of the uppermost surface film is observed.

Beyond top 60 nm, the hardness is relatively constant for all samples. Also note that there is much less data, and thus the confidence intervals are much wider for the data, in this region. When the confidence intervals for individual samples at these depths are compared, they greatly overlap, indicating that no significant differences between samples can be concluded. Seeing that the most significant changes in individual samples occur in the top 60 nm, it is concluded that there are negligible differences between the hardness values of different samples at these depths.

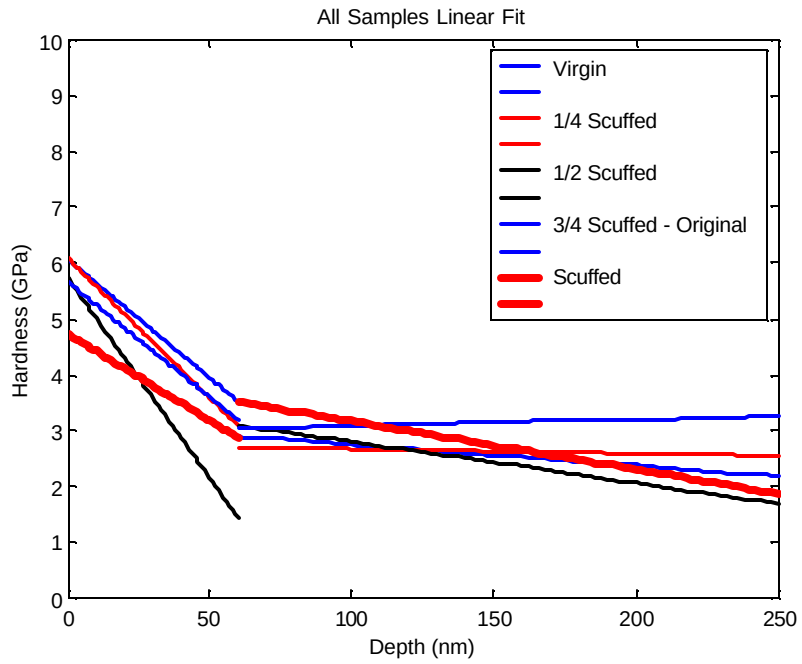

Figure 79: All samples linear fit of data, hardness profile

The reduced elastic modulus trendlines of all five samples (developed in Section 4.11) are shown below in Figure 80. As shown in the discussion of Section 4.11, there is a large amount of scatter in the data, especially at lower depths. This is attributed to surface roughness, non-uniform layers, and microstructural differences, as discussed prior. At higher depths, the contact area is larger, yielding more consistent results. Examination of these curves shows that the elastic modulus is relatively independent of the depth, and no significant trends between samples can be observed.

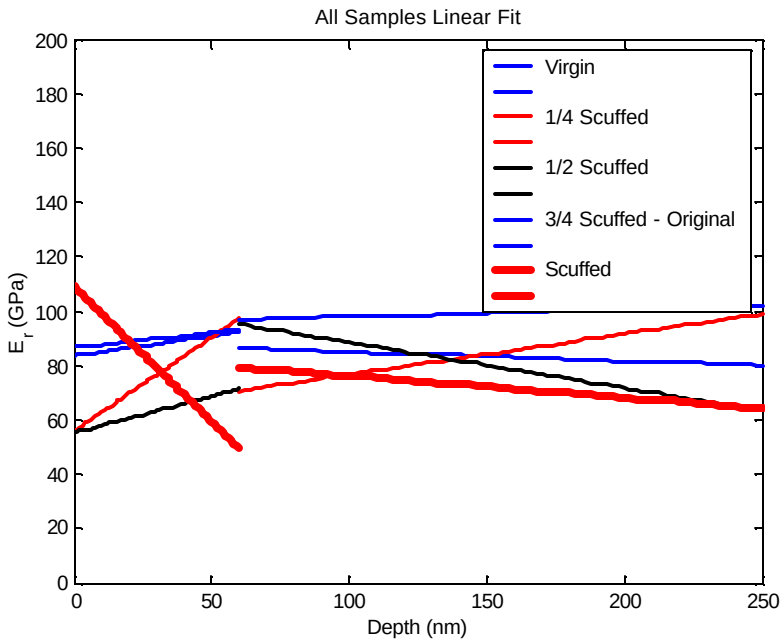

Figure 80: All samples linear fit of data, reduced elastic modulus profile

4.13 Conclusions

Nano-indentation is a method of obtaining thin film mechanical properties, commonly used in the semi-conductor and magnetic storage Hard Disk Drive industries. Based on very precise load and displacement measurement techniques, a very sharp tip is pressed into a material with an extremely light load. Through examination of tip load-displacement data, the material hardness and reduced elastic modulus values can be computed.

Appropriate tips have been selected based on the estimated surface material properties and desired depths of penetration in the material. For low depth indentations (i.e. less than 50 nm), a 90° cube corner tip was selected. This tip has a relatively high aspect ratio and a sharper tip radius, allowing more localized deformation, and thus making it more appropriate for shallower depths. This tip is limited to shallower penetrations, as excessive blunting would result at higher loads and deeper penetrations. To obtain data at deeper penetrations, a Berkovich tip was used for these tests. This tip has a much lower aspect ratio and a larger tip radius, making it less prone to blunting. On the other hand, this tip is not appropriate for shallower depths because of low sensitivity and minimal plastic deformation. Tips have been calibrated based on the procedure laid out in Oliver and Pharr. By performing multiple indentations at various depths on a uniform material of known material properties (i.e. fused quartz), the projected tip area as a function of tip penetration depth has been computed. This area is then used in the calculation of material properties. The calibration procedure has been verified on a silicon sample, which has a very thin oxide layer of approximately 4 nm thickness, but otherwise constant material properties throughout various depths. Relatively constant material properties have been obtained, independent of either depth of tip geometry, thus verifying the calibration procedure.

Engineering surfaces are very different from typical surfaces that are analyzed using nano-indentation. Properties such as extreme surface roughness, non-uniform surface layers and microstructural differences hinder the use of nano-indentation to obtain thin film material properties on engineering surfaces. Numerous sets of loading curves have been extensively analyzed, and subsequently, a criterion has been established to determine when an indent on a silicon particle (see microstructural analysis in Section 2.3.1) occurs. It has then been determined that the inclusion of silicon data in the overall surface data will skew the surface data of interest, and is not representative of the actual failure surface. Thus, data obtained from an indent on a silicon particle is removed for further analysis.

Shown in Figure 81 through Figure 85 are hardness and elastic modulus plots for all five samples, containing nano, micro, and macro/meso test data. Nano-scale measurements were obtained from nano-indentation experiments, micro-scale from Vickers indents (Section 3.3.1.3), and macro/meso-scale from Rockwell B tests (Section 3.2.1.2). By combining all test data on a single plot, various depths can be displayed covering a range of over four orders of magnitude. One important note is that the nano and micro/macro hardness numbers are based on slightly different definitions. The micro/macro definition of hardness is the applied load divided by the residual, projected area of the indent, while the nano definition of hardness is defined as the peak load divided by the maximum projected area. Assuming that the elastic recovery of the material is relatively small in comparison to the total plastic deformation, these definitions should be very comparable.

These figures all show some common trends. Most noticeable is that the top 100 nm shows a significantly higher hardness than the rest of the data. The hardness at a depth of 10 nm is approximately 6 GPa, while bulk hardness is approximately 1.6 – 1.9 GPa. Also note that the bulk hardness is reached at a depth not greater than 100 nm, and that there is a very good hardness correlation between scales. This gives great support for further studies that examine changes in material properties at the nano-level. Another observation is that there is progressively more scatter in the data as one proceeds from the macro to the micro to the nano scale. As discussed extensively in Section 4.9, as indents become smaller and smaller, more localized properties are examined. Surface roughness, non-uniform layers and microstructural differences give rise to increased scatter in the data, while with a macro test, many of these surface variations are averaged out over a much larger area. None-the-less, by practicing careful experimental techniques and thorough data analysis, meaningful data can be obtained through the use of nano-indentation on engineering surfaces.

When comparing sample trends, it has been shown that there is a gradual weakening (lower hardness) of the uppermost 60nm as the wear process proceeds. Examination of the scuffed sample in this range shows a large amount of scatter in the data. This is expected as the scuffed surface is a very complex surface, comprised of a wide variety of different materials and structures. The scuffed sample also shows that even at the material surface (depth approximately equal to zero), softer spots corresponding to bulk hardness can be found. This further illustrates that the protective surface layer is removed, at least at some points of the surface, thus exposing the bulk material to contact.

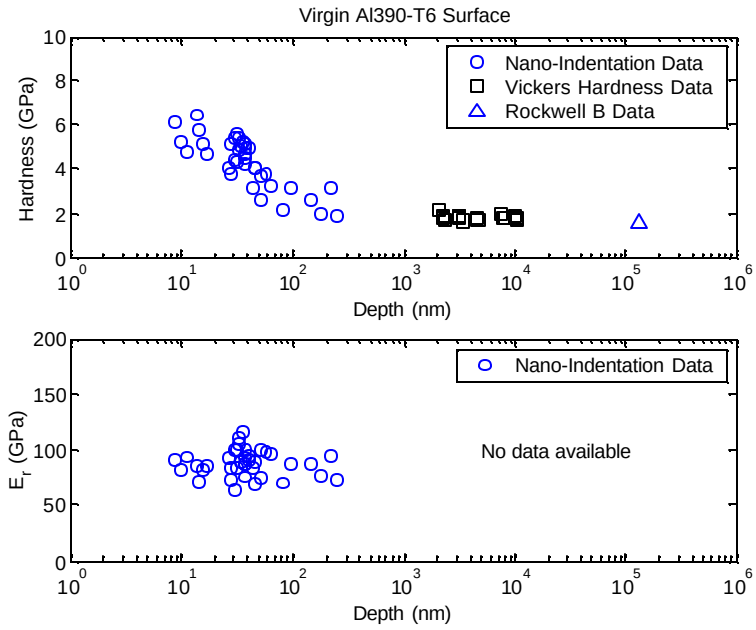

Figure 81: Virgin sample H and Er continuum

Also examined was the elastic modulus of the material. It has been found that the elastic modulus is relatively constant, and independent of the depth from the surface. When comparing sample trends, there is no clear relationship between the elastic modulus and the wear process.

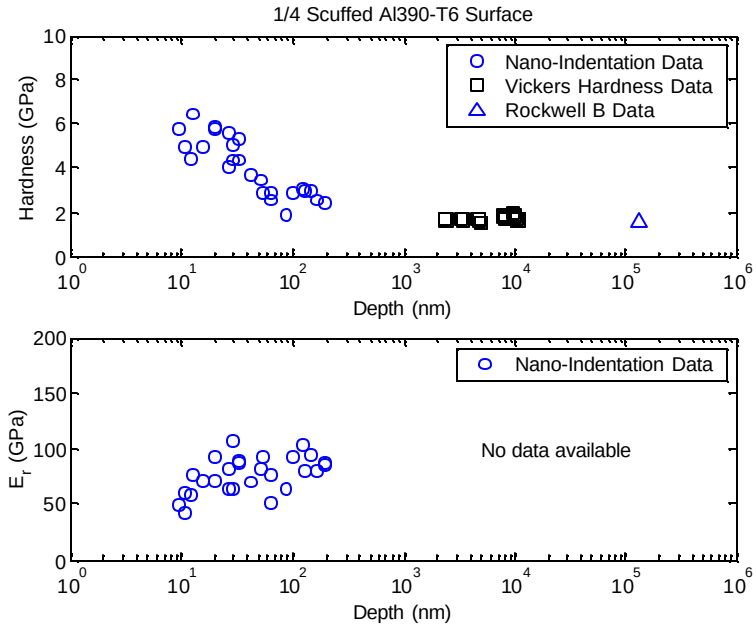

Figure 82: 1/4 Scuffed sample H and E_r continuum

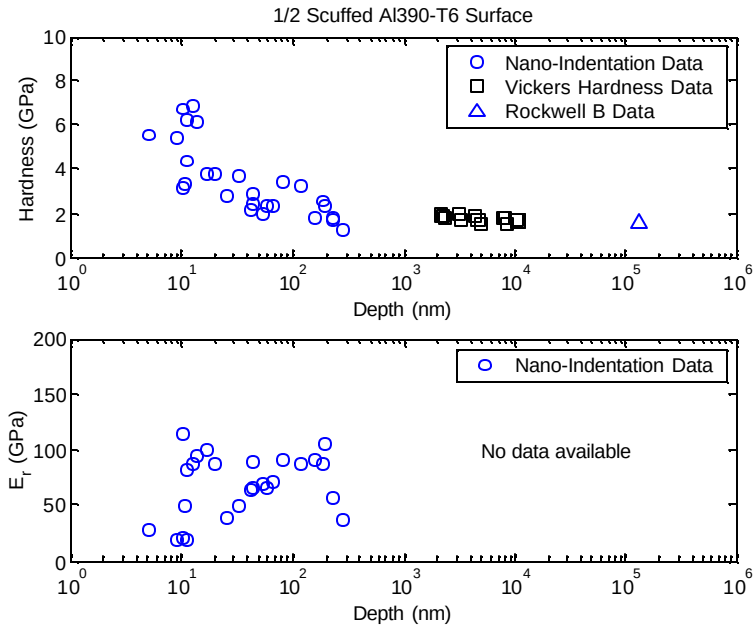

Figure 83: 1/2 Scuffed sample H and E_r continuum

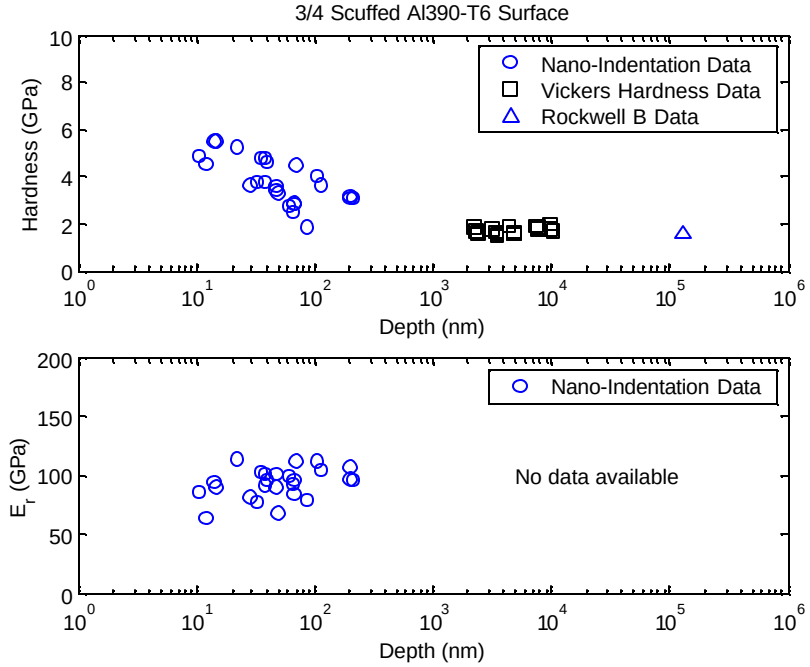

Figure 84: 3/4 Scuffed sample H and E_r continuum

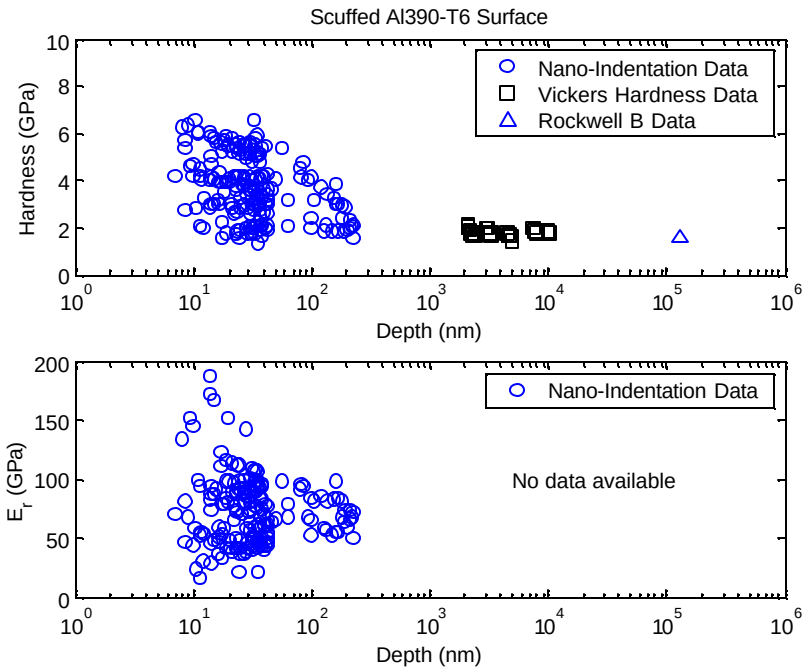

Figure 85: Scuffed sample H and Er continuum

Chapter 5: Nano-Scratch Technique

5.1 Introduction

Nano-indentation has proven to be a great resource in determining the mechanical properties of surface layers, but this method does have its limitations. In order to eliminate substrate effects, indents must be made directly on the thin surface layer, but at a depth not to exceed 10-20% of the total layer thickness. Using current technology, this is nearly impossible for thin films, with thicknesses in the 20 nm range and below. Extremely shallow indents, on the order of a few nano-meters and less, also provide inconsistent results (due to blunting of the tip, surface roughness, instrument limitations, tip limitations, etc.). Other issues result from the fact that an extremely small area is isolated for each respective nano-indentation, which is on the same order of magnitude as the grain structure and grain boundaries of the material. Thus, it is conceivable that different grain particles, grain boundaries could have dramatically different material properties. Furthermore, non-uniform surface layer thicknesses make nano-indentation extremely dependent on the location of the indentation. The nano-scratch technique may be used to overcome some of these obstacles.

Similar to nano-indentation, nano-scratch is commonly used on extremely thin films and surfaces common in the semi-conductor and magnetic storage applications. The nano-scratch technique uses a finite radius (nanometer to micron dimensions) diamond tip to traverse along a surface (several microns in length), with a prescribed vertical load profile. Through analysis of *in-situ* scratch test data (forces and displacements), as well as examination of the residual scratch profile, several conclusions about the surface material can be made. The analysis emphasizes tangential force and cross-sectional area of the resulting scratch (not the normal force nor the normal area as in nano-indentation), and thus minimizes the substrate effect. This gives the nano-scratch test the ability to examine much thinner films than is possible with nano-indentation tests. Since the test obtains data over several microns lateral range, it has more of an averaging effect between different grain structures, grain boundaries, and peaks and valleys, than that of nano-indentation. The qualitative aspects of this test are strong, and fairly well developed (for typical semi-conductor/HDI applications). This technique is often used to obtain relative film "hardness" measurements by quantifying a relative resistance to penetration depth, during a test. It has also been used to model single asperity friction / wear tests. Qualitative layer thickness, as well as the delamination point of surface layers, can also be analyzed. These aspects can become quantitative with the use of appropriate analysis techniques. Other researchers [Kral, et al] have quantified surface hardness based on analysis of the *in-situ* scratch data, in combination with the residual scratch profile.

The nano-scratch aspect of this project is two-fold. Firstly, engineering surfaces are very different from typical nano-scratch surfaces. They are extremely rough, consist of non-uniform surface layers, and non-homogeneous surface microstructure. All three add considerable difficulty to the test, as well as analysis. Thus, the first aspect of the project will consist of a feasibility study to determine if this technique can yield reproducible results on engineering surfaces. Secondly, the aspect of this project will be to draw connections between the results obtained from nano-scratch tests to those obtained from previous nano-indentation tests. These connections will be used to obtain a better understanding of the changes in the surface layers that occur during the wear/scuffing process.

5.2 The Instrument Used for Nano-Scratch Experiments

The Hysitron Nano-Scratch apparatus is an attachment to a Multimode Atomic Force Microscope (AFM) shown in Figure 86 below. The Multimode AFM uses a two-dimensional piezo-elecric crystal to obtain precise displacement resolution of the stage. The 2-D transducer for scratch is also shown in Figure 86 below. This transducer has the ability to measure very small forces (with the use of a capacitive load cell with multiple plates) in both the vertical and lateral directions. The instrument is located in the Center for Microanalysis of Materials in the Materials Research Laboratory at The University of Illinois at Urbana-Champaign.

A detailed scratch procedure is described below. In general, a scratch profile is developed, defining both the lateral displacement and the normal load on the tip. This scratch profile is then executed, while the transducer records displacement and force in both the normal and lateral directions. From the analysis of these data, as well as analysis of the residual scratch data, a material hardness can be obtained.

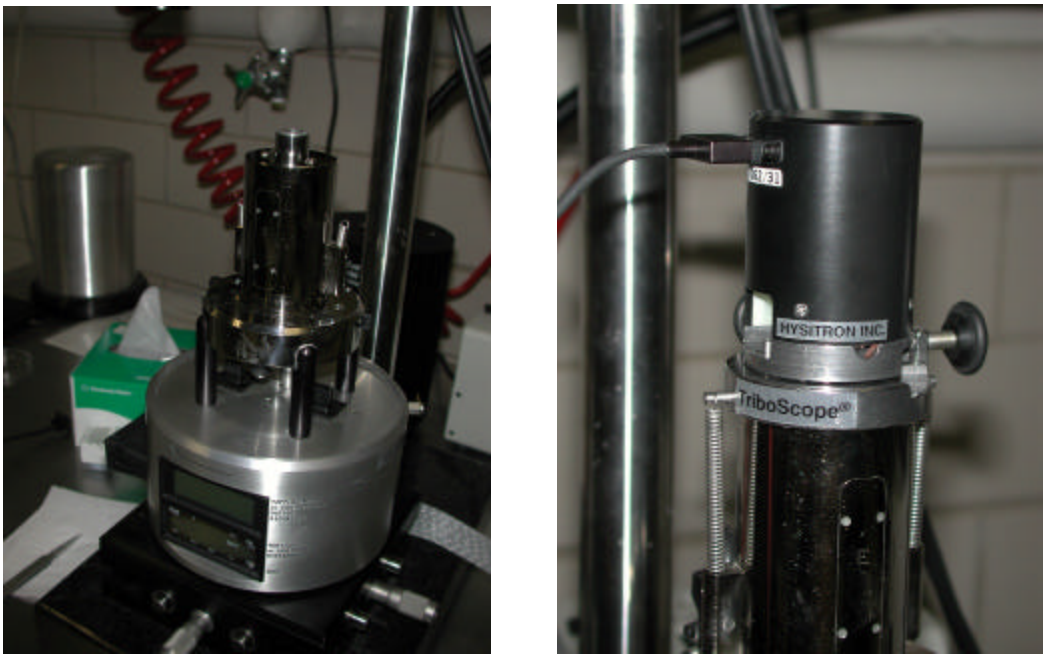

Figure 86: Multimode AFM and 2-D transducer

5.3 Calculation of Material Hardness

Kral et al. [Kral *et al*, 1996], propose a method of relating the material hardness obtained from a scratch experiment to that obtained from an indentation experiment. The accuracy of their model was verified using finite element simulations, with some experiments. The major assumption of the model is that the plowing object is spherical in shape. Conducting a force balance, and subsequently separating the lateral force into a plowing and a shearing component, one obtains the following equation:

$$H = F\left\{r^2\left[\sin^{-1}\left(\frac{w}{2r}\right)-\left(\frac{w}{2r}\right)\sqrt{1-\left(\frac{w}{2r}\right)^2}\right]+2mr^2\left[1-\sqrt{1-\left(\frac{w}{2r}\right)^2}\right]\right\}^{-1} \qquad (12)$$

The material hardness is H, F is the lateral force, w is the total width of the scratch during the scratch, r is the radius of the plowing tip, and μ is the coefficient of friction. The lateral force and the normal force are both measured during the test (therefore can obtain coefficient of friction as lateral force divided by normal force). Since in-situ imaging of the scratch width is not possible, the residual scratch width is used in the equation, which introduces negligible error. The residual scratch width, w, and residual scratch depth, h, can be related to the effective radius of the plowing tip, r, by:

$$r = \frac{1}{2}\left(h + \frac{w^2}{4h}\right) \tag{13}$$

The residual scratch is imaged immediately after the scratch, with the same tip that was used to perform the scratching. Due to elastic recovery after the scratch, the residual scratch will have a radius larger than that of the imaging tip (i.e. the plowing tip), and thus an adequate scratch profile can be obtained. The width edges of the residual scratch are defined as "any evident change in the slope of the sidewalls." The residual depth, is the maximum depth subtracted from the average vertical position of the edge width endpoints. By using these methods, a material hardness that is comparable to that obtained from the nano-indentation tests can be calculated.

5.4 Nano-Scratch Tips

As stated earlier, nano-scratch experiments must be performed within the spherical regime of the tip. Thus, the size of the radius, as well as the included angle of the tip defines the maximum depth that the tip can be used to scratch, while still maintaining a spherical profile. Figure 87 below illustrates a typical tip, with an included angle of α, and a spherical end.

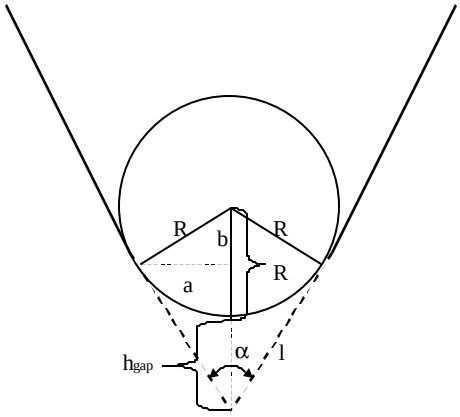

Figure 87: Nano-scratch tip profile

Based on the known tip radius, R, and the known included angle, α, the maximum scratching depth for spherical contact is equal to R-b. The calculations are shown below. The unknowns h_{gap}, l, a, and b can be calculated from left to right:

$$(R + h_{gap}) \cdot \sin\left(\frac{a}{2}\right) = R \qquad l \cdot \sin\left(\frac{a}{2}\right) = a \qquad b = \sqrt{R^2 - a^2}$$

$$(R + h_{gap}) \cdot \cos\left(\frac{a}{2}\right) = l \qquad a^2 + b^2 = R^2$$

In order to eliminate any possible directionality (scratch data dependent on the orientation of the tip), it is important to use a tip that is uniform in all directions, i.e. a conical tip. Based on the previous calculations and the need for a uniform geometry, a 60° conical tip with a 1 µm radius was selected and shown in Figure 88. The value of the tip radius is limited by current manufacturing limitations. Currently, the smallest available conical tip radius (from Hysitron, Inc.) is denoted as 'less than 1 µm radius.' Since there is no guarantee how small this radius may be, the next larger tip radius, a 1 µm radius tip, was selected (significantly cheaper). This tip should thus be capable of obtaining plastic deformation at the shallowest depths. Therefore, this tip should be appropriate for measuring properties of the thinnest possible films, down to a few nanometers thick. Based on the geometry, the maximum depth that this tip can be used to scratch (while maintaining a spherical profile) is approximately 500 nm (see prior calculations).

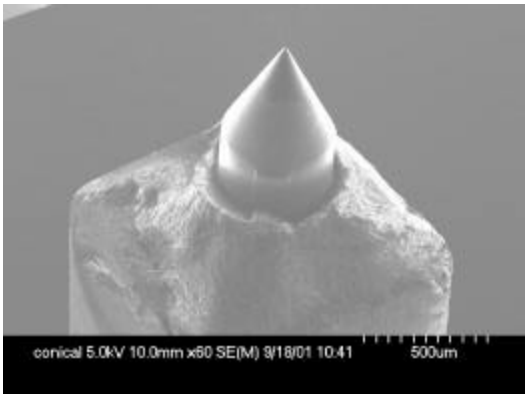

Figure 88: 60°, 1 µm radius conical tip; SEM image

Several researchers suggest using a blunted 90° cube corner tip to measure the properties of very thin films, due to its smaller tip radius when compared to that of the conical tip. This does have its merits, but using a three-sided tip introduces directionality errors into the scratch, which will affect the results. Thus, the conical tip was used in this work

5.5 Procedure

Obtaining accurate and repeatable results from nano-scratch techniques requires careful calibration each time the instrument is used. The sensor drift and tip cleaning procedures are the same as those described in the nano-indentation procedure, as stated in Sections 4.6.1 and 4.6.2, respectively.

5.5.1 Transducer Constants

Once the nano-scratch is set-up and the proper tip is cleaned and installed, it is necessary to obtain the correct transducer constants. This procedure (modified from Hysitron's *Calibration of X Axis* and *Advanced Lateral Force* manuals) compensates for any differences in mounting or levelness of the transducer, which may cause

scattered and/or unrepeatable data, as well make data analysis very difficult. These errors can first be minimized by carefully leveling the transducer each time of use (accomplished by adjusting the air table). The correct transducer constants can be obtained through an air indent (z-axis), followed by an air scratch (x-axis). See nano-indentation procedure for air indent procedure and calibration of the z-axis. An air scratch is used to obtain x-axis transducer specific constants such as plate spacing, electro-static force, and displacement offset. An air scratch is performed in much the same way as an air indent. The tip is positioned sufficiently far from the sample, and the *'x-axis-calibration-scratch'* profile (shown below, Figure 89) is loaded and executed. The scratch profile defines both the normal force and the lateral displacement of the tip, as a function of time, during a scratch. The *'x-axis-calibration-scratch'* is performed in the air, and thus the normal force is zero at all lateral positions.

The first step in the x-axis calibration procedure is to define the transducer limits of lateral travel (these values can be altered by leveling differences associated with the transducer). This is accomplished through a long air scratch (i.e. –25 µm to +25 µm), with the image position set to zero. The image position defines the placement of the tip, relative to the position of the acquired image, such that the scratch is actually placed in the center of the imaged surface. A sample result of such an air scratch is shown below in Figure 90. Note that during a scratch, the instrument software records the normal force, normal displacement, lateral force, lateral displacement and time signals.

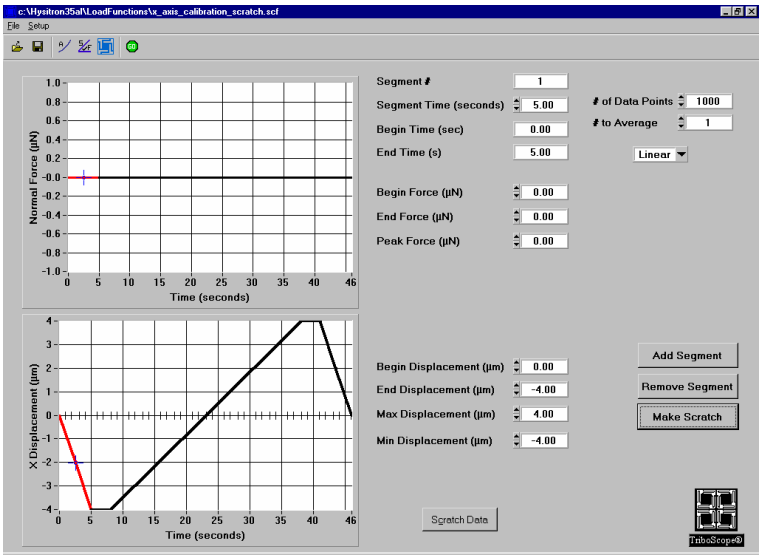

Figure 89: x-axis-calibration-scratch profile

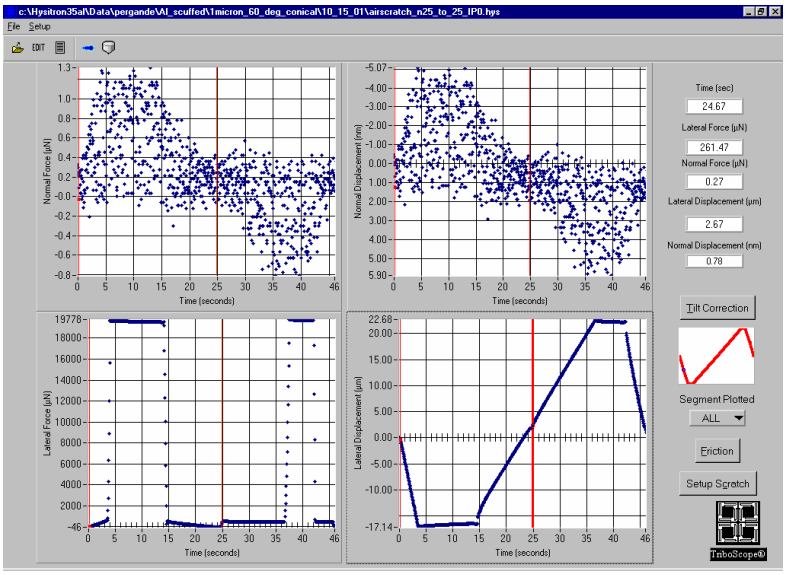

Figure 90: Air scratch from -25µm to +25µm, with Image Position set to 0

Examining the graph of lateral displacment vs. time in the lower right of Figure 90, it is clear that the limits of lateral travel (specific for *this* transducer under *this* mounting configuration) correspond to –17.14 µm and +22.68 µm. These points correspond to the plate spacings at which the center plate and the respective drive plates snap together, causing a large lateral force, as illustrated in the lower left graph of lateral force vs. time. These values will change slightly, depending on the levelness of the transducer. The transducer breakpoint is the point at which the actuator control switches from one drive plate to the other. At this point, the voltage is zero for an instant, causing the transducer to lose control of the lateral force feedback. Thus, there is a discontinuity in the lateral force signal (lower left graph) and a flattened region in the lateral displacment signal (lower right graph) at the position marked by the vertical line at a time of 25 seconds. For data analysis purposes, a scratch must be confined to the longest linear region bounded by either of the two lateral displacment limits and the transducer breakpoint. For this case, this region corresponds to lateral displacments bounded by +3 µm and +22.68 µm. The image position is set to the center of this range (i.e. 13 µm), and scratches from the lateral positions of –10 µm to +9.68 µm can be performed (based on the new 'shifted' scale).

Now that the image position has been optimized, it is necessary to obtain the x-axis transducer specific constants such as plate spacing, electro-static force, and displacement offset, which is accomplished through another air scratch. Using the set image position defined prior and air scratch profile defined in Figure 89, an air scratch is performed over a range approximately 20% longer than the scratches to be performed (i.e. 10 µm calibration range for 8 µm length scratches). The resulting data is shown in Figure 91 below.

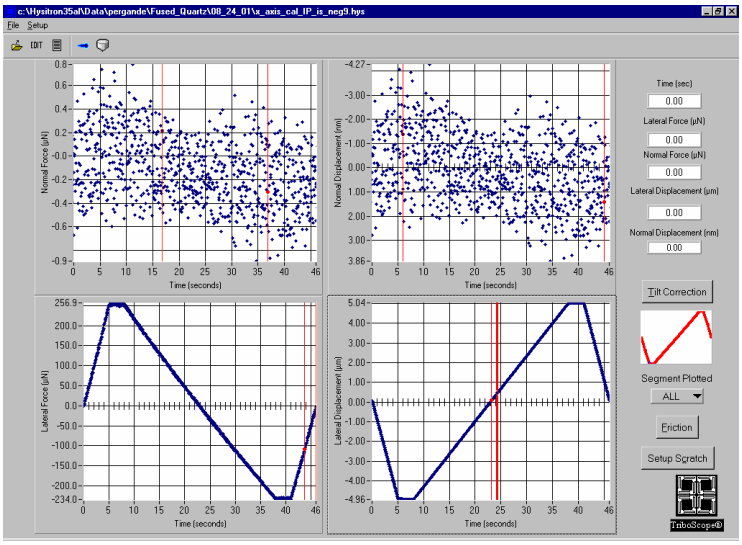

Figure 91: Resulting data from x-axis-calibration-scratch from -4 µm to +4 µm

Note that the normal force and displacment curves (top) are approximately zero (within instrument noise limitations) because the z-axis transducer constants have been changed appropriately during the air indent. Examine the lateral force curve (lower left), and note that this curve is not zero (even though this data results from a scratch performed in the air). The non-zero forces observed are due to the internal springs of the transducer displacing, and must thus, be compensated for. By choosing File ➔ Calibrate, the software compensates for these forces by adjusting the x-axis transducer constants mentioned above. The resulting curve is shown in Figure 92 below. Thus, the force seen during segment 3, the scratching segment, is now approximately zero (within instrument noise limitations), for all lateral displacements. Note that the instrument noise in the normal force is much smaller than that observed in the lateral force (approximately ten times less). This is a sensitivity characteristic of the transducer. Now the transducer is fully calibrated and surface scratches may be performed.

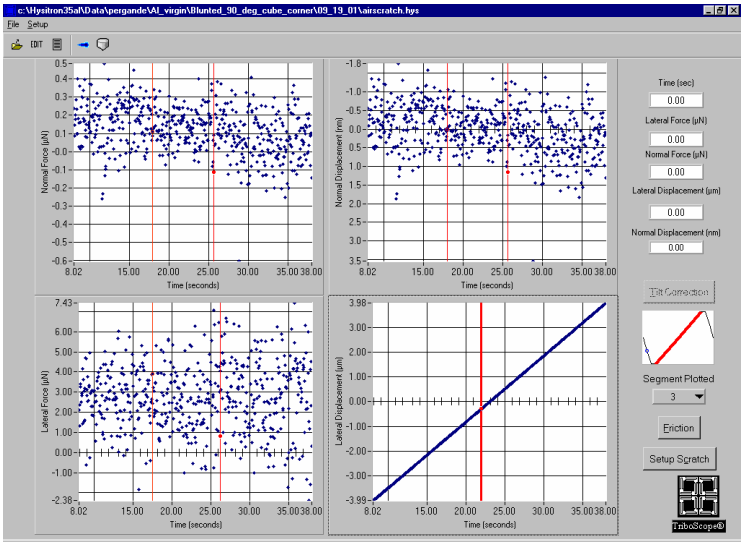

Figure 92: Data after transducer constants are calibrated

5.5.2 Test Procedure

After engaging the tip on the sample, a pre-scratch image of the surface is obtained. The Multimode AFM is used to scan the surface under a low load (set point of 1.5 to 2 μN), using the same tip that will be used to make the ensuing scratch. The set point is the load applied to the tip, through a feedback loop, such that the tip maintains contact with the surface. Once an accurate image is obtained and all drift settles out of the piezo-sensor, the desired scratch profile is executed. The scratch profile defines the normal force and the lateral displacement of the tip, as a function of time of the scratch. Both the normal force and the lateral displacement are controlled via a feedback control loop. Longer scratches exhibit a better sample average, while shorter scratches focus more on localized behavior. The maximum scratch length is limited by the maximum range of the piezo-electric sensor, as well as the limits of the transducer, and is typically on the range of 10-12 μm. The scratches in this study range between 6 and 8 μm in length, which will provide adequate averaging, and also maximize the efficiency of the test. Disengaging the tip, moving to a new region, and reengaging the tip is a time consuming procedure that should be minimized to maximize the efficiency of the test. But, in order to avoid the strain hardening effects of other close proximity scratches, they must be placed at least four to five residual scratch widths away from the next nearest scratch. Thus, an appropriate balance must be achieved. Typical scratch profiles for comparing sample surface hardness (resistance to deformation) or layer thicknesses are either constant force scratches or ramp force scratches. The details will be discussed later. During the scratch, several quantities are measured *in-situ*: normal displacement, normal force, lateral displacement, lateral force, and time.

The normal force, lateral force and lateral displacement measurements can be used directly in the analysis, but the normal displacement measurements contain data due to the tilt of the sample (i.e. slope of the scratch surface) as well as sample roughness. The sample tilt may be as small as a few nano-meters vertical change per micron of lateral travel, but is extremely significant when characterizing surfaces at the nano-level. Thus, in order to perform any scratch depth analysis, both the tilt and the sample roughness must be taken out of the displacement data. Hysitron includes a built-in function to take the tilt out of the normal displacement measurements by analyzing an area of the resulting data (based on the user inputs) in which the normal force is zero, but there is some normal displacement (i.e. the normal displacement should be zero). By compensating for this sample tilt with a linear correction, a scratch depth profile can be obtained as if the scratch was performed on a level sample (see Results for Fused Quartz under a constant normal load, Section 5.6.1). This procedure works well for very smooth samples (such as fused quartz and silicon wafers) in which the sample roughness is negligible compared to the scratch penetration depth. For engineering surfaces, the surface roughness is significant, and may be on the same order of magnitude as the scratch penetration depth and tilt of the sample. Thus, a simple linear tilt correction is inadequate. Therefore, a pre-scratch scan of the scratch surface prior to the scratch must be incorporated into the procedure, and then subtracted from the scratch data to obtain data as if the scratch was performed on a flat, level sample. The method of obtaining a pre-scratch scan will be discussed later in Section 5.6.

Another problem with long scratches on engineering surfaces is that it is very easy for the tip to lose contact with the surface, especially at the extremities of lateral and/or normal displacement. Figure 93 below illustrates a pre-scratch scan profile (top line) of an aluminum sample, as well as the *in-situ* scratch profile (lower

line). The pre-scratch scan profile was obtained with a set point of 2 µN, in combination with an additional 10 µN tip load. The horizontal points in the scan profile indicate a constant normal displacement during a specific segment of the scratch (i.e. changing lateral position). Since this is an engineering sample, these flat regions would be extremely rare, if occurring at all, thus indicating that the tip has lost contact with the surface. At these points, the tip is 'floating' in air and maintaining a constant normal displacement. As the surface rises and the tip comes into contact with a peak, the tip once again begins tracking the actual surface profile. The actual scratch was performed under a higher normal load, and thus more correctly maps the actual surface profile, although surface deformation occurs due to the high load (see Figure 93).

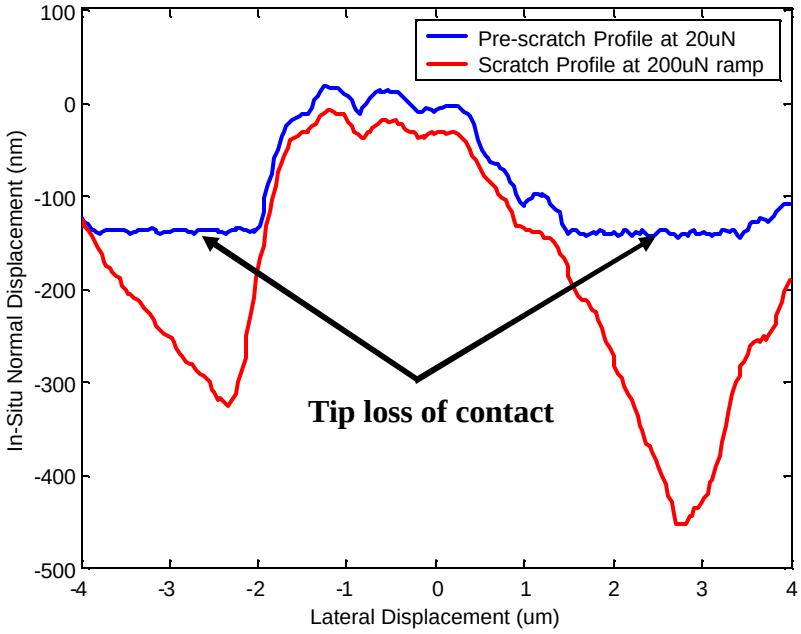

Figure 93: Pre-scratch and scratch profile; tip loss of contact during pre-scratch scan

There are two solutions to ensure that the tip maintains contact with the surface during the scan. Either the set point (i.e. the normal load applied to the tip to maintain contact with the surface), or the pre-scan load should be increased appropriately. The set point was increased to 8 µN from 2 µN, while the pre-scan of the surface profile was performed at 20 µN normal load. For fused quartz and silicon surfaces, a 6 µN set point and a 0 µN scan load was adequate. Figure 94 illustrates correct scan and scratch profiles, showing that the tip maintains contact with the surface during the entire scan length.

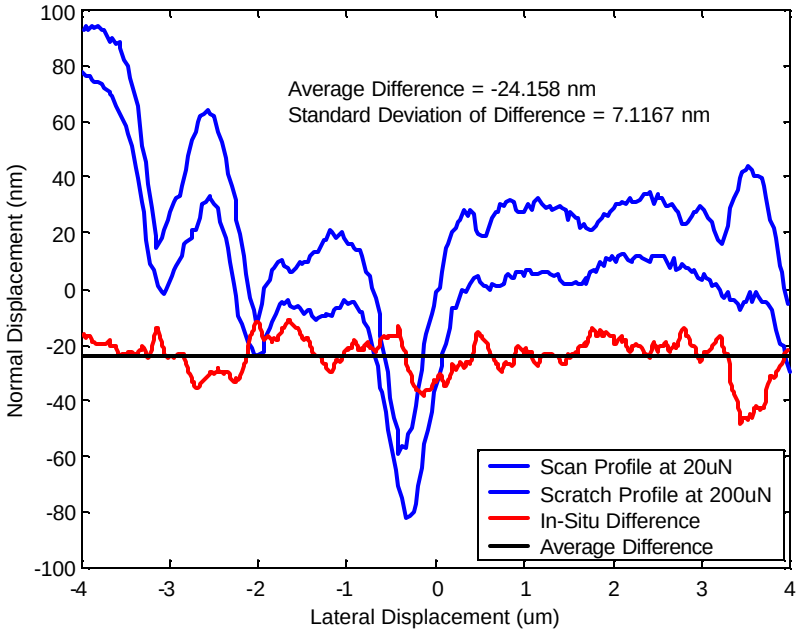

Figure 94: Pre-scratch scan and scratch profile with set point = 8 µN, scan load = 20 µN

By incorporating a low pre-scratch surface scan load of 20 µN, one must determine if this load is sufficient to cause permanent plastic deformation of the surface, thus altering the surface prior to the scratch, as well as the results. Based on Hertzian analysis (assuming a 1 µm tip radius, an average asperity radius of 10 µm (see Patel), E* = 80 GPa, W = 8 µN + 20 µN), the maximum contact pressure due to the scan is approximately 3.5 GPa. Based on the conclusions drawn from the nano-indentation results, this is less than the surface hardness, and thus, will not cause plastic deformation of the surface. Further support for the chosen pre-scan load is that this load causes an *in-situ* normal displacement of 4-5 nm, which is relatively small when compared to the maximum scratch depths that one is interested in (i.e. 20 – 200 nm). Upon releasing the load, it is observed that the material fully recovers elastically, thus indicating no permanent surface deformation.

5.6 Constant Force Scratches

Constant force scratches apply a constant normal load to the scratch tip, while laterally scratching the tip over a prescribed path. Often, they are used to obtain qualitative data for comparing the relative resistance to deformation of different films, under the same normal load. By using a set normal load, and executing the same scratch profile on different samples, qualitative analysis can be performed on the depth of the penetration, which can, in-turn, be used to study the relative hardness of the films.

Three typical constant force scratch profiles are shown below in Figure 95 through Figure 97. The first is appropriate for scratches on very smooth surfaces where the roughness is relatively negligible. Thus, only the *in-situ* profile of this scratch is studied. The profiles in Figure 96 and Figure 97 incorporate a pre-scan of the surface profile under low load (20 µN). This pre-scan surface profile can be removed from the scratch data in order to analyze the scratch depth, independent of the sample roughness and tilt. The profile shown in Figure 96 is used on

the fused quartz, silicon and engineering surfaces examined later. The 3rd profile has the added benefit of a low load scan (20 μN) of the residual surface profile, and may aid in the analysis of elastic recovery (discussed later) of the scratched section. This profile was not used in this project, but would be beneficial to include in later tests. The scratch profile is the same for all scratches (pre- and post- scratch scans use the same profile under a lower load), and is composed of 7 different segments (see Figure 95):

1.) Laterally traverse from center of image position to negative lateral limit under zero normal force (4 seconds)
2.) Maintain constant lateral position and ramp up normal load to desired value (5 seconds)
3.) Obtain steady state conditions of normal force and lateral displacement (3 seconds)
4.) Scratch sample – laterally traverse tip from negative lateral displacement limit to positive lateral displacement limit under a constant normal load (30 seconds)
5.) Obtain steady state conditions of normal force and lateral displacement at the end of the scratch (3 seconds)
6.) Linearly decrease normal load to zero at a constant lateral position (5 seconds)
7.) Laterally traverse from positive lateral displacement scratch limit to center of image position under zero normal load (4 seconds)

The pre/post scratches use the same scratch profile (7 segments) described above, but use a smaller normal load.

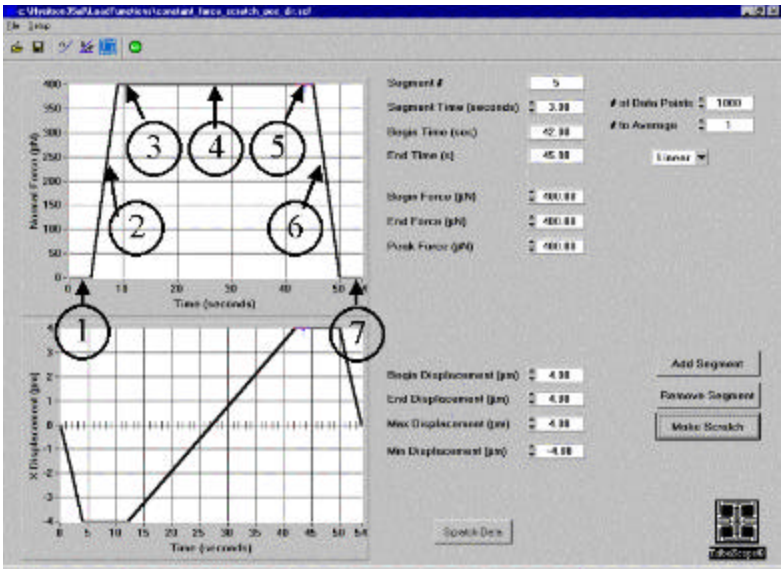

Figure 95: Constant force scratch profile

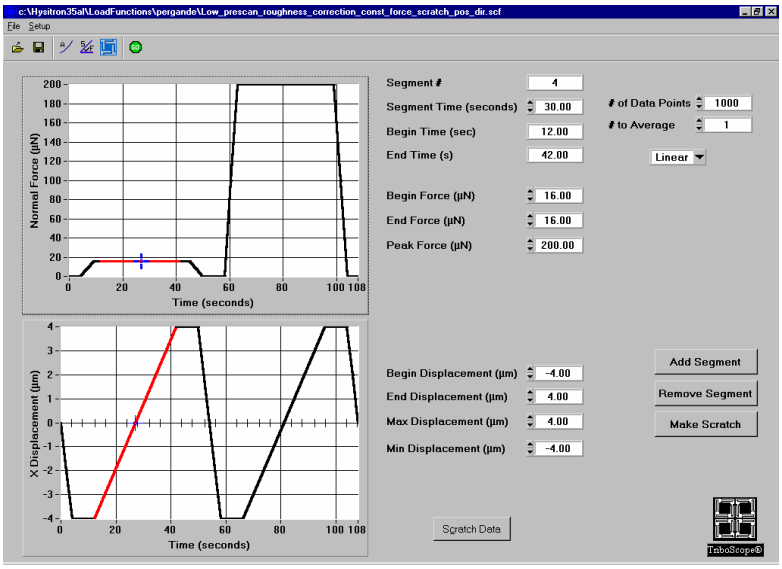

Figure 96: Constant force scratch profile with a 20 µN pre-scan load; test profile

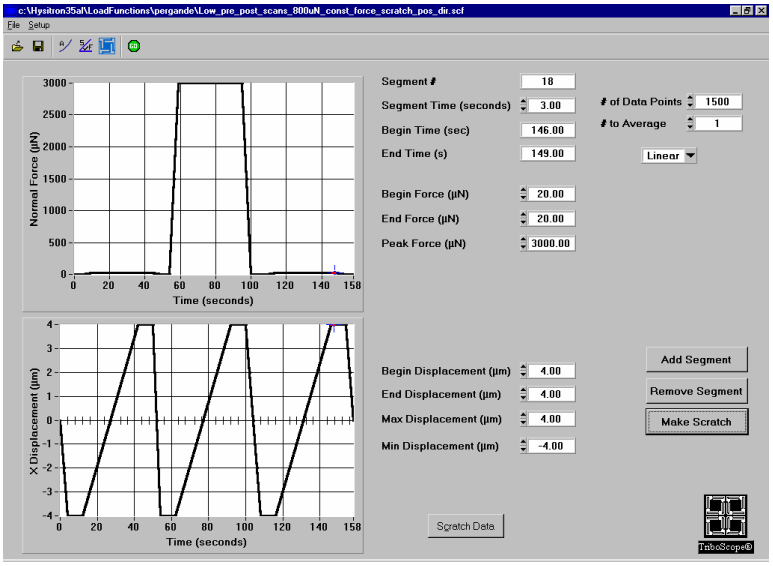

Figure 97: Constant load scratch with a 20 µN pre-scan and post-can load

5.6.1 Fused Quartz Results

Fused quartz is a standard test material used to verify the scratch procedure, as well as to obtain results that can subsequently be compared to for other samples. It is a consistent material (no surface oxide layers) with consistent material properties, independent of depth. It is also a relatively smooth sample, with an average roughness of R_a < 5 nm. Thus, fused quartz serves as an excellent test material that minimizes many of the difficulties associated with engineering samples. Several scratches on fused quartz are shown below in Figure 98. All four scratches were performed with a blunted 90° cube corner tip. The left two scratches correspond to scratches made under a constant load of 1000 µN, while the right two were made under a constant load of 400 µN. Note the

consistency along the length of all the scratches, in both the width and the depth of the residual scratch. These scratches typical of those performed on an ideal surface.

Figure 99 is a close-up of one of the 1000 µN scratches. Using a section analysis, the corresponding residual scratch width and depth can be determined (see Figure 100 below). The residual scratch width, measured from the inflection point of the scratch profile (see Kral et al), is approximately 336 nm, while the residual scratch depth is 41 nm.

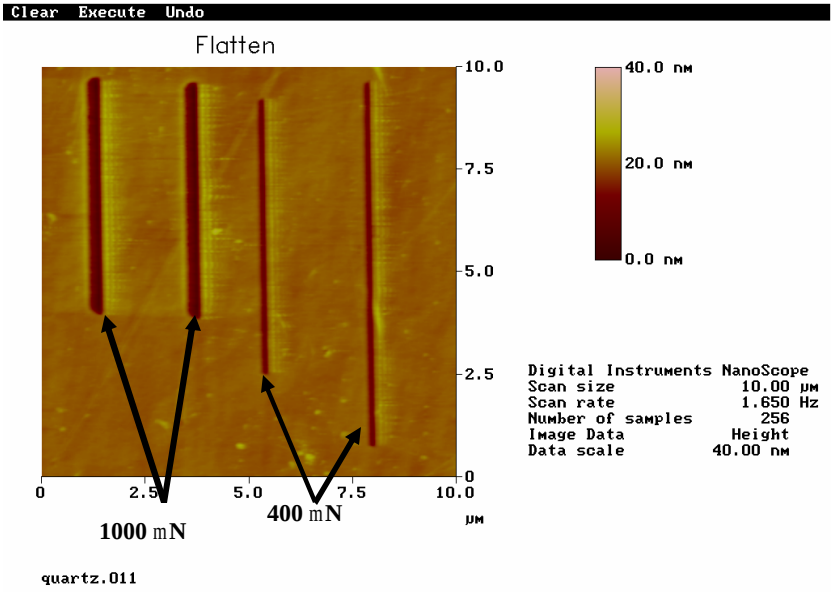

Figure 98: 1000 µN and 400 µN constant force scratches on Fused Quartz

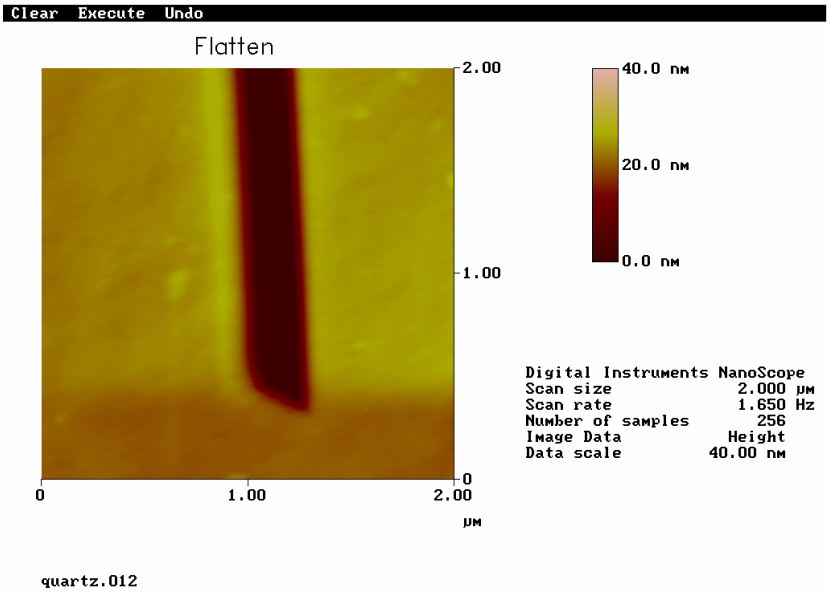

Figure 99: 1000 µN constant force scratch on Fused Quartz

Shown in Figure 101 is the *in-situ* load and displacement data for both the normal and the lateral direction, during one of the 1000 µN scratches discussed prior. Examining the normal displacement plot (upper right), one can see that even though the normal load (upper left) is zero (time of 0-4 seconds), there is normal displacement. This is due to a tilt of the sample, and has a value of approximately 7.5 nm over a 1 µm lateral length. By removing the tilt from all displacement data, an accurate displacement profile, as if the scratch was from a 'flat' sample, can be obtained. Note that this 'tilt correction' affects only the normal displacement depth data. The adjusted plots are shown in Figure 102. The slight dip in normal displacement (upper right) as the scratch begins is attributed to an increased maximum stress observed by the sample due to the combination of normal and lateral force.

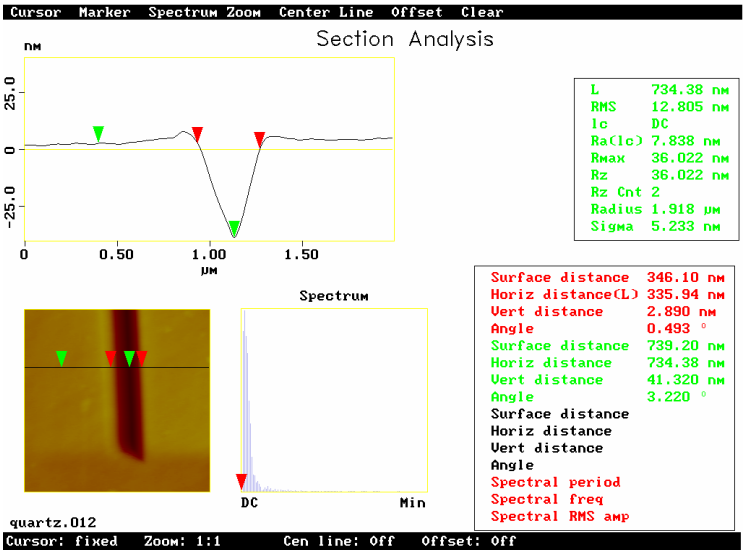

Figure 100: Residual scratch profile; 1000 µN constant force scratch; Fused Quartz

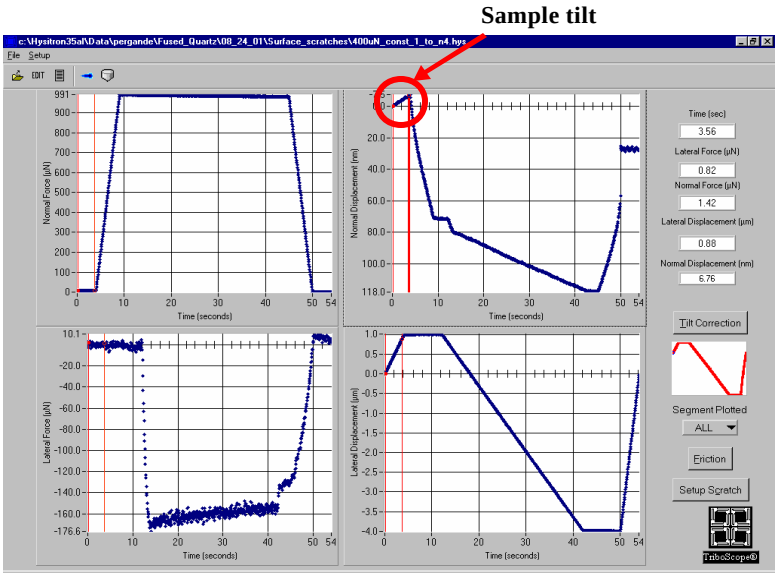

Figure 101: Raw data from a 1000 µN, constant force scratch on Fused Quartz

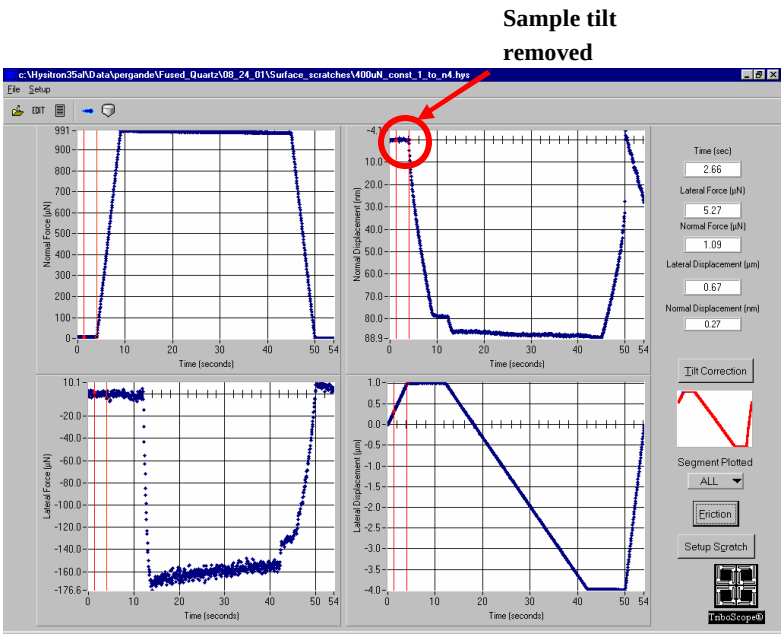

Figure 102: Constant force, 1000 µN scratch on Fused Quartz with tilt correction

The friction coefficient (labeled as LF/NF in Hysitron software) is defined as the *in-situ* lateral force normalized by the *in-situ* normal force. The Hysitron plot of *in-situ* friction is displayed in Figure 103 below.

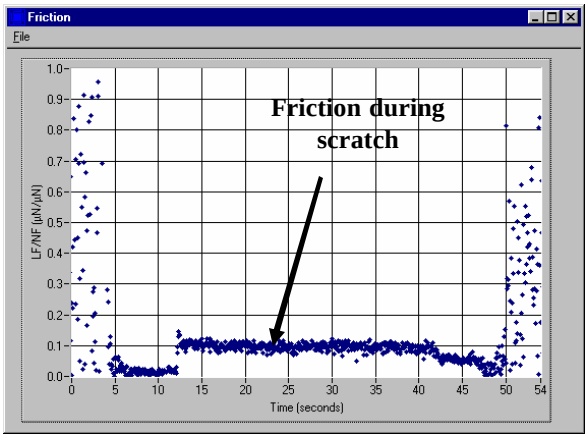

Figure 103: Friction coefficient on Fused Quartz

Based on the measurements of lateral force and friction coefficient obtained from the software, combined with the measurements of residual scratch width and depth, the material hardness of these scratches is calculated according to the procedure outlined in Section 5.3. The hardness calculations are highly dependent on the spherical nature of the tip (which is not always the case). Constant force scratch profiling was used to obtain more qualitative data.

Several experiments on fused quartz were performed using the 60°, 1µm radius conical tip, under a constant normal load, and the results are discussed below. All scratches were 8 µm long. Since the surface roughness is negligible compared to the depth of the scratches, a pre-scan of the scratch surface was not needed (but was incorporated anyway for consistency purposes). The constant load scratch profile in Figure 96 was used, with varying peak loads from 750 µN to 6000 µN. Figure 104 illustrates the normal load as a function of lateral displacement for these scratches. Note that the load is constant throughout the length of the scratch.

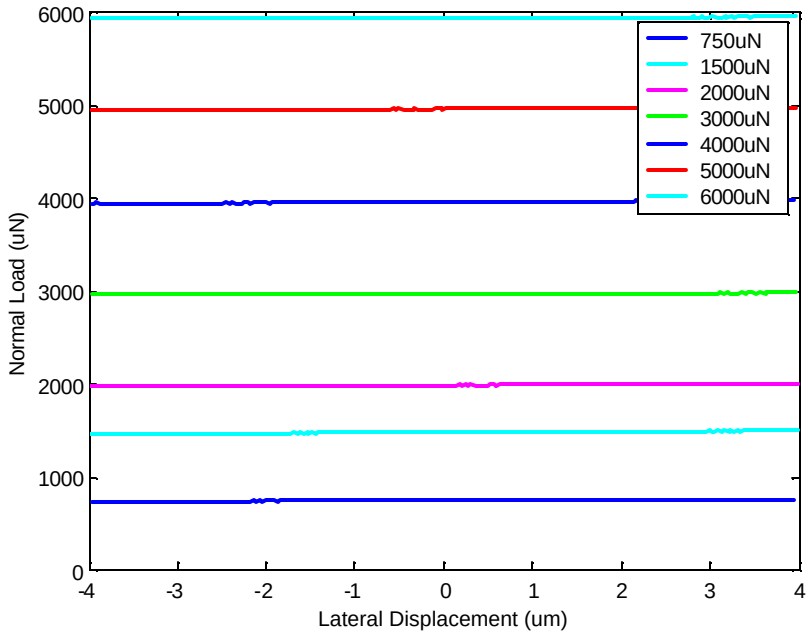

Figure 104: Several constant load scratches on fused quartz; 60°, 1 µm radius conical tip

The *in-situ* normal displacement as a function of lateral displacement is depicted in Figure 105. As expected, the normal displacement increases with increasing normal force. Note that for low load scratches (i.e. 750 µN), a steady state depth is reached almost immediately, while for larger loads (i.e. 6000 µN), steady state scratch depth is reached after 0.5-1 µm of scratch length. At the start of the scratch (i.e. lateral displacement = -4 µm), the maximum stress on the sample is due to only the presence of a normal load. When the scratch is initiated, the maximum stress on the sample is increased because a lateral force component is added, in combination with the normal force. Due to the increased maximum stress, more material yields, and the tip penetrates further into the sample. These effects are magnified for larger forces. Also, the fact that a steady state value is reached indicates the homogeneous nature of the material, as expected. There is a low standard deviation of the depth once the steady state value is reached, and scratches are extremely repeatable.

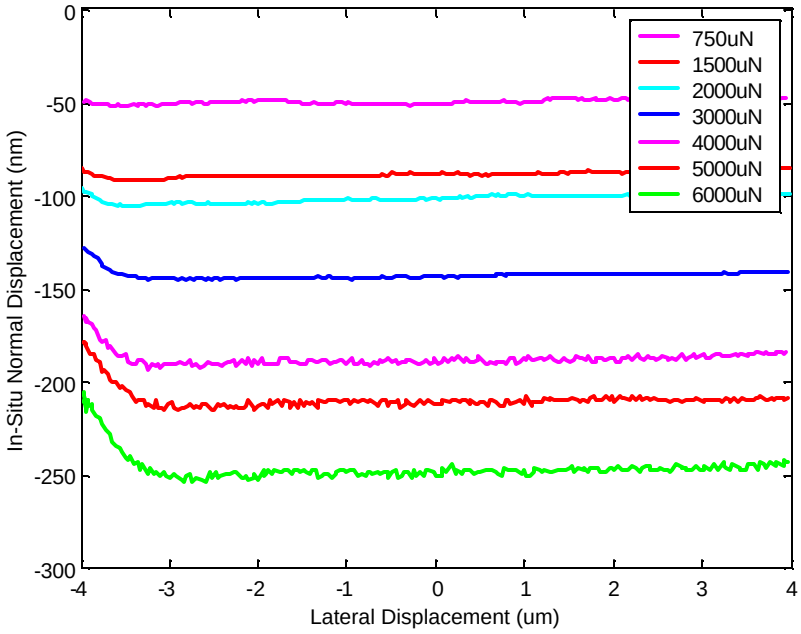

Figure 105: Several constant load scratches on fused quartz; 60°, 1 µm radius conical tip

The steady state in-situ normal displacement as a function of normal load is illustrated in Figure 106. There are no bursts in normal displacement as a function of normal load, therefore no surface layers are seen (which is expected).

Figure 107 plots friction coefficient versus lateral displacement for those constant force scratches discussed earlier. Besides the different amount of time to reach steady state, there are two main differences between the curves. As the normal load is increased, the friction coefficient increases. Also, the scatter in the data is greater for lower normal loads, up to a point. Beyond a certain depth, it is hypothesized that there are inconsistencies due to the shearing component of the tip. The normal load is controlled via a feedback loop, and is thus relatively constant throughout the scratch. The differences lie in the measurement of the lateral force, which is the resistance of the material to the plowing of the tip. At high normal loads, the normal penetration is great, and the lateral force is directly related to the area of the tip involved in 'plowing' the sample. At these large penetrations, the roughness is negligible and this 'plowing' area dominates, and is relatively unaffected by the roughness of the sample. As the normal load is decreased, and the penetration decreases, the area of the plower also decreases. Since the lateral force for low normal load scratches is relatively small, the lateral force can vary greatly, depending on the roughness of the sample (i.e. contact with peak face, valley edge, etc.).

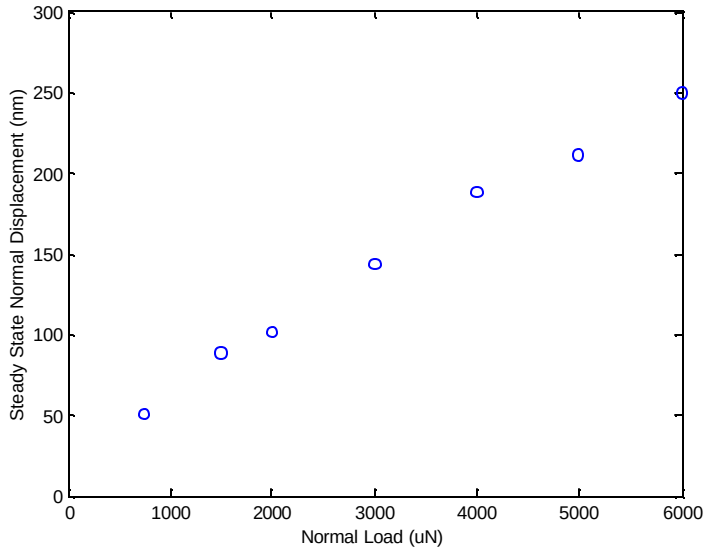

Figure 106: Steady state normal displacement; Fused Quartz; 60°, 1 µm radius conical tip

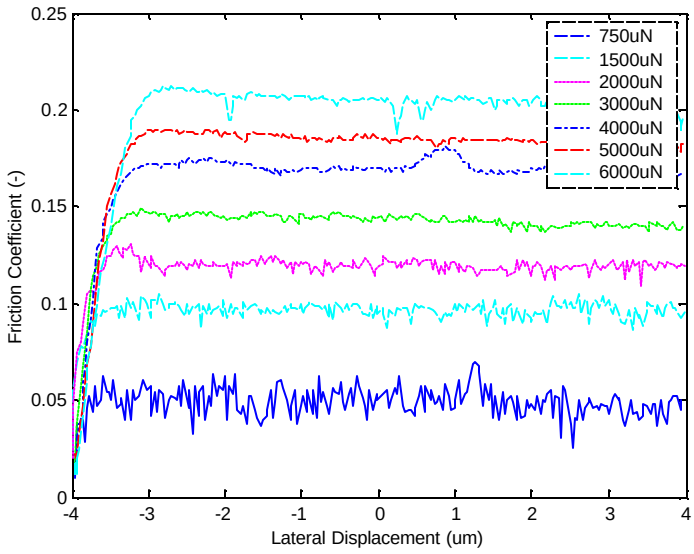

Figure 107: Friction coefficient; Fused Quartz; 60°, 1 µm radius conical tip

The steady state friction coefficient values for these scratches are shown in Figure 108.

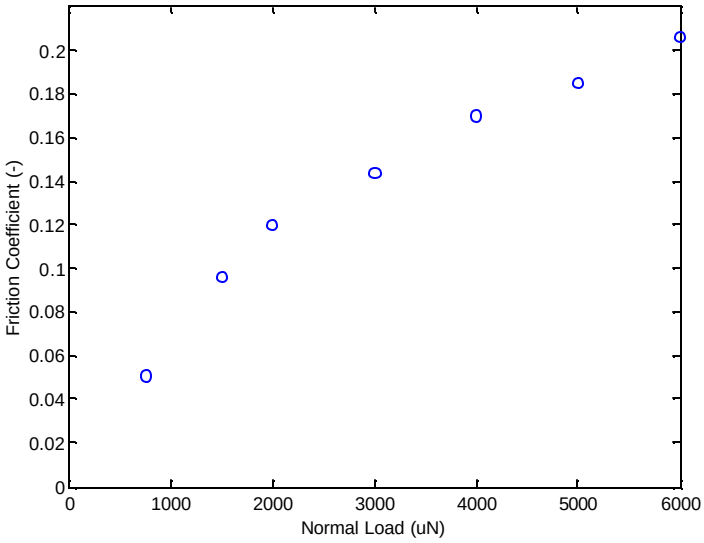

Figure 108: Average friction coefficient; Fused Quartz, 60°, 1 µm radius conical tip

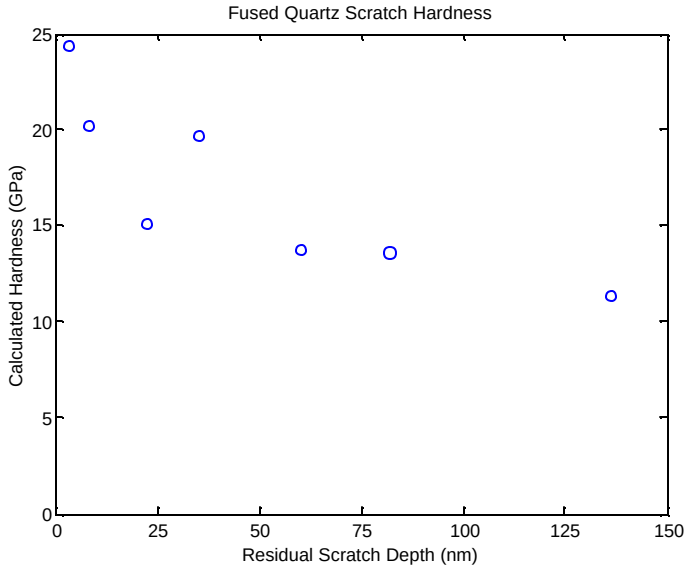

Figure 109: Scratch hardness profile, Fused Quartz

Residual scratch profiles have been analyzed, and, in combination with in-situ scratch data, the material hardness has been calculated (based on the equations presented in Section 5.3). The results are shown below in Figure 109. Since these scratches were performed on fused quartz, a constant hardness of approximately 9.6 GPa should be measured, independent of the depth of the measurement. One can see that the calculated material hardness is highly dependent on the depth of the scratch, and is much higher for low depths.

The hardness equations developed by Kral et al, rely on the fact that the plowing tip is spherical in profile. Since the material hardness is directly related to the projected area of the plower, precise knowledge of this area is needed. Examine the SEM image of a tip shown in Figure 110.

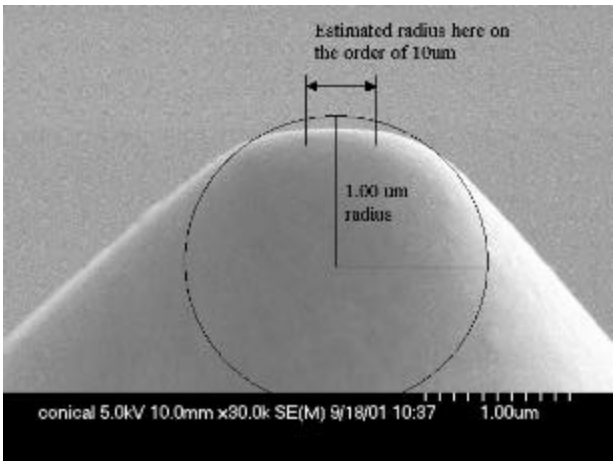

Figure 110: Nano-scratch tip; SEM image; this is not an image of the tip used in tests

From the figure, one can determine that the tip has a non-uniform radius; i.e. a flat tip gently rounded up towards the base. Thus, there is no simple equation to model the projected area of the plowing tip. The only way to obtain a projected area profile is through curve fitting in a calibration procedure, which does not currently exist. By having a flat on the end, the radius on the end is much greater than the overall tip radius. Also, the effective radius (given by Equation (13)) changes as a function of the depth of the scratch. See Figure 111. Ideally, the effective radius should be a constant, and approximately equal to 1 μm. Since w >> h in Equation (2), a lower residual scratch depth will cause the effective radius to greatly increase, thus greatly increasing the calculated material hardness. Because of the inconsistent results observed, as well as other difficulties associated with the calculated scratch hardness, the hardness calculations are not used for further analysis.

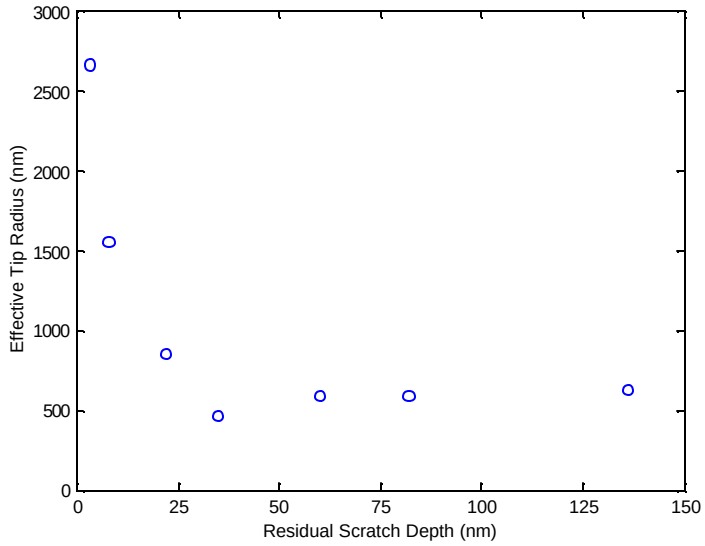

Figure 111: Calculated effective tip radius at the 60°, 1 μm radius conical tip

5.6.2 Silicon (111) Results

Silicon provides another opportunity to further understand the scratch test and interpret results. Silicon is a relatively hard material, with known bulk properties. The bulk hardness is approximately 12.2 GPa, while it's elastic modulus is approximately 150 GPa. A thin oxide layer is present on the top 4-5 nm, while the rest of the material is homogeneous. The sample is also extremely smooth, with an R_a of approximately 1-2 nm (measured on a 10 x 10 μm size).

Included below is the *in situ* data as a function of time (Figure 112 and Figure 113) from a 300 μN constant force scratch with the blunted 90° cube corner tip. The normal displacement and friction coefficient are relatively constant, as expected for a smooth material with a relatively homogeneous structure.

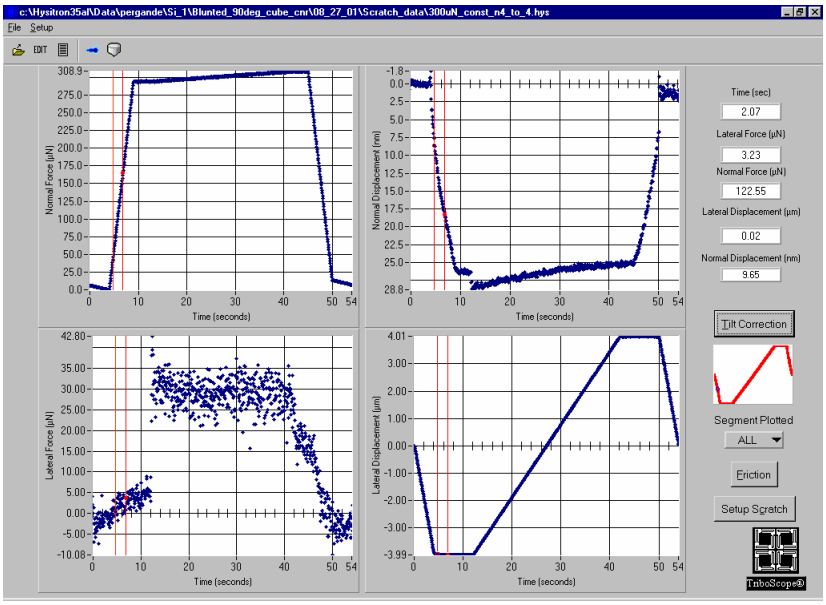

Figure 112: Tilt corrected data from a 300 μN constant force scratch on Silicon

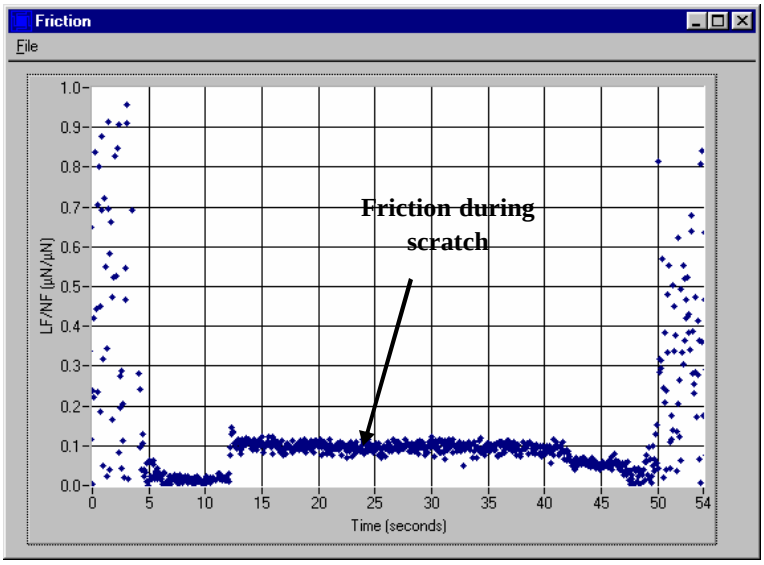

Figure 113: Friction data from a 300 μN constant force scratch on Silicon

The residual scratch profile from the same scratch is shown below in Figure 114, with corresponding scratch cross-section analysis shown in Figure 115.

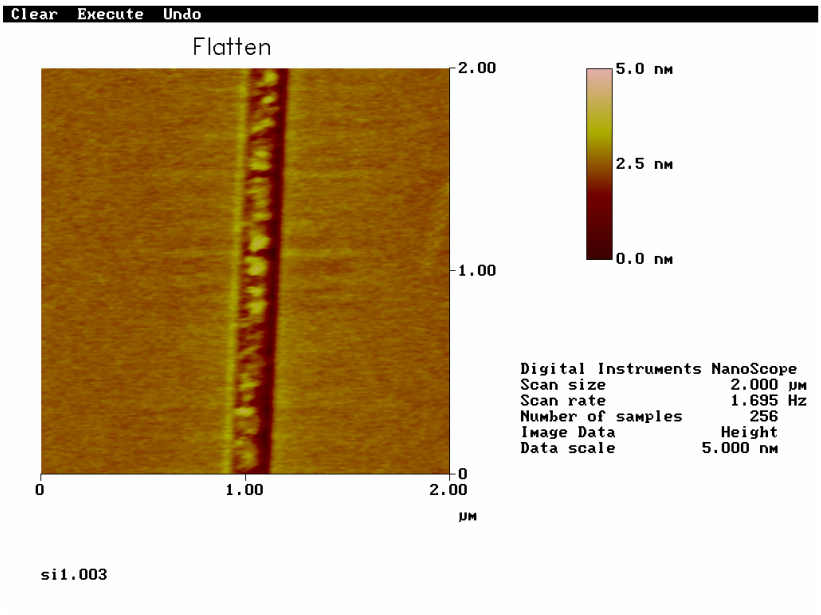

Figure 114: 300 µN constant force scratch on Silicon, residual image

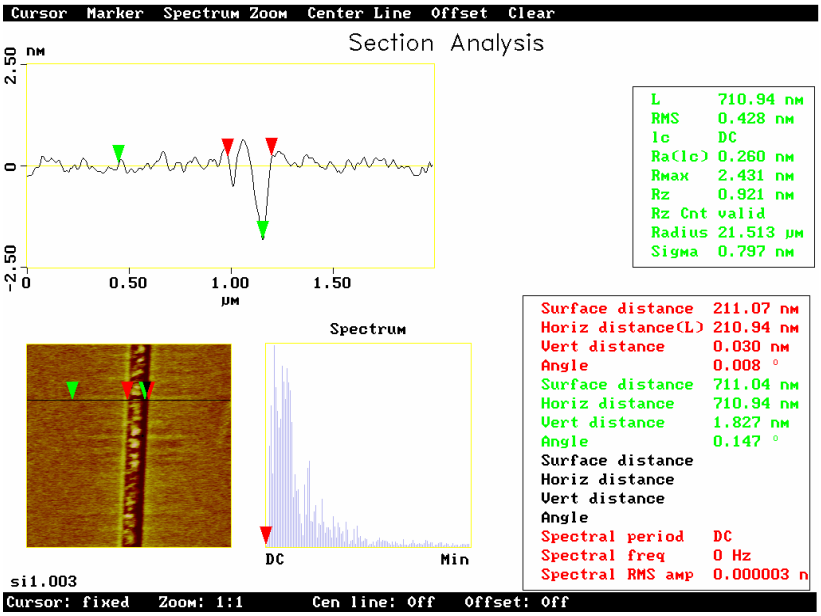

Figure 115: Scratch cross-section profile of a 300 µN constant force scratch on Silicon

Examining these images, they appear to be non-uniform scratches. There are a few possibilities for this effect: (a) the material is bonding to the tip, which would cause poor image quality; (b) that there was some sort of material transfer, and that some of this material was left behind in the residual scratch profile; (c) perhaps the most reasonable explanation is that silicon is an extremely brittle material, and thus, subject to non-uniform deformation

of the surface in contact with the tip. Nonetheless, the *in-situ* normal displacement and lateral force data (Figure 112) are very consistent and relatively independent of the lateral displacement. Thus, the measured data is accurate.

Several experiments on silicon were performed using the 60°, 1 μm radius conical tip, under a constant normal load, and the results are discussed below. Scratches were either 6 or 8 μm in length. Since the surface roughness is negligible compared to the depth of the scratches, a pre-scan of the scratch surface was not needed, however, it was incorporated anyway for consistency purposes. The constant load scratch profile in Figure 96 was used, with varying peak loads from 1000 μN to 5000 μN. The *in-situ* normal displacement as a function of lateral displacement is shown below in Figure 116. As expected, the depth of penetration (normal displacement) increases with increasing normal force. After examination of the residual scratches, it is observed that the two scratches at 1000 and 2000 μN normal loads, exhibit very little permanent plastic deformation. Note that for low normal loads (1000 μN), a steady state normal displacement is reached as soon as the scratch is started. While, for larger normal loads, a steady state normal displacement is reached after 0.5 – 1 μm lateral displacement. This trend was also exhibited by the fused quartz testing. The data for each scratch is very consistent, with small variations in normal displacement as a function of lateral displacement. This occurs because of the consistency of the material and it's relatively smooth surface.

The steady state *in-situ* normal displacement as a function of normal load is illustrated in Figure 117. Looking at the graph, there are definitely two different regimes present. The data indicates that there is a definite change between normal loads of 2000 and 3000 μN, as indicated by a change in slope of the graph. At this point, delamination of the 4-5 nm oxide layer occurs, and the bulk material is reached. Since the bulk material is softer than the oxide layer, the normal displacement increases at a faster rate once the oxide layer is penetrated (note the greater slope beyond 3000 μN). The delamination occurs at a normal displacement between 35 and 55 nm, which is much greater than the thickness of the oxide layer of 4-5 nm. This is because the radius of the tip is relatively large (~1 μm), and the bulk material is contained elastically by the oxide layer. Once delamination occurs, the protective oxide coating is no longer present to resist deformation, and normal displacement occurs at a faster rate.

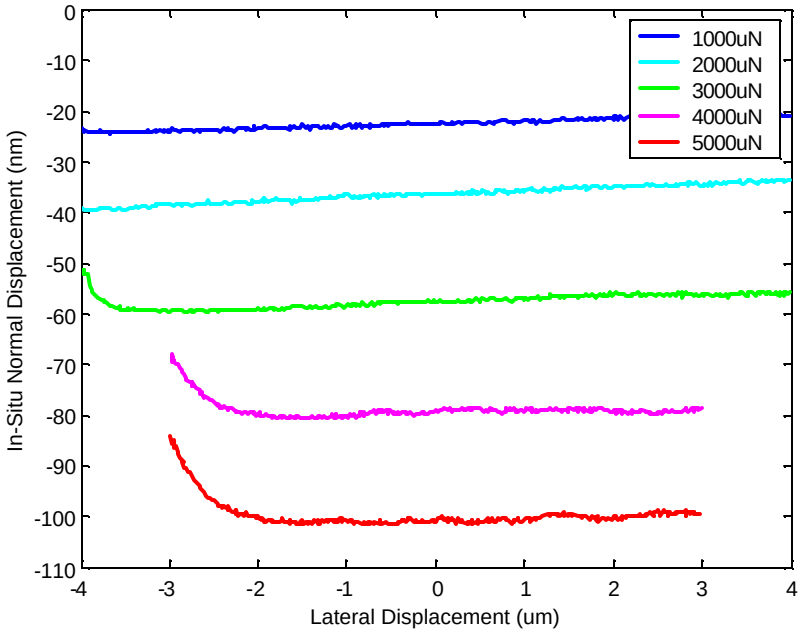

Figure 116: Constant force scratches on Silicon; 60°, 1 µm radius conical tip

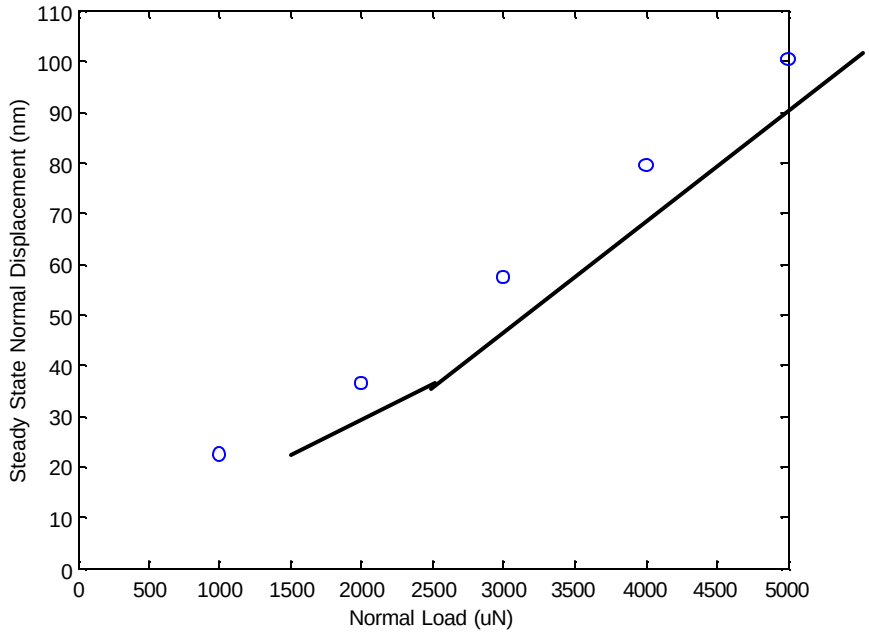

Figure 117: Steady state normal displacement as a function of constant normal load

Figure 118 illustrates the coefficient of friction for these same scratches on silicon. The two cases for which the normal load is 1000 and 2000 µN respectively, yield some interesting conclusions. By increasing the normal load, the spread in the data is reduced, but the coefficient of friction does not increase. The decrease in the

spread of the data has also been verified by the fused quartz tests, but the lack of increase in the friction coefficient is unexplained. In the previous discussion, it was noted that delamination of the oxide layer occurred between the loads of 2000 and 3000 μN. Thus, for both of these cases, the oxide layer is not penetrated. The presence of this protective oxide layer seems to result in a low, relatively constant coefficient of friction. For the normal load cases of 3000, 4000, and 5000 μN, the oxide layer is penetrated, and the coefficient of friction is much higher. The cases in which the oxide layer is penetrated have similar to the fused quartz tests, where increasing the normal load increases the coefficient of friction. This is a good model for single asperity contact. For the case in which the normal load is 5000 μN, the coefficient of friction is somewhat oscillatory. This indicates significant plastic deformation and brittle behavior.

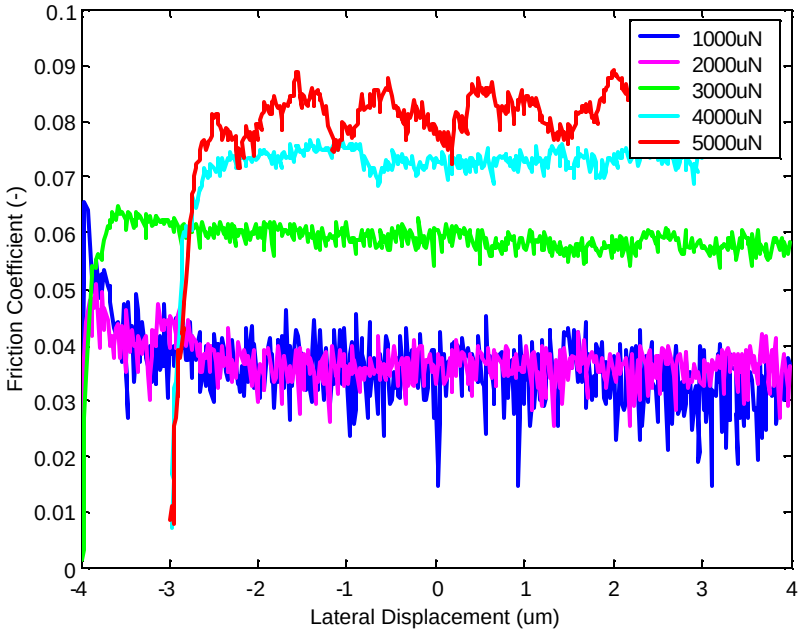

Figure 118: Friction coefficient of several constant force scratches on silicon

Figure 119 illustrates the steady state friction coefficient as a function of the normal load.

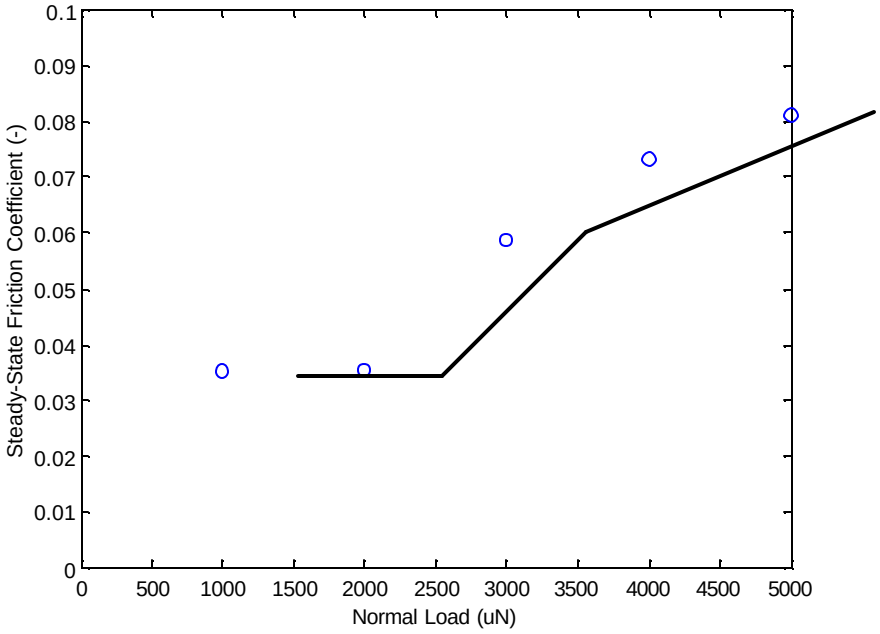

Figure 119: Steady-state friction coefficient for several constant force scratches on silicon

5.6.3 Al390-T6 Results

The Aluminum test samples incorporate some unique challenges in the application of nano-scratch. First, the samples are from engineering surfaces, and thus possess higher roughness than typical "scratch" surfaces. A typical sample may have R_a values of the order of 200 or 300 nm. Second, the surfaces contain multiple, non-uniform surface layers, whose properties are not usually known. As the surface proceeds through the wearing process, these layers may be non-uniformly altered, making the analysis even more difficult. Finally, the aluminum alloy is a non-homogeneous material with many different alloying elements and grain structures. Silicon particles, etc have been identified through microstructure analysis, and confirmed to affect mechanical properties through nano-indentation experiments. These difficulties will be examined in hopes of determining an accurate and repeatable method for determination of relative layer thicknesses and mechanical properties of the samples.

Nano-scratch tests on the aluminum alloy are performed in much the same method as on fused quartz and silicon. A pre-scan of the surface is required in order to obtain a surface reference from which the scratch data will be analyzed. The pre-scan load is 20 μN, with the corresponding scratch profile illustrated in Figure 96. All scratches are 8 μm in length, while the maximum load is varied with each scratch. Constant load scratches of 200 μN and 800 μN were examined for these tests, using the 60°, 1 μm radius conical tip. In order to obtain an appropriate sample average, scratches were performed on an area at least 1-2 mm away from other scratches at the same normal load.

5.6.3.1 Virgin Results

Figure 120 shows an 8 μm by 8 μm topographical pre-scan image of a virgin Al390-T6 surface. Note that the vertical peak to valley scale is 230 nm, whereas for silicon and fused quartz, it was 5 and 15 nm, respectively. Shown in Figure 121 and Figure 122 are two post-scan images of that same surface after a 200 μN constant load

scratch, using a blunted 90° cube corner tip. The corresponding cross-section profile is shown in Figure 123. The scratch location can be vaguely pin-pointed, although it is somewhat difficult to locate due to the extreme roughness of the surface. From the analysis, it is estimated that the residual scratch width and residual scratch depth are approximately 338 nm and 43 nm, respectively, although there is a great deal of variability in the residual scratch profile.

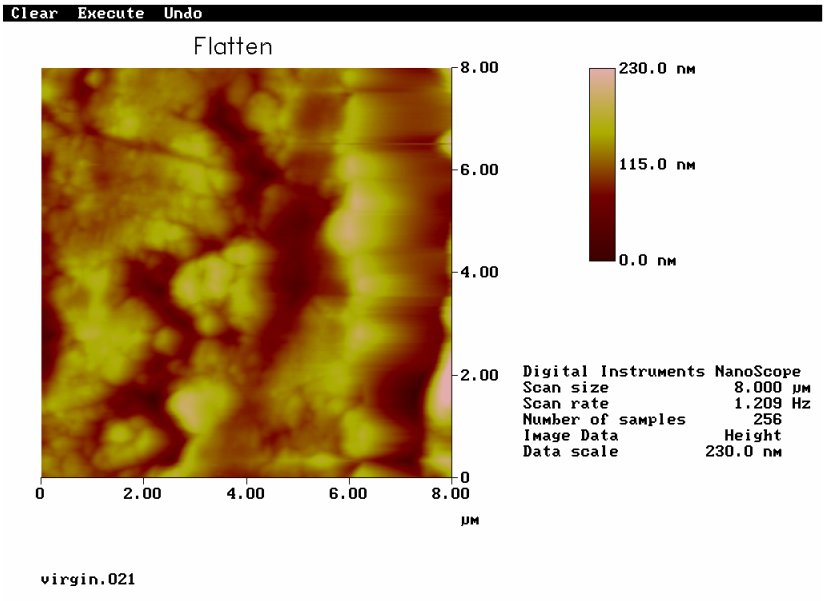

Figure 120: Pre-scan of virgin aluminum surface; 8 µm x 8 µm

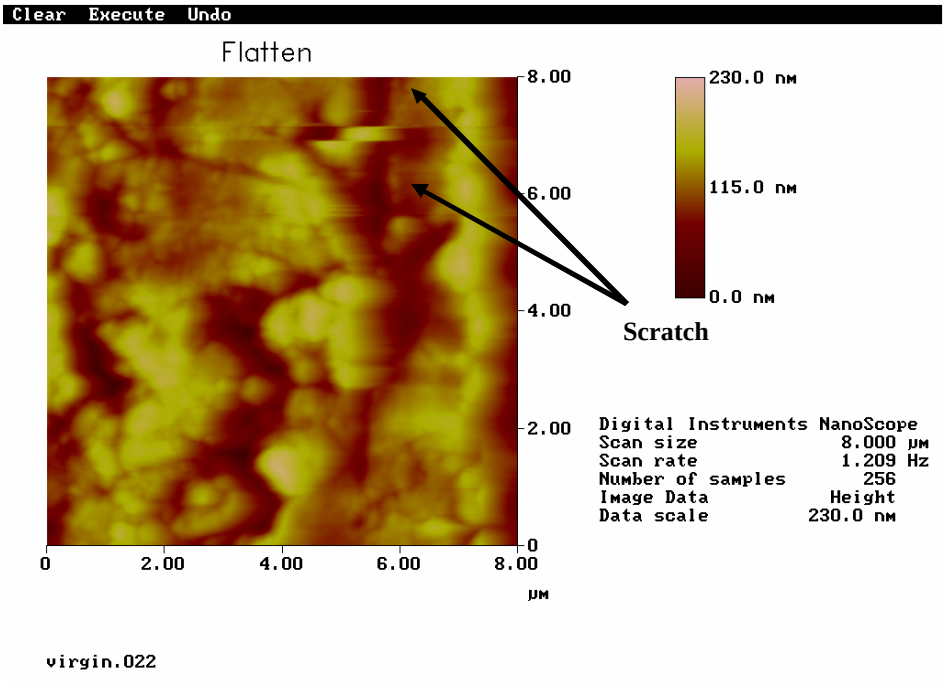

Figure 121: Virgin surface, post-scratch image of 200 µN scratch; 8 µm x 8 µm

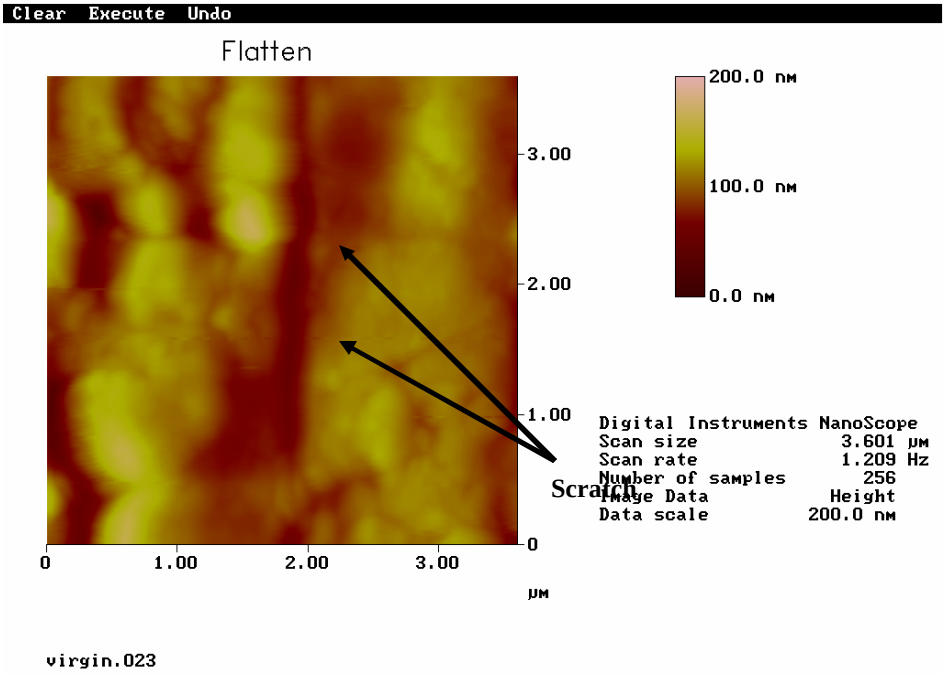

Figure 122: Virgin surface, post-scratch image of 200 µN scratch; zoomed in

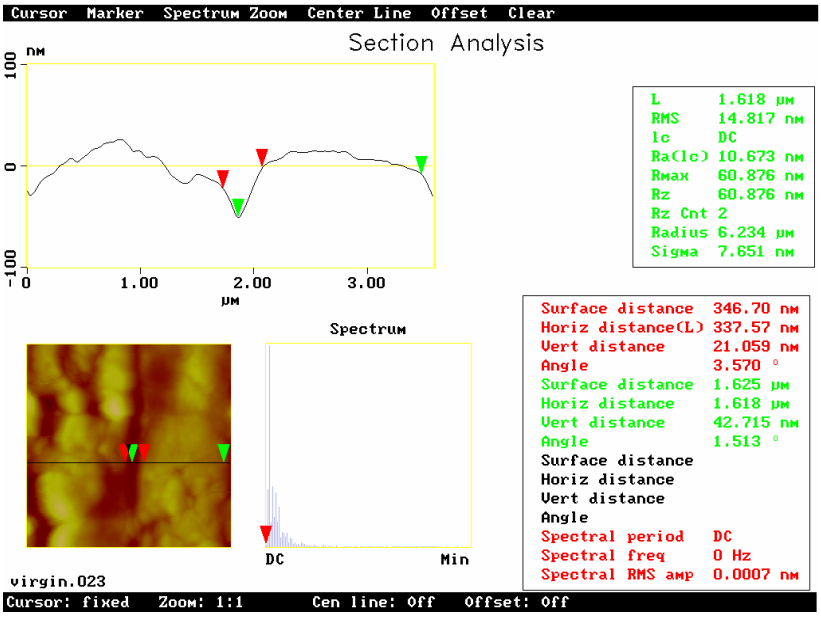

Figure 123: Section analysis of 200 µN scratch on virgin aluminum

The analysis below examines 8 µm length scratches made with the 60°, 1 µm radius conical tip, under constant loads of 200 and 800 µN. The scratch profile (Figure 96) incorporates a pre-scratch scan of the surface to aid in the analysis. Figure 124 illustrates the *in-situ* normal displacement versus lateral displacement of one of the 200 µN constant load scratches. The top line in the figure corresponds to the pre-scan of the surface under a low,

20 µN load. This pre-scan maps the original surface profile. The scratch profile under a 200 µN normal load is shown directly below (Figure 124). From the two profiles shown, the scratch profile roughly follows the same profile as that obtained from the pre-scan under a low load. The difference between the pre-scan and the scratch profile is the amount of elastic/plastic deformation of the surface under the load applied to the tip. Thus, the surface roughness can be factored out of the data in order to examine the scratch as if it was performed on an ideally flat sample. The point-by-point difference, as well as the average difference, are both shown. These differences use the pre-scratch scan displacement as a zero reference, and base all calculations from this original profile. The standard deviation refers to the standard deviation of the difference from the average difference. This scratch has an average *in-situ* penetration of 24 nm, with a standard deviation of 7.1 nm. Figure 125 is a similar graph for the virgin Al390-T6 surface, but with a larger normal load of 800 µN. As expected, the normal penetration is larger under a larger normal load. For this scratch, the average depth of penetration is 84 nm, with a standard deviation of 13.6 nm. The standard deviation in the depth of an individual scratch is relatively small in both cases. This data is comparable to that obtained from the fused quartz and silicon tests discussed prior. The standard deviation of the virgin sample is slightly higher, but consistent with the standard materials, thus indicating a relatively consistent material in close proximity of the scratch.

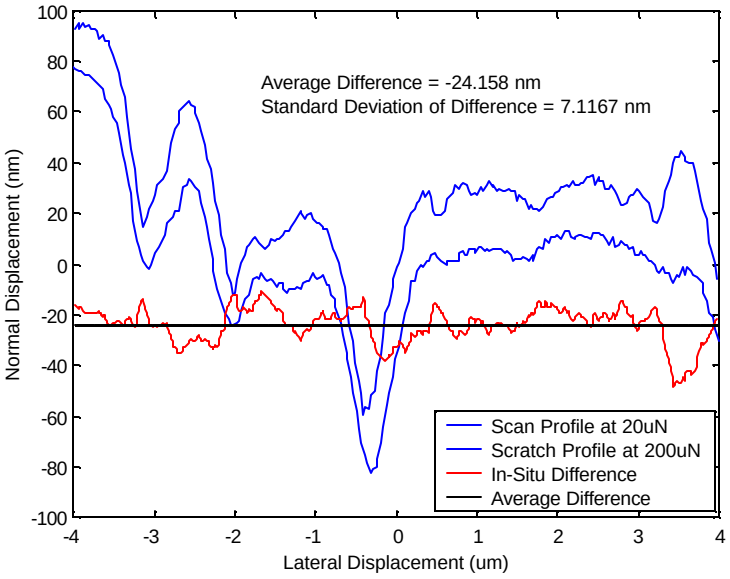

Figure 124: 8 µm scratch on Virgin surface; 200 µN constant load

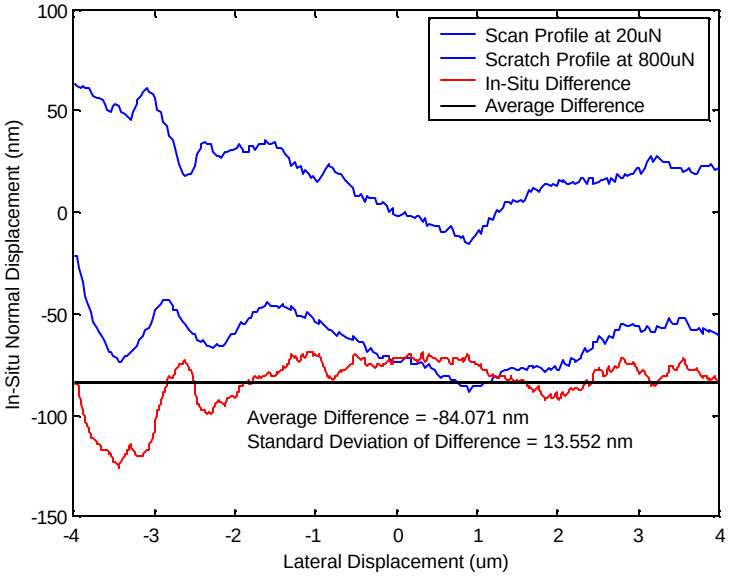

Figure 125: 8 µm scratch on Virgin surface; 800 µN constant load

Figure 126 shows the results from Figure 124 and Figure 125 in combination with several more experiments, and illustrates the average normal penetration of the tip for different constant load scratches (200 µN and 800 µN). Once again, the normal penetration increases with increasing normal load. This trend is expected, and has been shown in both the fused quartz and the silicon tests discussed prior. The standard deviation (standard deviation in reference to the average penetration depth of different scratches) between 200 µN scratches is small (3.33 nm), as well as the standard deviation between 800 µN scratches (6.67 nm). This, combined with the fact that there is a relatively insignificant amount of variation within a single scratch, leads to the conclusion that the virgin surface is relatively consistent throughout the surface (not to be confused with consistent properties as a function of depth). By repeating these scratches at a wide variety of loads, it would be possible to gain a better understanding of layer thicknesses, as in the case with silicon (see Section 5.6.2). This will be further examined in the analysis of the ramp load profile discussed in Section 5.7.

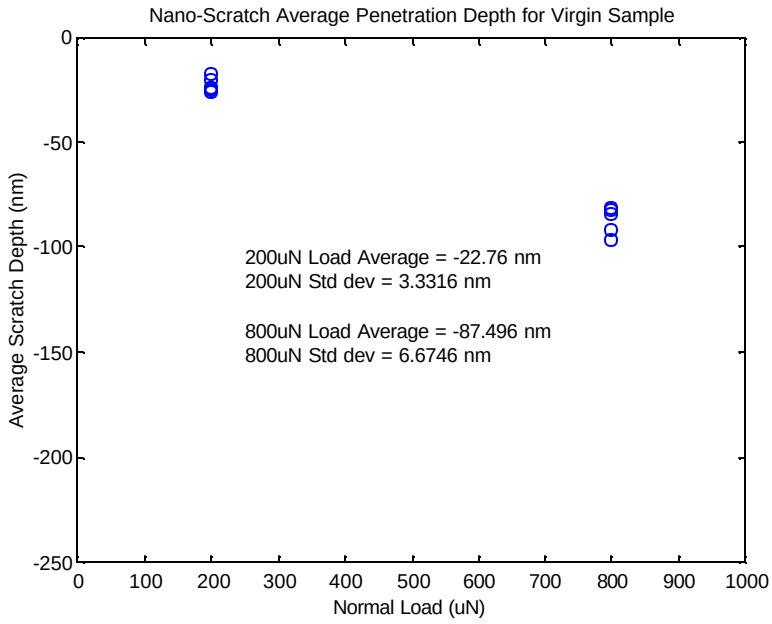

Figure 126: Normal penetration of 8 µm scratches on virgin surface

Figure 127 illustrates the coefficient of friction measured during the scratch of both a 200 µN and an 800 µN constant load scratch. The 200 µN scratch has a significantly lower average coefficient of friction (µ ~ 0.10), but significantly more scatter associated with it. The 800 µN scratch exhibits a higher coefficient of friction, but much less scatter. Both of these trends were also seen on the fused quartz and silicon samples, and discussed earlier.

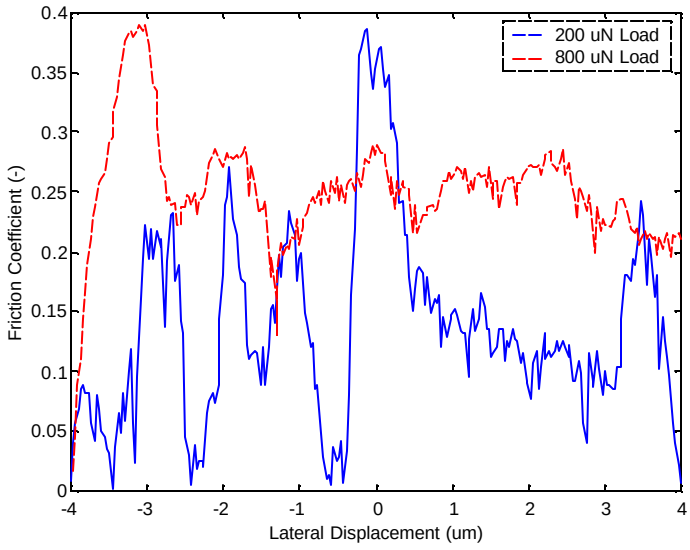

Figure 127: Friction coefficient, 8 mm scratch, constant load; Virgin surface

5.6.3.2 Scuffed Results

The analysis below examines 8 µm length scratches on the scuffed surface made with the 60°, 1 µm radius conical tip, under constant loads of 200 and 800 µN. The scratch profile (Figure 96) incorporates a pre-scratch scan of the surface to aid in the analysis. Figure 128 illustrates the normal displacement during a 200 µN constant load scratch on a scuffed surface. Both, the pre-scratch and scratch profiles are shown, as well as the difference and the average difference. The average depth of penetration of this scratch is 28 nm, with a standard deviation of 7.3 nm. This data is very similar to that of the virgin surface under a 200 µN load. Figure 129 is a similar graph for a scratch under a load of 800 µN. In this case, the average penetration is 225 nm, with a standard deviation of 70 nm. The normal penetration, under 800 µN load, is much greater than that observed in the virgin sample. Also, the penetration depth varies from 70-370nm within the scratch, indicating that the material is not consistent, even within such a small range as the length of the scratch.

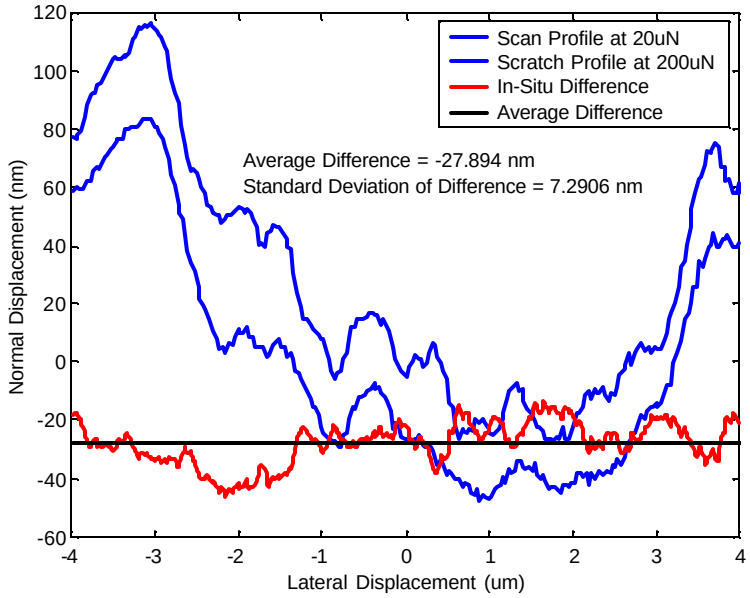

Figure 128: 8 µm scratch on Scuffed surface; 200 µN constant load

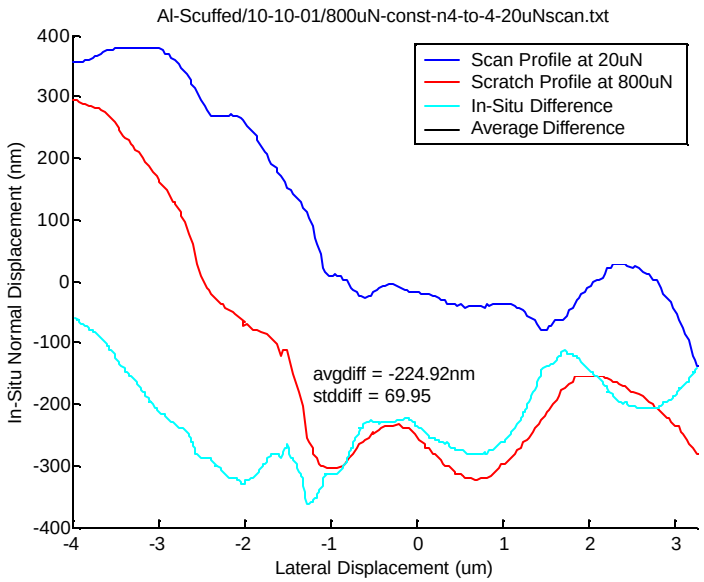

Figure 129: 8 µm scratch on Scuffed surface; 800 µN constant load

The average scratch depth of multiple scratches performed at 200 µN and 800 µN loads are shown in Figure 130. At the 200 µN load, the penetration and the scatter in the data are small, and comparable to that of the virgin surface. It is hypothesized that this is the result of the formation of the natural oxide layer on the aluminum. As discussed earlier, this natural oxide layer is on the order of three to four nano-meters thick, and is formed on aluminum surfaces exposed to the air in a matter of seconds. At this *in-situ* depth, the oxide layer is not penetrated (see Section 5.7.2, ramp load silicon results), thus negating any differences between the samples due to the wear process. Under the 800 µN load, there is a significant amount of scatter within the data. This scatter was also observed during individual scratches, as well as in the analysis of nano-indentation data on the scuffed surface. This indicates that the material is extremely non-uniform, even on the micron scale, and has been illustrated through microstructural analysis. Nonetheless, under the 800 µN load, the tip penetrates significantly deeper into the scuffed sample compared to the virgin sample, indicating a weakening of the surface films at this level. Figure 131 further illustrates the results of these two samples.

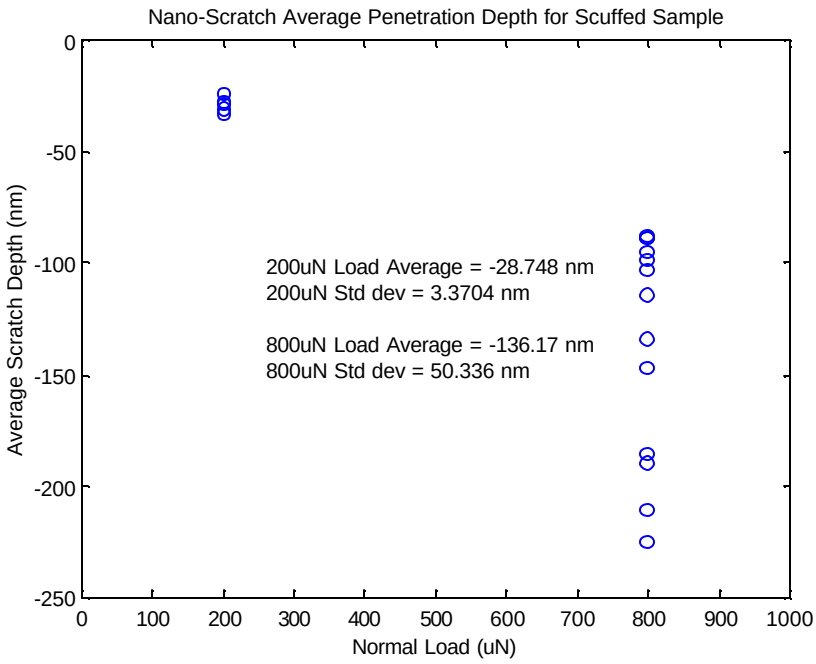

Figure 130: Normal penetration of 8 mm scratches on scuffed surface

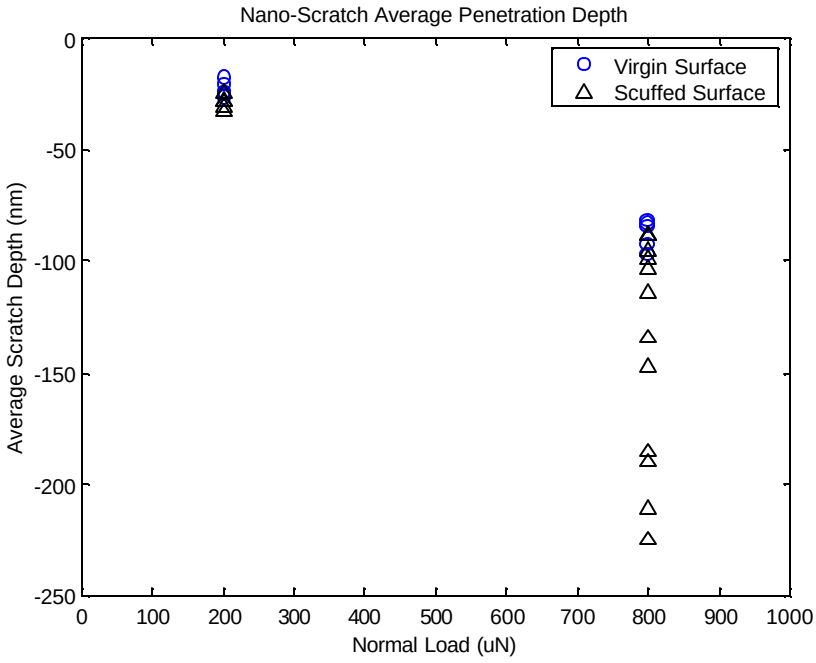

Figure 131: Average nano-scratch penetration depths

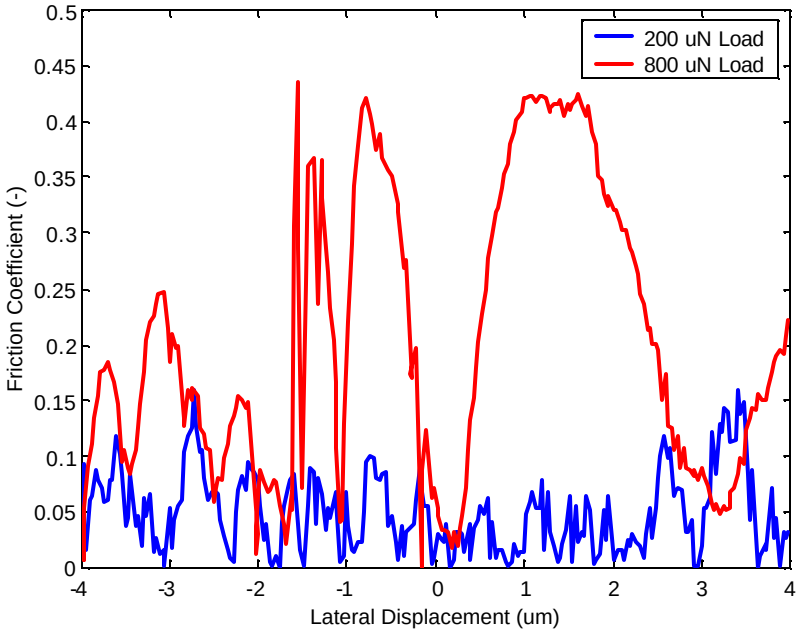

Figure 132: Friction coefficient, 8 μm scratch, 200 μN constant load, Scuffed surface

5.7 Ramp Load Scratch Profile

Ramp load scratches refer to a linear progression of the normal load on the scratch tip, while laterally scratching the tip over a prescribed path. These scratches are often used to qualitatively compare the relative thickness of different films. By scratching the surface at a constantly increasing normal force, the critical load and depth in which delamination of surface layer occurs can be found. This data can be used to analyze relative surface layer thicknesses and to obtain qualitative comparisons between samples.

Two typical ramp load scratch profiles are shown in Figure 133 and Figure 134. The first profile is appropriate for smooth surfaces where the surface roughness is negligible compared to the scratch data (i.e. fused quartz, silicon). The second profile includes a 20 μN pre-scratch scan, to obtain a surface profile of the surface before the scratch. The pre-scan profile can then be removed from the scratch data in order to examine the scratch as if it was on a perfectly flat sample. The basic ramp scratch profile (as defined by Hysitron, Inc.) is composed of 5 different segments:

1.) Laterally traverse from center of image position to negative lateral limit, under zero normal force (5 seconds)
2.) Obtain steady state condition of lateral displacement (3 seconds)
3.) Scratch sample – start at zero normal load and begin to laterally traverse the tip across sample; linearly increase load such that peak load is reached at the point when the tip reaches the positive lateral limit of the scratch (30 seconds)
4.) Linearly decrease normal load to zero, while maintaining constant lateral position (2 seconds)

5.) Laterally traverse the tip from the positive lateral displacement limit to the center of the image position, under zero normal force (5 seconds)

The profile is somewhat modified to incorporate a pre-scratch scan feature, as described below:

1.) A constant load profile of 20 μN is used as the pre-scan profile (see constant load profile, as described prior)

2.) The normal force is linearly ramped up to the pre-scan value (20 μN), while the tip is stationary at its negative limit. The scratch profile then begins from 20 μN, not 0 μN as described prior

Using these modifications, it is possible to obtain an accurate profile of the original surface, as well as obtain repeatable scratch data, independent of surface roughness. In all tests, the loading profile shown in Figure 134 (with various normal loads) is used. This will enable the acquisition of accurate, repeatable results that will allow true differences in surfaces to be correctly interpreted.

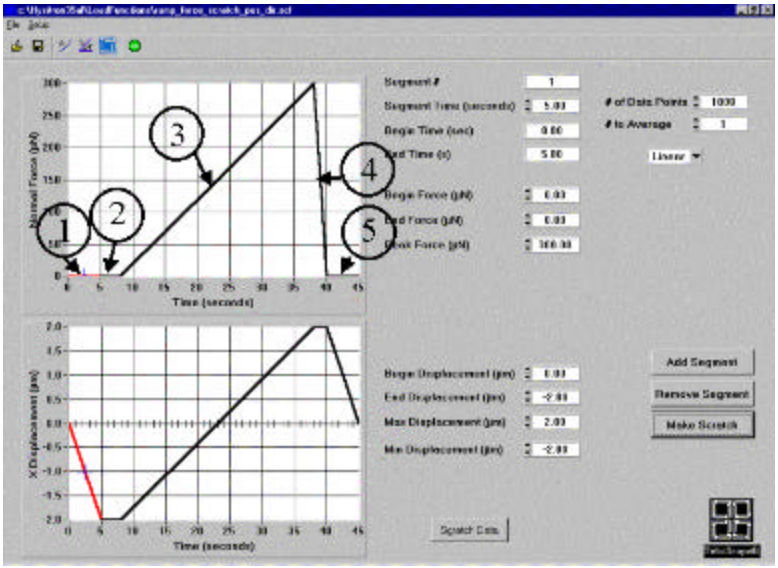

Figure 133: Ramp load scratch profile

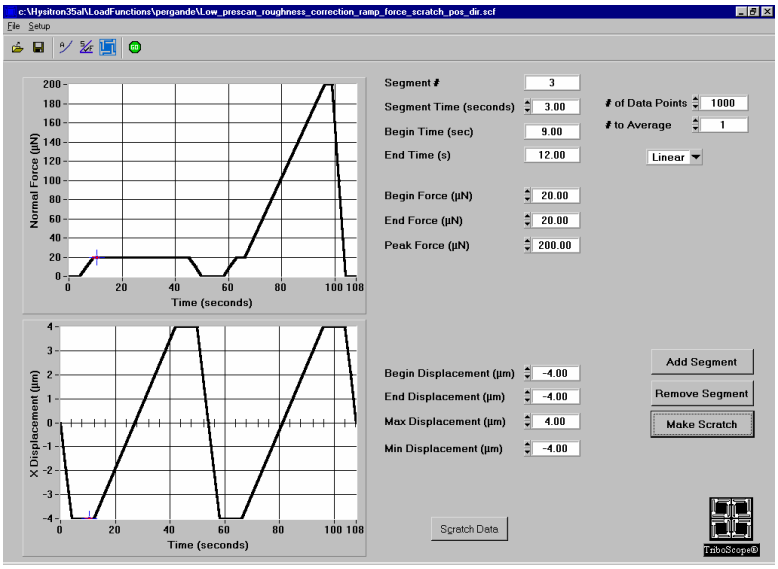

Figure 134: Ramp-load scratch profile, with pre-scan of surface

5.7.1 Fused Quartz Results

Several ramp load scratches were performed on fused quartz in order to study the response of such a scratch profile on a uniform material, with no surface layers. All scratches were performed with the 60°, 1 µm radius conical tip. Scratches were 8 µm in length, and made with the scratch profile shown in Figure 133. The peak loads were 1000, 3000, and 5000 µN, respectively.

Figure 135 illustrates the *in-situ* normal load recorded during several scratches, as a function of the scratch lateral displacement. Note that the normal load is a ramp profile, as designated by the scratch profile (normal load is included in the feedback loop). Engineering samples will be compared with the use of the same scratch profile, including the same scratch length and loading rate. Thus, in order to gain an understanding of the response of a pure homogeneous material, the scratch length was maintained constant, while the loading rate was varied. This choice will be supported later, and is further emphasized by the fact that no materials tested exhibit significant creep (see Section 4.92 for Al390-T6 creep discussion).

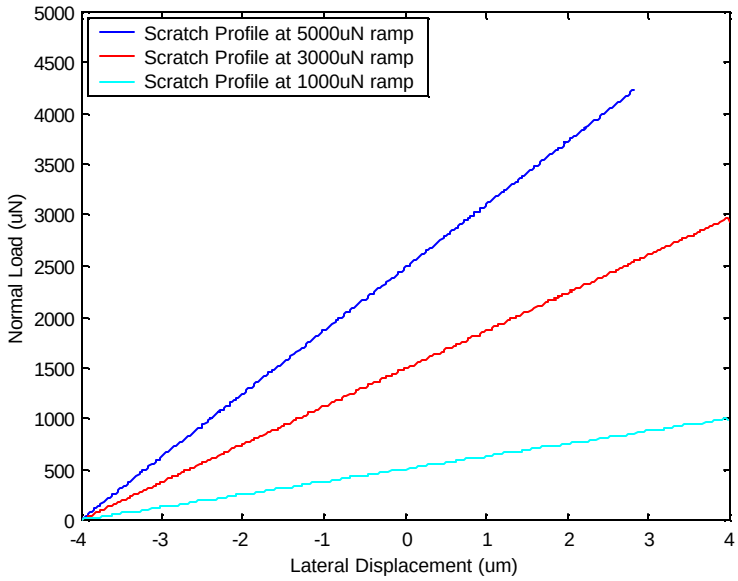

Figure 135: Normal load (ramp profile) of several 8 µm length scratches on fused quartz

The normal displacement, as a function of normal load, is shown in Figure 136. This profile is directly related to the tip area function discussed prior in the nano-indentation section (see Section 4.3), in that the scratch depth is a function of the tip area function. These curves all overlap, as should be expected from a test on uniform material. This also shows that the response is independent of the loading rate (discussed with Figure 135). This curve is continuous, with no sharp changes in slope or appearance, indicating a pure material with no surface layers, as expected.

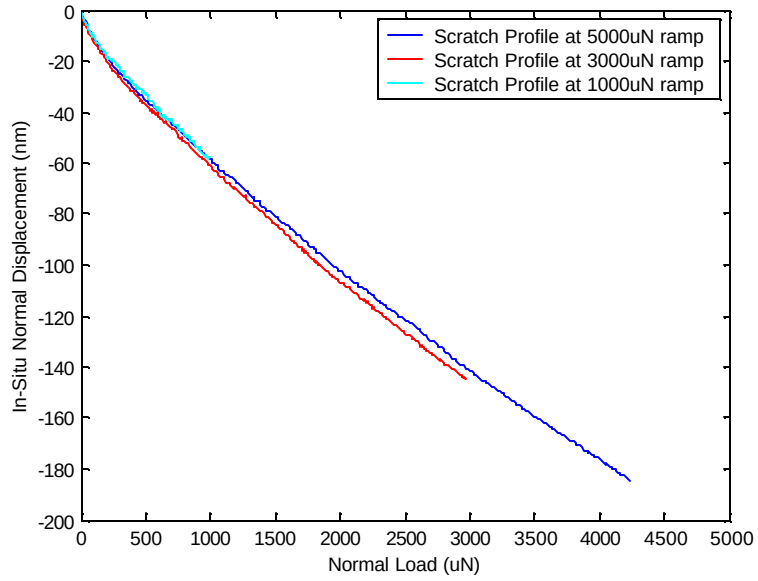

Figure 136: Normal displacement of several 8 µm length scratches on fused quartz

The coefficient of friction as a function of normal displacement is shown in Figure 137 below. For all three scratch profiles, the friction coefficient starts out high as the tip begins to scratch. By definition, the coefficient of friction is the lateral force divided by the normal force on the tip. At low displacements, the normal force is very small (approximately zero), while there are fluctuations in the lateral force signal (due to instrumentation limitations, etc.). Thus, at points when the normal load approaches zero, the coefficient of friction rises. As the displacement increases (normal load increases correspondingly), the coefficient then drops to a negligible value (dynamic friction under no permanent plastic deformation), until it starts to increase as the depth of penetration increases. Both, the low coefficient of friction under no permanent plastic deformation and an increased coefficient of friction for larger penetration depths, has also been observed with the constant load profile results, as shown earlier. The curves are reasonably consistent, with no dramatic differences between curves nor sharp jumps in the curves, which further emphasizes the response of a pure and uniform material. The scatter at low penetrations is larger than that observed at high penetrations, which has also been discussed with the constant load profile.

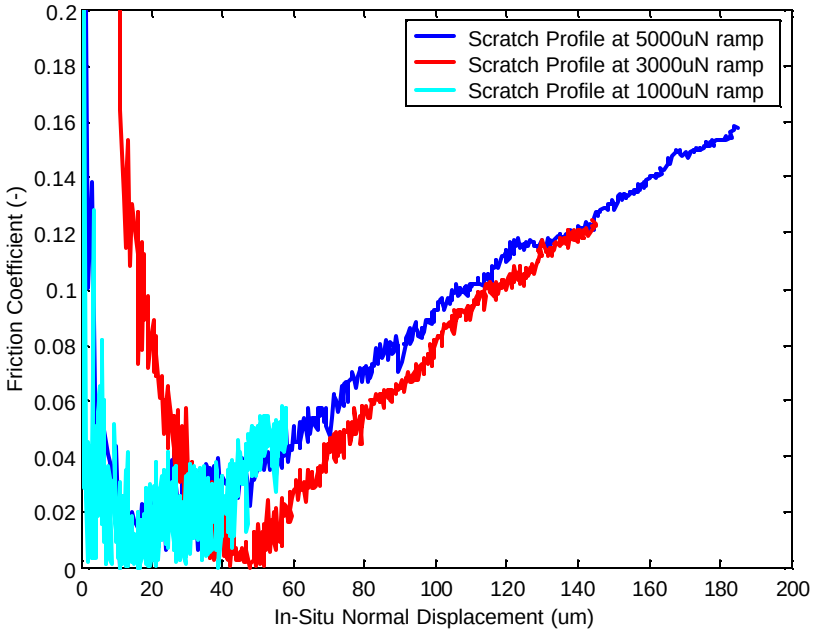

Figure 137: Coefficient of friction of several 8 µm length scratches on fused quartz

5.7.2 Silicon Results

Silicon will once again be used as a test material to understand the response of a ramp load scratch profile on a material with a known oxide layer of approximately 4-5 nm. Discussed below are the results of several 6 µm length scratches, with the load profile shown in Figure 133. The peak load was set at 1000, 3000, and 5000 µN, respectively. A 60°, 1 µm radius conical tip was used for all tests. Scratches were performed at least 1-2 mm away from other scratches in order to obtain an appropriate sample average.

Figure 138 illustrates the recorded normal load profile during the scratch of three scratches. These curves are very similar to those obtained from the fused quartz tests prior. Once again, silicon is a creep independent material, and thus the response should be independent of the loading rate.

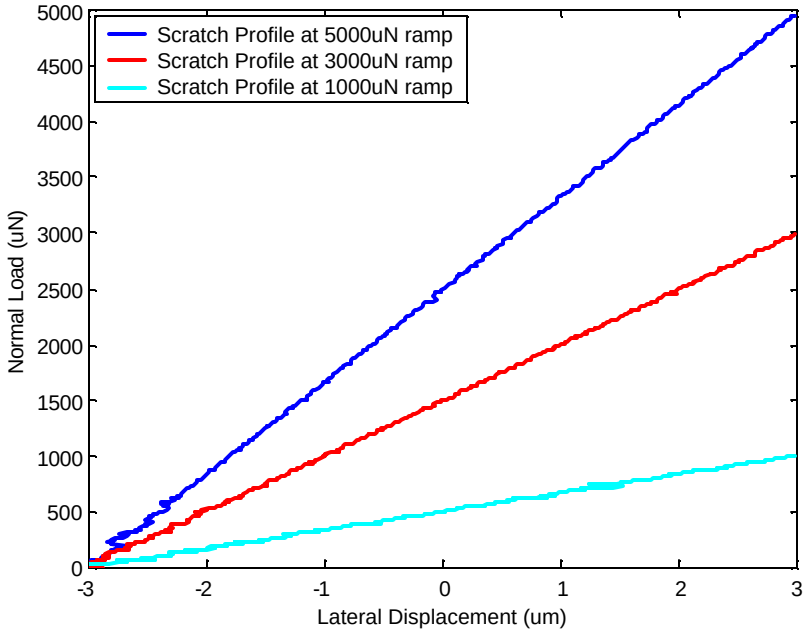

Figure 138: Normal load (ramp profile) of several 8 µm scratches on Silicon

Figure 139 illustrates the normal displacement as a function of normal load of the three scratches described earlier. The curves are extremely consistent for all scratches, as expected for a uniform material. There is also a point, at a normal displacement of 48 nm and corresponding normal load of approximately 2900 µN, in which the slope of the curve changes dramatically. This is the point at which delamination of the oxide film occurs, indicating that the protective oxide film has been penetrated. The load at this point is known as the critical load of the film. Examining the slopes of the curves gives relative information about the hardness of the film compared to the substrate. The slope of the initial portion is flatter than that of the response in the substrate material. This indicates that under the same external load, the tip will penetrate less into the oxide layer than it would if only the substrate were present. Thus, the oxide layer is harder than the substrate material. Also note that the 3000 and the 5000 µN load curves show the delamination point at the exact same point, at 48nm in normal penetration depth. Once again, this shows the consistency of the material, as well as the uniform thickness of the oxide layer. Based on prior knowledge, it is known that the thickness of the oxide layer is 4-5 nm, not the 48 nm that is observed from the delamination during the ramp load test. The differences lie in the radius of the tip. The tip radius of the scratch tip is approximately 1 µm, compared to the 50 nm radius tip used in the nano-indentation experiments. A sharper tip will lead to much more local plastic deformation, and thus more accurate portrayal of layer thicknesses. A larger radius tip will penetrate deeper before plastic deformation on the surface is reached (deformation is contained elastically). Nonetheless, this test will still allow for relative, qualitative comparisons between the layer thickness of

different samples. The analysis can be made somewhat quantitative through careful analysis techniques. Knowing that the true thickness of the oxide layer is approximately 4 – 5 nm, while it is observed at approximately 48 nm, gives a general idea about the relationship between the two values. This can be used on other surfaces to obtain a general idea of the layer thickness.

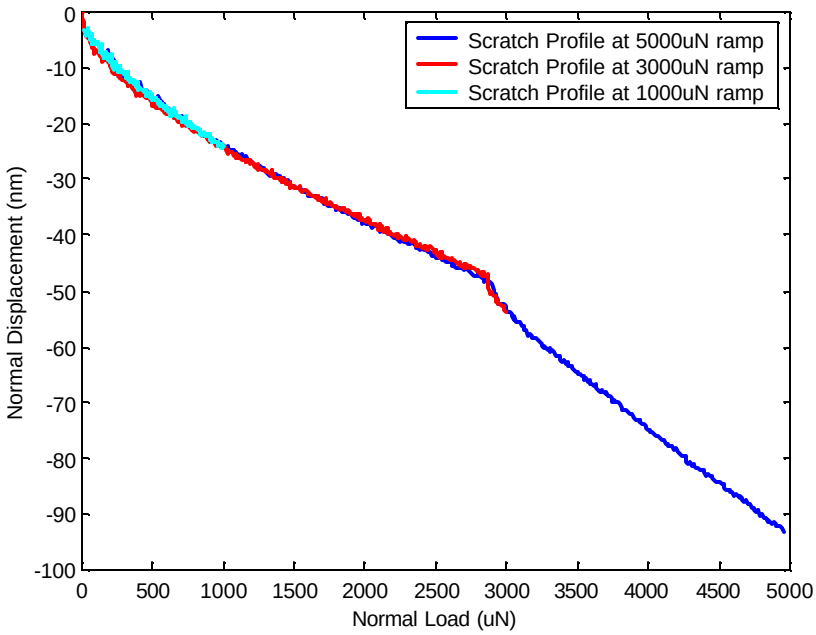

Figure 139: Normal displacement of several 8 µm scratches on Silicon

Figure 140 below illustrates the coefficient of friction of these three scratches. The coefficient of friction starts out high, as discussed in the fused quartz results (see Section 5.6.1). It then approaches an insignificantly small value. As normal depth increases, the coefficient of friction rises, but all the while, approaching zero fairly often. At approximately 45 nm in normal displacement, there seems to be a sharp rise in friction, after which it steadily increases. After this point, the coefficient of friction does not approach insignificantly small values, for any larger depths. This sharp rise in the mean friction coefficient is another indication of delamination of the oxide layer, and occurs at approximately the same depth as the change in slope of the normal displacement plot in Figure 139 (approximately 45 nm). These scratches are also extremely consistent, as expected for a uniform material.

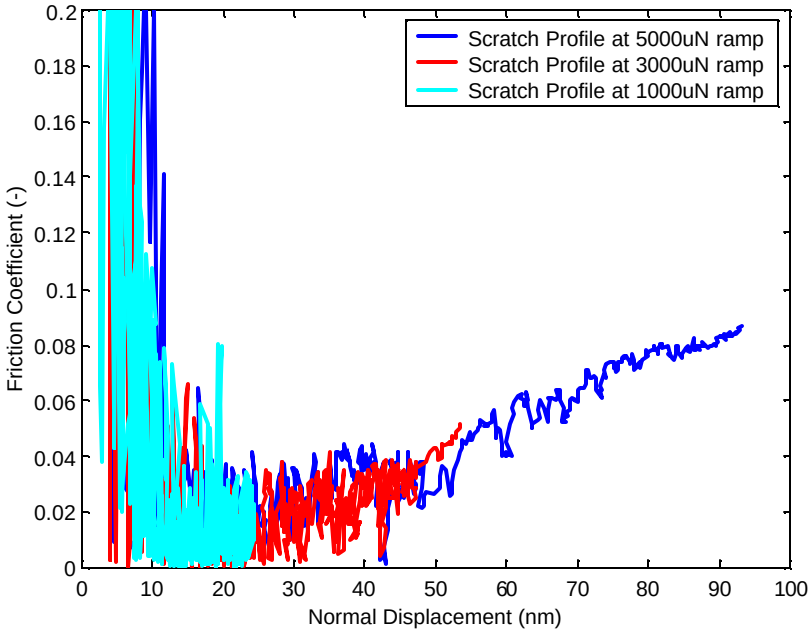

Figure 140: Coefficient of friction of several 8 µm scratches on Silicon

5.7.3 Al390-T6 Results

The ramp load scratch profile will be used for testing on the aluminum samples in order to gain a qualitative understanding of the variation of layer thickness during the wear process. The scratches are 8 µm in length, and use the ramp profile shown in Figure 134 in order to obtain a pre-scan profile of the surface prior to the scratch. The peak load is set at 200 µN. Thus, all tests maintain the same loading rate. All scratches are performed with the 60°, 1 µm radius conical tip.

A typical normal load profile for a ramp load scratch on an engineering sample is shown below in Figure 141. This profile is for a 200 µN ramp load scratch with a pre-scan load of 20 µN. The scratch begins with a positive load in order to compensate for the pre-scratch scan load offset. The load then increases, almost linearly, as designated by the ramp load function. Due to the roughness and non-uniform nature of the surface, this curve is significantly more jagged than those observed from the test samples, but is still linearly dominated.

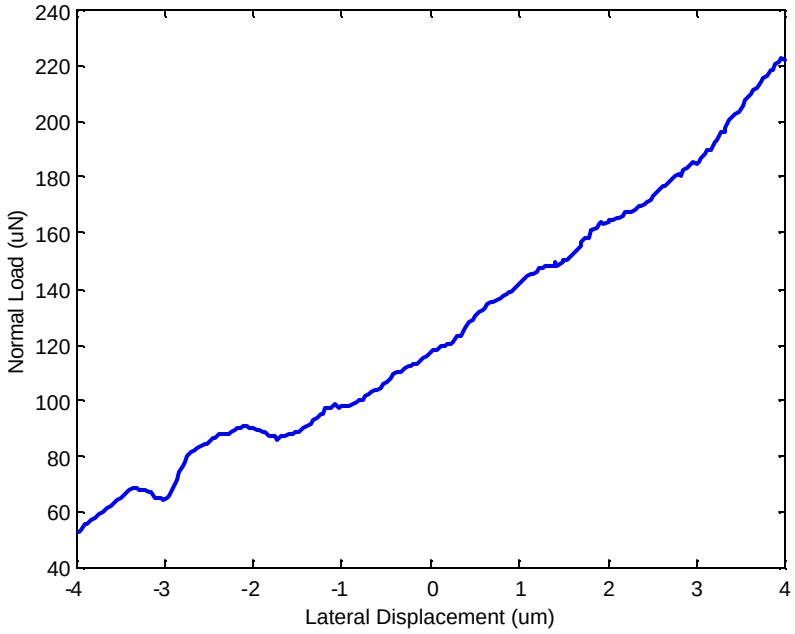

Figure 141: Normal load profile of an 8 µm scratch on the virgin surface

5.7.3.1 Virgin Results

Figure 142 is a corresponding scratch profile obtained from one of the 200 µN ramp load scratches on the virgin aluminum sample. The top line is a surface profile under the 20 µN scan load, while the line directly below is the *in-situ* normal displacement of the tip due to the ramp load scratch profile. The difference between the curves is also shown in the graph, taking the original, pre-scratch scan profile as the zero reference. Figure 143 shows a close-up of this difference. The normal displacement profile shows significantly more scatter than was observed on either the fused quartz or the silicon surfaces, but is in-line with those results seen from the constant load experiments.

Figure 144 shows the normal displacement as a function of the normal load. Examination of this curve shows a 'burst' at approximately 25 nm normal displacement, indicating that a film was penetrated (delaminated) at this point. This 'burst' does not indicate a film thickness of 25 nm (surface deformation is contained elastically due to a large tip radius, as discussed prior). But, based on the results from the silicon ramp load tests, it is estimated that this film is on the order of 3-4 nm thick. This corresponds quite well with the thickness of the native oxide layer on a pure aluminum surface, as discussed prior [Dowling, 1999].

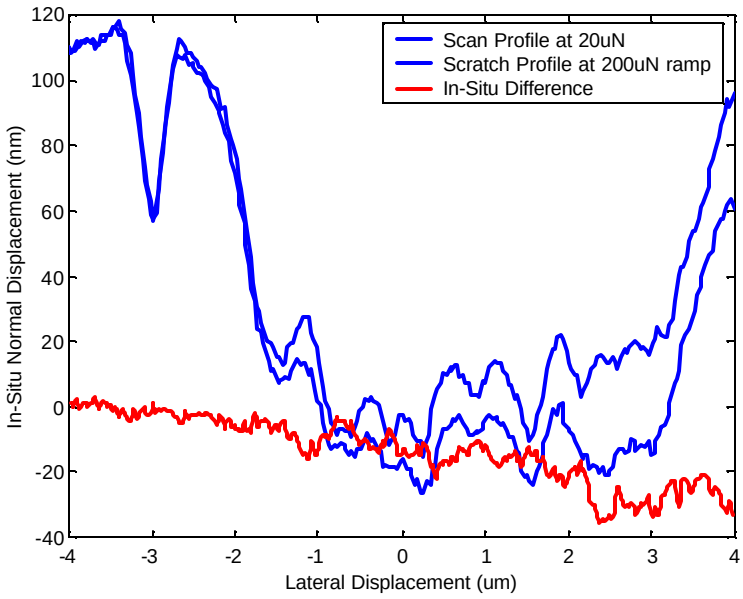

Figure 142: Normal displacement of an 8 mm scratch on the virgin surface

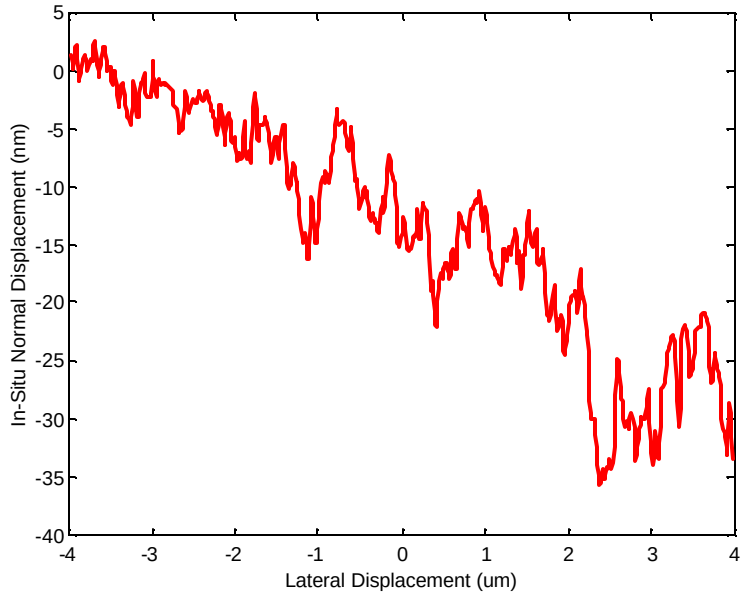

Figure 143: Normal displacement difference of an 8 mm scratch on the virgin surface

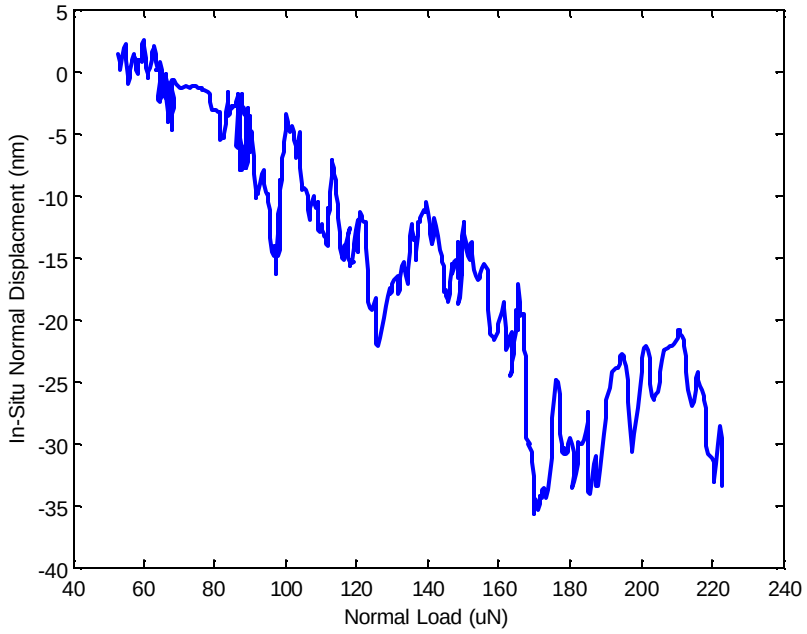

Figure 144: Normal displacement of an 8 µm scratch on the virgin surface

Figure 145 illustrates the friction coefficient as a function of the normal load. Ideally, the friction coefficient would be represented as a function of the normal displacement, but due to the scatter in the data associated with an engineering sample, this is impractical. But, these results, in combination with Figure 144, lead to a similar representation. There is a 'jump' in friction (i.e. friction coefficient no longer approaches zero) at a normal load of 160 – 185 µN (i.e. critical load). From Figure 144, this occurs at a normal displacement of 20-25 nm, which is very similar to the point of the 'burst' in normal displacement in Figure 143.

Figure 146 shows the response of several representative ramp load scratches on the virgin surface. There is a large amount of scatter in all data due to the extreme roughness of the engineering surface. Examining the graphs, all profiles show a 'burst' in normal displacement at some point between 12 – 25 nm depth. This seems to indicate the delamination of a similar film in all cases. In order to validate this finding, the friction coefficient of these profiles is examined in Figure 147. Scratch #1 clearly shows the 'jump' in friction, as discussed prior, but the other two scratches do not exhibit similar behavior. Thus, it can be hypothesized that a film delamination occurred at depth of approximately 15 – 20 nm, but further tests need to be run to verify this conclusion.

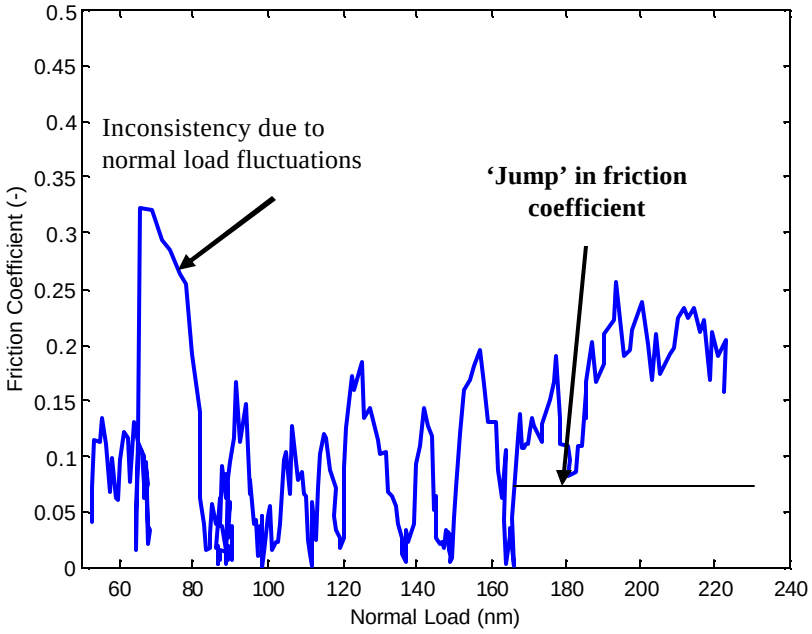

Figure 145: Coefficient of friction of an 8 µm scratch on the virgin surface

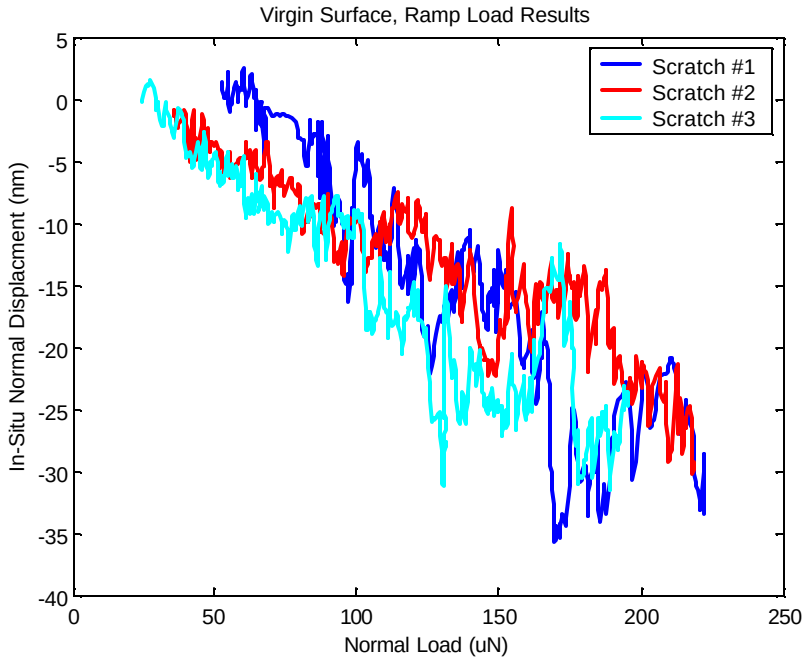

Figure 146: Ramp load normal displacement profile, virgin surface

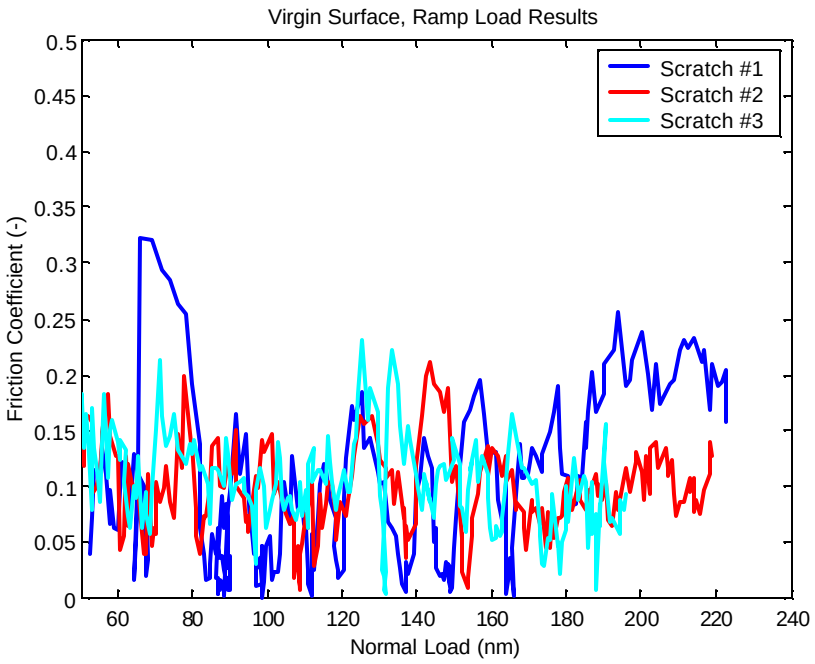

Figure 147: Ramp load friction profile, virgin surface

5.7.3.2 Scuffed Results

Similar 200 μN ramp load scratches were performed on the scuffed surface, and analyzed appropriately. One typical scratch profile is shown in Figure 148 below, with a magnified view of the roughness corrected scratch profile shown in Figure 149. These results are very similar to those observed on the virgin surface. It seems that there is a 'burst' in normal displacement at approximately 5 nm depth, corresponding to a delamination of this film at that point.

Figure 150 illustrates the corresponding friction coefficient from this scratch, as a function of the normal load. From this plot, the determination of the critical load is inconclusive, as there is never a 'jump' in the friction coefficient, after which, the friction coefficient does not return to zero. Thus, no clear conclusions about film thickness can be made.

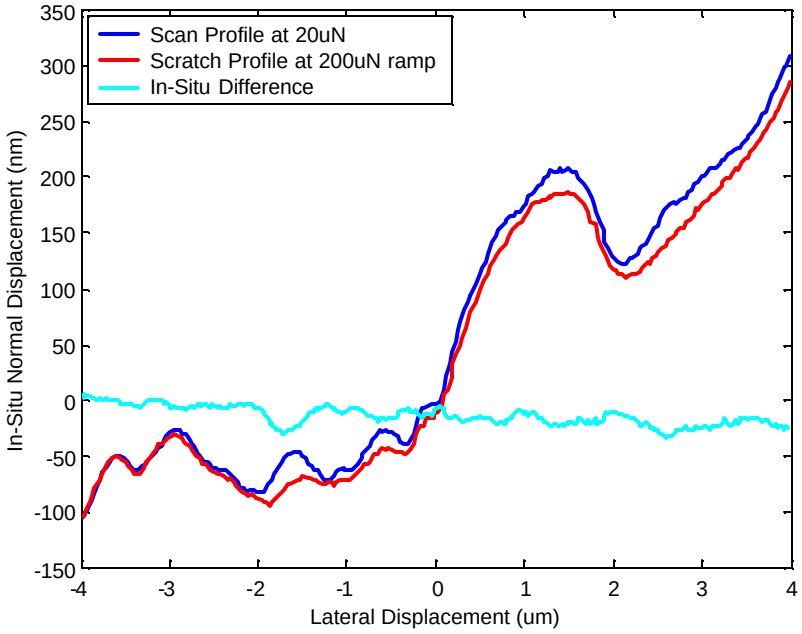

Figure 148: Ramp load scratch profile on scuffed surface

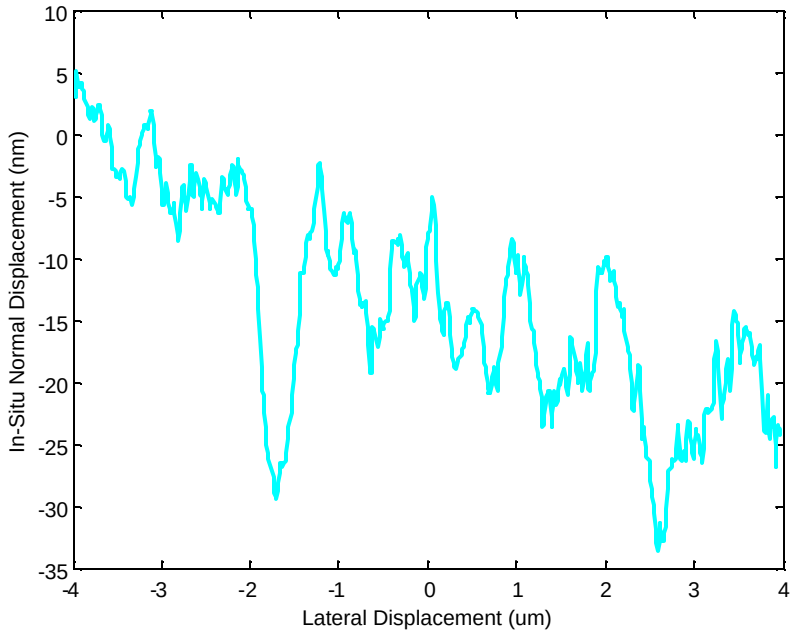

Figure 149: Ramp load roughness corrected scratch profile on scuffed surface, zoomed in

The normal displacement results of several ramp load scratches on the scuffed surface are shown below in Figure 151, with the corresponding friction coefficient profile shown in Figure 152. These plots show 'bursts' in displacement at a wide variety of depths. This is due, in part, to the complex nature and composition of the scuffed

surface. No clear trends can be observed from the friction coefficient plot. Thus, the use of the ramp load profile on the scuffed surface is inconclusive.

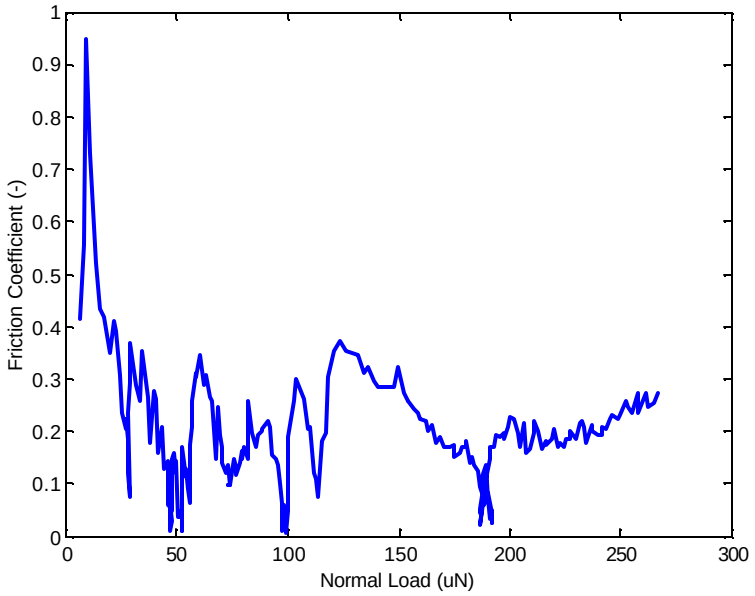

Figure 150: Ramp load friction coefficient profile on scuffed surface

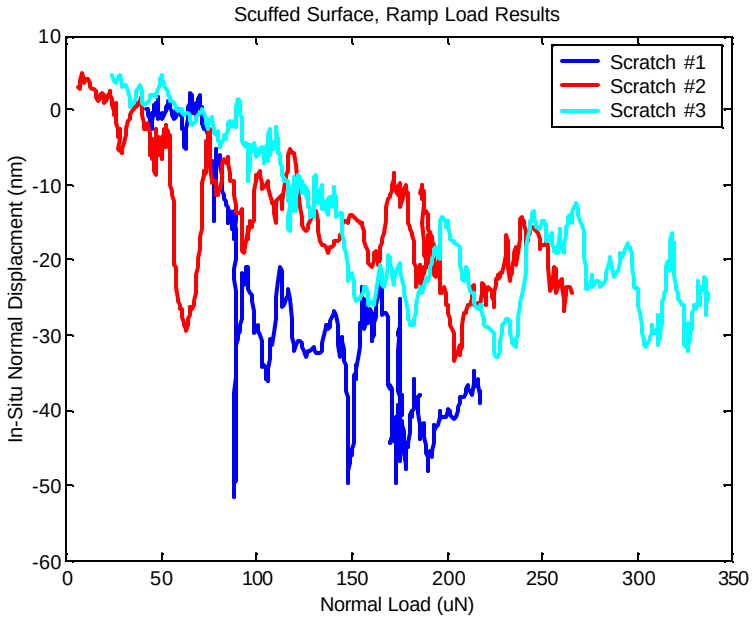

Figure 151: Ramp load, normal displacement profile, scuffed surface

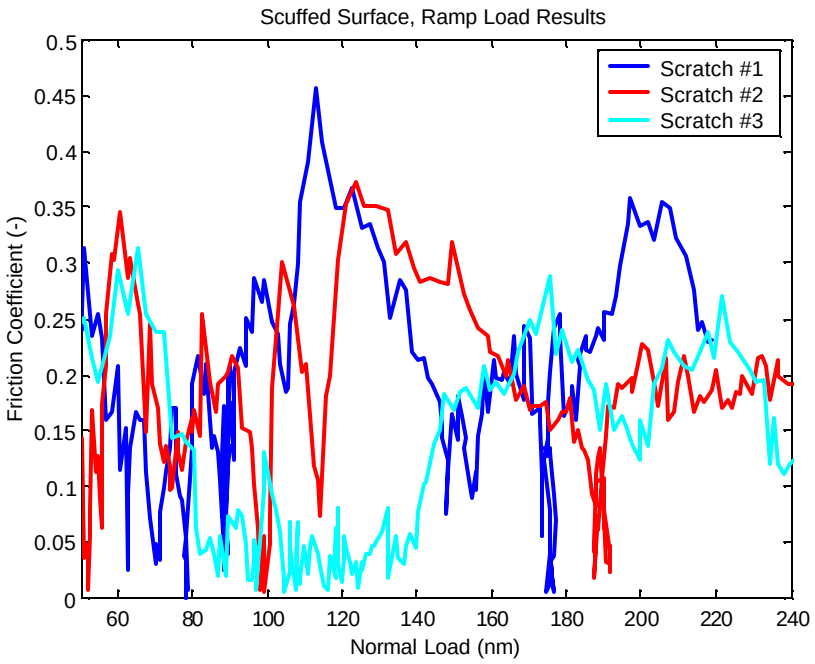

Figure 152: Ramp load, friction coefficient profile, scuffed surface

5.8 Conclusions

Nano-scratch is a technique that has been developed to better understand the mechanical behavior of thin films, at the nano-meter level. Similar to nano-indentation, this technique is commonly used in the semi-conductor and magnetic storage hard disk drive industries. The method consists of traversing a sharp tip over a prescribed lateral path, while applying a prescribed normal load on the tip. Both qualitative and quantitative analysis aspects of this test exist. Qualitative aspects include characterization of film hardness as a relative resistance to scratch penetration depth, as well as the analysis of relative film thickness. Quantitative film hardness results can be obtained through analysis of the scratch data. The benefits of nano-scratch are the ability to examine thin film material properties of films at extremely shallow depths (i.e. less than 10 nm), as well as an averaging effect of surface microstructure and non-uniform layer thickness over a several micron range. Thus, the results are more representative of the entire surface, rather than a particular point on the surface.

A 60°, 1 µm radius conical tip was selected for this aspect of the project, based on several criteria. The conical shape eliminates any possible directionality associated with the tip during a scratch. The 1 µm tip radius is one of the smallest radii that currently can be manufactured on a conical tip. Thus, this tip is the most appropriate tip for examining thin films at the nano-meter level.

Quantitative scratch hardness experiments have been performed on fused quartz, in order to evaluate scratch hardness equations. Based on the subsequent analysis, it was found that the scratch hardness of this material varies from 11 – 25 GPa, depending on the penetration depth (actual fused quartz hardness is approximately 9.6 GPa). This wide variability results from a major assumption that the tip is spherical in the corresponding scratch depth regime. In actuality, many tips do not have a perfectly spherical shape at the end of the tip, and thus the scratch hardness analysis is inaccurate. Thus, scratch hardness analysis is not used for the Al390-T6 surfaces.

Engineering surfaces incorporate several problems when analyzing scratch data. One of the most important is that of the large surface roughness, compared to typical "scratch" surfaces. This roughness must be removed from the normal displacement data in order to analyze accurately the scratch depth. By performing a pre-scratch scan of the surface, a reference is established, from which all subsequent scratch depth measurements can be based. This pre-scratch profile is incorporated into all scratches performed on engineering surfaces.

The use of two different type scratch profiles has been used on the Al390-T6 surfaces, to examine changes that occur during the wear process. These profiles are constant load scratches and ramp load scratches. Constant load scratches can be used to determine relative film hardness through the analysis of scratch penetration depths, at various normal loads. These scratches have been performed on the virgin and the scuffed surfaces, under normal loads of 200 μN and 800 μN. The average *in-situ* normal displacements of the scratches, resulting from these loads, are shown below in Figure 153 and Figure 154, respectively.

Both the virgin and the scuffed surfaces exhibit consistent results, and similar scratch penetration depths, under the 200 μN constant load (although, scratches on the scuffed surface penetrate slightly deeper than on the virgin surface), see Figure 153. Based on these findings, it is hypothesized that the protective oxide layer has not been penetrated, at this depth. Thus, the measured properties are those of the oxide layer (formed on the surface immediately after the wear test), and not of the actual wear surface. Thus, many of the differences between the surfaces are nullified at this depth level. Other researchers have quantified the oxide layer thickness, on pure aluminum, as 3 – 4 nm thick. Examining the penetration data in Figure 153, the average penetration ranges from 15 – 35 nm, which is larger than the published value of the oxide layer thickness. Due to the relatively large radius of the scratch tip (micron-range), the deformation on the surface is contained elastically by the subsurface material (through Hertzian analysis), thus allowing a deeper penetration before the surface material yields. Thus, this analysis is purely qualitative in nature.

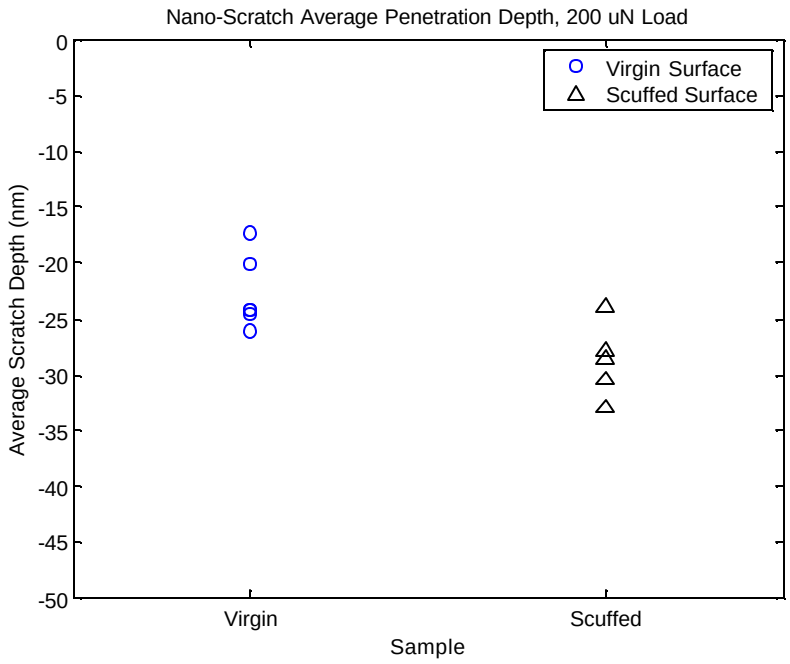

Figure 153: Nano-scratch average penetration depth, 200 µN normal load

The average scratch penetration depths resulting from the 800 µN constant load are shown in Figure 154. As expected, the scratches on both surfaces penetrate deeper, under the larger normal load. The depths on the virgin surface are very consistent, indicating a somewhat consistent and uniform material. The penetrations on the scuffed surface show much more variability than those observed on the virgin surface. The minimum scratch penetration depth on the scuffed surface is very similar to that observed on the virgin sample (i.e. approximately 80 nm), but there are also a large number of scratches with a much larger average penetration depth (up to 230 nm). These trends indicate a weakening of the uppermost layers of the scuffed surface (the residual depths resulting from these scratches range from 10 – 30 nm), as well as the very complex material composition of the surface (as illustrated by the large variability in the measurements).

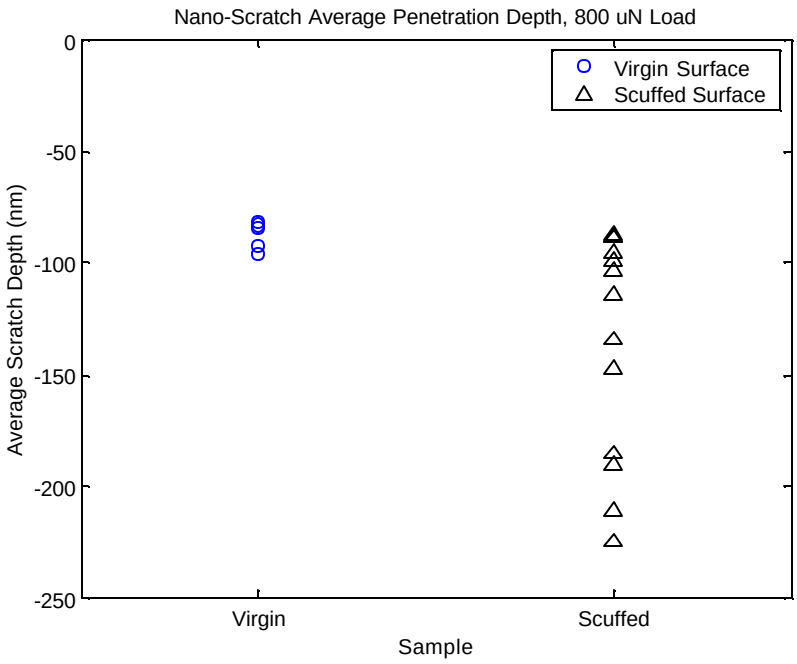

Figure 154: Nano-scratch average penetration depth, 800 µN normal load

These trends observed from the results of the 800 µN normal load scratches, correspond quite well with those results obtained from nano-indentation experiments on the virgin and scuffed surfaces (see Section 4.11.1 and 4.11.5). Examining the virgin surface hardness profile (Figure 155), the results are very consistent, showing low scatter, at low depths (less than 60 nm). The scuffed surface hardness profile shown in Figure 156 shows much more variability in the film hardness at low depths (less than 60 nm). Both profiles have a similar upper-bound on the hardness, but the scuffed surface exhibits some points with a much lower hardness than is observed on the virgin surface (i.e. more scatter). Similar trends are observed from the results of the 800 µN constant load scratches, as discussed prior.

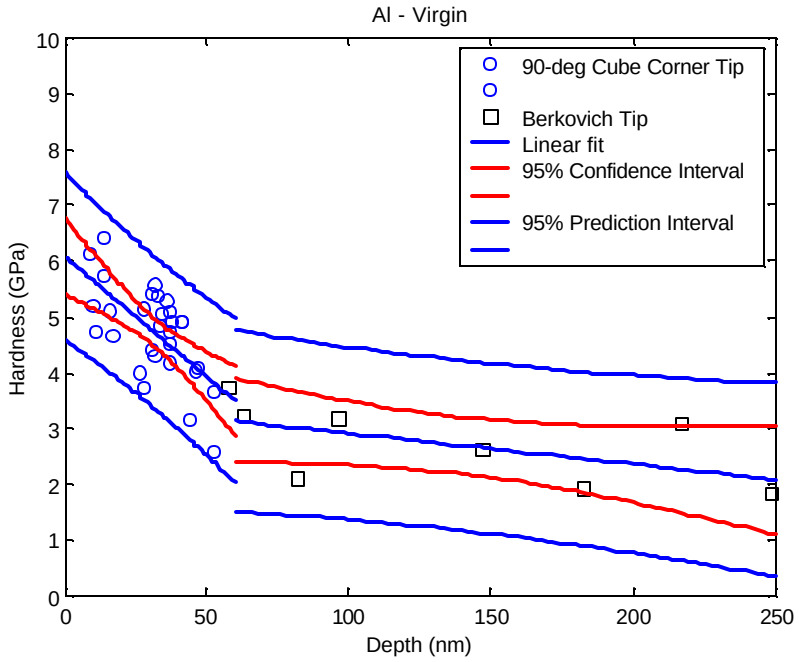

Figure 155: Nano-indentation hardness profile, Al390-T6 virgin surface

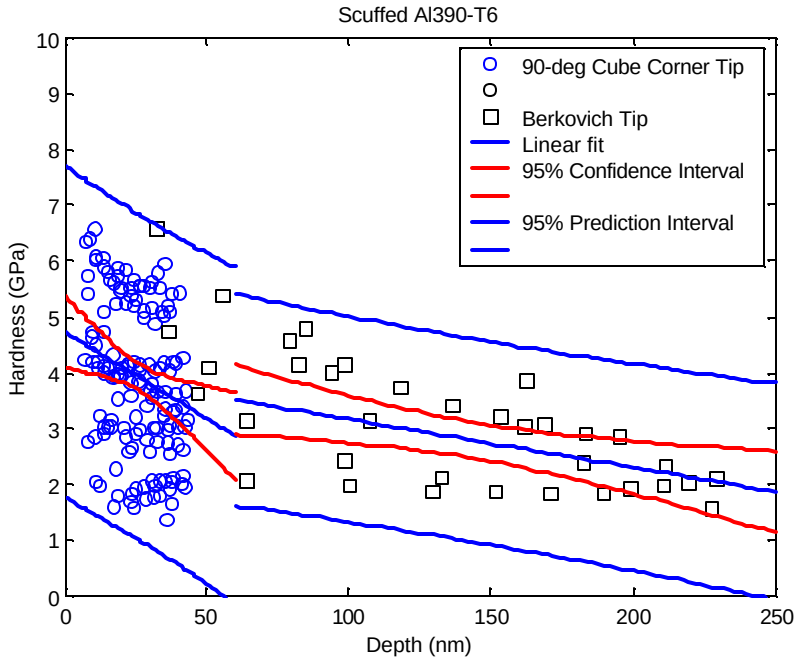

Figure 156: Nano-indentation hardness profile, Al390-T6 scuffed surface

Ramp load profiles can be used to determine relative layer thickness, through analysis of normal displacement and friction plots. In general, delamination of the film can be observed as either a change in slope / discontinuity in the normal displacement plot, or as a sudden increase in the measured friction coefficient. These

results are mainly qualitative. The results from the use of the ramp load profile on the Al390-T6 wear surfaces are much more difficult to interpret (compared to the constant load scratch results), due to the extreme roughness associated with engineering surfaces. In general, the delamination depth of the oxide layer on the virgin surface can be established as 15 – 25 nm penetration depth. These results are fairly consistent from scratch to scratch. The delamination depth of the oxide layer on the scuffed surface is much more difficult to determine, due, in part, to the complexities / variability associated with the scuffed surface. Thus, no clear conclusions can be made at this time. Future work based on the analysis of ramp loads should focus on larger loads (i.e. deeper depths) to try to determine the changes in layer thicknesses below the surface.

Chapter 6: Conclusions and Recommendations

6.1 Introduction

Scuffing is a very complex process, without a clear understanding of the fundamental causes behind its occurrence. It is clear that there are many factors that affect this process, but it is only through obtaining an in-depth understanding of the actual conditions (i.e. chemical, topographical, mechanical, and microstructural analyses), that a fundamental cause can be determined. Most prior research has focused on examination of subsurface changes at the micron level. Recent findings suggest that the most significant changes occur in the top 50 – 100 nm of the surface, not at the micron level as previously suggested. The goal of this project is to substantiate this claim that the most significant changes occur in the top 50 – 100 nm, and to quantify the changes in material properties at this level. Microstructural analysis and nano-mechanical methods of determining thin film material properties have been used to accomplish these goals.

6.2 Conclusions from this Study

Microstructural analysis has greatly improved the understanding of both the underlying material microstructure, as well as the thickness and appearance of the deformed layers due to scuffing. The 'bulk' microstructure is composed of a variety of different areas, corresponding to dramatically different chemical composition. The majority of the surface (>50%) is covered by the aluminum matrix, which is composed of mainly aluminum, with a small amount of soluble copper and silicon. The most noticeable feature is that of the presence of large, insoluble silicon particles, which have a width of 10 – 20 μm and occupy approximately 10% of the surface area. The rest of the surface is composed of several different smaller regions, imbedded within the aluminum matrix, that have correspondingly different chemical compositions. This microstructure must be considered when attempting to analyze hardness data, depending on the size of the indentation. Sample cross-section analysis shows some interesting results. The scuffed sample subsurface shows a microstructurally transformed layer up to depths of 500 – 700 nm, while the depth of the plastically deformed region is approximately 3 – 5 μm. These thicknesses are significantly smaller than those shown in other studies that suggest these thicknesses are 5 – 10 μm and 50 – 60 μm, respectively. It has also been shown that the presence of silicon is an inhibitor of surface deformation in these regions.

Meso and micro hardness tests have been performed on the respective samples, and no significant changes in surface hardness, at depths from 2 – 130 μm, nor any differences between samples, have been observed. Based on the relative microstructural dimensions discussed earlier, these tests, by enlarged show an averaging effect of the microstructure due to the relatively large size of the indenter, and resulting in mainly consistent data.

Nano-indentation has been used to characterize the surface/subsurface changes in material properties at the nano level, thus extending the meso/micro analysis aspects into the near surface depths associated with nanometer depths. This technique is typically used on semi-conductor and magnetic storage Hard Disk Drive surfaces, which are very different from those surfaces in this study. These samples have significantly rougher surfaces, non-homogeneous structure, and are composed of unknown and non-uniform surface layers. These aspects add considerable difficulty to the use of this technique on engineering surfaces. Through thorough data analysis

techniques, in combination with microstructural knowledge, it is possible to develop repeatable method for the use of nano-indentation on these surfaces. Several conclusions can be made based on the results of these tests:

1.) The top 60 nm is significantly harder for all samples. The hardness at a depth of 10 nm is approximately 3 – 4 times larger than that of the bulk material. The hardness decreases significantly in this region.
2.) 'Bulk' properties are reached after approximately 100 nm below the surface. Below approximately 100 nm, the subsurface hardness is relatively constant.
3.) There is good correlation and continuity between the nano, micro, and meso hardness scales, thus gaining support for the applicability of nano-indentation on engineering surfaces.
4.) A hardness lower bound for all samples and scales exists at approximately 1.6 GPa, which is the value corresponding to the hardness of the bulk material.
5.) There is reasonable consistency (within the context of engineering surfaces) in the measurements on all surfaces. Added support for the use of nano-indentation on engineering surfaces.
6.) A gradual weakening of the uppermost 60 nm occurs as the wear process proceeds.
7.) There are no significant differences between samples beyond 100 nm, as the wear process proceeds.
8.) The scuffed surface is very complex. Hardness values ranging from those of the 'bulk' material (low) to those observed on the virgin surface (high) can be obtained at very small depths (<15 nm).
9.) The Elastic Modulus is relatively insensitive to depth from the surface.

Nano-indentation results further substantiate the finding that the most significant changes occur in the top 60 nm below the surface. These results also support that a weakening of this film occurs during the wear process, as was suggested by a depletion of silicon on the surface finding in an earlier study. Beyond this range, the changes in hardness are minimal. This contradicts earlier studies that suggested the most important/significant surface layers were on order of 5 – 150 μm below the surface.

Nano-scratch has been used as a method to verify some of the findings from the nano-indentation tests. At low scratch loads and depths (~3 – 4 nm residual depth), the virgin and the scuffed samples show similar penetration depths, thus indicating similar material properties at this depth. These similarities have been attributed to the presence of a natural oxide layer on the surface of aluminum, which has a thickness of 3 – 4 nm, thus nullifying any potential differences between the samples. At higher scratch loads, and thus deeper penetration depths, the results from the virgin sample are very consistent, as was observed from nano-indentation. The use of larger scratch loads on the scuffed surface show a significant amount of scatter in the data, ranging from penetration depths observed on the virgin sample to much greater penetration depths due to a much softer material. These results are very similar to those observed from nano-indentation tests, showing that the scuffed surface is significantly weaker than that of the virgin surface, and also that the scuffed surface shows a very complex structure, as noted by a large amount of scatter in the data.

6.3 Recommendations

Scuffing is a very complex process. Researchers have spent over 60 years trying to understand the underlying causes of this phenomenon, and as of to date, not found a conclusive answer to explain all aspects. The microstructural and material property characterization is only a small part of the overall study, although the conclusions made here are very significant to the overall understanding of the scuffing mechanism.

Future work on the material property characterization should focus on repeating these experiments with different samples, material combinations, lubricants, refrigerants, etc., in an effort to examine if these occur for a wide range of test conditions. The use of an extremely sharp nano-indentation tip known as the 'North Star' should be investigated, as this tip is capable of obtaining accurate material properties at depths of less than 10 nm. The use of nano-scratch should be further investigated with a sharper tip in order to get the more localized plastic deformation needed to obtain accurate data of thin films in less than 20 nm (i.e. conical tip is too blunt). The ramp load function should also be investigated at different load/tip combinations, in an effort to quantify some of the changes in thickness of the oxide layers that may accompany the wear process.

A next step in the fundamental study of the scuffing mechanism is to incorporate these surface material properties into a Finite Element Model, in order to examine the effects of temperature on the surface/subsurface interface.

References

Bhattacharya, A. K. and Nix, W. D., "Finite Element Simulation of Indentation Experiments," *Int. J. Solids Structures,* Vol. 24, No. 9, 1988, pp. 881-891.

Bhushan, B., "Nanoscale tribophysics and tribomechanics," *Wear,* 225-229 (1999), pp. 465-492.

Blok, H., "Theoretical Study of Temperature Rise at Surfaces of Actual Contact Under Oiliness Conditions," *Inst. Mech. Eng. General Discussion on Lubrication,* 2 (1937), pp. 222-235.

Bradley, E. F., "Improving Friction Behavior with Surface Treatments," *Metals Engineering Quarterly,* 7 (1967) 2, pp. 29-32.

Buehler, Inc., Instructions: Micromet® II Microhardness Testers, 1984.

Carpick, R. W., Salmeron, M., "Scratching the Surface: Fundamental Investigations of Tribology with Atomic Force Microscopy," *Chem. Rev.,* 1997, 97, pp. 1163-1194.

Cavatorta, M. P., and Cusano, C., "Running-in of aluminum/steel contacts under starved lubrication Part I: surface modifications," *Wear,* 242 (2000), pp. 123-132.

Cavatorta, M. P., and Cusano, C., "Running-in of aluminum/steel contacts under starved lubrication Part II: Effects on scuffing," *Wear,* 242 (2000), pp. 133-139.

Consiglio, R., Randall, N. X., Bellaton, B., Von Stebut, J., "The nano-scratch tester (NST) as a new tool for assessing the strength of ultrathin hard coatings and the mar resistance of polymer films," *Thin Solid Films,* 332 (1998), pp. 151-156.

Dowling, Norman E., Mechanical Behavior of Materials: Engineering Methods for Deformation, Fracture, and Fatigue, Second Edition. Prentice-Hall, Inc., Upper Saddle River, New Jersey, 1999, pp. 50.

Dyson, A., "Scuffing – A Review, Part I," *Tribology International,* 8, 1975, pp. 117-125.

E-140-88, ASTM Annual Book of Standards, American Society for Testing and Materials, Philadelphia, PA.

Factor, M., Roman, I., "Vickers microindentation of WC – 12% Co thermal spray coating Part I: statistical analysis of Microhardness data," *Surface & Coatings Technology,* 132 (2000), pp. 181-193.

Factor, M., Roman, I., "Vickers microindentation of WC – 12% Co thermal spray coating Part II: the between-operator reproducibility limits of microhardness measurement and alternative approaches to quantifying hardness of cemented-carbide thermal spray coatings," *Surface & Coatings Technology,* 132 (2000), pp. 65-75.

Greenwood, J. A., and Williamson, B. P., "Contact of Nominally Flat Surfaces,"*Proc. R. Soc. London, Ser A,* 295, pp. 300-319.

Hay, J. C., Bolshakov, A., Hugher, B., and Pharr, G. M., 1999, "A Critical Examination of the Fundamental Relations Used in the Analysis of Nanoindentation Data," *J. Mater. Res.,* Vol. 14, No. 6, pp. 2296-2305.

Hysitron, Inc., "Advanced Lateral Force," User Manual, 3/4/99, pp. 1-7.

Hysitron, Inc., "Nano-Scratch User Manual."

Johnson, K. L., "The Correlation of Indentation Experiements," *J. Mech. Phys. Solids,* 1970, Vol. 18, pp. 115-126.

Komvopoulos, K., Ye, N., "Three-Dimensioal Contact Analysis of Elastic-Plastic Layered Media With Fractal Surface Topographies," *Transactions of the ASME,* Vol. 123, July 2001, pp. 632-640.

Kral, E. R., Komvopoulos, K., Bogy, D. B., "Hardness of Thin-Film Media: Scratch Experiments and Finite Element Simulations," *Journal of Tribology,* January 1996, Vol. 118, pp. 1-11.

Kuhn, L., "The TriboScope® Nanomechanical Testing System," Hysitron, Inc., July 7, 1998.

Kuhn, L., Corcoran, S., Wyrobek, T., "Measuring the hardness of ultra-thin coatings," *Data Storage,* July 1998, pp. 55-57.

Kurath, P., "Hardness Testing," University of Illinois at Urbana-Champaign, Undergraduate Mechanical Testing Laboratory.

Kuromoto, N. K., Fiusa, D. L., Cantao, M. P., Lepienski, C. M., "Nanoscratching characterization of austenitic stainless steels modified by cathodic hydrogenation," *Materials Science and Engineering*, A269 (1999), pp. 83-89.

Li, X., Bhushan, B., "Micro/nanomechanical and tribological characterization of ultrathin morphous carbon coatings," *Journal of Materials Research*, Vol. 14, No. 6, June 1999, pp. 2328-2337.

Lo, Roger Yu. Bogy, David B., "Compensating for elastic deformation of the indenter in hardness tests of very hard materials" *Journal of Materials Research*, vol. 14, n. 6, 1999, pp. 2276-2282.

Lu, W., Komvopoulous, K., "Nanotribological and Nanomechanical Properties of Ultrathin Amorphous Carbon Films Synthesized by Radio Frequency Sputtering," *Journal of Tribology*, July 2001, Vol. 123, pp. 641-650.

Naghavi, N., Rougier, A., Marcel, C., Guery, C., Leriche, J. B., Tarascon, J. M., "Characterization of indium zinc oxide thin films prepared by pulsed laser deposition using a Zn3In2O6 target" *Thin Solid Films.*, vol. 360, n. 1-2, Feb 1 2000, pp. 233-240.

Oliver, W. C., and Pharr, G. M., "An improved technique for determining hardness and elastic modulus using load and displacement sensing indentation experiments," *J. Mater. Res.*, Vol. 7, No. 6, June 1992, pp. 1564-1582.

Park, K. B., Ludema, K. C., "Evaluation of the plasticity index as a scuffing criterion" *Wear*, vol. 175, n. 1-2, Jun 1994, pp. 123-131.

Patel, Jayesh Jitendra, "Investigation of the Scuffing Mechanism Under Starved Lubrication Conditions Using Macro, Meso, Micro, and Nano Analytical Techniques," M.S. Thesis, University of Illinois, May 2001.

Randall, N. X., Consiglio, R., "Nanoscratch tester for thin film mechanical properties characterization," *Review of Scientific Instruments*, Volume 71, No. 7, July 2000, pp. 2796-2799.

Rockwell Hardness Testing, University of Illinois at Urbana-Champaign, Undergraduate Mechanical Testing Laboratory.

Sheiretov, T. K., "Scuffing of Aluminum/Steel Contact Under Dry Sliding Conditions," PhD Thesis, The University of Illinois at Urbana-Champaign, 1997.

Sheiretov, T., Van Glabbeek, W. Van., and Cusano, C., "Simulative friction and wear study of retrofitted swash plate and rolling piston compressors," *Int. J. Refrig*, Vol. 18, No. 5, 1995, pp. 330-335.

Sheiretov, T., Yoon, H., and Cusano, C., "Scuffing Under Dry Sliding Conditions: Part I – Experimental Studies," *Tribology Transactions*, Vol. 41 (1998), 4, pp. 435-446.

Somi Reddy, A., Pramila, B. N., Murthy, K. S. S., Biswas, S. K., "Mechanism of seizure of aluminium-silicon alloys dry sliding against steel" *Wear*, vol. 181-183, n. 2, Mar 1995, pp. 658-667.

Vander Voort, George, "Preparation of Cast Aluminum-Silicon Alloys," *Tech – Notes: Using Microstructural Analysis to Solve Practical Problems*, Published by Buehler Inc., 1999, Volume 3, Issue 2.

Walpole, R. E., Myers, R. H., Myers, S. L., Probability and Statistics for Engineers and Scientists, Prentice Hall, New Jersey, 1998.

Wear Control Handbook, Peterson and Winer, Editors, Glossary of Terms and Definitions in the Field of Friction, Wear and Lubrication, pp. 1182.

Wei, B., Komvopoulos, K., "Nanoscale Indentation Hardness and Wear Characterization of Hydrogenated Carbon Thin Films," *Journal of Tribology*, April 1996, Vol. 118, pp. 431-438.

Williams, J. A., Engineering Tribology, Oxford University Press, New York, NY, 1998, pp. 167.

Yoon, H. K., "Scuffing Under Starved Lubrication Conditions," PhD Thesis, University of Illinois at Urbana-Champaign, 1999.

Yoon, H., Sheiretov, T., and Cusano, C., "Scuffing behavior of 390 aluminum against steel under starved lubrication conditions," *Wear*, 237 (2000), pp. 163-175.

Yoon, H., Sheiretov, T., and Cusano, C., "Scuffing of Area Contacts Under Starved Lubrication Conditions," *Tribology Transactions,* Vol. 43 (2000), pp. 722-730.

Yoon, H., Sheiretov, T., and Cusano, C., "Tribological evaluation of some aluminum-based materials in lubricant/refrigerant mixtures," *Wear,* 218 (1998), pp. 54-65.

Zamfirova, G. Dimitrova, A., "Some methodological contributions to the Vickers Microhardness technique," *Polymer Testing,* 19 (2000), pp. 533-542.

Zhao, Y, Chang, L., "A Model of Asperity Interactions in Elastic-Plastic Contact of Rough Surfaces," *Journal of Tribology,* October 2001, Vol. 123, pp. 857-863.